CONTROL STRATEGIES FOR ELECTRIC VEHICLE CHARGING INFRASTRUCTURE

by

AAKASH KUMAR SETH

Department of Electrical Engineering

A Thesis submitted

in partial fulfillment of the requirements

for the Award of the Degree of

Doctor of Philosophy

To the

DEPARTMENT OF ELECTRICAL ENGINEERING

DELHI TECHNOLOGICAL UNIVERSITY

DELHI, INDIA

DECEMBER-2021

CERTIFICATE

This is certified that the thesis entitled **"Control Strategies for Electric Vehicle Charging Infrastructure"** being submitted by **Mr. Aakash Kumar Seth** for the award of degree of Doctor of Philosophy in the Department of Electrical Engineering, Delhi Technological University, Delhi. It is the record of student's own work carried out by him under my supervision. The contents of this research work have been submitted in part or full to any other university or institute for award of any degree.

Date: _____/____/____

Prof. Mukhtiar Singh
Department of Electrical Engineering
Delhi Technological University, Delhi
Shahbad Daulatpur, Delhi-110042
India

ACKNOWLEDGEMENT

I wish to express my sincere appreciation to those who have contributed to this thesis and supported me in one way or the other during this amazing journey of my research.

Firstly, I would like to express my sincere gratitude to my research director ***Prof. Mukhtiar Singh*** for his continuous support during my Ph.D. study and related research. His patience, motivation, and immense knowledge have been an inspiration and guiding light for me. His guidance helped me in all the time during this research work and writing of this thesis. I am also highly obliged for his unlimited support on my personal front without which it would not have been possible for me to finish my work.

Besides my supervisor, I would like to thank ***Prof. Kapil Sharma***, ***Prof. M.M Tripathi***, ***Prof. Ram Bhagat***, ***Prof. S.K Valluru*** and ***Mr. D.C. Meena*** for helping me wherever required and provided me continuous motivation during my research.

I also want to specially mention about our Head of Department (EE), ***Prof. Uma Nangia*** and ***Prof. Dheeraj Joshi*** (OIC) who provided me an opportunity to do research and gave access to the laboratory and research facilities. Without their precious support, it would not be possible to conduct this research.

I thank to my seniors & colleagues, ***Dr. Ashutosh Trivedi***, ***Dr. Dinesh Kumar***, ***Aditya Narula***, ***Dr. Hemant Saxena***, ***Dr. Ajishek Raj***, ***Dr. Suryakant Shukla***, ***Pankhuri Asthana***, ***Avdesh Kumar***, ***Saket Gupta***, ***Snigdha Sharma***, ***Kailash Rana*** and ***Nimmi***, who were always present there with me during my research discussion and suggestions. I would like to show my gratitude to ***Mr. Vivek Raiwani*** and ***Mr. Shivam Kr. Sundaram*** for their help in assembling the hardware setup. There are other numerous names of friends that should be mentioned here, especially ***Mr. Sumit Kumar***, ***Mr. Vipin Singh*** and ***Mr. Shubhendra Yadav***, who support me spiritually and emotionally throughout my research.

I would especially like to thank our Power Electronics Laboratory staff Late ***Sh.Vinod Kumar***, ***Ms. Renu***, ***Ms. Vandana*** and ***Mr. Raju*** for their continuous support and help during my research work.

Last but not least, I am always indebted to my grandparents Late ***Smt. & Sh. Dal Chand Seth***, my parents ***Smt. & Sh. Om Prakash***, my brothers ***Mr. Arvind Seth***, ***Mr. Abhishek Seth*** and all other family members for supporting me during all the ups and down throughout my life.

Date: ___/___/___

Aakash Kr. Seth

(2K17/PHD/EE/10)

Dedicated to my beloved parents

Smt. Raj Dulari & Sh. Om Prakash

ABSTRACT

The Electric Vehicles (EVs)/ plug-in hybrid EVs (PHEVs) are slowly and steadily making inroads, in public as well as personal vehicle markets worldwide. The limited fuel reserves and pollution caused due to conventional internal combustion engine (ICE) driven vehicles are the main driving elements for allowing a paradigm shift towards EVs. However, with the rapidly increasing demand of EVs, many experts had a manifest concern regarding the charging infrastructure and thus, several studies have been presented over it. With the growing popularity of EVs, power distribution networks are under stress to accommodate the charging infrastructure. The large-scale penetration of EV charging loads in low voltage network may lead to severe voltage fluctuations, overloading of distribution transformer and harmonics related power quality issues.

To subsides the negative effect of EVs on distribution system, smart charging technique must be required. During one of the two operating mode, EV charger transfers active power to grid as well as compensating reactive power and known as Vehicle to grid (V2G) mode. This mode requires a bidirectional EV charger which may operate in all over the active-reactive (P-Q) power plane.

Moreover, single phase single stage EV chargers have inherent problem of producing second order ripple component on DC side. This problem is further exaggerated during vehicle-to-grid (V2G) mode of operation where it may be normally controlled to supply both active as well as reactive power. During the V2G reactive power compensation, the second order harmonics ripple component at DC side will increase which further reduces the life cycle and performance of battery pack. Therefore, the second order ripple component must be minimized for improving the life of battery pack.

Therefore, the main aim of proposed study is to develop a robust control system for EV charger to operate it in wide range of G2V and V2G mode of operations while maintain the amount of ripple content on DC side within the permissible limit. The EV charger may supply active power to grid if required and compensate reactive power (inductive or capacitive) if a battery charges at slower rate. In that case, the remaining rating of charger is utilized for compensating the reactive power for optimally utilization of charger's rating. Moreover, if the battery is not connected to the charger, then the EV charger can work as an active power filter and improves the power quality.

In this regard, total four control techniques based on proportional integral (*PI*), proportional resonant (*PR*), plant integrated proportional integrated (*PIPI*), repetitive controller (*RC*), and adaptive neuro-fuzzy inference system (*ANFIS*) have been presented in this thesis for two stage EV charger. The two control techniques have been presented for both ON board and OFF board EV charger. These EV chargers having two conversion stages i.e., AC-DC and DC-DC converter. Both the converters have their separate controller. Moreover, for single phase single stage ON board EV charger, a control technique has been proposed for minimization of second order ripple presented on DC side. For this, single phase AC-DC converter is utilized for charging purpose. Further, all the EV chargers are able to compensate the reactive power of local load. They all have active and reactive power input references where active command depends on customer desire charging rate and reactive command is requested by grid. All EV charger prototype is controlled by using dSPACE 1104 in laboratory.

LIST OF CONTENTS

LIST OF FIGURES

LIST OF TABLES

LIST OF ABBREVIATIONS

C_{DC}	DC-link capacitance
C_f	DC-DC converter filter capacitance
d	Duty ratio
I_{abc}, I_{Gabc}	Three-phase grid current
I_{bat}	Battery current
I_{Cabc}	Three-phase charger current
I_d	Direct-axis current component of grid
I_{Labc}	Three-phase load current
I_q	Quadrature-axis current component of grid
L_f	DC-DC converter filter inductance
L_s	Grid side inductor
P, P_G	Grid side active power
P_C	Charger active power
P_L	Load active power
V_{abc}, V_{Gabc}	Three-phase grid voltage
V_{bat}	Battery voltage
V_{Cabc}	Three-phase charger voltage
V_{DC}	DC-link voltage
V_d	Direct-axis voltage component of grid
V_{Labc}	Three-phase load voltage
V_q	Quadrature-axis voltage component of grid
Q, Q_G	Grid side reactive power
Q_C	Charger reactive power
Q_L	Load reactive power
AC & DC	Alternating current & Direct current
ANFIS	Adaptive neuro fuzzy inference system
BEV	Battery electric vehicle
CCS	Combine charging system
EV	Electric vehicle
FEV	Fuel cell electric vehicle
G2V	Grid to vehicle
HEV	Hybrid electric vehicle

IEC	International electrotechnical commission
IEEE	Institute of electrical and electronics engineers
IGBT	Insulated gate bipolar transistor
PCC	Point of common coupling
PHEV	Plug-in hybrid electric vehicle
PI	Proportional integral
PIPI	Plant integrated proportional integrating
PR	Proportional resonant
PWM	Pulse width modulation
RC	Repetitive controller
SAE	Society of automotive engineers
SOC	State of charge
THD	Total harmonic distortion
V2G	Vehicle to grid
V2V	Vehicle to vehicle

INTRODUCTION CHAPTER 1

Chapter Outline

1.1 Why Electric Vehicle?

With depletion of oil reserve, a paradigm shift is required from fossil fuel vehicle to zero emission, more efficient and sustainable electric vehicle (EV). To discourage the use of fossil fuel usage in order to get rid of pollution and greenhouse emission, the interest in research for EVs has increased significantly in last two decades [1]. Although, the industry of such vehicle is massively growing but the obstacle of short driving range is creating a hindrance in the pathway of overruling the automotive industry where fuel based conventional vehicles is still a priority for consumers [2]. Therefore, hybrid electric vehicles (HEVs) are gaining popularity. These types of vehicles having minimum two energy sources in which one of them is providing electrical energy [3]. They carry a conventional gasoline engine and an electric motor. Therefore, a HEV provides long driving range but highly reliant on gas. Since, a hybrid vehicle has two powertrains, they are much more complex, highly expensive and required more maintenance in comparison with gasoline and electric vehicle as they have single

powertrain. However, the EVs are clean alternative for environment as there is no need of liquid fuel. They are highly responsive, provide a high torque and may save more on fuel consumption and maintenance in comparison with other gasoline based vehicles [4].

1.2 EVs, Chargers and Charging Power Levels

1.2.1 Classification of Electric Vehicles (EVs)

Generally, EV can be classified as Battery Electric Vehicle (BEV), plug-in hybrid electric vehicle (PHEV), HEV and Fuel Cell Electric Vehicle (FCEV) [5] [6].

Table 1.1: Comparison of EV types.

EV Type	Driving Component	Source	Merits	Demerits
BEV	Electric motor	Battery, Ultracapacitor	No carbon emission, less running cost, less maintenance cost in comparison with HEV & PHEV.	Battery life and its cost, short driving range and charging time
HEV	Gasoline engine, Electric motor	Battery, Ultracapacitor, Gas	Moderate emission, higher range than BEV.	Expensive, required more maintenance, highest running cost and complex architecture
PHEV	Gasoline engine, Electric motor	Battery, Ultracapacitor, Gas	Very less emission, highest driving range.	Highly expensive, required large battery pack than HEV and complex architecture
FCEV	Electric motor	Fuel cell	No carbon emission, not depends on electricity and required less time to refuel.	High fuel cell cost, transportation and production of hydrogen and life cycle of fuel cell

a) Battery Electric Vehicle (BEV): **-** The EV which has only single source of energy i.e., battery is known as BEV. The BEV only depends on energy available in battery pack. Hence, the range of BEV directly depends on capacity of battery pack. Generally, these vehicles can go 100-250 KM on single charge, whereas the vehicles having larger battery bank can cover around 300-500 KM. However, these ranges may vary and depends on driving style and conditions. Moreover, BEVs are environmental friendly and very less running cost [7].

b) <u>Hybrid Electric Vehicle (HEV)</u>: - These types of EVs have two sources of energy i.e., fuel and battery pack. They have both internal combustion (IC) based engine and electrical powertrain. The electrical energy source can be used in low-speed conditions, urban areas and when low power is required. It can help in reduction of fuel consumption in case of traffic jams condition. When high speed is required, these vehicles switch to IC engine. Moreover, both drivetrains can be used together to increase the performance of vehicle. However, due the two energy sources the cost of HEVs is higher than the BEVs. Further, the working modes of HEV is discussed below [8], [9].

(i) Electric only

In Electric only working mode, the vehicle is driven by battery energy only as shown in Fig. 1.1. Here, the electrical energy is passed through the DC-DC and AC-DC converters. During this mode, there is no consumption of fuel and vehicle is driven by electrical energy of battery pack. Due to that, this mode is very much suitable for environmental point of view.

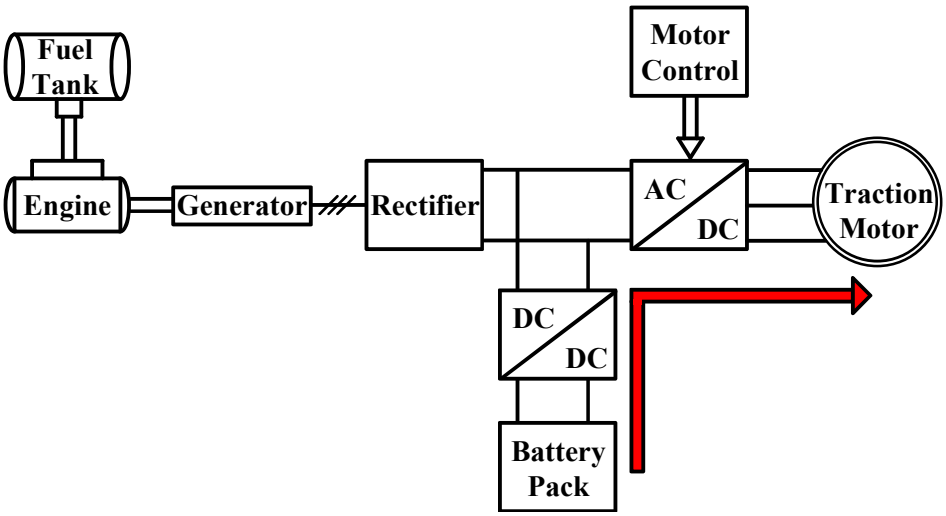

Figure 1.1: *Electric only mode of HEV.*

(ii) Hybrid Electric Assist

In this working mode, both IC engine and battery pack supplies energy to wheels as shown in Fig. 1.2. This working mode is used to improve the driving performance of vehicle. However, during this the stress on mechanical coupling is increased due to the simultaneously operation of IC engine and electric motor. Generally, small vehicles use this combination because of its compact configuration.

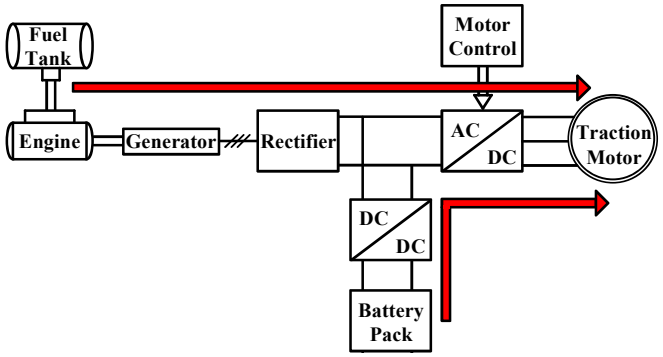

Figure 1.2: *Electric assist mode of HEV.*

(iii) Battery Charging

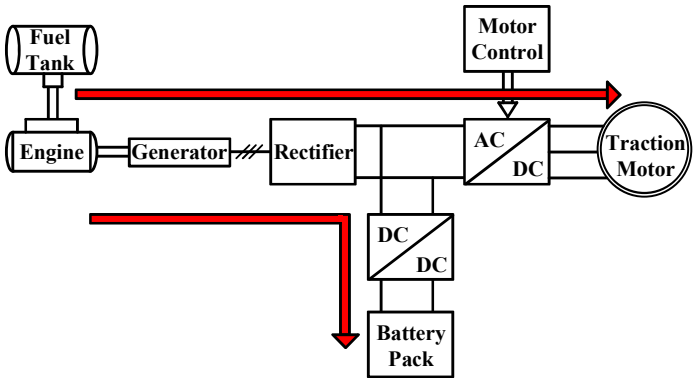

Figure 1.3: *Battery charging mode of HEV.*

During this mode, the IC engine drives traction motor while charging the battery pack as shown in Fig. 1.3. However, this required two back-to-back conversion stages i.e., AC-DC and DC-AC to drive the motor and a DC-DC conversion to charge the battery pack. This increases the stress on IC engine as it performs two operations simultaneously.

(iv) Regenerative Braking

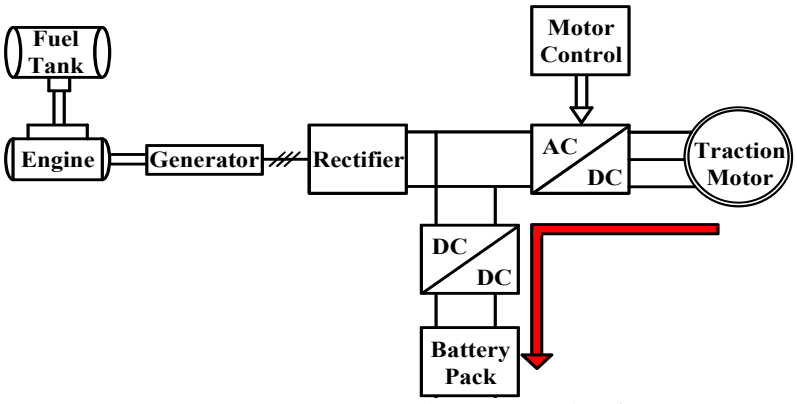

Figure 1.4: *Regenerative braking mode of HEV.*

Fig. 1.4 shows the regenerative braking mode, during this, the electric motor works as a generator and charge the battery pack by the energy available on wheels. During this, the kinetic energy available in motor is converted into electrical energy and supplied back to the battery pack.

c) Plug-in Hybrid Electric Vehicle (PHEV): - The PHEVs have also two powertrains (i.e., gasoline engine and electric motor) like HEVs but the electric propulsion is main driving force in PHEVs. Therefore, it requires larger battery pack than HEV, whereas the gasoline engine provides a boost in driving range or charge up the battery source [10].

d) Fuel Cell Electric Vehicle (FCEV): - The EVs which has fuel cell source to provide power to drivetrain are known as FCEVs. The advantage of such vehicle is the electricity produce by fuel cells emits no carbon and time required to refueling it is same as convention vehicle. However, due to the demerits in FCEVs such as high fuel cell cost, hydrogen storage, transportation and production of hydrogen and life cycle of fuel cell, these vehicles are not much popular [11].

On the other hand, the major barriers that has stagnated the overall success of EVs are high cost, battery life, energy storage capacity, charging complications, short driving range and lack of charging infrastructure [12]. Table 1.1 summaries the comparison of above discussed EV types.

The EV mainly consist of three electric parts: an electric motor with gear box, energy storage system (battery) and power electronics converter for battery charging and motor driving as shown in Fig. 1.5 [13]. To overcome the problem of short driving range in EV, the establishment of fast EV chargers is mandatory [14]. The system employs two types of charging i.e., ON board charging and OFF board charging [15]. The OFF board chargers are known as outdoor chargers, whereas ON board chargers are installed onto the vehicle. The EV chargers may be two or single stage [16]. A single stage charger consists of one power conversion stage i.e., AC to DC. In which the grid is connected across the AC side and vehicle battery pack is connected to the DC side [17]- [18]. Whereas, dual-stage EV charger consists of two back-to-back connected power conversion stages i.e., AC-DC and DC-DC converters [19]. The second stage DC-DC converter reduces the ripple at battery side and provides galvanic isolation between grid

and battery pack [20]. From the battery life point of view, it is suggested to use a DC-DC stage in between battery and AC-DC conversion stage. However, the use of DC-DC stage will increase the hardware cost, with decreased efficiency and increased component count. Moreover, in comparison of two stage charger the control complexity is quite low for single stage charger but it must have higher voltage at DC link than the amplitude of the AC side voltage. However, the EV charger attains the requisite voltage level by two-stage conversation in accordance with battery parameters [21].

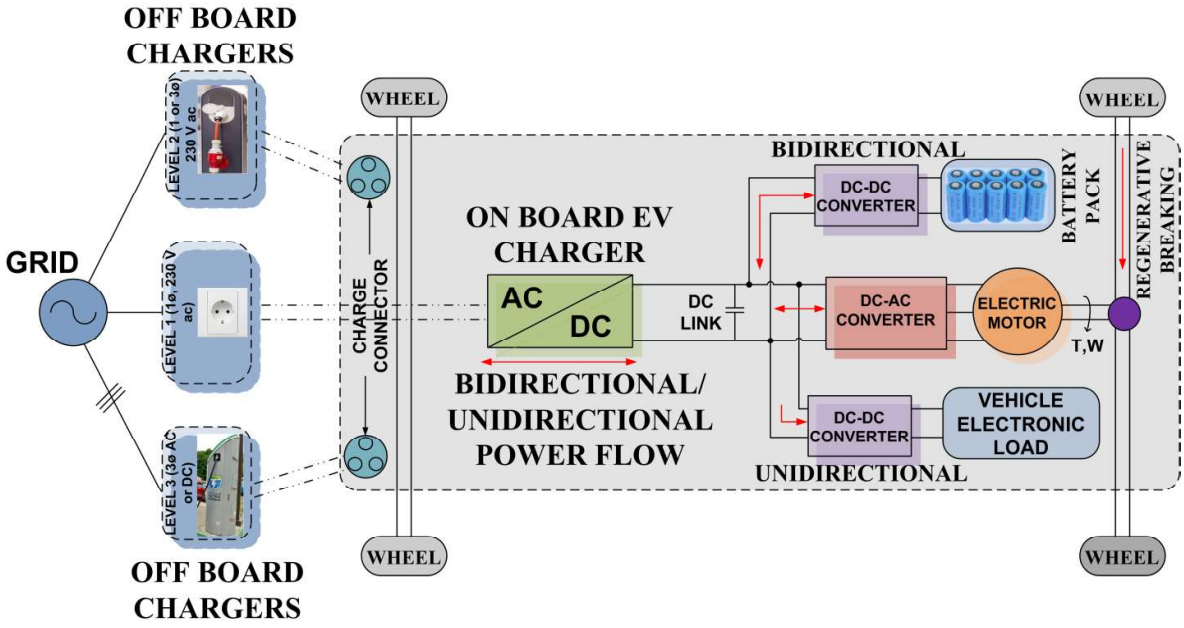

Figure 1.5: *Typical EV architecture.*

1.2.2 Electric Vehicle Chargers

The charging systems can be inductive and conductive as shown in Fig. 1.6 [15]. The inductive power transmission systems transfer the power without physical electric connection. It can transfer power from transmitter to receiver wirelessly by using electromagnetic (EM) field [22]- [23]. Therefore, the efficiency of inductive charger is less and it is expensive than conductive method. However, the conductive system has physical electric contact between transmitter and receiver. Therefore, it has higher efficiency and lesser in cost than the inductive systems [24].

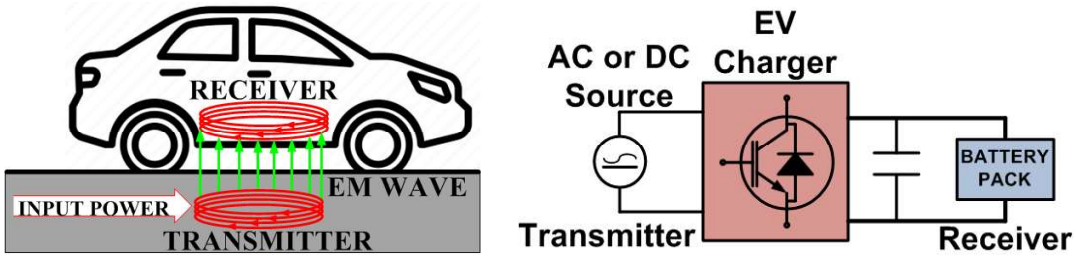

(a) (b)

Figure 1.6: *EV charger (a) Inductive and (b) Conductive.*

1.2.3 Charging Levels

The charging system are further categorized on the basis of charging time as level 1 (slow), level 2 (semi-fast) and level 3 (fast) charging [45], [46], [47]. Level 1 is slow charging method generally used for overnight charging at home or office. The voltage level required for ON board slow charger is 120 V AC or 230 V AC. Level 2 (semi-fast) charging method for both public and private and required 230 V AC outlet. Level 3 (fast) is OFF board fast charging method for commercial and public applications and required 208-600 V 3-phase AC or DC.

Some important specifications including level 2 charging time are listed in Table 1.2. It can observe that generally the vehicle has nominal battery pack voltage around 350 V. However, it depends on arrangement of cells and it varies from vehicle to vehicle. The trend of higher battery pack voltage can be seen in Table 1.2 for example Porsche taycan has 800 V battery pack [42]. Generally, the rating of ON board charger is between 3 kW to 7 kW. By using level 2 charging, Honda e takes 6 hrs to fully charge the 35.5 KWh battery pack via 6.6 kW ON board charger [33]. On the other hand, it takes 9 to 10 hrs to fully charge the 64 KWh battery pack of Kia Niro [37]. Therefore, the charging time depends on the battery pack capacity and ON board charger rating.

In level 3 (fast) charging, first AC voltage is converted into DC and vehicle is DC connected to OFF board charger or charging station [48]. The charging current is very high in comparison with ON board charging. Therefore, it takes very less time to charge the battery pack. Nevertheless, this high value of current will diminish the battery pack life span due to the heat develop in batteries. Generally, the time required to charge the battery pack from 20% state of charge (SOC) to 80% via level 3 charging is around 30 minutes. As an example, the Porsche taycan takes 22.5 minutes to charge the battery pack upto SOC 80% [42].

Table 1.2: Some EVs specifications.

Vehicle	Type	Battery Size (KWh)	Electric Range (KM)	Battery Voltage (V)	Charger Power (KW)	Level-2 Charging Time (Hrs)
BMW i3 [25]	EV	42.2	246	352	7.4	5
Jaguar I-Pace [26]	EV	90	470	390	7	10 (80%)
Nissan Leaf [27]	EV	40	230-250	360	6.6	8
Polestar 2 [28]		78	442.5	N/A	7.4	7.7
MG ZS [29]	EV	44.5	340		6.6	6-8
Tata Nexon [30]	EV	30.2	312	320	3.3	8
Hyundai Kona [31]	EV	39.2	452	356	7.2	6
Toyota Prius [32]	Hybrid	4.4	40	201.6	3.3	2.1
Honda e [33]	EV	35.5	220	N/A	6.6	6
Audi eTron [34]	EV	90	400	396	11	10.5
Mercedes-Benz B-Class [35]	EV	28	140	360	11	3.5
Ford Focus-Electric **[36]**	EV	23	185	240	6.6	5.5
Kia Niro [37]	EV	64	384	356	7.2	9-10
Renault Zoe [38]	EV	52	394	375	7.4	6-7
Peugeot [39]	Hybrid	50	310	400	7.4	7.7
Tesla Model 3 [40]	EV	54	250	350	7	13
Chevrolet Volt [41]	EV	60	383	360	7.2	9.3
Porsche Taycan [42]	EV	93.4	388-412	800	9.6	12
Volkswagen e-Golf [43]	EV	35.8	300	323	7.2	6
Mitsubishi i-Mi [44]	EV	16	160	360	3.6	6

1.3 Battery Technology, Charging Definitions and Profiles

1.3.1 Battery Definitions

Battery Capacity

It is the generation of free charge at negative electrode by active material and consume by positive electrode is known the battery capacity. In other words, it is the total amount of energy which can battery stored. It is measured in Ampere-hour (Ah) or watt-hour (Wh), where 1 Ah = 3600 coulomb (C) [49].

Specific Energy

It is gravimetric energy stored by battery and measured in watt-hours per kilogram (Wh/Kg). The gravimetric energy is amount of energy stored in correlation to its weight.

Energy Density

It is volumetric energy stored by battery and measured in watt-hours per liter (Wh/l). The volumetric energy is amount of energy stored in correlation to its volume.

State of Charger (SOC)

It is the amount of energy available in battery. The SOC of fully charged battery is 1 or 100 % and 0 or 0 % of fully discharge battery. It is found by Equation (1.1).

$$SOC = \frac{Q_i \pm \int i_{bat} dt}{Q_c} \times 100 \tag{1.1}$$

Where, Q_i is the battery initial charge before discharging/charging it, i_{bat} is battery charging/discharging current and Q_c is nominal charge capacity of battery. The battery current is negative in case of charging and vice versa. It means, SOC will increase in case of charging and vice versa.

State of Discharge (SOD)

It is complement to SOC, means that it tells the amount of energy has been consume from the battery. It also terms as depth of discharge (DOD). The SOC and SOD always sum to 1.

$$SOD = 1 - SOC \tag{1.2}$$

State of Health (SOH)

A method of estimation to calculate the condition of battery is known as state of health (SOH). It is relative evaluation to new battery. It gives the battery condition and determines that whether battery is working above its guaranteed operating condition or not. The only method of assessing SOH is battery management system (BMS) in which the history of usage is recorded.

Charging Rate (C-rate)

Every battery has its rated charging current rate and it is termed as C-rate. C is the amount of battery charging current that will fully charge it in one hour. The battery charging current is n times of rated charging rate i.e. $n \times C$. The value of n can be less or greater than one. For example, $n = 0.5$ means battery is charging at half of rated current and takes two hours to fully charge, similarly for $n = 2$ means battery is charging at twice of rated current and takes half an hour to fully charge [50].

1.3.2 Life of Electric Vehicle Battery

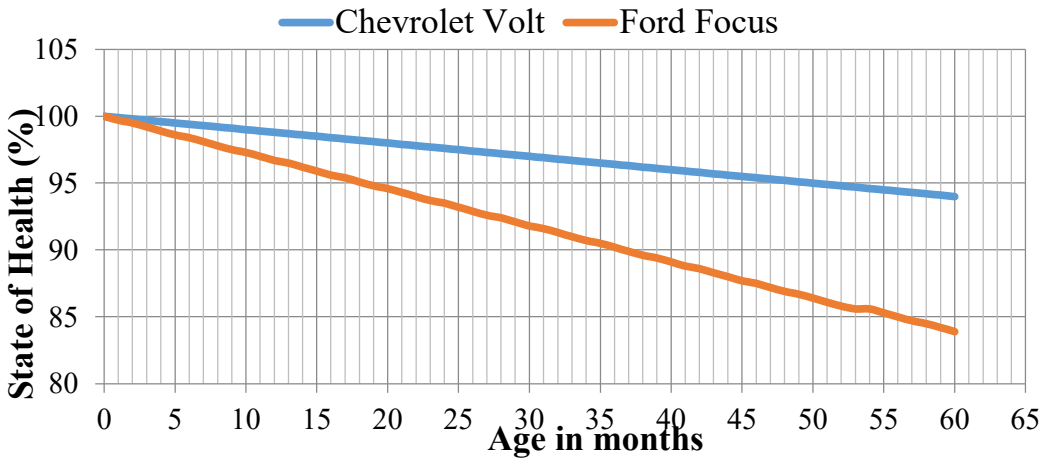

Figure 1.7: *Battery life comparison of Chevrolet Volt and Ford Focus.*

The battery plays a very important role for EVs. However, the biggest hindrance in the success of EV is availability of a small size high energy storage device. Since, the driving range of EV depends on capacity of battery pack, therefore a large battery pack is required to minimize the obstacle of short driving range. The battery energy is measured in watt-hour (Wh) or amp-hour (Ah) [51], however the researchers focus on specific

energy i.e., watt-hour per kilogram (Wh/Kg) or energy density i.e., watt-hour per liter (Wh/l) due to the limited space available in EV.

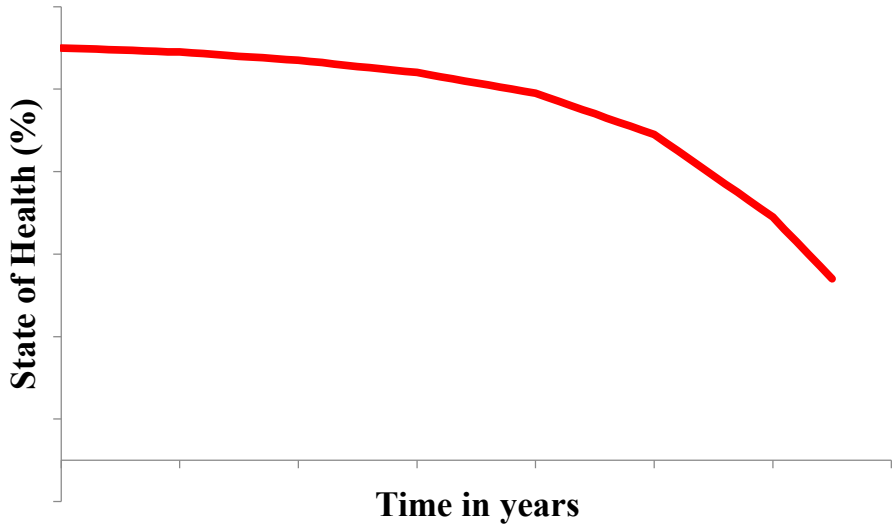

Figure 1.8: *Battery life degradation with time.*

The charging time of battery is always important because usually it is slower than discharging. However, with the advancement in battery technology, they can charge at high current value, tendering a better and fast charging solutions and may overcome the problem of range anxiety. The modern EV usually takes around 30 minutes for fast charging to 10 hours or more for semi-slow/slow charging to fully charge the battery pack. However, the high current during fast charging diminishes the life cycle of battery faster. The life of battery is measured by two ways i.e., minimum calendar year and number of charger/discharge cycles. It is expected that the average life of an EV battery is 15 years with minimum degradation [52]. However, the charge/discharge cycle may be two types i.e., shallow and deep. The deep charge/discharge cycle means completely charge the battery from 20% to 90% of SOC and completely discharge up to 20% of SOC, respectively. A shallow charge/discharge cycle having very narrow SOC band i.e., 40% to 60%. Since, a narrow SOC band is used in shallow cycle, it is more preferable than deep cycle because it affects the battery life lesser in comparison with deep cycle. The Fig. 1.7 shows the life cycle of 2015 model of Chevrolet Volt and Ford Focus [53]. It is observed that during the initial time life degradation rate of Chevrolet Volt is around 1.2% annually, whereas it is around 3% in case of Ford Focus. Therefore, it means that a Chevrolet volt lose the driving range of 5 KM in first years which has initial driving range of is 383 KM. The initial degradation rate is very less and linear but it increases

with the time and finally a significant drop is experienced at the end of battery life as shown in Fig. 1.8. Therefore, the overall battery life curve is non-linear [54].

1.3.3 Types of EV batteries

Table 1.3: Comparison of batteries.

Battery Type	Energy Density (Wh/l)	Charge-Discharge Cycles	Self-discharge rate (per month)	Merits	Demerits
Li-ion	250-693	300-500	< 10%	Highest energy density, low self-discharge rate, low maintenance, no need of periodically discharge.	Very expensive, moderate discharge rate, required protection from overcharge and overheat.
NiMH	140-300	180-2000	13.9-70.6% (at room temperature)	High charging efficiency, environment friendly, recyclable, resistant to overcharge and overheat.	Very high self-discharge rate, limited discharge rate, required periodically discharge, high maintenance.
Lead-acid	80-90	200-300	3-20%	Inexpensive, lowest self-discharge rate, low maintenance, high discharge rate.	Low energy and power density, environment unfriendly, cannot discharge beyond 20% of rating.

Generally, three types of batteries are used for supplying electrical energy in EVs and these are nickel metal hydride (NiMH), lithium-ion (Li-ion) and lead acid. The Li-ion battery is very much popular among all other batteries due to its high specific energy and energy density. It can provide high discharge current for faster acceleration applications (for e.g., electric bus and train) and increases the driving range. Moreover, lighter weight and higher efficiency make them much better for EV applications. It has admirable energy density i.e., 250-693 Wh/l and for graphite material, it provides 4 V at 100% SOC and 3 V in discharge stage. Comparatively, it has very less life degradation rate and low self-discharging rate i.e., less than 10% per month. However, it is expensive and suffers from overcharging, which result heat develop above 100°C and

decomposition of anode. Therefore, it requires equalizer to balance the charge of each cell in more precise way. Moreover, it also needs a battery management system (BMS) to make suitable them for abusive weather conditions and save from overheating and overcharging [55].

A NiMH battery is the advancement in nickel family batteries named as Nickel-Cadmium (NiCd) and Nickel-Hydrogen (NiH_2). It has high power and energy density (i.e., 140-300 Wh/l) and longer life cycle i.e., up to 2000 charge/discharge cycles. The energy density is nearly two times compared to lead-acid battery. Therefore, the driving range of vehicle having NiMH battery is double compared to lead-acid battery based vehicle. It has resistant to damage, therefore it can allow deep discharge and limited overcharging. Due to the low internal resistance, it has a capability to accept high charge which outcomes in high charging efficiency i.e., up to 92% at room temperature. However, the efficiency may diminish in high temperature conditions. Moreover, the NiMH battery suffers from high self-discharging rate which is 5-10% on first 24 hours and after that around 0.5-1% per day at ambient temperature. It has a very limited discharging rate and requires full discharge regularly to restrict crystalline formation. The decrement of 200-300 life cycles is experienced if supplying power to high current loads [56].

The lead acid battery was most usable for EV applications because of low cost, simple in manufacturing, high cell voltage (i.e., 2.1 V) and high reliability. It has good discharging rate which makes it preferable for quick acceleration applications and also capable to respond fast for load variations. It has very low self-discharging rate i.e., 3-20% per month. However, it has low power and energy density (i.e., 80-90 Wh/l) and short life span (i.e., < 300 cycles) limits it for the use in wheeled applications. The presence of electrolyte and lead content makes it environment unfriendly because they may result environmental damage. Moreover, it cannot be leave in discharge condition [57].

1.3.4 Charging Profile

Generally, two types of charging profile are used for battery charging purpose i.e., constant voltage (CV) and constant current (CC) charging. The CC charging is used at starting, during this a constant value of current is supplied to the battery. The charging method is transferred to CV charging after reaching certain voltage level. During this,

constant value of voltage is regulated across the battery terminal and very less amount of charging current flows in battery. In CC charging, the battery is charged up to 80% SOC and rest 20% is charged by CV charging. The time taken by CC charging is around 25% and rest 75% of complete charging time is taken by CV charging. From the observation of lithium-ion battery having 4.2 V of maximum voltage, the charging time during CC charging is around 50 minutes and 2 hours 40 minutes during CV charging as depicted in Fig. 1.9. Therefore, the total charging time of abovementioned battery is around 3 hours 30 minutes [58].

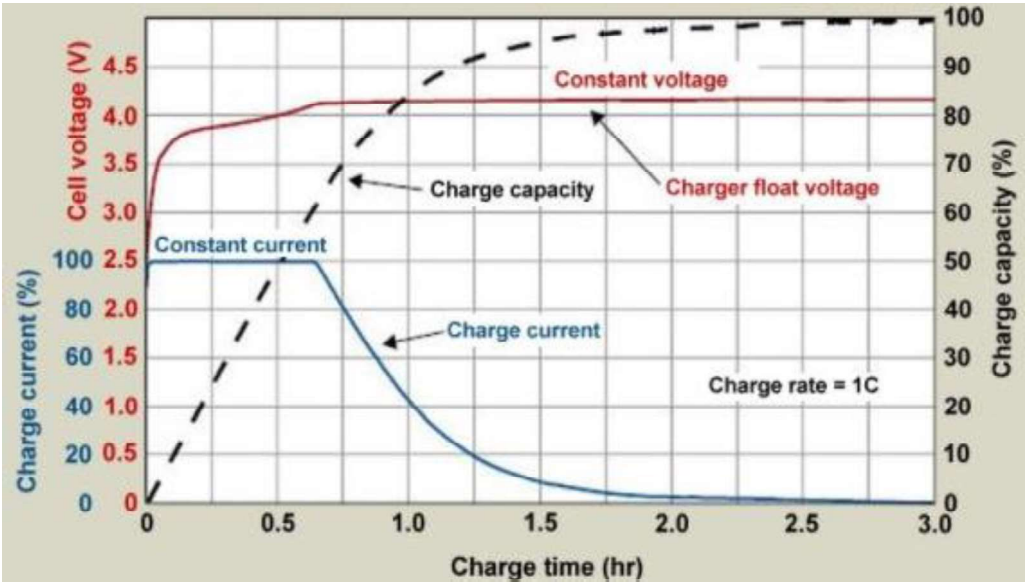

Figure 1.9: *Battery Charging Profile [50].*

1.4 Effect of Ripple in Charger Output on Battery Life

The EV charger must comply two important requirements that the output DC voltage and current are well regulated. The amount of ripple available is as small as possible and ideally it is zero. Moreover, the availability of ripple component is low or does not exceed the permissible limit. At present, the information of allowable ripple of Li-ion battery without affecting its lifetime is not available. However, the allowable amount of current ripple in lead-acid battery without affecting the lifetime is different and varies with the manufacturers. Some of the manufacturers allow the amount of current ripple is C/10 or C/20, where C is the charging current of battery. It means if a battery charging current is 100 Amps, then the allowable ripple is 10 Amps for C/10 type of battery and 5 Amps for C/20 [59]. Therefore, ripple in output of the charger must be within that permissible limit to prevent the battery from overheating and life degradation.

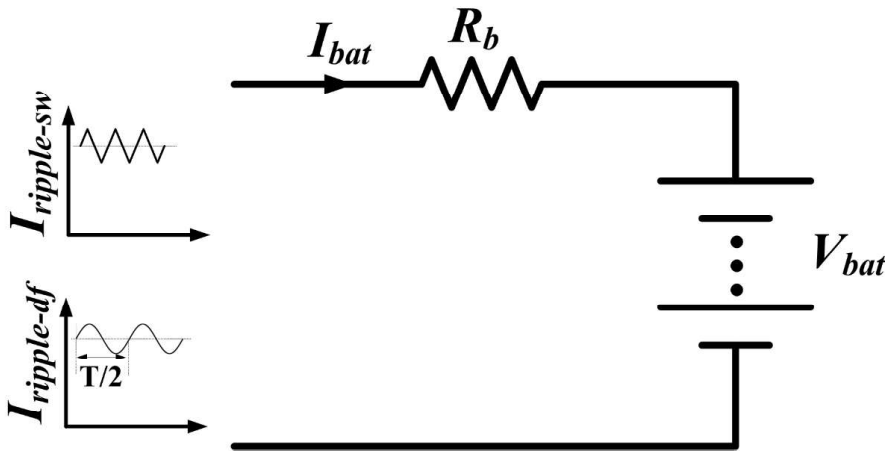

Figure 1.10: *Battery model.*

The EV charger affects battery life by producing two frequency ripples: one is low frequency ripple ($I_{ripple-df}$) and converter switching frequency ripple ($I_{ripple-sw}$) [60]. To apprehend the outcome of current ripple on battery life, first it is required to know that how the extra heat is developed by ripple current. For this, consider a battery model shown in Fig. 1.10, where R_b is internal resistance of battery and $V_{bat-ripple}$ is the root mean square (rms) value of battery voltage ripple. The extra heat developed by ripple current is due to battery internal resistance (R_b) and it is equal to the power loss across R_b due to ripple current.

$$I_{ripple} = \frac{V_{bat-ripple}}{R_b}$$
$$P_{ripple} = I_{ripple}^2 \cdot R_b \tag{1.3}$$

Moreover, the battery internal resistance varies with change in frequency and it increases with decrement in frequency. Therefore, low frequency ripple across the battery affects more as it increases the internal resistance and P_{ripple}. However, the frequency of switching ripple is very high and correspondingly does not produce extra heat in large amount because of electro-chemical process in battery.

This unfavorable ripple component poorly affects the battery life span because of internal heating and also raises the count of micro charge/discharge cycles of EV battery pack which deplete the life span more rapidly. This ripple component may diminish by using the large filter circuit or a proper control design. The use of large filter circuit may increase filter component cost, size, overall vehicle weight and system order which

increases control complexity. Therefore, it is convenient to design a controller for minimizing this ripple on DC side in case of EV charging.

Therefore, EV charger designer must keep in mind that the amount of ripple in output current and voltage must be restricted within the allowable limit of battery to minimize the excessive heat generation. As the heat generation by switching ripple is very less, the designer must focus on reducing the low frequency ripple.

1.5 Electric Vehicle Charging Standards

1.5.1 International Electrotechnical Commission (IEC)

The international electrotechnical commission (IEC) is an international standard developing organization. It formulates the international standards for all related technologies of electrical and electronic [61]. The IEC standards cover wide range of technology from power grid, solar energy, semiconductors, batteries, nanotechnology and many more. The IEC has also developed many standards which deal with many aspects of EV charging. Such as, IEC 61851 discussed about the general requirements of EV charger and IEC 62196 deals with socket outlets, connectors, plugs and vehicle inlets [62]- [63]. Whereas, IEC 61980 discussed about the wireless charging system of EV [64].

Table 1.4: IEC 62196 charging standards.

Charging Method	Voltage level (V)	Supply system	Maximum Current (Amp)	Maximum Power (KW)
AC Level 1	240	AC Single-phase	16	3.3
AC Level 2	240	AC Single-phase	32	7.6
AC Level 3	415	AC Three-phase	250	120
DC Fast Charging	600	DC	400	240

The IEC 61851 comprises following standards: -

- IEC 61851-1: General requirements.
- IEC 61851-21-1: Requirements for electromagnetic compatibility of on-board EV charger.
- IEC 61851-21-2: Requirements for EV AC to DC conductive charger and electromagnetic compatibility of off-board EV charger.

- IEC 61851-23: Requirements for DC EV charging station.
- IEC 61851-24: Requirements for digital communication between EV and DC charging station for control charging.

The IEC 62196 comprises following standards: -

- IEC 62196-1: General requirements of socket outlets, connectors, plugs and vehicle inlets.
- IEC 62196-2: Requirements for dimensional compatibility and interchangeability of contact tube accessories and AC pin.
- IEC 62196-3: Requirements for dimensional compatibility and interchangeability of contact tube vehicle couplers, DC and AC to DC pin.
- IEC TS 62196-3-1: Vehicle inlet, connectors and cable assembly of DC charging must be used thermal management system.
- IEC TS 62196-4: Requirements for dimensional compatibility and interchangeability for contact tube accessories and DC pin of class II or III applications.
- IEC 62196-6: Requirements for dimensional compatibility and interchangeability for contact tube vehicle coupler of DC charger supply equipment where electrical separation is ensured.

IEC 62196 charging standard: - IEC 62196 comprises of four charging standards as listed in Table 1.4. It defined three AC charging levels namely AC level 1, AC level 2 and AC level 3 and a fast DC charging standard [65].

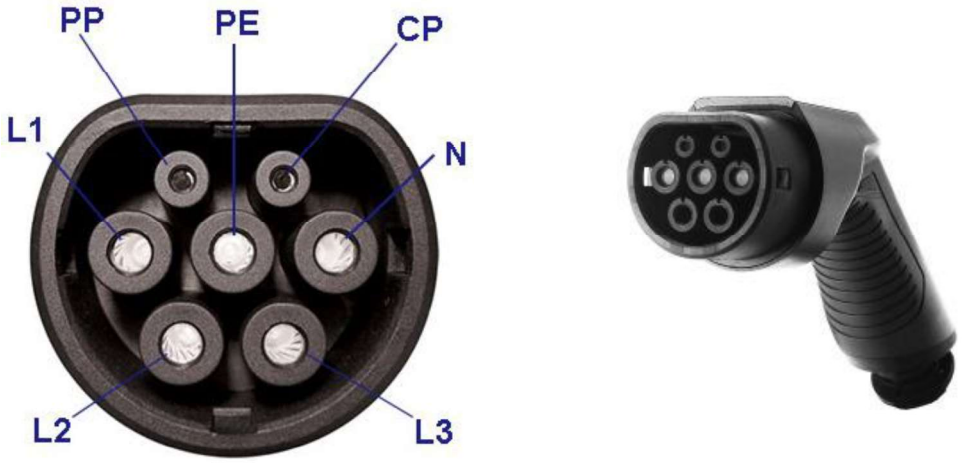

(a) (b)

Figure 1.11: *(a) Vehicle inlet and (b) IEC 62196 type-2 connector.*

IEC 62196 type-2 connector: - The IEC 62196 type-2 connector is round in shape with flat top edge as shown in Fig. 1.11. It has seven pins in which two are small and five are larger in size. The top row contains two small pins i.e., proximity pilot (PP) and control pilot (CP). These two pins are used for signaling purposes. The middle row consists three larger pins i.e., line-1 (L1), protective earth (PE) and neutral (N). The rest two larger pins i.e., line-2 (L2) and line-3 (L3) are used for phase connection in case of three phase AC fast charging [66].

(a) (b)

Figure 1.12: *(a) CSS connector and (b) Vehicle inlet.*

Combine Charging System (CCS): - The CCS is extension of IEC 62196 type 1 and 2 connectors and named as combo 1 and 2 connectors. In CCS, two extra contacts are provided for fast DC charging. It can charge the battery pack up to 350 KW. Several electric car makers like General Motors, BMW, Audi, Volvo, Porsche has already introduced this CCS (combo 1) in 2012. Moreover, in 2019 tesla introduced combo 2 type CCS which has the features of fast DC charging and home plug facilities. The CCS connector and vehicle inlet are shown in Fig. 1.12 [67].

1.5.2 Society of Automotive Engineers (SAE)

Table 1.5: SAE J1772 Charging Standards.

Charging Method	Voltage level (V)	Supply system	Maximum Current (Amp)	Maximum Power (KW)
AC Level 1	120	AC Single-phase	12	1.44
			16	1.92
AC Level 2	208 to 240	AC Single-phase	16	3.3
			32	7.6
			80	19.2
DC Level 1	200 to 450	DC	80	36
DC Level 2	200 to 450	DC	200	90
DC Level 3	200 to 600	DC	400	240

The society of automotive engineers (SAE) is an American based standard developing organization for various discipline in engineering [68]. It also provides forum

for government agencies, industries, research institutes and consultants to develop many standards for EV and designing of charger connectors. The SAE standard J1772 covers general requirement for EV conductive charging levels and designing of connectors in North America. Moreover, SAE is also developing a combine charging system (CCS) for fast DC charging [69].

SAE J1772 charging standard: - The SAE characterized five charging levels in October 2017 as listed in Table 1.5. It defined two charging levels for AC charging and three for DC charging system [70].

Moreover, J1772 standard also ensuring the safety of EV charging in wet conditions and level of shock protection. The interior of connector must be isolated with connection pins and ensure that there is no physical connection between them.

SAE 1772-2009 connector: - This type of connector is also known as J plug and has a formal title "SAE EV conductive charge coupler". It has diameter of 43 millimeter and five pins i.e., line, neutral, control pilot, proximity pilot and protective earth as shown in Fig. 1.13. It is directly connected to the single phase (120 or 240 V) grid from other side. The proximity pilot is used to provide a control signal to vehicle so that it prevents the vehicle movement while charging. The control pilot is a communication line between vehicle and charger which is used to inform the charging level and other parameters of EV [71].

Figure 1.13: *SAE 1772-2009 connector.*

Combo Coupler System: - The SAE proposed a combo coupler design which has additional pins in J 1772-2009 connector (combo 1). The extra pins are used for fast DC charging at voltage level of 250-450 and power rating up to 90 KW [72]. The above-mentioned combo system also uses communication system between EV charger, EV and smart grid without any extra pins in connector.

1.5.3 CHAdeMO

CHAdeMO is trade name of fast DC charging method which can deliver up to 400 KW of power by 1000 V, 400 A DC supply as listed in Table 1.6. It is the shortening of "CHArge de MOve" which is corresponding to charge n go. The CHAdeMO charger can charge a low range (120 KM) vehicle in less than 30 minutes [73]. Moreover, the CHAdeMO is currently developing a 900 KW ultra-high power charger with collaboration of China electricity council [74]. The fast DC charger aim to charge battery pack up to 80 % SOC as charging mode from 80 % to 100 % is changed to constant voltage charging. The CHAdeMO connector has ten pins in which two for input DC supply, two for communication, one for ground and rest are start/stop and connection check as shown in Fig. 1.14.

Table 1.6: CHAdeMO Charging Standards.

Charging Method	Voltage level (V)	Supply system	Maximum Current (Amp)	Maximum Power (KW)
DC fast charging	1000	DC Single-phase	400	400

Figure 1.14: *CHAdeMO Connector.*

1.5.4 Charging Standards in India

In India, bureau of Indian standards (BIS) has developed IS: 17017 for EV charging [75]. It covers the safety norms and general requirements for charger. The charging standard in India is summrized in Fig. 1.15. The home charger has developed

with 230 V, 15 Amps single phase AC supply that delivers 3.3 KW of power. This uses grid AC supply and charge the battery pack via ON board EV charger. Till now, there is no special standard or policy has been defined for home EV charger. However, the use of residual current circuit breaker (RCCB) and IEC 60309 connector are mandatory as per Bharat EV specifications [76].

Moreover, the government of India has defined standards for public EV charging stations for low voltage EVs (<120 V). They published two specifications for EV charger namely: Bharat EV charger AC 001 and Bharat EV charger DC 001 [77].

The Bharat EV charger AC 001 can supply maximum 15 Amps of current at 230 V to three vehicles simultaneously. Each vehicle can take 3.3 KW of power at a time. According to alliance for an energy efficient economy (AEEE) report, the cost of AC 001 charger equipments varies from 41,800 to 52,500 Indian rupees (INR) [78]. However, there is no communication protocol has been defined for AC 001 charger yet. They use open charge point protocol international standard to communicate between charger and central management system (CMS) over the internet.

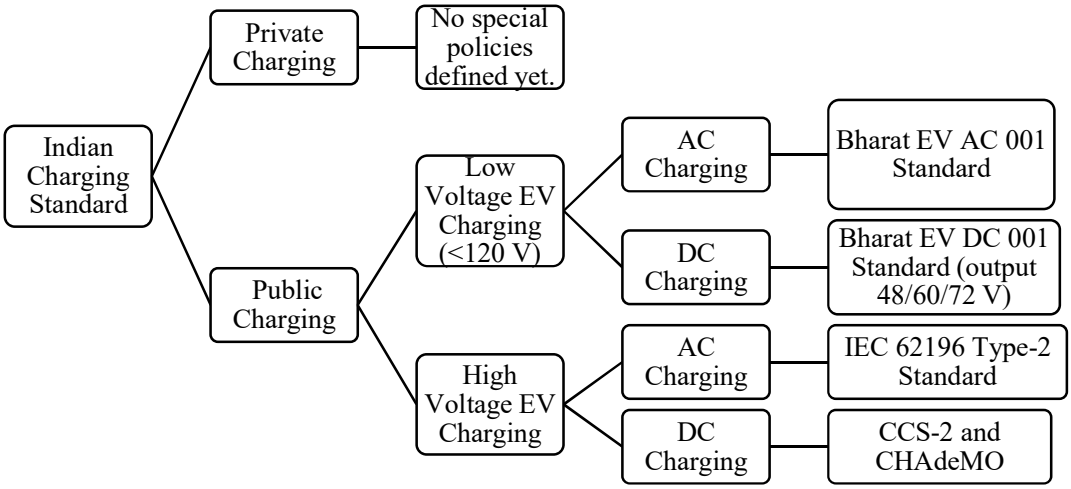

Figure 1.15: *Indian EV Charging Standards.*

The Bharat EV charger DC 001 can supply maximum 15 KW of power with 200 Amps of current at. It generates the output DC voltage of 48/60/72 V according to vehicle battery pack and uses three-phase 415 V grid voltage as input. According to AEEE report, the cost of DC 001 charger varies from 2,02,800 to 2,63,500 INR [78]. The DC 001 charger uses chinese charging communication GB/T 27930 to communicate between charger and CMS. Whereas, the existing vehicles use controller are network (CAN) protocol for internal communication. However, the department of heavy industry

(DHI) has announced standard of DC 001 in 2017, they added an extra output for 3.3 KW of power, where the communication protocol for second output has not been defined till now.

For high voltage vehicle charging like Mahindra and TATA electric cars, BIS published standard in 2018 IS: 17017-1, which uses the protocols of CCS-2 and CHAdeMO for DC charging purpose. However, IEC 62196 type-2 standard is used for high voltage AC charging. Therefore, the government of India has planed to install all Bharat standard, IEC 62196 type-2, CCS-2 and CHAdeMO charging point at all public charging stations [79].

1.6 Motivation

The EVs are future of transportation industry. India is a growing country in the field of EV and it is assumed that the sales of EV is increased up to 80% of two and three wheelers, 30% of private cars, 70% of commercial cars and 40% of buses by 2030. The efficiency of EVs is much more than IC engine-based vehicle. They are less noisy, simple in design, do not pollute environment and required less maintenance.

Since, the population of EVs is increasing day by day, it is assumed that large number of EVs will be connected to grid at a particular time. This can be very advantageous to utility in respect of stability. The EV can support grid actively as well as reactively. It can supply active power to grid in case of emergency and can compensate reactive power as well simultaneously. Moreover, the EV can pollute grid if operated by improper control. Therefore, a proper charging control is must from the battery life and grid quality point of view.

The reactive power compensation by EV charger further increases the power quality by supplying the reactive power (inductive or capacitive), filtering the current harmonics and voltage regulation to certain extent. Supporting reactive power by EVs can curtails the installation and maintenance cost of reactive power compensators such as static synchronous compensators, static VAR compensators, and capacitor banks [61]. Moreover, the controlled exchange of reactive power further reduces the chances of voltage fluctuation. This helps the grid remains stable and meet the set standards. However, the reactive power compensation through EV charger may put lot of stress on battery and reduce its life cycle due to the presence of unwanted ripple current

component in EV charger as explained in [56]. This unfavorable low frequency ripple component of current adversely affect the battery lifetime because of internal heating, and also raises the count of charge/discharge micro cycles of the battery pack which deplete the lifetime more rapidly as discussed above. During the continuous operation of charger in V2G mode, there are chances of enhanced power conversion losses and battery discharge.

Moreover, single phase single stage EV chargers have inherent problem of producing second order ripple component on DC side. This problem is further exaggerated during vehicle-to-grid (V2G) mode of operation where it may be normally controlled to supply both active as well as reactive power. During the V2G reactive power compensation, the second order harmonics ripple component at DC side will increase which further reduces the life cycle and performance of battery pack. Therefore, the second order ripple component must be minimized for improving the life of battery pack.

Hence, the proper charging of EVs can help truly towards grid stability and cost reduction of reactive power compensators. This is the vision and motivation of developing robust control algorithms for EV charging. Therefore, in this thesis, the control techniques have been designed for both ON and OFF board EV chargers. The EV charger is commanded to perform charging operation of battery pack, ripple minimization and grid supporting whenever required.

1.7 Scope of Research Work

This research work proposes the design of EV charger controller. In this regard, an EV charger prototype by using dSPACE 1104 has been designed in laboratory. This study presents the design of control architecture for OFF board, on-board EV charger and minimization of second order ripple in single stage on-board EV charger. A novel control architecture for single stage on-board EV charger has been designed to minimize the inherent feature of producing second order ripple on DC side. For this, single phase AC-DC converter is utilized for charging purpose. Further, the control system has been designed for both on-board and off-board EV chargers. These EV chargers having two conversion stages i.e., AC-DC and DC-DC converter. Both the converters have their separate controller and these are based on proportional integral (*PI*), proportional resonant (*PR*), plant integrated proportional integrated (*PIPI*), repetitive controller (*RC*),

and adaptive neuro-fuzzy inference system (*ANFIS*). All EV chargers are able to compensate the reactive power of local load. They all have active and reactive power input references where active command depends on customer desired charging rate and reactive command is requested by grid.

Therefore, the main aim of proposed study is to develop a robust control system for EV charger to operate it in wide range of G2V and V2G mode of operations while maintain the amount of ripple content on DC side within the permissible limit. The EV charger may supply active power to grid if required and compensate reactive power (inductive or capacitive) if a battery charges at slower rate. In that case, the remaining rating of charger is utilized for compensating the reactive power for optimally utilization of charger's rating. Moreover, if the battery is not connected to the charger, then the EV charger can work as an active power filter and improves the power quality.

The performance of all EV charger's controllers has been tested in eight different modes including charging/discharging and compensating linear/non-linear reactive power. The performances of all proposed control strategies have been simulated and verified in MATLAB/Simulink environment with the real time validation through hardware prototype.

1.8 Thesis Structure

Chapter -1: This chapter describes the introduction and basic features of EV and its charger. The overview of various EV charger ratings used in latest EVs throughout the world are presented. Various issues of battery during charging and standards of EV charger have also been discussed.

Chapter -2: This chapter presents the operating modes of EV charger i.e., G2V, V2G and reactive power compensation. Further, the development of hardware prototype and design of its components required for experimental validation has been discussed.

Chapter -3: This chapter deals with the design of two stage bidirectional EV charger. The chapter includes mathematical modelling of first stage AC-DC converter, second stage DC-DC converter and battery pack.

Chapter -4: This chapter deals with the design of two stage bidirectional off-board EV charger. The charger comprises of two bidirectional stages i.e., first (AC-DC)

and second (DC-DC) conversion stages. The first control strategy is based on *PI* regulator and second one is based on adaptive neuro-fuzzy inference system (ANFIS). Both controllers can work in all possible active (*P*)-reactive (*Q*) power cases.

Chapter –5: This chapter deals with the design of single phase, single stage on-board EV charger. The single phase single stage EV chargers have inherent problem of introducing second order ripple component on DC side. This problem is further exaggerated during vehicle-to-grid (V2G) mode of operation where it may be normally controlled to supply both active as well as reactive power. During the V2G reactive power compensation, the second order harmonics ripple component at DC side will increase which further reduces the life cycle and performance of battery pack. Therefore, a second order ripple component compensation technique is proposed by pre-compensating the reference current itself. The resultant reference current is periodic in nature and accordingly, repetitive controller (*RC*) is used to track the reference current.

Chapter -6: This chapter deals the control design and implementation of two stage ON board EV charger. The charger is controlled to perform four quadrants operation in active-reactive (*P*-*Q*) power plane. Therefore, in this chapter the inner control is performed in AC domain where the signals are periodic. The proportional plus resonant (*PR*) controller is found to be very useful in tracking such type of periodic signals of fixed frequency in case of single-phase system and accordingly, it has been designed and successfully implemented for the proposed work. Moreover, a reduced order plant integrated proportional integrating (*PIPI*) controller for on-board EV charger has been proposed. The proposed technique has all the functionalities of conventional *PR* controller and can track any periodic signal.

Chapter -7: This chapter of thesis presents a summary of the work presented and some suggestions for future work scope.

ELECTRIC VEHICLE CHARGER OPERATION AND PROTOTYPE DEVELOPMENT

CHAPTER 2

Chapter Outline

2.1 Electric Vehicle Charger Operating Modes

The EV charger can be categorised based on location (OFF board or ON board), supply type (AC or DC), topology (integrated or dedicated), connection type (conductive or inductive) and power flow direction (bidirectional or unidirectional) [80]. This section focuses on the operating modes of EV charger. Fig. 2.1 shows the general structure of on-board EV charger. Generally, two stage on-board EV charger is used to charge the battery pack. This consist of AC-DC power conversion in first stage and DC-DC power conversion in second stage. Each of these stages consists of many active and passive elements combination like capacitor, inductor and semiconductor devices.

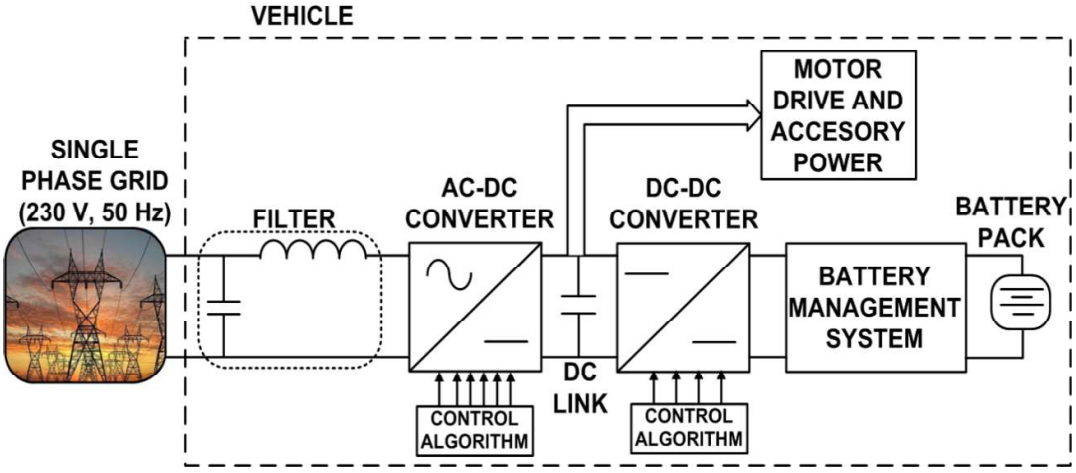

Figure 2.1: *General structure of ON board EV charger.*

On the basis of direction of power flow, on-board EV charger can be categoried by two ways in terms of active power transfer and reactive power support as listed in Table 2.1 [81].

Table 2.1: Type of Charger.

Type of Charger	Active Power Transfer	Reactive Power Operation
Unidirectional	Grid to vehicle (G2V) only/ Charging only	NO
Bidirectional	Grid to vehicle (G2V)/ charging and vehicle to grid (V2G)/ discharging	Both capacitive and inductive

2.1.1 Operation of Unidirectional EV Charger

The unidirectional topologies transfer active power from grid to vehicle (G2V) only with almost unity power factor [82]. This mode is also known as battery charging mode. This type of charger mostly used in today's EV and it allows only to control the active power command to charge the battery pack. Since, it does not allow the control of reactive power, the charger works only on right side of x-axis of *P-Q* plane as shown in Fig. 2.2.

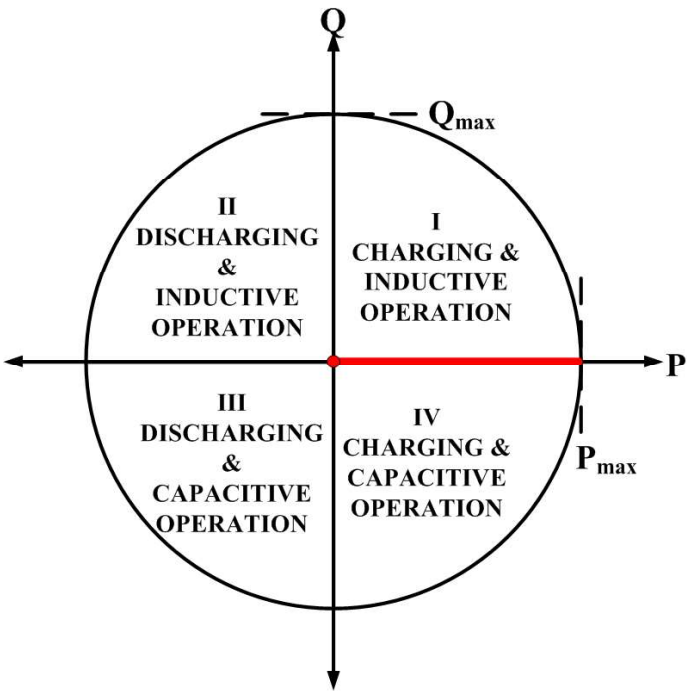

Figure 2.2: *Operating mode of unidirectional charger.*

Fig. 2.3 shows the relation between voltage and current during the operation of unidirectional charger. As the main function of unidirectional charger is to charge the battery pack, the grid voltage and current are in approximately same phase.

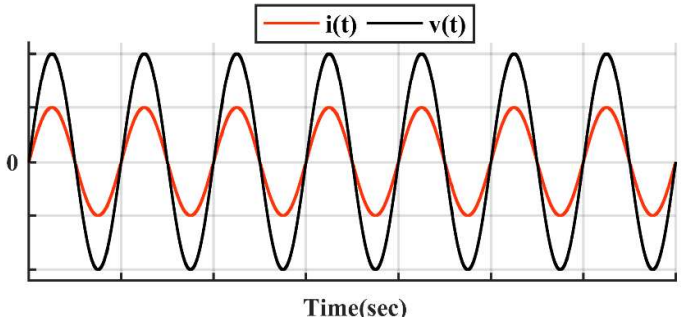

Figure 2.3: *Current and voltage relation of unidirectional charger.*

2.1.2 Operation of Bidirectional EV Charger

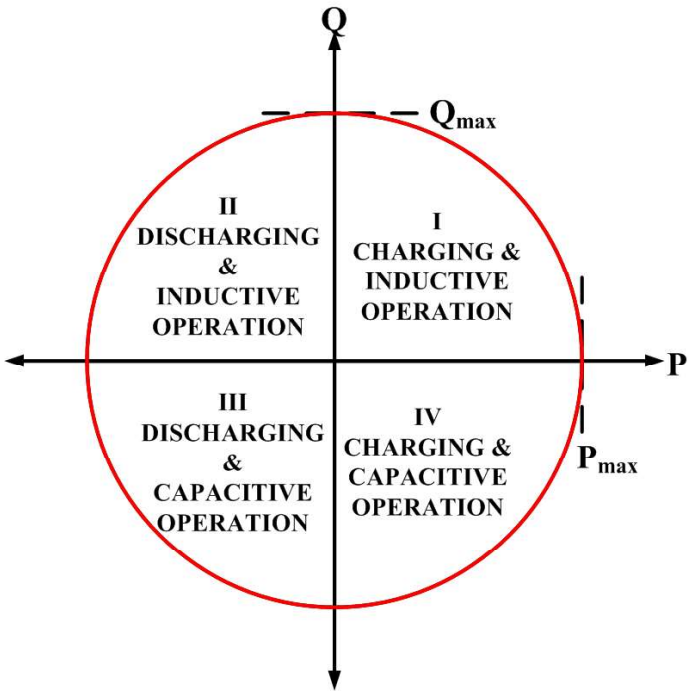

Figure 2.4: *Operating mode of unidirectional charger.*

The second type of charger is bidirectional, it has capability to transfer the active power in both directions, therefore, it can work in both G2V and vehicle to grid (V2G) mode [83]. It allows the controlling of both active as well as reactive power as shown in Fig. 2.4. By employing V2G technology, EV customers can sell the battery energy to the distribution grid during peak hours or transfer this energy to other vehicles, this operation is known as vehicle-to-vehicle (V2V). The bi-directionality of EV chargers supports the grid to meet the peak load demands or to provide instantaneous power

during intermittences. The main purpose of bidirectional EV charger is to have the exchange of active as well as reactive power between grid and vehicle. Thus, the EV may supply active power to grid whenever there is sudden increase in demand and may also absorb it in case of availability of surplus power. Therefore, the large amount of EVs in distribution network may not only help in absorbing the mismatch in demand and supply but also very useful in the large-scale integration of intermittent renewables in to the grid. Moreover, the control of reactive power may supply the harmonic current within the permissible limit of charger.

Table 2.2 - Charger Operating Modes.

Mode	Active Power (W)	Reactive Power (VAR)	Operation	Power Factor
1	Positive	Zero	Charging	1
2	Negative	Zero	Discharging	-1
3	Zero	Positive	Inductive	0
4	Zero	Negative	Capacitive	0
5	Positive	Positive	Inductive-Charging	Lagging
6	Positive	Negative	Capacitive-Charging	Leading
7	Negative	Positive	Inductive-Discharging	Lagging
8	Negative	Negative	Capacitive-Discharging	Leading

Here, it is worthwhile to mention that in four quadrant operation with exchange of active and reactive power, only eight modes of operation are possible as listed in Table 2.2. The Fig. 2.4 shows the operating modes of EV charger on active-reactive plane. The reactive power is positive in mode- 3,5 and 7, negative in mode- 4,6 and 8 and zero in mode-1 and 2. Similarly, active power is positive in mode- 1,5 and 6, negative in mode- 2,7 and 8 and zero in mode 3 and 4. Note that the power transfer from the grid to vehicle takes positive sign and vice versa.

The traces of voltage and current waveforms during all operating modes are shown in Fig. 2.5. Here the main aim is to demonstrate the variation in phase angle between voltage and current during different mode of operation. The positive active power (P) indicates the charging operation as power is transferred to the vehicle while the negative power shows the discharging operation. For inductive operation, reactive power (Q) is positive and in capacitive operation it is taken as negative. Mode 1 and 2 shows the exchange of active power i.e., charging and discharging of battery,

respectively, while the reactive power is kept at zero. Therefore, the current is in phase with voltage in mode 1 as shown in Fig 2.5 (a) and out of phase in mode 2 as shown in Fig. 2.5 (b). Similarly, the compensation of inductive and capacitive reactive power without exchange of active power are related to mode 3 and 4, respectively. In that case, the current is lags behind voltage by 90° during mode 3 as shown in Fig. 2.5 (c) and leads by same angle during mode 4 as shown in Fig. 2.5 (d). Mode 5 and 6 are associated with the exchange of reactive power (i.e., inductive and capacitive respectively) while

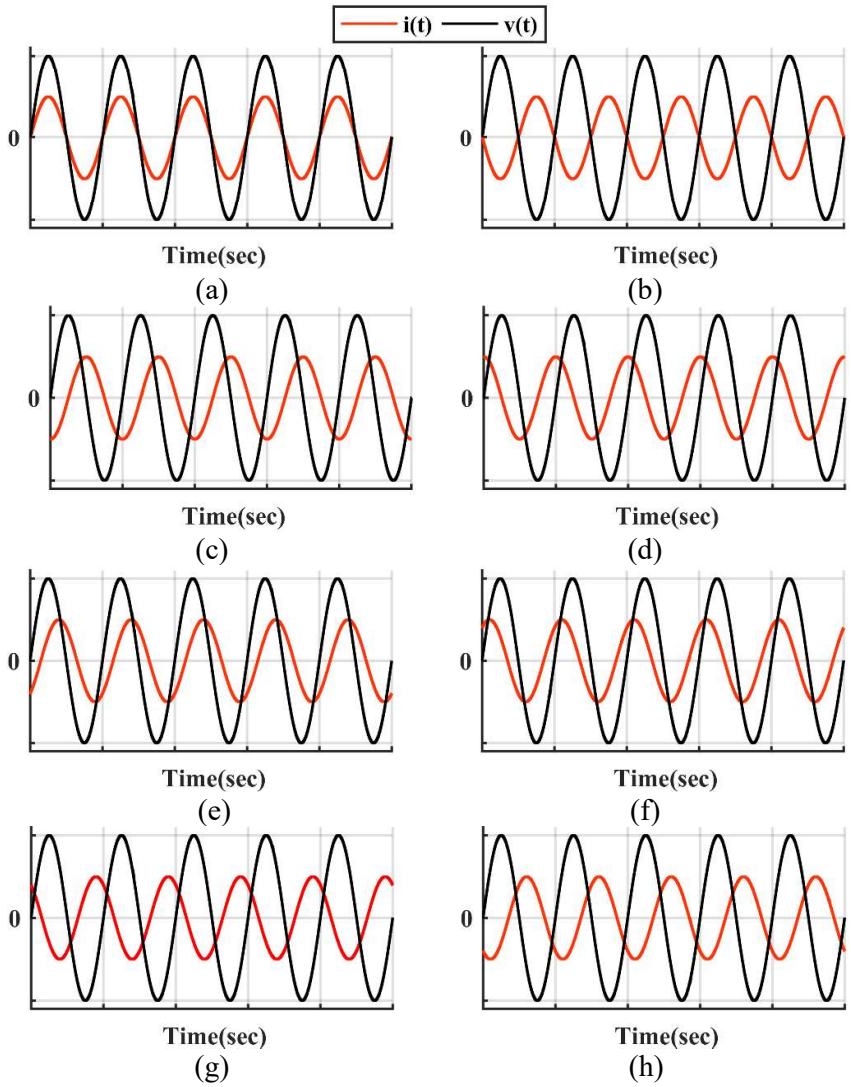

Figure 2.5: *Current and voltage relation during (a) mode-1 (b) mode-2 (c) mode-3 (d) mode-4 (e) mode-5 (f) mode-6 (g) mode-7 and (h) mode-8.*

charging of battery simultaneously. Since, being a G2V mode, the active power flows from grid to battery while the reactive power supplied may be inductive or capacitive. Accordingly, the current lags or leads the voltage while having phase difference less than 90° as shown in Fig 2.5 (e) and Fig. 2.5 (f), respectively. Similarly, during V2G mode,

the active power is supplied back from battery to grid while the reactive power may be inductive or capacitive. Accordingly, the current lags or leads the voltage while having phase difference more than 90° as shown in Fig 2.5 (g) and Fig. 2.5 (h), respectively.

2.2 Reactive Power Support by EV Charger

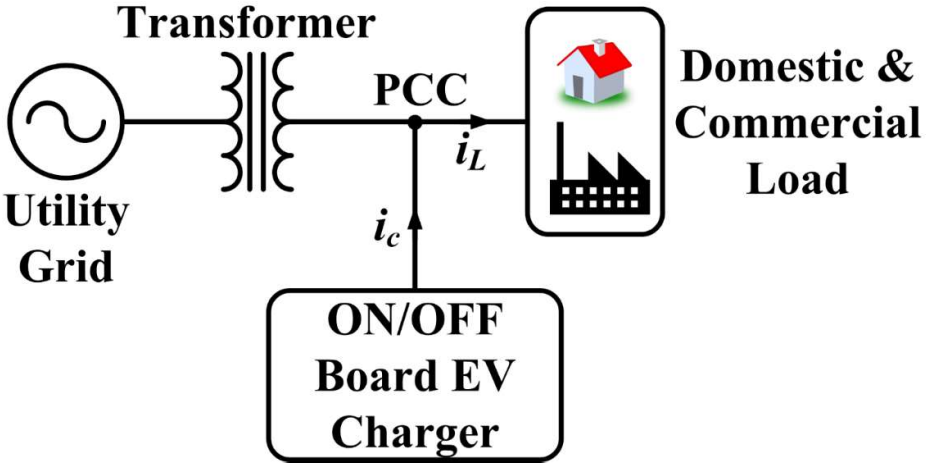

Figure 2.6: *EV charger with reactive power support.*

Fig. 2.6 shows the application of EV charger in improving the grid power quality. The EV consumer can allow on-board charger to negotiate with grid for supporting the utility reactively also. The charger can supply reactive current (i_c) of local load. This will help in improving the efficiency of transmission line and decrease the overloading on distribution transformer [84]- [85].

The reactive power compensation mode may further enhance the power quality by supplying the reactive power (inductive or capacitive), filtering the current harmonics and voltage regulation to certain extent. The application of EV charger for reactive power compensation has been discussed in technical literature [86]. Supporting reactive power by EV chargers can curtail the installation and maintenance cost of reactive power compensators such as static synchronous compensators, static VAR compensators, and capacitor banks [87]. Moreover, the controlled exchange of reactive power further reduces the chances of voltage fluctuation. This helps the grid remains stable and meet the set standards. However, the reactive power compensation through EV charger may put lot of stress on battery and reduce its life cycle due to the presence of unwanted ripple current component in EV charger as explained in [88]. This unfavorable low frequency ripple component of current adversely affect the battery lifetime because of internal heating, and also raises the count of charge/discharge micro cycles of the battery

pack which deplete the lifetime more rapidly as discussed above. During the continuous operation of charger in V2G mode, there are chances of enhanced power conversion losses and battery discharge.

Therefore, the requirement of a robust control system is mandatory which can command EV charger to work in both modes without violating the ripple limitation.

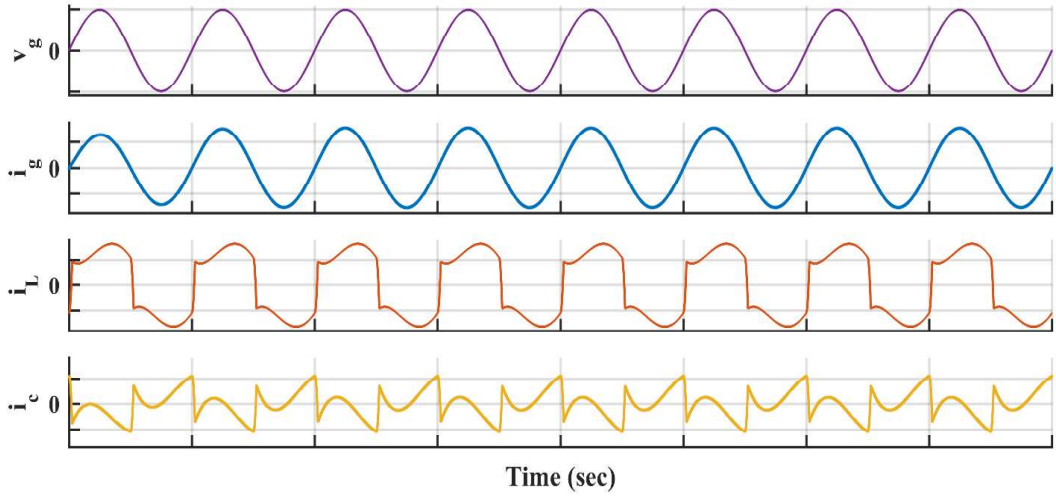

Figure 2.7: *Load current harmonic compensation.*

Moreover, the on-board EV charger can be used as active power filter and compensate harmonic component of current generated by single phase non-linear load. Fig. 2.7 shows the waveform of load current harmonic compensation. Where, v_g, i_g, i_L and i_c are grid voltage, grid current, load current and charger current, respectively. The EV charger can be commanded to supply harmonics component of load current which results in purely sinusoidal of grid current. The on-board EV charger can compensate this harmonic component of non-linear load current while charging of battery pack or without charging.

2.3 System Configuration

Fig. 2.8 and 2.9 shows the system architecture of off and on-board EV charger respectively. The system having AC-DC (first) and DC-DC (second) conversion stages. Here, in case of on-board EV charger, single phase AC-DC converter is used and three-phase in case of off-board EV charger. Both the converters are based on insulated gate bipolar transistor (IGBT). The AC-DC stage consist six IGBTs and two in DC-DC stage. Each switch has voltage blocking limit is V_{dc} and a maximum conduction current of $\sqrt{2}$ I_g where, I_g is root-mean-square (RMS) grid current. The first stage is directly linked to

the three-phase grid via interfacing inductors (L_s) and battery is connected across the second stage. The second stage acts as bidirectional buck-boost, which acts as buck converter in case of charging/G2V mode or vice versa. The charger architecture is capable to operate in all possible active-reactive power commands cases. The simulation and experimental parameters of both on and off-board EV chargers are listed in Appendix A.

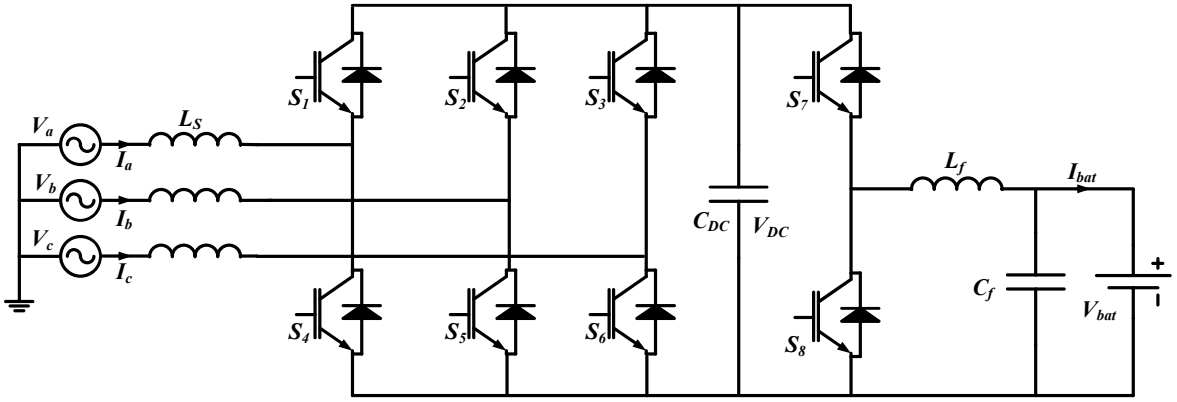

Figure 2.8: *OFF board EV charger.*

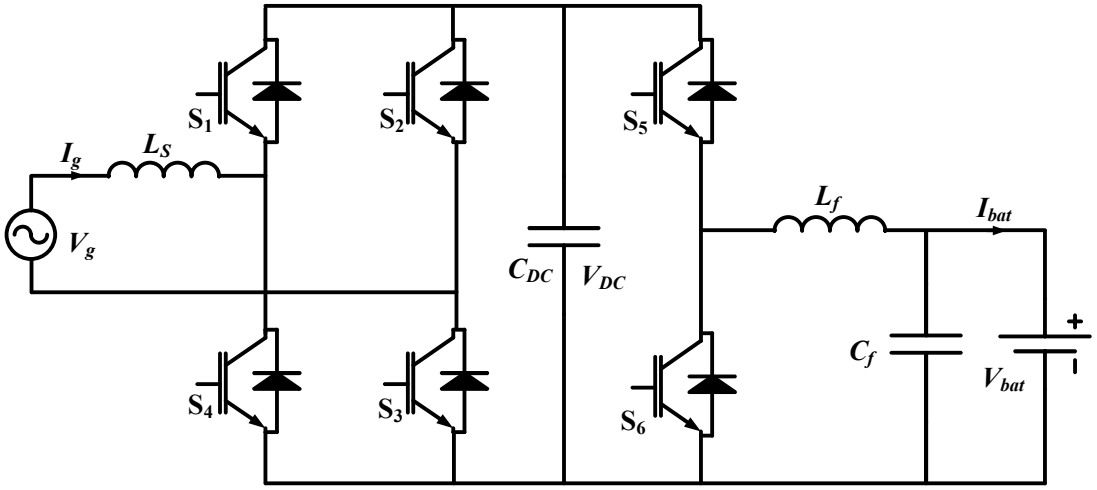

Figure 2.9: *ON board EV charger.*

2.3.1 Designing of components for EV charger Development

In this section the designing of both on-board and off-board EV charger has been presented. The major difference in on-board and off-board EV charger is rating and operating voltage and the values of EV charger components depend on these values. From the literature survey, it has been found that the rating of on-board EV charger is varies between 3.3 to 9.4 KW, therefore it has been designed and simulated in MATLAB for 6.6 KW. The off-board EV charger is rated around 100 KW, however it is designed and simulated for 12.5 KW. The designed parameters are listed in Table A.1 and A.2.

Selection of AC-DC and DC-DC Converters

In present case, the first stage AC-DC converter is used for charging as well as reactive power compensation. Therefore, it is good enough if charger can compensate the total reactive and harmonic demand of load. However, for this reason, the charger rating cannot be increased and EV charger can be fully utilized in compensation of reactive and harmonic demand of external load if battery is charging at lower rate or not charging. Therefore, in simulation both converters are rated as 12.5 KW for off-board EV charger and 6.6 KW in case on-board EV charger. Moreover, in case of hardware, higher rating of converters has been designed for safety reasons.

Selection of DC Link Voltage

The DC link voltage in both on-board and off-board EV charger is between 400-800 V. For proper rectification operation, it must be greater than the peak of line-to-line voltage and battery voltage. Generally, battery voltage is around 350 V and it varies according to the SOC. Therefore, the DC link voltage has been selected 600 V and 400 V in case of off-board and on-board EV charger respectively.

The minimum DC link voltage in case of off-board EV charger is,

$$V_{DCmin_{off}} > \sqrt{2} \cdot \sqrt{3} V_{ph}$$
$$> \sqrt{2} \cdot \sqrt{3} \cdot 230 > 563.38 \text{ V} \quad (2.1)$$

Where, V_{ph} is phase voltage.

The minimum DC link voltage in case of on-board EV charger is,

$$V_{DCmin\_on} > \sqrt{2} \cdot V_{ph}$$
$$> \sqrt{2} \cdot 230 > 325.26 \text{ V} \quad (2.2)$$

Selection of DC Link Capacitance

The DC link capacitor of first stage AC-DC converter of off-board EV charger has been found as follow [89],

$$C_{DC\_off} = \frac{6k_1 V_{ph} \propto I_{ph} t}{(V_{dc}^2 - V_{dcmin}^2)}$$
$$= \frac{6 \times 0.1 \times 230 \times 1.2 \times 20 \times 0.015}{(600^2 - 563.38^2)} = 1166.11 \text{ μF} \quad (2.3)$$

Where, V_{DC} is nominal DC link voltage, V_{DCmin} is minimum DC link voltage, α is overloading factor and taken 1.2, k_1 is energy variation constant during dynamics and selected 10% = 0.1, V_{ph} and I_{ph} are phase voltage and current respectively and t is time

taken by DC link voltage to be recovered. From the above formula, the DC link capacitance is calculated as 1166.11 µF and selected as 1200 µF in simulation.

In case of on-board EV charger,

$$C_{DC\_on} = \frac{2k_1 V_{ph} \propto I_{ph} t}{(V_{dc}^2 - V_{dcmin}^2)}$$

$$= \frac{2 \times 0.1 \times 230 \times 1.2 \times 30 \times 0.015}{(400^2 - 325.26^2)} = 458.25 \text{ µF} \quad (2.4)$$

The DC link capacitor for on-board EV charger is selected as 500 µF.

Selection of Grid Side Inductor

The grid side inductors of first stage AC-DC converter of off-board EV charger have been found as follow [90],

$$L_{s\_off} = \frac{\sqrt{3} \cdot m \cdot V_{DC}}{12 \cdot \alpha \cdot f_s \cdot I_{crpp}}$$

$$= \frac{\sqrt{3} \times 1 \times 600}{12 \times 1.2 \times 20000 \times 2} = 1.8 \text{ mH} \quad (2.5)$$

Where, V_{DC} is nominal DC link voltage, m is modulation index and selected to be 1, α is overloading factor and taken 1.2, f_s is switching frequency and I_{crpp} is ripple in grid current and selected 10% of grid current i.e. 2. The switching frequency depends on speed of processor and here it is selected as 10 kHz. From the above formula, the grid side inductor is calculated as 1.8 mH and selected as 2 mH in simulation.

In case of on-board EV charger,

$$L_{s\_on} = \frac{\sqrt{3} \cdot m \cdot V_{DC}}{12 \cdot \alpha \cdot f_s \cdot I_{crpp}}$$

$$= \frac{\sqrt{3} \times 1 \times 400}{12 \times 1.2 \times 20000 \times 3} = 0.8 \text{ mH} \quad (2.6)$$

The grid side inductor for on-board EV charger is selected as 1 mH.

Selection of DC-DC converter Filter

The DC-DC converter is bidirectional and works in both buck and boost mode. To find out the filter inductor and capacitor, first duty cycle in buck and boost mode is

calculated as follows [91]. For this, the DC link voltage is represented by V_1 and battery voltage by V_2.

$$D_{buck} = \frac{V_2}{V_1} = \frac{350}{600} = 0.5833 \tag{2.7}$$

$$D_{boost} = 1 - \frac{V_2}{V_1} = 1 - \frac{350}{600} = 0.4167 \text{ V} \tag{2.8}$$

The filter inductance and capacitance are calculated as follows,

$$L_f = \frac{V_2 \times D_{boost}}{\Delta I_L \times f_s} = \frac{350 \times 0.4167}{3.5 \times 20 \times 10^3} = 2.1 \text{ mH} \tag{2.9}$$

$$C_f = \frac{1 - D_{buck}}{8 \cdot L_f \left(\Delta V_2 / V_2\right) f_s^2} = \frac{1 - 0.5833}{8 \times 2.1 \left(\frac{35}{350}\right) \times (20 \times 10^3)^2} = 6.2 \text{ µF} \tag{2.10}$$

Where, ΔI_L is ripple in inductor current which is taken as 10% and f is switching frequency and taken as 20 kHz. The inductor and capacitor values for off-board EV charger are found from above equations and selected as 2.5 mH and 10 µF respectively. In case of on-board EV charger these values are selected as 1.5 mH and 5 µF.

Selection of Switch Ratings

The rating of switch (in present case it is IGBT) of both AC-DC and DC-DC converters is given as,

$$V_r = V_{DC} + \Delta V_{DC} = 600 + 60 = 660 \text{ V} \tag{2.11}$$

Where, ΔV_{DC} is 10% overshoot in DC link voltage under dynamic conditions. The reference DC link voltage in case of off-board EV charging is 600 V. Then the minimum switch rating must be 660 V.

The current rating can be calculated as,

$$I_r = 1.25(3 \times I_{ph} + I_{cr}) = 1.25(3 \times 20 + 2) = 77.5 \text{ amps} \tag{2.12}$$

Where, I_{ph} is phase current and I_{cr} is ripple in grid current and taken as 10%. The minimum current rating is required 77.5 amps.

2.4 Hardware Prototype Development

The development of EV charger prototype and its various components are presented here. This prototype requires the selection and development of first stage AC-DC converter, DC link capacitor, second stage DC-DC converter, voltage and current sensing units, interfacing inductors, filter inductance and capacitance and linear/non-

linear load. The development of three phase AC-DC converter is presented here. However, in case of single phase on-board charging, two legs of AC-DC converter is utilized.

2.4.1 Hardware Configuration of EV Charger prototype

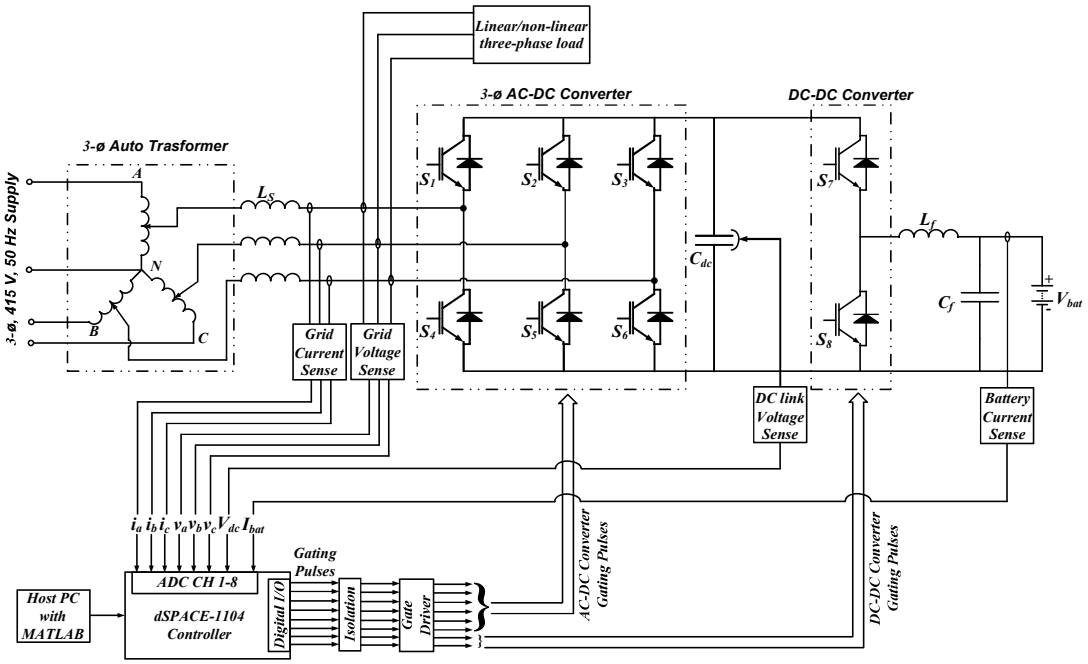

Figure 2.10: *Layout of OFF board EV charger.*

The hardware prototype of off-board EV charger is designed in laboratory. The system is designed at lower rating of 500 VA with 70 V (line-to-line voltage), 50 Hz supply. Fig. 2.10 shows the layout of EV charger developed in laboratory. The three-phase auto transformer is connected to three phase grid supply of 415 V and 50 Hz. The output of auto transformer is set at 70 V (line-to-line). This step downed AC voltage is given to AC side of bidirectional three-phase AC-DC converter. The three-phase AC-DC converter is made up of six insulated gate bipolar transistors (IGBTs) which has a diode in antiparallel. A high value of DC link capacitor is connected at the output of first stage AC-DC converter. This is used to minimize the ripple in DC link voltage. In the second stage, a bidirectional buck-boost DC-DC converter is used. This also consists of two IGBTs and works in buck mode in case of battery charging and boost mode in case of discharging. A LC filter circuit (L_f and C_f) is used to filter out the ripple in battery voltage and current. At the end of system, a battery pack is connected for charging/discharging purpose. A linear/non-linear load is connected at the point of common coupling (PCC) to generate the demand of external active and reactive power.

The control algorithm is developed in *dSPACE 1104* controller board. This controller takes the sensed output of voltage and current sensors and used these signals in development of control logic in MATLAB simulink environment. For charging purpose, it takes the three-phase grid voltage and current sensed signals, where in case of harmonic current compensation, it takes load current sensed signal also. The MATLAB simulink control logic generates the pulses of three-phase AC-DC converter and DC-DC converter. These pulses are given to the optocoupler which isolates the controller with physical system. The output of optocoupler is given to gate driver circuit which gives the pulses to IGBT switches. Fig. 2.11 shows the photograph of hardware prototype developed in laboratory.

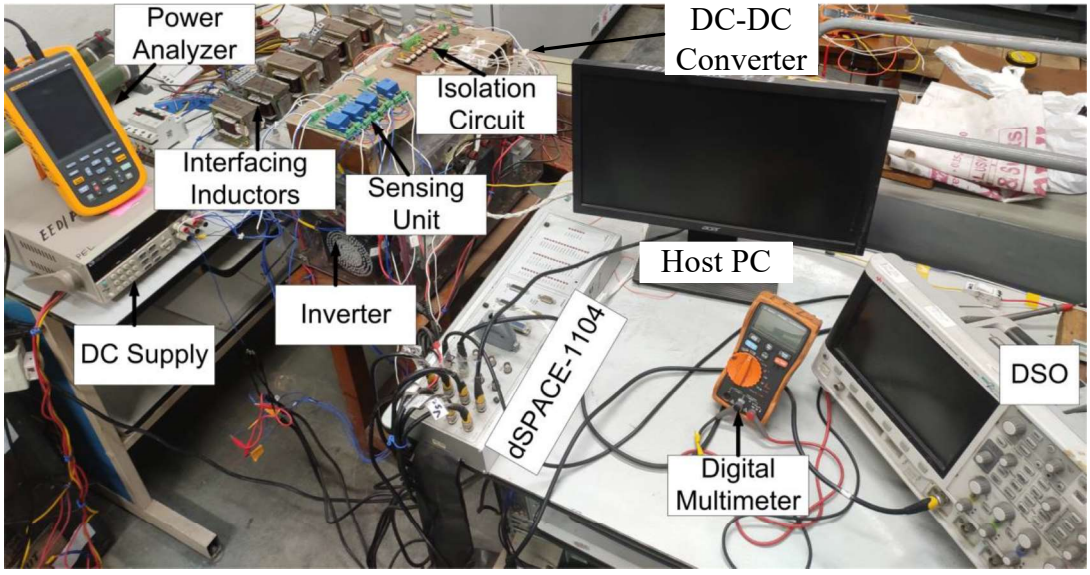

Figure 2.11: *Experimental prototype developed in laboratory.*

2.4.2 Development of First Stage AC-DC Converter

Fig. 2.12 shows the development of first stage AC-DC converter. The AC-DC converter consists of three IGBT legs (Semikron make- SKM75GB12T4). Each leg is rated as 1200 V/ 75 amps and consists of two IGBT switches. The schematic of each IGBT leg is shown in Fig. 2.12 (c). The DC link capacitor connected at DC side is rated as 1650 µF and 800 V. The gate pulses are given to pin 4 and 6 and requires 15 V pulses to turn on the switches. The photograph of complete first stage AC-DC converter is shown in Fig. 2.13.

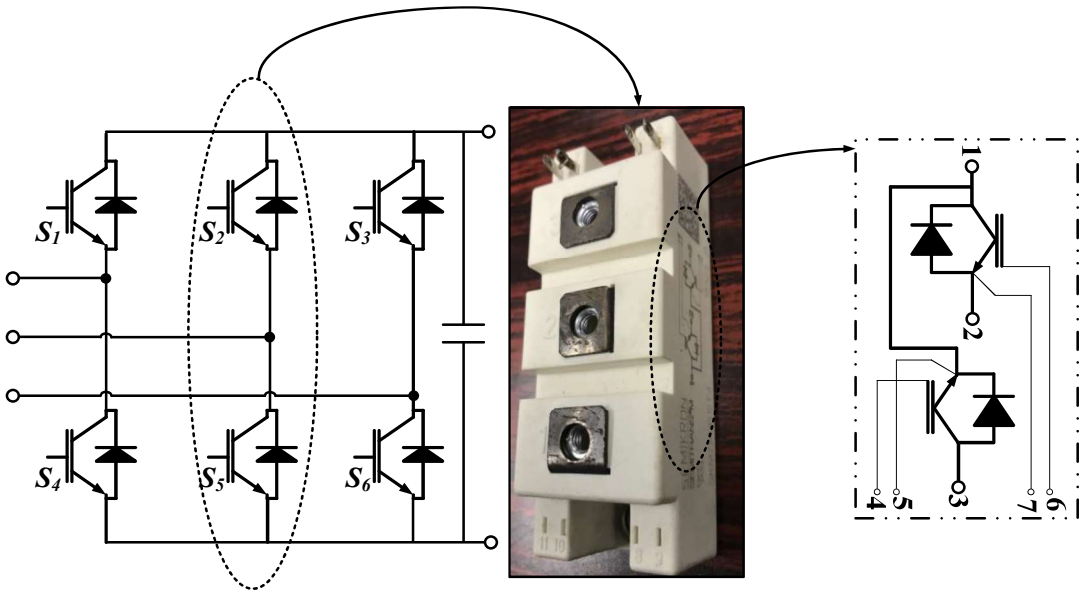

(a) (b) (c)

Figure 2.12: *(a) Schematic of AC-DC converter, (b) IGBT leg, and (c) Schematic of IGBT leg.*

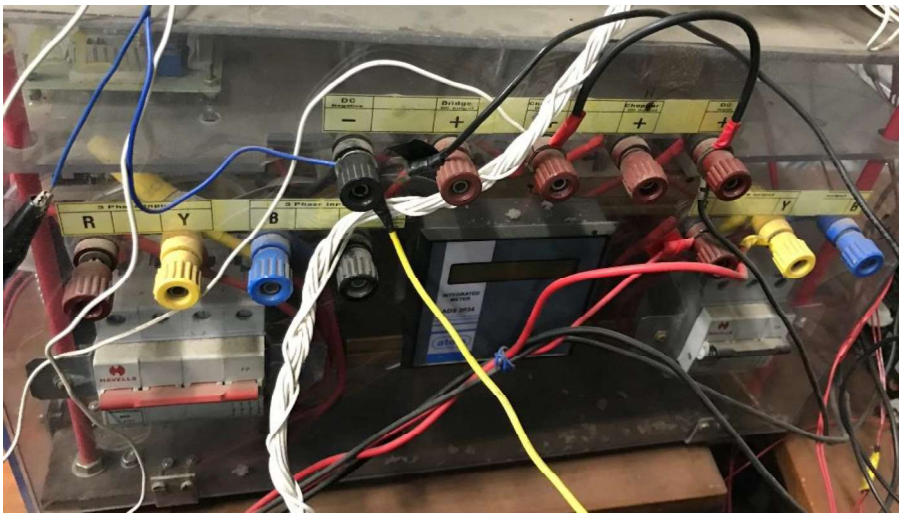

Figure 2.13: *Three leg IGBT based AC-DC Converter.*

2.4.3 Development of Second Stage DC-DC Converter

The second stage DC-DC converter is shown in Fig. 2.14. The same IGBT leg (Semikron make- SKM75GB12T4) is used for developing the second stage DC-DC converter. The terminal 1 is connected to positive of battery and terminal 2 is connected to negative side of battery pack. The terminal 3 of IGBT leg is connected to positive side of the DC link capacitor.

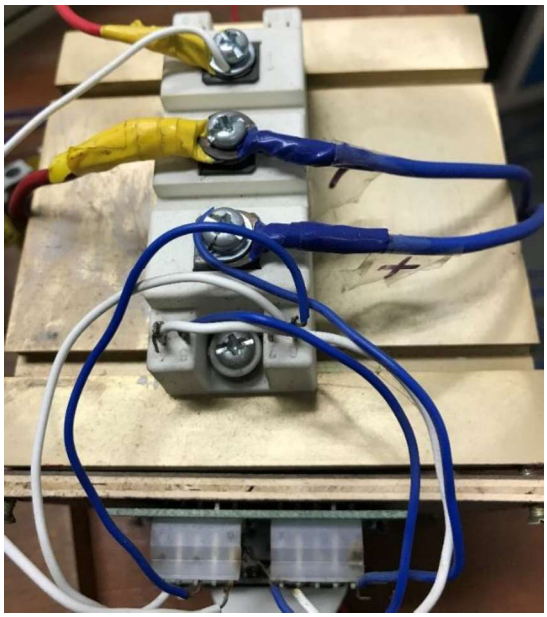

Figure 2.14: *DC-DC converter.*

2.4.4 Development of Grid Side Inductors

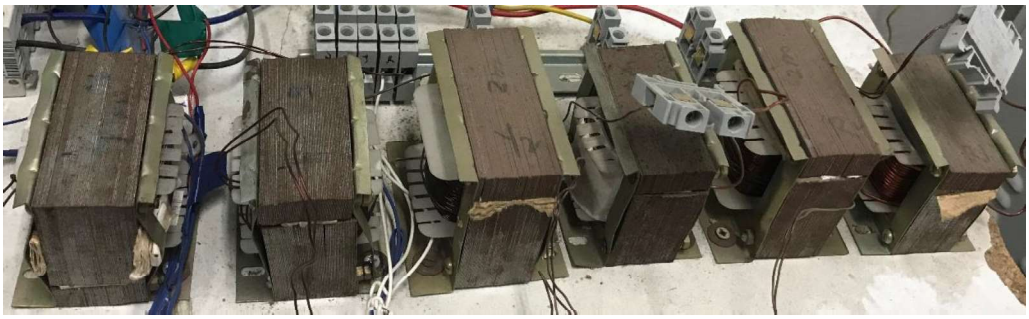

Figure 2.15: *Grid side inductors.*

Fig. 2.15 shows the photograph of grid side interfacing inductors and designing of inductor is discussed in previous section. Due to the change in switching frequency, the inductor value is changed, which is 2 mH for on-board EV charger and 4 mH for off-board EV charger, where the switching frequency is 10 kHz. Total six inductors are made, each of 2 mH and 10 A current rating. A 2 mH inductor is used for on-board EV charging where two inductors are connected in series in case of off-board EV charging. The number of turns for each inductor is calculated as,

$$N = \frac{L \cdot I_m}{A_c \cdot B_m} = \frac{2\times10^{-3}\times10\sqrt{2}}{8.658\times10^{-4}\times1} \approx 33 \tag{2.13}$$

Where, L is the inductance value in Henry, I_m is magnitude of inductor current in A, A_c is cross-section area in m^2 and B_m is flux density in Tesla and taken as 1 for CRGO. The value of number of turns is calculated 33 from the above equation 2.13 and selected as 35. The wire gauge is found as,

$$a = \frac{I}{J} = \frac{10}{3} = 3.33 \text{ mm}^2 \quad (2.14)$$

Where, I is r.m.s value of inductor current and J is current density in A/mm^2. The wire gauge is calculated 3.33 mm^2. The air gap length is found as,

$$l_g = \frac{\mu_0 \cdot N^2 \cdot A_c}{L} = \frac{4\pi \times 10^{-7} \times 35^2 \times 8.658 \times 10^{-4}}{2 \times 10^{-3}} = 0.6 \text{ mm} \quad (2.15)$$

Where, μ_0 is permeability of free space. The air gap value is 0.6 mm. The above calculated values are used to design the grid side inductor having value of 2 mH.

2.4.5 Development of DC-DC Converter Filter Circuit

The filter inductance and capacitance are found from the equations 2.9 and 2.10. However, the switching frequency in case of hardware is 10 kHz. Therefore, the value of inductance and capacitance are selected as 6 mH and 47 µF respectively. Fig. 2.16 shows the photograph of DC-DC filter circuit and battery current sensor.

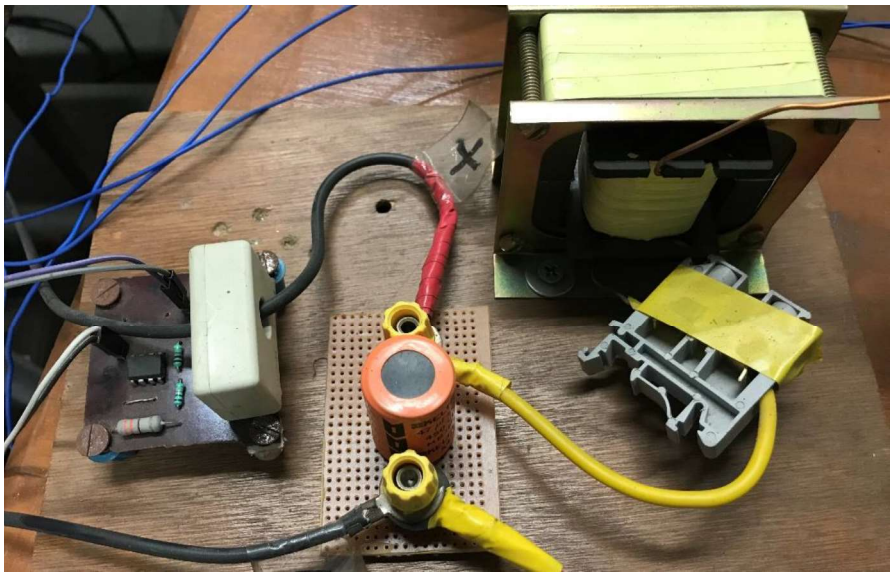

Figure 2.16: *DC-DC filter circuit and battery current sensor.*

2.4.6 Development of Sensing Units

The sensors are play very important role in development of any control logic. They take actual signal as input and generate their equivalent voltage signal as output. Hall effect voltage and current sensors are used to measure the high voltage and current signals. They are preferred in most cases because they can measure both AC and DC signals without change in scaling and configuration. In present case, the LEM (LEM 25P – 500 V) voltage sensor and LEM (LEM LA 55-P) current sensor are used to sense the actual voltage and current signal. Both the sensors required ± 15 V DC supply to energies. Further, the output is fed to ADC channels of dSPACE controller. The

schematic and photograph of both sensors are shown in Fig. 2.17 and 2.18 respectively [92], [93].

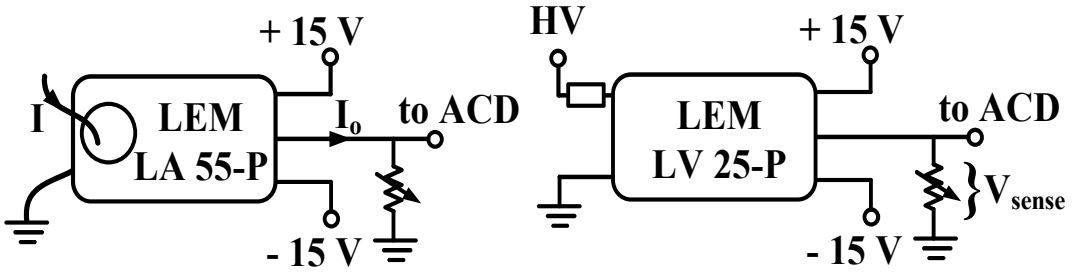

(a) (b)

Figure 2.17: *Schematic of (a) Current Sensor and (b) Voltage Sensor.*

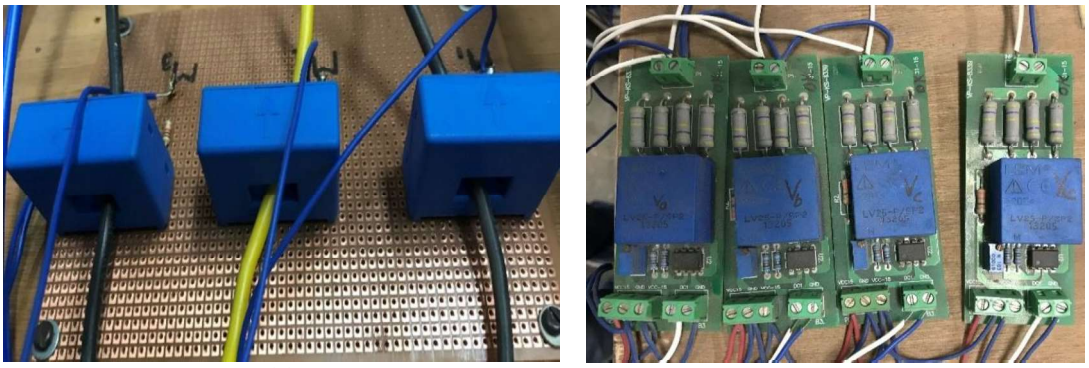

(a) (b)

Figure 2.18: *(a) Current sensors and (b) Voltage Sensors.*

2.4.7 Battery Bank

To analyze the charger/discharge behavior of battery pack, a stack of eight batteries is used in laboratory. Each battery is lead-acid (Rocket make) and has nominal rating of 12 V, 7 AH. All batteries are connected in series to make a 96 V battery pack. Each battery has stand by voltage of 13.50 V to 13.80 V at 20°C, where the charging voltage is 14.4 V to 15 V for constant voltage charging. The photograph of battery pack is shown in Fig. 2.19.

Figure 2.19: *Battery pack.*

2.4.8 Driver Circuit

To turn on the IGBT leg, SKYPER 32 gate driver circuit board has been used. It has two output channels and under voltage/short circuit protection features. It has two isolated gate driving circuits for both switches. It requires 15 V DC supply and generates 80 mA to 150 mA of current. The photograph of SKYPER 32 driving circuit board is shown in Fig. 2.20 [94].

Figure 2.20: *Gate driver circuit.*

2.4.9 Development of Isolator Circuit

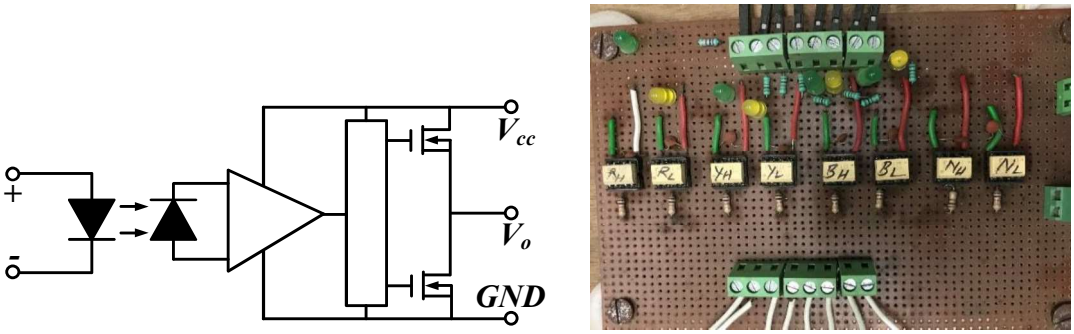

(a) (b)

Figure 2.21: *(a) Schematic of TLP 350 and (b) Isolator board.*

An isolator is an electronic integrated circuit (IC) which transfer the electrical signal by using light between two isolated circuits. To isolate dSPACE controller from

physical system, TLP 350 optocoupler IC is used. This is an eight pin IC and can work up to 100°C of temperature. It has internal Faraday shield which guaranteed provides ±15 kV/µs common mode transient immunity. The photograph of isolator board developed in laboratory and schematic of TLP 350 is shown in Fig. 2.21 [95].

2.4.10 Linear/Non-linear Load

Three-phase load is connected at PCC to generate the external active/reactive power and harmonic current demand. The combination of variable inductors, capacitors and resistances are connected whereas the non-linear load is made by three-phase diode bridge rectifier. The photographs of external loads are shown in Fig 2.22.

(a) (b)

(c)

Figure 2.22: *External load (a) Resistance and inductors, (b) Variable capacitor load and (c) Three-phase diode bridge.*

MATHEMATICAL MODELING OF ELECTRIC VEHICLE CHARGER

CHAPTER 3

Chapter Outline

3.1 Introduction

This chapter deals with the design of two stage bidirectional EV charger. The chapter includes mathematical modelling of first stage AC-DC converter, second stage DC-DC converter and battery pack.

3.2 Modeling of Single-phase AC-DC Converter

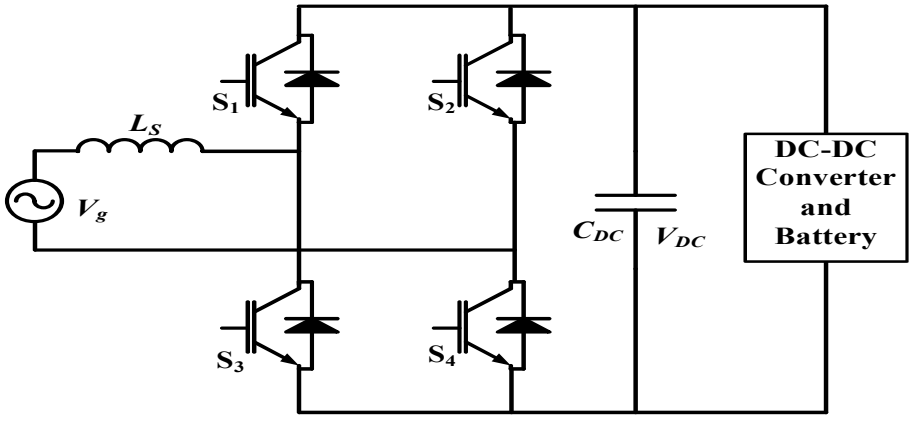

Figure 3.1: *First stage AC-DC converter of ON board EV charger.*

The configuration of first stage AC-DC converter is shown in Fig. 3.1. The control of AC-DC converter consists of two control loops i.e., outer and inner. The outer loop is slow and used for voltage control and inner loop is fast acting and used for grid current control. The explanation of switching model, average mode and small signal model is shown below.

3.2.1 Switching Model

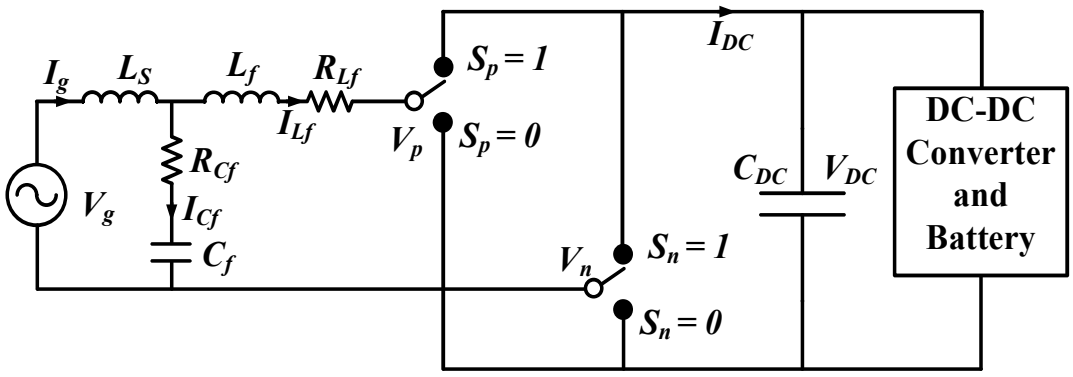

Figure 3.2: *Switching model of single phase AC-DC converter.*

The switching model of single-phase AC-DC converter is shown in Fig. 3.2. Each leg of Fig. 3.1 is represented by single pole double throw switch. In which, the grid voltage is represented by V_g, L_s is grid side inductor, L_f and C_f is AC side filter inductance and capacitance respectively and R_{Lf} and R_{Cf} is equivalent series resistance (ESR) of filter inductance and capacitance respectively. The representation of on state of switch S_1 and S_3 is S_p = 1 and S_p = 0 respectively. Where, S_n = 1 and S_n = 0 is the representation of on state of switch S_2 and S_4 respectively. Therefore, when switch S_1 and S_4 are on and S_3 and S_2 are off then the grid current I_g is equal to DC side current I_{DC} and V_{pn} equals to V_{DC}. The on state of switch S_1 and S_4 is expressed as [96],

$$\begin{aligned} V_{pn} &= V_p - V_n \\ &= S_p \cdot V_{DC} - S_n \cdot V_{DC} = (S_p - S_n) V_{DC} \\ &= S_{pn} \cdot V_{DC} \end{aligned} \tag{3.1}$$

Where,

$$S_{pn} = S_p - S_n \tag{3.2}$$

And

$$I_{DC} = (S_p - S_n) I_{Lf} = S_{pn} \cdot I_{Lf} \tag{3.3}$$

Now apply kirchhoff's voltage law (KVL) in outer loop and neglecting capacitor ESR,

$$V_g = V_{Ls} + V_{Cf}$$
$$\frac{dI_g}{dt} = \frac{V_g}{L_s} - \frac{V_{Cf}}{L_s} \tag{3.4}$$

Now apply KVL in inner loop gives,

$$V_{Cf} = V_{Lf} + I_{Lf} \cdot R_{Lf} + V_{pn}$$
$$\frac{dI_{Lf}}{dt} = \frac{V_{Cf}}{L_f} - \frac{I_{Lf} \cdot R_{Lf}}{L_f} - \frac{V_{pn}}{L_f} \tag{3.5}$$

Now apply kirchhoff's current law (KCL) at junction,

$$I_g = I_{Lf} + I_{Cf}$$
$$\frac{dV_{Cf}}{dt} = \frac{I_g}{C_f} - \frac{I_{Lf}}{C_f} \tag{3.6}$$

3.2.2 Average Model

The average model of system is acquired by applying averaging operator to switching model over one switching period. The averaging operator for a time varying variable *y* is defined as,

$$\tilde{y} = \frac{1}{T}\int_0^T y(\tau)d\tau \tag{3.7}$$

The $\tilde{y}$ represents the average value. Therefore, by applying averaging operator to above derived state-space equations 3.4-3.6, produce following equations,

$$\frac{d\widetilde{I_g}}{dt} = \frac{\widetilde{V_g}}{L_s} - \frac{\widetilde{V_{Cf}}}{L_s} \tag{3.8}$$

$$\frac{d\widetilde{I_{Lf}}}{dt} = \frac{\widetilde{V_{Cf}}}{L_f} - \frac{\widetilde{I_{Lf}} \cdot R_{Lf}}{L_f} - \frac{d_{pn} \cdot V_{DC}}{L_f} \tag{3.9}$$

where,

$$d_{pn} = \widetilde{S_{pn}} \tag{3.10}$$

$$\frac{d\widetilde{V_{Cf}}}{dt} = \frac{\widetilde{I_g}}{C_f} - \frac{\widetilde{I_{Lf}}}{C_f} \tag{3.11}$$

The average value of S_{pn} is represented by d_{pn} and V_{DC} is average DC link voltage.

3.2.3 Small Signal Model

The small signal model is constructed by composing the steady state values of average model and superimposed small AC variations. The small signal equations of above derived equations 3.8, 3.9 and 3.11 are,

$$\frac{d\tilde{\tilde{I}}_g}{dt} = \frac{\tilde{\tilde{V}}_g}{L_s} - \frac{\tilde{\tilde{V}}_{Cf}}{L_s} \tag{3.12}$$

$$\frac{d\tilde{\tilde{I}}_{Lf}}{dt} = \frac{\tilde{\tilde{V}}_{Cf}}{L_f} - \frac{\tilde{\tilde{I}}_{Lf} \cdot R_{Lf}}{L_f} - \frac{\widetilde{d_{pn}} \cdot V_{dc}}{L_f} \tag{3.13}$$

$$\frac{d\tilde{\tilde{V}}_{Cf}}{dt} = \frac{\tilde{\tilde{I}}_g}{C_f} - \frac{\tilde{\tilde{I}}_{Lf}}{C_f} \tag{3.14}$$

Taking Laplace transform of above equations,

$$S\tilde{\tilde{I}}_g = \frac{\tilde{\tilde{V}}_g}{L_s} - \frac{\tilde{\tilde{V}}_{Cf}}{L_s} \tag{3.15}$$

$$S\tilde{\tilde{I}}_{Lf} = \frac{\tilde{\tilde{V}}_{Cf}}{L_f} - \frac{\tilde{\tilde{I}}_{Lf} \cdot R_{Lf}}{L_f} - \frac{\widetilde{d_{pn}} \cdot V_{dc}}{L_f} \tag{3.16}$$

$$S\tilde{\tilde{V}}_{Cf} = \frac{\tilde{\tilde{I}}_g}{C_f} - \frac{\tilde{\tilde{I}}_{Lf}}{C_f} \tag{3.17}$$

From equation (3.15)

$$\tilde{\tilde{I}}_g = \frac{\tilde{\tilde{V}}_g}{SL_s} - \frac{\tilde{\tilde{V}}_{Cf}}{SL_s} \tag{3.18}$$

Put equation (3.18) in equation (3.17),

$$S\tilde{\tilde{V}}_{Cf} = \frac{1}{C_f}\left(\frac{\tilde{\tilde{V}}_g}{SL_s} - \frac{\tilde{\tilde{V}}_{Cf}}{SL_s}\right) - \frac{\tilde{\tilde{I}}_{Lf}}{C_f}$$

$$\tilde{\tilde{V}}_{Cf} = \frac{\tilde{\tilde{V}}_g}{S^2L_sC_f + 1} - \frac{\tilde{\tilde{I}}_{Lf} \cdot SL_s}{S^2L_sC_f + 1} \tag{3.19}$$

Put equation (3.19) in equation (3.16)

$$S\tilde{\tilde{I}}_{Lf} = \frac{1}{L_f}\left(\frac{\tilde{\tilde{V}}_g}{S^2L_sC_f + 1} - \frac{\tilde{\tilde{I}}_{Lf} \cdot SL_s}{S^2L_sC_f + 1}\right) - \frac{\tilde{\tilde{I}}_{Lf} \cdot R_{Lf}}{L_f} - \frac{\widetilde{d_{pn}} \cdot V_{dc}}{L_f}$$

$$\tilde{\tilde{I}}_{Lf} = \frac{\tilde{\tilde{V}}_g}{S^3L_fL_sC_f + S^2L_sC_fR_{Lf} + S(L_f + L_s) + R_{Lf}} - \widetilde{d_{pn}} \cdot V_{dc}\left(\frac{S^2L_sC_f + 1}{S^3L_fL_sC_f + S^2L_sC_fR_{Lf} + S(L_f + L_s) + R_{Lf}}\right) \tag{3.20}$$

If it is assumed that the disturbance from the grid voltage is zero, the final relation is as follows;

$$\widetilde{\widetilde{I_{Lf}}} = -\widetilde{d_{pn}} \cdot V_{dc}\left(\frac{S^2 L_s C_f + 1}{S^3 L_f L_s C_f + S^2 L_s C_f R_{Lf} + S(L_f + L_s) + R_{Lf}}\right) \tag{3.21}$$

At high frequencies, the above equation approaches to,

$$\widetilde{\widetilde{I_{Lf}}} = \frac{-\widetilde{d_{pn}} \cdot V_{dc}}{SL_f + R_{Lf}} \tag{3.22}$$

From the above equation it is found that d_{pn} increases with decrement in $\widetilde{\widetilde{I_{Lf}}}$ due to negative sign. Therefore, the plant transfer function is,

$$G_{Pac} = V_{dc} \cdot \frac{1}{SL_f + R_{Lf}} \tag{3.23}$$

In this study, different controllers are used to control the grid current in inner control loop as shown in Fig. 3.3.

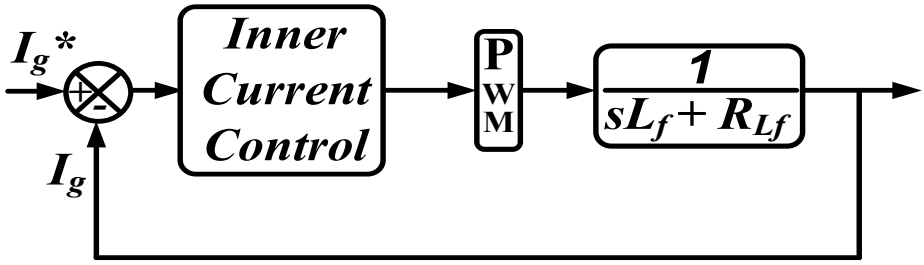

Figure 3.3: *Inner current control loop.*

3.3 Modeling of Three-phase AC-DC Converter

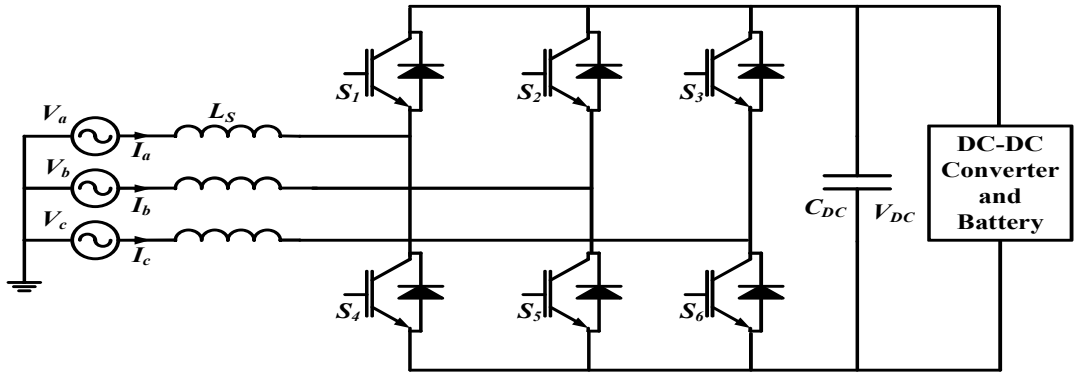

Figure 3.4: *First stage AC-DC converter of OFF board EV charger.*

The configuration of three-phase AC-DC converter is shown in Fig. 3.4. The switching model shown in Fig. 3.5 is represented by three single pole double throw switches (S_a, S_b and S_c). The grid voltage is represented by V_{abc} where each phase voltage of charger is represented by V_{ga}, V_{gb} and V_{gc}, and line-to-line voltage is V_{gab}, V_{gbc} and

V_{gca}. The value of single pole double throw switch is 1 in case of upper switch on and 0 in case of lower switch on. The equations of three-phase voltages and currents are as follows,

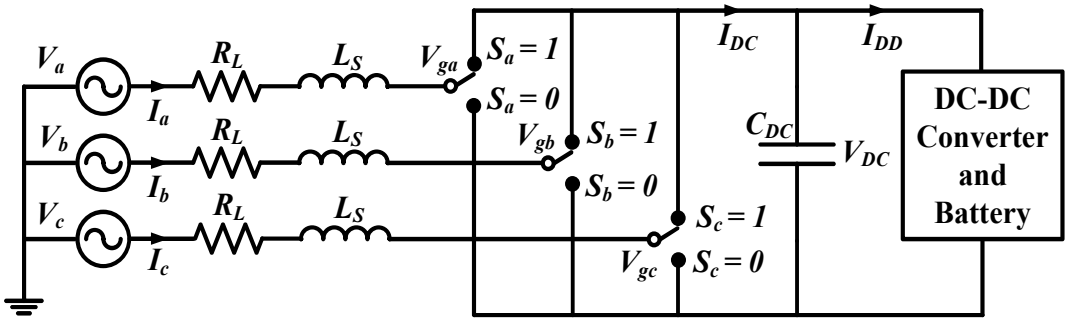

Figure 3.5: *Switching model of three phase AC-DC converter.*

$$V_{ga} = V_m \cos(\omega t)$$
$$V_{gb} = V_m \cos\left(\omega t - \frac{2\pi}{3}\right)$$
$$V_{gc} = V_m \cos\left(\omega t - \frac{4\pi}{3}\right) \quad (3.24)$$

and current equations are,

$$I_a = I_m \cos(\omega t + \emptyset)$$
$$I_b = I_m \cos\left(\omega t + \emptyset - \frac{2\pi}{3}\right)$$
$$I_c = I_m \cos\left(\omega t + \emptyset - \frac{4\pi}{3}\right) \quad (3.25)$$

Since, neutral is not used here, we obtain

$$I_a + I_b + I_c = 0 \quad (3.26)$$

From the switching model, the line-to-line voltage can be written as,

$$V_{gab} = (S_a - S_b) \cdot V_{DC} \quad (3.27)$$
$$V_{gbc} = (S_b - S_c) \cdot V_{DC} \quad (3.28)$$
$$V_{gca} = (S_c - S_a) \cdot V_{DC} \quad (3.29)$$

Where, the switch (S_a, S_b and S_c) values are 1 in case of upper switch on and 0 in case of lower switch on.

$$V_{ga} = fa \cdot V_{DC} \quad (3.30)$$
$$V_{gb} = f_b \cdot V_{DC} \quad (3.31)$$
$$V_{gc} = f_c \cdot V_{DC} \quad (3.32)$$

where,

$$f_a = S_a - S^* = S_a - \frac{1}{3}(S_a + S_b + S_c) \tag{3.33}$$

$$f_b = S_b - \frac{1}{3}(S_a + S_b + S_c) \tag{3.34}$$

$$f_c = S_c - \frac{1}{3}(S_a + S_b + S_c) \tag{3.35}$$

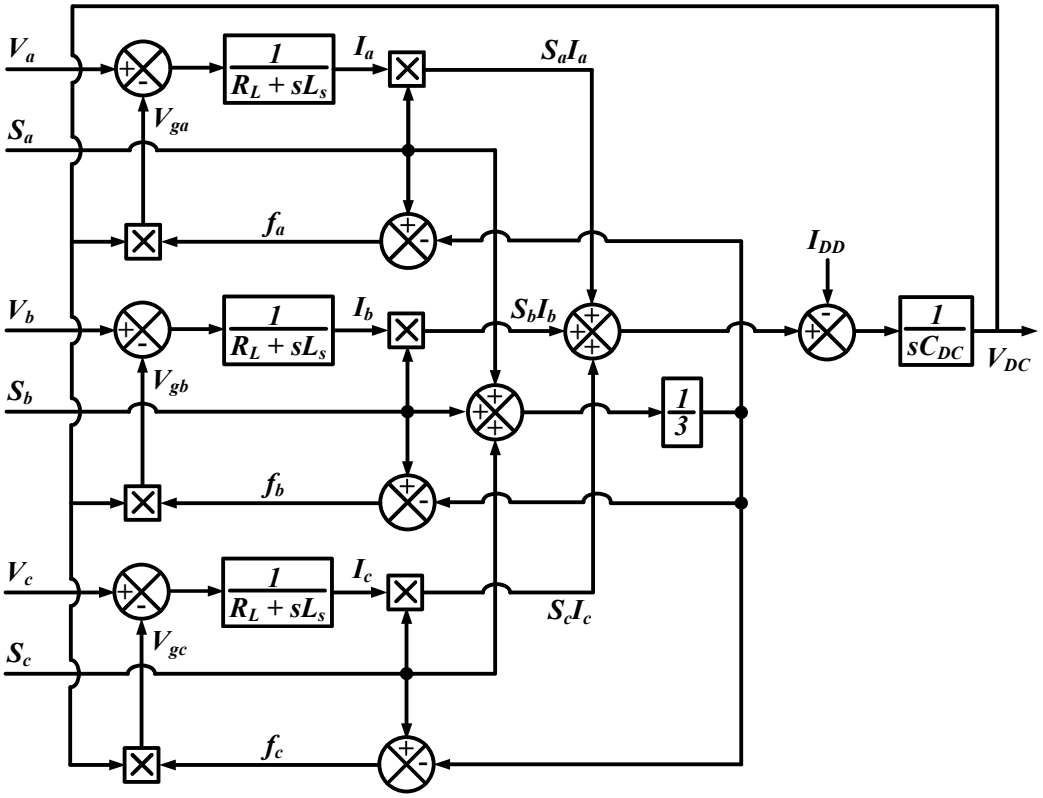

Figure 3.6: *Block diagram of three phase AC-DC converter.*

By applying KVL in each phase,

$$V_a = R_L \cdot I_a + L_s \frac{dI_a}{dt} + V_{ga} \tag{3.36}$$

$$V_b = R_L \cdot I_b + L_s \frac{dI_b}{dt} + V_{gb} \tag{3.37}$$

$$V_c = R_L \cdot I_c + L_s \frac{dI_c}{dt} + V_{gc} \tag{3.38}$$

By applying KCL at DC side,

$$C_{DC} \frac{dV_{DC}}{dt} = S_a I_a + S_b I_b + S_c I_c - I_{DD} \tag{3.39}$$

The block diagram of above derived equations is shown in Fig. 3.6.

3.3.1 Modeling of Three-Phase AC-DC Converter in *dq* Frame.

The modeling in rotating reference frame (*dq* frame) is used due to its well-known advantages like control development is easy, the noise in DC signal can be easily filter out and decouple the active and reactive power [97].

The *abc-dq* transformation matrix form is given below,

$$\begin{bmatrix} d \\ q \end{bmatrix} = \frac{2}{3}\begin{bmatrix} \cos\theta & \cos\left(\theta - \frac{2\pi}{3}\right) & \cos\left(\theta + \frac{2\pi}{3}\right) \\ -\sin\theta & -\sin\left(\theta - \frac{2\pi}{3}\right) & -\sin\left(\theta + \frac{2\pi}{3}\right) \end{bmatrix}\begin{bmatrix} a \\ b \\ c \end{bmatrix} \tag{3.40}$$

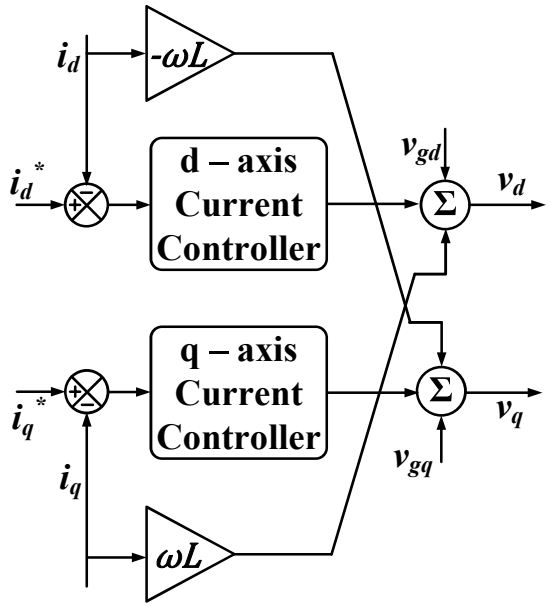

Figure 3.7: *Inner current control in dq frame.*

By applying abc-dq transformation in equations 3.40 to 3.43 we get,

$$V_d = R_L \cdot i_d + L_s \frac{di_d}{dt} - \omega L_s i_q + V_{gd} \tag{3.41}$$

$$V_q = R_L \cdot i_q + L_s \frac{di_q}{dt} + \omega L_s i_d + V_{gq} \tag{3.42}$$

$$C_{DC} \frac{dV_{DC}}{dt} = \frac{3}{2}(S_d i_d + S_q i_q) \tag{3.43}$$

The block diagram of inner current control loop is same as shown in Fig. 3.3. Moreover, the current control loop of three-phase AC-DC converter in *dq* frame along with decoupling terms is shown in Fig. 3.7.

Further, the direct (V_{gd}) and quadrature (V_{gq}) axis component of converter AC side voltage are expressed as $d_d \cdot V_{DC}$ and $d_q \cdot V_{DC}$ respectively. The equations (3.41) and (3.42) are expressed as follows:

$$V_d = R_L \cdot i_d + L_s \frac{di_d}{dt} - \omega L_s i_q + d_d \cdot V_{DC} \tag{3.44}$$

$$V_q = R_L \cdot i_q + L_s \frac{di_q}{dt} + \omega L_s i_d + d_q \cdot V_{DC} \tag{3.45}$$

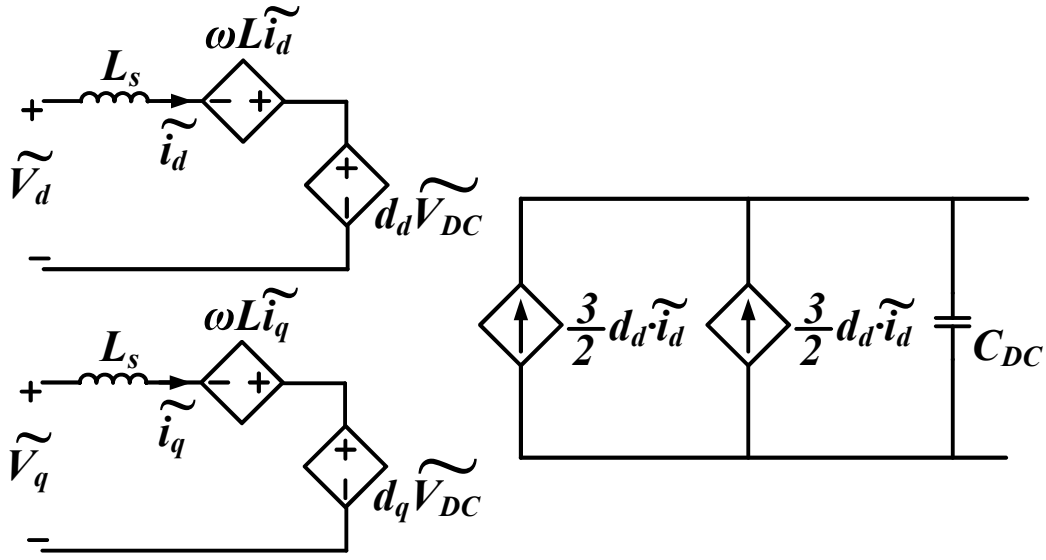

Figure 3.8: *Equivalent model of three phase AC-DC converter.*

Now by applying averaging operator to equations (3.44) to (3.45), produce following equations,

$$\widetilde{V_d} = R_L \cdot \tilde{i_d} + L_s \frac{d\tilde{i_d}}{dt} - \omega L_s \tilde{i_q} + d_d \cdot \widetilde{V_{DC}} \tag{3.46}$$

$$\widetilde{V_q} = R_L \cdot \tilde{i_q} + L_s \frac{d\tilde{i_q}}{dt} + \omega L_s \tilde{i_d} + d_q \cdot \widetilde{V_{DC}} \tag{3.47}$$

$$C_{DC} \frac{d\widetilde{V_{DC}}}{dt} = \frac{3}{2}(d_d i_d + d_q i_q) \tag{3.48}$$

where,

$$d_{dq} = \widetilde{S_{dq}} \tag{3.49}$$

The equivalent circuit of above averaged equations are shown in Fig. 3.8.

3.4 Modeling of Battery Pack

Due to the well-known advantages of Li-ion cell, it is used to developed the structure of battery pack. For the nominal cell voltage 3.3 V, the cut off voltage of Li-ion cell is 2.95 V at lowest SOC value i.e., 20%. The maximum output voltage is 3.6 V when SOC reach to 90%. The nominal current capacity of each cell is 18 Ah. To develop the 350 V battery pack, the number of cells required in each string connected in series is 350/3.3 = 106.06. The nearest integer value is 107 cells. Therefore, the maximum voltage attain by this battery pack is 107×3.6 = 385.2 V and minimum voltage is 107×2.95 = 315.65 V. The nominal capacity of each string is 18 Ah × 350 V = 6.3 KWh. Whereas, the capacity of battery pack can be increased by connecting one more string in parallel.

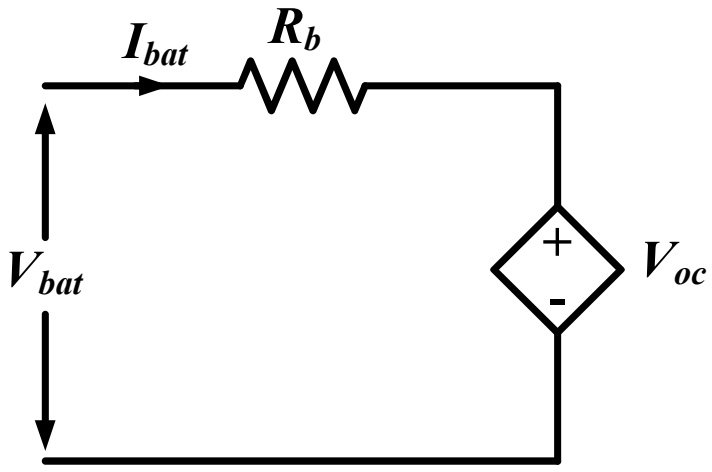

Figure 3.9: *Equivalent model of battery pack.*

The equivalent model of battery pack is shown in Fig. 3.9. The R_b is internal resistance of battery and V_{oc} is battery pack open circuit voltage. From the battery manufacturer data sheet, the initial internal resistance is less than 4 mΩ for 1 kHz AC battery charging current. However, this internal resistance is valid for 0.55 C charging rate i.e., 10 A. Generally, the internal resistance of Li-ion battery is more because it is proportional to charging current. Therefore, it is selected as 10 mΩ per cell. Since, there are 107 cells connected in each string in series, the total internal resistance is 10 mΩ × 107 = 1.07 Ω. Moreover, the battery open circuit voltage is varies according to the current SOC.

3.5 Modeling of DC-DC Converter

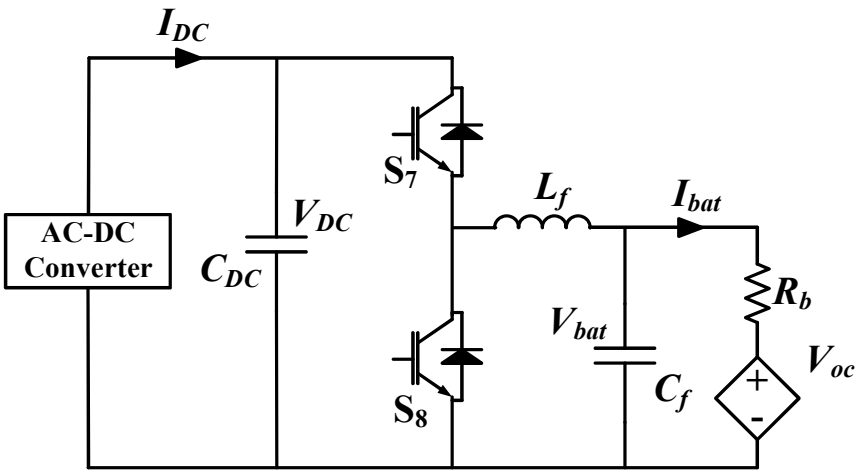

Figure 3.10: *DC-DC converter topology.*

The second stage DC-DC converter topology is shown in Fig. 3.10. It consists of two IGBT switches and works in both the directions. It works in buck mode in case of charging of battery and boost mode while transferring the active power to grid [98].

Switch S_7 is on and S_8 is off: -

The average modeling of DC-DC converter during switch S_7 on is discussed below. Fig. 3.11 shows the direction of current flow during on state of switch S_7 and off state of switch S_8.

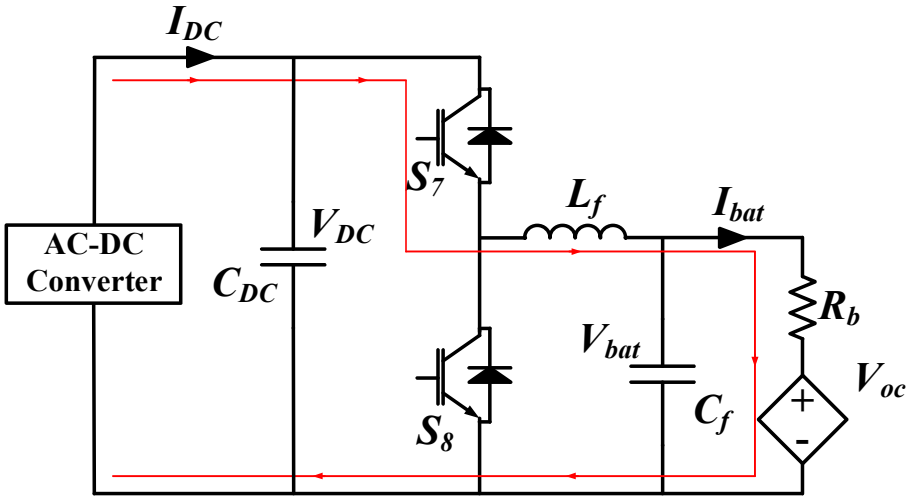

Figure 3.11: *DC-DC buck operation on state.*

KVL in outer loop gives,

$$V_{DC} = V_{Lf} + V_{bat}$$

$$\frac{dI_{Lf}}{dt} = \frac{V_{DC}}{L_f} - \frac{V_{bat}}{L_f} \tag{3.50}$$

Where, V_{Lf} and V_{bat} are the voltage across filter inductance L_f and capacitance C_f respectively and I_{Lf} is current across the inductor.

Now KCL at battery side gives,

$$I_{Lf} = I_{Cf} + I_{bat}$$
$$\frac{dV_{bat}}{dt} = \frac{I_{Lf}}{C_f} - \frac{I_{bat}}{C_f} \tag{3.51}$$

Where, I_{Cf} is the current through capacitor C_f.

Now KCL at DC link capacitor side gives,

$$I_{DC} = I_{CDC} + I_{Lf}$$
$$\frac{dV_{DC}}{dt} = \frac{I_{DC}}{C_{DC}} - \frac{I_{Lf}}{C_{DC}} \tag{3.52}$$

Where, I_{CDC} is the current through DC link capacitor C_{DC}.

Now, Fig. 3.12 shows the direction of current flow during off state of switch S_7 and on state of switch S_8.

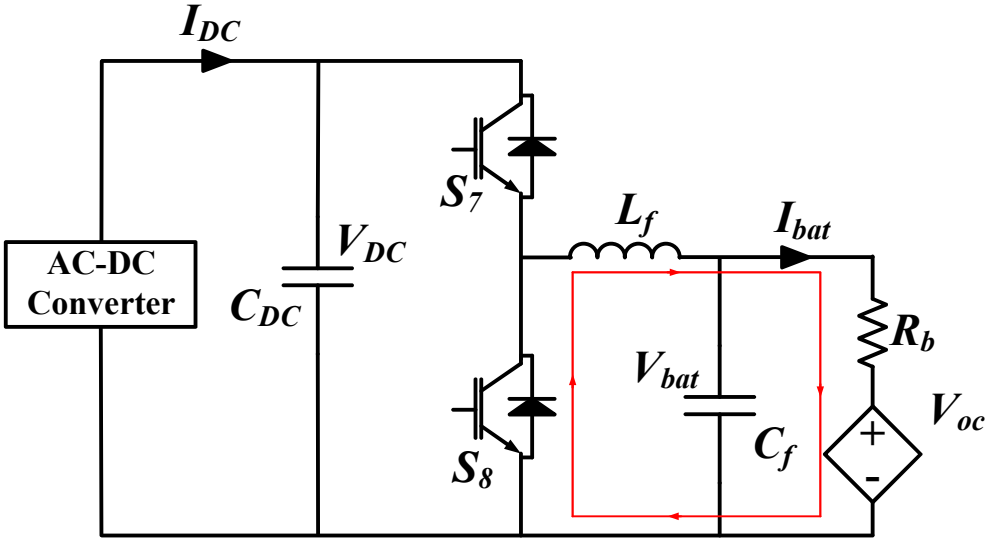

Figure 3.12: *DC-DC buck operation OFF state.*

KVL in battery loop gives,

$$0 = V_{Lf} + V_{bat}$$
$$\frac{dI_{Lf}}{dt} = -\frac{V_{bat}}{L_f} \tag{3.53}$$

Now apply KCL at battery side gives,

$$I_{Lf} = I_{Cf} + I_{bat}$$
$$\frac{dV_{bat}}{dt} = \frac{I_{Lf}}{C_f} - \frac{I_{bat}}{C_f} \tag{3.54}$$

Now KCL at DC link capacitor side gives,

$$I_{DC} = I_{CDC}$$
$$\frac{dV_{DC}}{dt} = \frac{I_{DC}}{C_{DC}} \tag{3.55}$$

The on and off states can be averaged by duty cycle *d* and (*1-d*) respectively. Where, *d* is the duty cycle for switch S_7.

Averaging of KVL equations (3.50) and (3.53) gives,

$$\frac{d\widetilde{I_{Lf}}}{dt} = d\left(\frac{\widetilde{V_{DC}}}{L_f} - \frac{\widetilde{V_{bat}}}{L_f}\right) + (1-d)\left(-\frac{\widetilde{V_{bat}}}{L_f}\right)$$
$$\frac{d\widetilde{I_{Lf}}}{dt} = \frac{d\cdot\widetilde{V_{DC}}}{L_f} - \frac{\widetilde{V_{bat}}}{L_f} \tag{3.56}$$

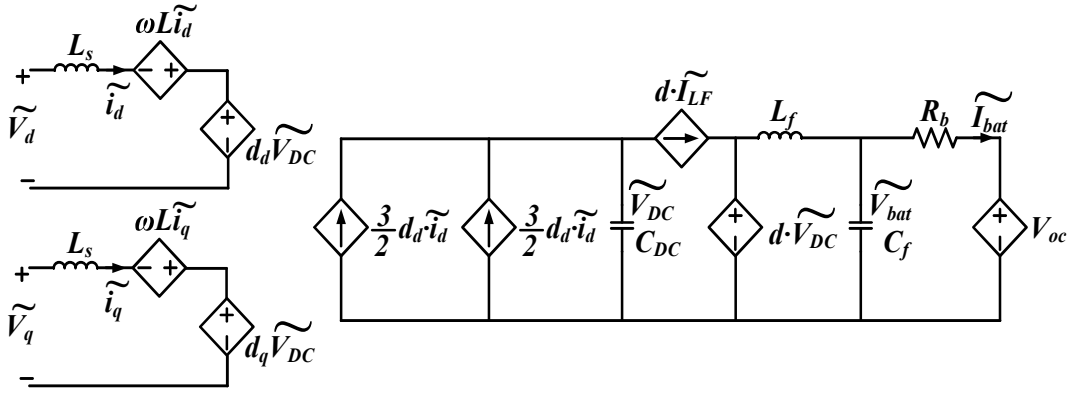

Figure 3.13: *Average model of two-stage bidirectional EV charger.*

and averaging of KCL equations (3.51) and (3.54) gives,

$$\frac{d\widetilde{V_{bat}}}{dt} = d\left(\frac{\widetilde{I_{Lf}}}{C_f} - \frac{\widetilde{I_{bat}}}{C_f}\right) + (1-d)\left(\frac{\widetilde{I_{Lf}}}{C_f} - \frac{\widetilde{I_{bat}}}{C_f}\right)$$
$$\frac{d\widetilde{V_{bat}}}{dt} = \frac{\widetilde{I_{Lf}}}{C_f} - \frac{\widetilde{I_{bat}}}{C_f} \tag{3.57}$$

and averaging of KCL equations (3.52) and (3.55) gives,

$$\frac{d\widetilde{V_{DC}}}{dt} = d\left(\frac{\widetilde{I_{DC}}}{C_{DC}} - \frac{\widetilde{I_{Lf}}}{C_{DC}}\right) + (1-d)\left(\frac{\widetilde{I_{DC}}}{C_{DC}}\right)$$
$$\frac{d\widetilde{V_{DC}}}{dt} = \frac{\widetilde{I_{DC}}}{C_{DC}} - \frac{d\cdot\widetilde{I_{Lf}}}{C_{DC}} \tag{3.58}$$

The equations (3.56), (3.57) and (3.58) shows the average expressions of DC-DC converter model.

Fig. 3.13 shows the equivalent circuit of both the conversion stages. This averaged model does not account the losses of converters for simplicity. However, the non-idealities of converter switches, inductors and capacitors are required for efficiency analysis, which is not the case here. The main focus of this model is presenting the dynamic behavior of designed EV charger.

CHAPTER 4

CONTROL OF OFF BOARD ELECTRIC VEHICLE CHARGER

Chapter Outline

4.1 Introduction

This chapter deals with the design of two controllers for a two-stage bidirectional off-board EV charger. The charger comprises of two bidirectional stages i.e., first (AC to DC) and second (DC to DC) conversion stages. The first control strategy is based on *PI* regulator and second one is based on adaptive neuro-fuzzy inference system (*ANFIS*). Both controllers can work in all possible active (*P*)-reactive (*Q*) power cases. The performance of controller is evaluated in eight modes including charging and reactive power compensation. The charger charges the battery pack as per desired by user and compensate the reactive power if requested by utility grid. Generally, the control of first-stage of EV charger consists of two loops i.e., outer (slow) loop and fast acting inner loop. The quantities to be controlled in outer loop are active (*P*) and reactive (*Q*) power which developed the direct and quadrature axis reference current. Since, these quantities are DC in nature, they can be easily handled. However, in inner loop, the grid current is regulated. For *PI* based controller, the grid current is controlled in *dq* frame by two *PI* controllers and pulses are generated by well-known pulse width modulation (PWM) technique.

Moreover, in *ANFIS* based technique, a unified *ANFIS* has been designed to estimate the direct and quadrature axis reference currents directly in outer loop while regulating two different quantities in single step only and hence, named as unified *ANFIS* controller. Further, in inner control loop, the grid current is controlled by hysteresis controller in *abc* frame. The proposed controller can compensate the harmonics of load current and act as an active power filter. The proposed EV charger is simulated in MATLAB/Simulink and controller performance is validated with scaled down hardware model in real time using *dSPACE-1104*. A simulation-based study has been presented of a 12.5 KVA EV charger and the hardware prototype rating of both controllers is 500 VA.

4.2 Proportional Integral Based EV Charger Controller

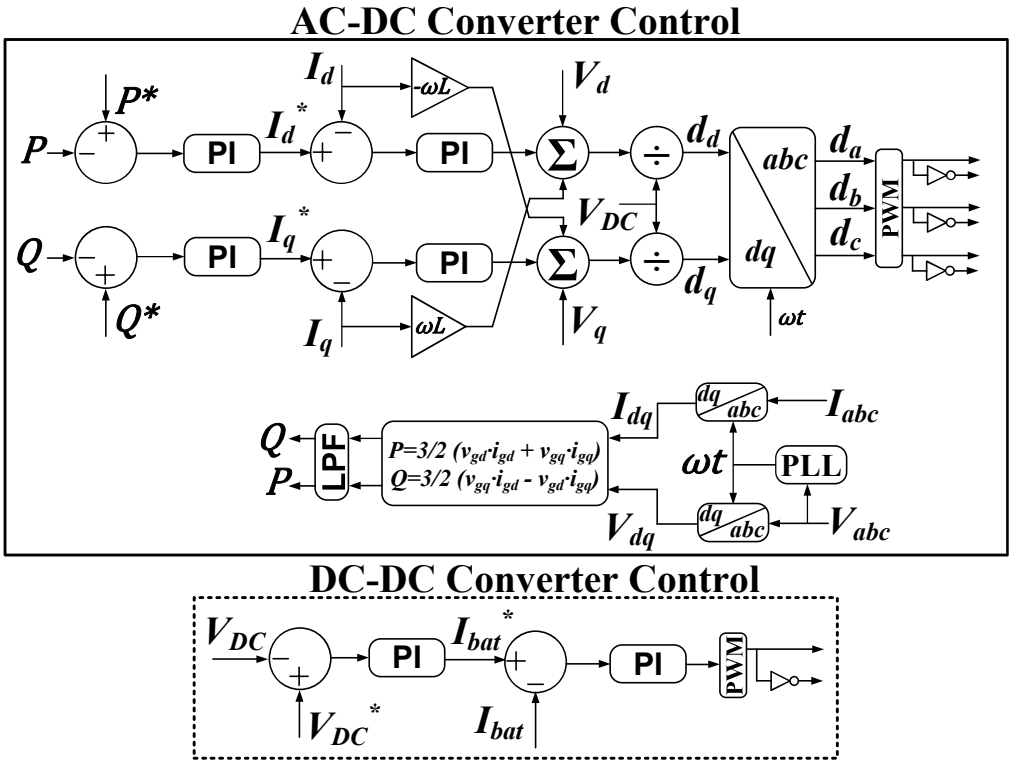

Figure 4.1: *PI based OFF board EV charger.*

The system architecture of off-board EV charger is shown in Fig. 2.8 and system description is given in section 2.3.

The EV charger controller is shown in Fig. 4.1. The controller is based on conventional *PI* regulators for two-stage off-board EV charger [99]. The charger comprises of a fully controlled three-phase AC-DC converter trailed by a bidirectional buck boost DC-DC converter. Both the conversion stages can work in positive as well as

negative side of *P*-*Q* power plane. In presented control strategy, five quantities are controlled namely, active-reactive power (*P*-*Q*), gird current (I_{abc}), battery current (I_{bat}) and DC link voltage (V_{DC}). Therefore, two separate controllers have been included each for both the stages. The control of AC-DC converter consists two loops i.e., outer (*P* and *Q*) control and inner one is for grid side current control. In outer loop, active and reactive power is regulated by utilizing two individual *PI* controllers. The outputs of outer power loop will generate reference of active (I_d^*) and reactive current component (I_q^*), respectively. These reference currents are in *dq* domain. Furthermore, these two current components are compared with the actual active and reactive current components of grid current and two *PI* controllers are employed to minimize the mismatch between them in inner current control loop. The decoupling terms i.e. ($-I_d \cdot \omega L + V_q$) and ($I_q \cdot \omega L + V_d$) are added in output of reactive and active current control loop, respectively. To produce the duty ratios in *dq* frame, both the quantities are normalized by DC link voltage. A *dq*-*abc* transformation is applied to develop the duty cycle for all three phases, and pulses of first stage AC-DC conversion are generated by well-known pulse width modulation (PWM) technique.

In the control design of DC-DC (second stage) converter, two quantities are regulated i.e., battery current (I_{bat}) and DC-link voltage (V_{DC}). This controller also has two loops, where in outer loop, the reference DC link voltage (V_{DC}^*) is compared with actual and error is minimized by *PI* controller. The outer loop generates the reference battery current (I_{bat}^*) and this reference is compared with actual battery current and controlled by *PI* controller in inner loop. Therefore, total five quantities, *P*, *Q*, I_{abc}, V_{DC} and I_{bat} are commanded to the control in this EV charger control [100].

AC-DC Converter Control

Here, the first task is to calculate active-reactive power at the AC side of EV charger in *dq* domain. For this, transformation from *abc* to *dq* domain is applied to grid side voltage and current. This is given as [101]:

$$\begin{bmatrix} V_d \\ V_q \end{bmatrix} = \begin{bmatrix} \sin(\omega t) & \sin(\omega t - 2\frac{\pi}{3}) & \sin(\omega t + 2\frac{\pi}{3}) \\ \cos(\omega t) & \cos(\omega t - 2\frac{\pi}{3}) & \cos(\omega t + 2\frac{\pi}{3}) \end{bmatrix} \times \begin{bmatrix} V_a \\ V_b \\ V_c \end{bmatrix} \tag{4.1}$$

$$\begin{bmatrix} I_d \\ I_q \end{bmatrix} = \begin{bmatrix} \sin(\omega t) & \sin(\omega t - 2\frac{\pi}{3}) & \sin(\omega t + 2\frac{\pi}{3}) \\ \cos(\omega t) & \cos(\omega t - 2\frac{\pi}{3}) & \cos(\omega t + 2\frac{\pi}{3}) \end{bmatrix} \times \begin{bmatrix} I_a \\ I_b \\ I_c \end{bmatrix} \tag{4.2}$$

The P and Q are calculated directly from dq component of grid current and voltage as follows:

$$P = \frac{3}{2}\left(V_d I_d + V_q I_q\right) \tag{4.3}$$

$$Q = \frac{3}{2}\left(V_q I_d - V_d I_q\right) \tag{4.4}$$

Now, these P and Q are compared with reference active (P^*)-reactive (Q^*) power and the errors are minimized by PI regulators. Theses PI regulators will generate the references of active (I_d^*)-reactive (I_q^*) current components in dq domain respectively as follows.

$$I_d^* = \left(K_{p1} + \frac{K_{i1}}{s}\right) \times (P^* - P) \tag{4.5}$$

$$I_q^* = \left(K_{p2} + \frac{K_{i2}}{s}\right) \times (Q^* - Q) \tag{4.6}$$

Here, K_{p1}, K_{p2}, K_{i1} and K_{i2} are proportional and integral constants for controllers tracking real and reactive powers respectively.

Further, similar PI loops are obtained for current control in inner loop. In this, two separate PI regulators are utilized to track I_d^* and I_q^*. The outputs of PI regulators are added with decoupling terms (±ωL) and after that it normalized by V_{dc}. Finally, duty ratio is obtained in dq frame as follows:

$$\begin{bmatrix} d_d \\ d_q \end{bmatrix} = \frac{1}{V_{dc}} \begin{bmatrix} e_d + V_d + 3\omega L_s \times I_q \\ e_q + V_q - 3\omega L_s \times I_d \end{bmatrix} \tag{4.7}$$

To generate the pulses for AC-DC conversion stage, the duty ratios are converted into abc frame and passed through the well-known PWM technique. The conversion from dq-abc gives [102],

$$\begin{bmatrix} D_a \\ D_b \\ D_c \end{bmatrix} = \sqrt{\frac{2}{3}} \begin{bmatrix} \sin \omega t & \cos \omega t \\ \sin\left(\omega t - \frac{2\pi}{3}\right) & \cos\left(\omega t - \frac{2\pi}{3}\right) \\ \sin\left(\omega t + \frac{2\pi}{3}\right) & \cos\left(\omega t + \frac{2\pi}{3}\right) \end{bmatrix} \begin{bmatrix} d_d \\ d_q \end{bmatrix} \tag{4.8}$$

DC-DC Converter Control

The quantities to be controlled in second stage of EV charger are battery pack current (I_{bat}) and DC-link voltage (V_{DC}). To design this control, two PI regulators are utilized. In outer loop, DC link voltage is equated with desired reference value and regulated by PI controller. This PI controller produces the reference of battery current

and regulated in inner control loop. Now, this inner loop controller produces the duty cycle and pulses are generated through PWM technique [103].

$$i_{bat}^{*} = \left(K_{p5} + \frac{K_{i5}}{s}\right) \times (V_{DC}^{*} - V_{DC}) \tag{4.9}$$

$$d_{DC-DC} = \left(K_{p6} + \frac{K_{i6}}{s}\right) \times (i_{bat}^{*} - i_{bat}) \tag{4.10}$$

The gains of PI based off-board EV charger controllers are listed in Table 4.1.

Table 4.1 – Controllers Gains of *PI* Based off-board EV Chargers

PARAMETER	SYMBOL	VALUE
Proportional constant of active power control loop	K_{p1}	0.85
Integral constant of active power control loop	K_{i1}	1.4
Proportional constant of reactive power control loop	K_{p2}	15
Integral constant of reactive power control loop	K_{i2}	12
Proportional constant of active current component control loop	K_{p3}	0.57
Integral constant of active current component control loop	K_{i3}	3.78
Proportional constant of reactive current component control loop	K_{p4}	5.45
Integral constant of reactive current component control loop	K_{i4}	0.84
Proportional constant of DC link voltage control loop	K_{p5}	3.74
Integral constant of DC link voltage control loop	K_{i5}	8.45
Proportional constant of battery current control loop	K_{p6}	4.65
Integral constant of battery current control loop	K_{i6}	2.95

4.3 Unified Adaptive Neuro-Fuzzy Inference System Based EV Charger Controller

This section deals with design of control algorithm based on adaptive neuro-fuzzy inference system (*ANFIS*) for a two-stage off-board bidirectional smart EV charger. The proposed EV charger is controlled to perform four quadrant operations as discussed above. Here, the 3-phase AC-DC converter and DC-DC converter are two main components, where the first one is controlled to regulate active/reactive power and current harmonics of nearby non-linear load. Where, the second one regulates the DC link voltage and battery current. An *ANFIS* has been designed to estimate the direct and quadrature axis reference currents directly while regulating two different quantities in single step only and hence, named as unified ANFIS controller.

Since, the main objective here is to achieve bidirectional active power flow while providing reactive power support and non-linear load compensation simultaneously, where the conventional controllers may fail due to sudden change in dynamics of highly non-linear system [104]. Therefore, to compensate the above stated problem a unified

adaptive neuro-fuzzy inference system (ANFIS) based controller is proposed. Due to the well-known capabilities of artificial neural network (ANN) in learning from process and managing uncertainties using fuzzy system [105], ANFIS has benefits in control and modeling of highly nonlinear systems [106]. Although, the ANFIS controllers for converter control have been proposed in past for several applications [107], but in majority of applications, separate ANFIS controllers have been used to regulate the different quantities [108]. Moreover, in majority of such controllers, two inputs were taken to regulate a single quantity: error and rate of change of error [109]. This kind of approach results in to more complexity in designing the controller and also enhances the computation burden in real time implementation [110]. Therefore, in proposed work, a novel unified ANFIS controller has been proposed which regulates the two different quantities in single step and does not require the calculation of decoupling terms. A hybrid method based on adaptive error backpropagation is employed to update the weights of the system for fast convergence of control under dynamic conditions.

Here, the main aim of proposed system is to develop a control law which enables the EV charger to have bidirectional active power flow while concurrently compensating the reactive power and current harmonics of non-linear load if any at point of common coupling (PCC). There are five main quantities to be regulated i.e., active power (P), reactive power (Q), charger AC side current (I_{Cabc}), DC link voltage (V_{DC}) and battery current (I_{bat}). The P/Q and I_{Cabc} are controlled by the AC-DC converter whereas V_{DC} and I_{bat} are controlled through DC-DC converter control.

4.3.1 System Description

Fig. 4.2 shows the schematic diagram of proposed system. The system consists of a two-stage off-board EV charger with linear/non-linear external load connected at PCC. In two-stage EV charger, first stage is AC-DC rectification stage and next is DC-DC transformation stage where both the converters comprise of bidirectional insulated gate bipolar transistors (IGBTs) [111].

The front-end AC-DC converter is controlled in such a way that the combination of charger and non-linear load appears as resistive load when seen from grid side. This not only enables the unity power factor operation, but also sorts out the issues related to power quality. Let us consider a linear/non-linear external load of charging station drawing complex power,

$$S_L = P_L + jQ_L \Rightarrow \underbrace{\bar{P}_L + \tilde{P}_L}_{P_L} + \underbrace{j\left(\bar{Q}_L + \tilde{Q}_L\right)}_{Q_L} \tag{4.11}$$

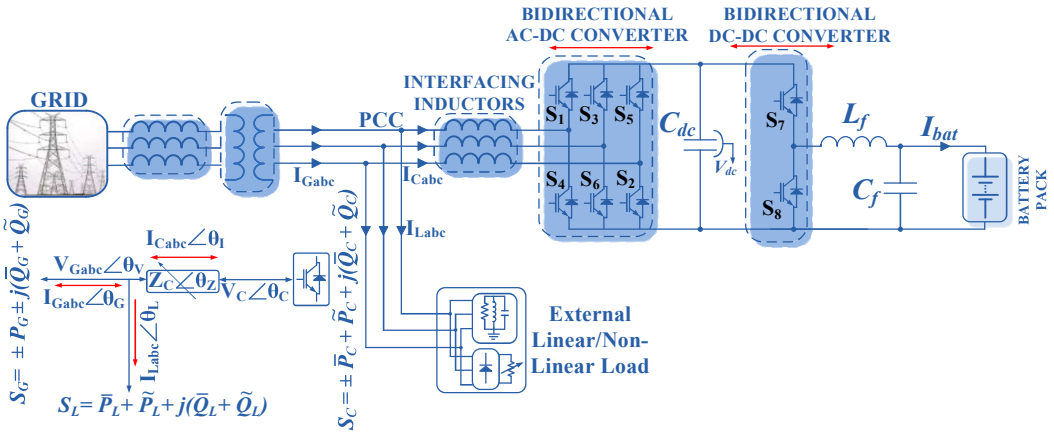

Figure 4.2: *OFF board EV charger architecture.*

Now if charger is able to compensate total reactive power i.e., $j\left(\bar{Q}_L + \tilde{Q}_L\right)$ and harmonic active power $\tilde{P}_L$ demand of local load, then the voltage and current of grid must be exactly in same phase (i.e., $V_{Gabc}\angle 0$, $I_{Gabc}\angle 0$). The total complex power of charger is,

$$S_C = V_{Gabc} \cdot I^*_{Cabc} \tag{4.12}$$

Here, I_{Cabc} is charger current

$$I^*_{Cabc} = \frac{V_C\angle\theta_C - V_{Gabc}}{Z_C\angle\theta_Z} \tag{4.13}$$

$$V_C = V_{Gabc} + I_{Cabc} \cdot Z_C\angle\theta_Z + \theta_I \tag{4.14}$$

Where, V_C is terminal voltage of charger with phase angle θ_I and Z_C is series impedance with phase angle θ_Z. On substituting equation (4.13) in (4.12).

$$\begin{aligned} S_C = V_{Gabc} \cdot \left(\frac{V_C\angle\theta_C - V_{Gabc}}{Z_C\angle\theta_Z}\right) \quad &= \frac{V_{Gabc} \cdot V_C\angle(\theta_C - \theta_Z)}{Z_C} - \frac{V^2_{Gabc}\angle\theta_Z}{Z_C} \\ = \left(\frac{V_{Gabc} \cdot V_C}{Z_C}\cos(\theta_Z - \theta_C) - \frac{V^2_{Gabc}}{Z_C}\cos(\theta_Z)\right) &\approx P_C \\ +j\left(\frac{V_{Gabc} \cdot V_C}{Z_C}\sin(\theta_Z - \theta_C) - \frac{V^2_{Gabc}}{Z_C}\sin(\theta_Z)\right) &\approx Q_C \end{aligned} \tag{4.15}$$

It is clear from equation (4.15) that desired charging current can be attained by controlling its phase angle, terminal voltage and impedance in such a way that the net sum of converter current and non-linear load current always appears to be resistive current when seen from grid side [25].

4.3.2 ANFIS Based Control System

The schematic of control design of proposed controller is shown in Fig. 4.3. The controller consist of two control laws for two different converters. The AC-DC converter controller regulates active (P_c)/reactive (Q_c) power of charger and charger AC side current, whereas DC-DC converter control works under constant charging mode and regulates V_{DC} and I_{bat} [112].

A. Control of AC-DC converter

To control the P_c/Q_c, first charger voltage (V_{Cabc}) and charger current (I_{Cabc}) are measured to calculate the front end converter active (P_c) and reactive power (Q_c) as discussed in previous case. Now, the calculated Q_c is compared with reference reactive power command (Q_c^*). The maximum reactive power that can be compensated must be within permisible limit and it is calculated as,

$$Q_{lim} = \pm\sqrt{S^2 - (\pm P_c)^2} \tag{4.16}$$

Where, S is the rating of charger and P_c is active power transfer by charger. Here, positive P_c indicates the battery charging from grid and negative sign is for battery discharging (reverse power flow from battery to grid). Moreover, if charger is not able to compensate the full reactive demand of load due to its rating limitations, then it is controlled to supply partial reactive power demand while rest is taken from grid.

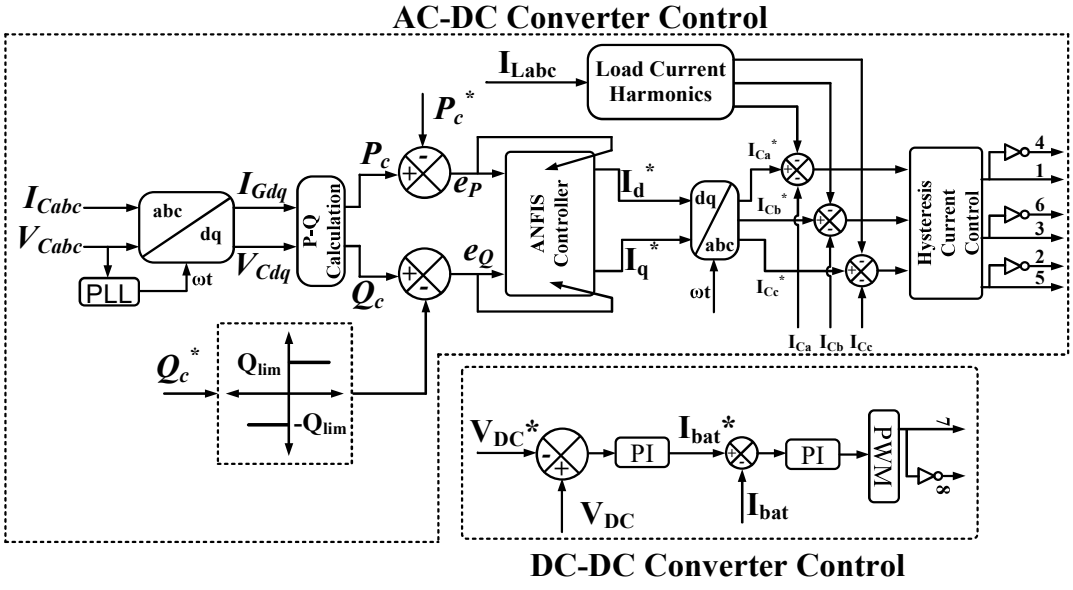

Figure 4.3: *ANFIS based EV charger controller.*

Here, the active power error (e_P) and Reactive power error (e_Q) are applied to Unified ANFIS controller, which are calculated in single step, yields the charger

reference current in its direct axis (I_d^*) and quadrature axis (I_q^*) form. The design of unified ANFIS is shown in Fig. 4.4. The 3-phase reference charger currents of each phase (I_{Ca}^*, I_{Cb}^* and I_{Cc}^*) are simply obtained through *dq-abc* transformatio. Since, the front end converter is also used to compensate the nearby non-linear current harmonics, accordingly the reference charging currents of each phase are slightly modified by adding the load harmonic currents into the respective phases of charger current. In inner loop, the tracking of the reference charger current in *abc* frame is done by hysteresis controller [113].

Design of ANFIS Controller

An unified ANFIS based on TSK having 2:6:3:3:2 architecture with two inputs (e_P and e_Q) and two outputs (I_d^* and I_q^*) [114]. Here, the consequent and precondition parameters are continuosly updated using gradient descent based error backpropogation algorithms as shown in Fig. 4.4 [115] [116]. The ANFIS controller mainly comprises 5 layers and the role of each layer is as follows:

Layer 1: This layer is represented by square and known as fuzzification layer. Here, three membership functions are assigned to each input. The triangular and trapezoidal type membership functions as shown in Fig. 4.5 have been opted to minimize the computational burden, and represented as:

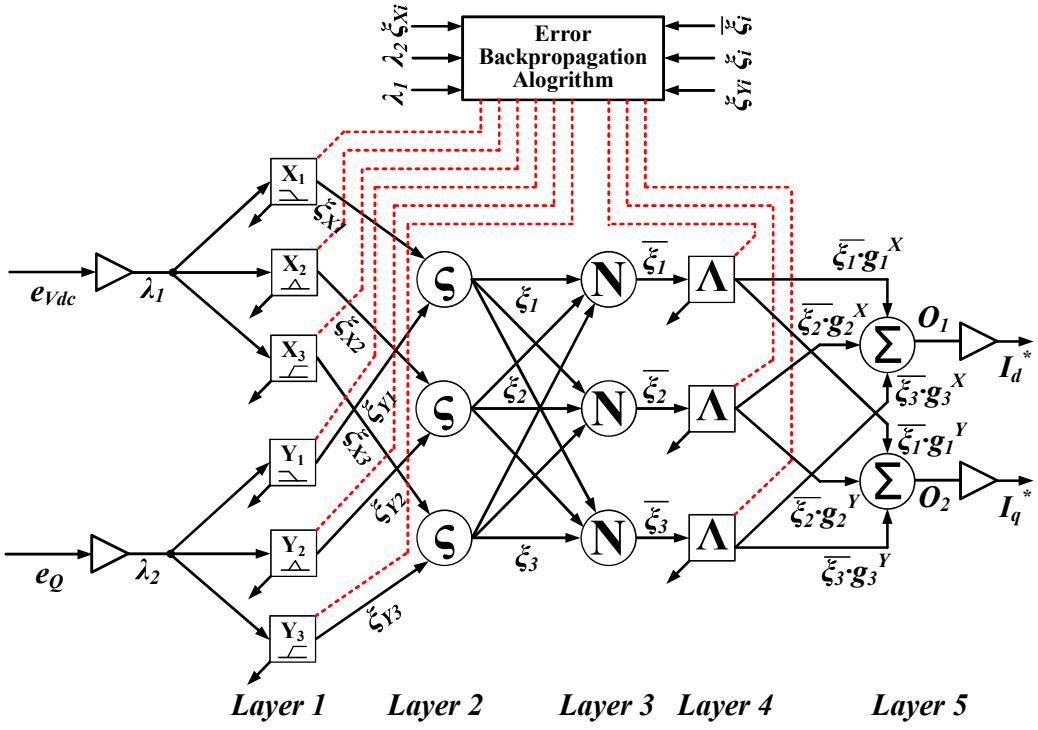

Figure 4.4: *Design of unified ANFIS.*

$$\xi_{X1}(\lambda_1) = \xi_{Y1}(\lambda_2) = \begin{cases} 1, & \lambda \le b_1 \\ \dfrac{\lambda - a_1}{b_1 - a_1}, & b_1 < \lambda < a_1 \\ 0, & \lambda \ge a_1 \end{cases} \tag{4.17}$$

$$\xi_{X2}(\lambda_1) = \xi_{Y2}(\lambda_2) = \begin{cases} 1 - \dfrac{\lambda - a_2}{0.5b_2}, & |\lambda - a_2| \le 0.5b_2 \\ 0, & |\lambda - a_2| \ge 0.5b_2 \end{cases} \tag{4.18}$$

$$\xi_{X3}(\lambda_1) = \xi_{Y3}(\lambda_2) = \begin{cases} 0, & \lambda \le a_3 \\ \dfrac{\lambda - a_3}{b_3 - a_3}, & a_3 < \lambda < b_3 \\ 1, & \lambda \ge b_3 \end{cases} \tag{4.19}$$

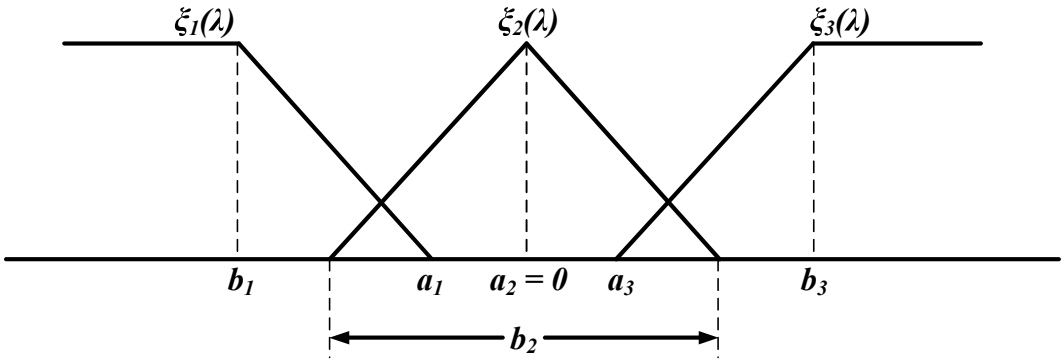

Figure 4.5: *Fuzzy membership functions.*

Where the parameters (a_i and b_i) are updated according to the value of error, and are popularly known as precondition parameters.

Layer 2: In this layer the nodes are represented by circle labeled as ς. Each node has two inputs, which multiplies them and transmits it to next layer.

$$\xi_k = \xi_{Xk}(\lambda_1) \cdot \xi_{Yk}(\lambda_2), \quad k = 1,2,3. \tag{4.20}$$

The output of layer (ξ_k) depicts the firing strength of a rule.

Layer 3: This layer normalized firing strength of each rule, where the nodes are represented by circle labeled as N.

$$\bar{\xi_k} = \frac{\xi_k}{\xi_1 + \xi_2 + \xi_3} \tag{4.21}$$

Layer 4: The nodes are represented by square labeled as Λ, whose output function is given as follows:

$$Z_k = \bar{\xi_k} \cdot g_k^j = \bar{\xi_k}\left(a_0^k + a_1^k \cdot \lambda_j\right), \quad j = 1,2. \tag{4.22}$$

Where the parameters (a_0^k and a_1^k) are also known as consequent parameters and updated regularly.

Layer 5: Represents the output layer, that calculates the O_1 and O_2 as follow:

$$O_1 = \bar{\xi_1} \cdot g_1^X + \bar{\xi_2} \cdot g_2^X + \bar{\xi_3} \cdot g_3^X \tag{4.23}$$

$$O_2 = \bar{\xi_1} \cdot g_1^Y + \bar{\xi_2} \cdot g_2^Y + \bar{\xi_3} \cdot g_3^Y \tag{4.24}$$

The actual active and reactive power current component i.e., I_d^* and I_q^* are obtained by multiplying the outputs of layer 5 with normalizing factor.

Online training of ANFIS controller: A gradient-descent technique is utilized for proposed ANFIS controller to minimize the error, where square of the error is taken as cost function. Here, the weights are updated by propagating the cost function from output *Layer 5* to input *Layer 1*. This phenomenon is known as backpropagation [30]. The training algorithm consists of two stages, i.e., consequent and precondition/premises parameter tuning.

$$e_P^2 = (P_C^* - P_C)^2 \tag{4.25}$$

Here, equation (4.25) represents the squared error of P_C, similarly squared error of Q_C can be found.

Precondition (Premises) Parameter Tuning: The fuzzy membership functions are updated by acquiring data from the precondition parameters as discussed in *Layer 1*. The variation in error function and precondition parameter are related as

$$\Delta a_{Xk} = -\eta \frac{\partial e_P^2}{\partial a_{Xk}} \tag{4.26}$$

Where, the proportionality constant (η) is defined as learning rate. The modified value of consequent parameters is defined as follows:

$$a_{Xk}(n+1) = a_{Xk}(n) + \Delta a_{Xk} \tag{4.27}$$

Or

$$a_{Xk}(n+1) = a_{Xk}(n) - \eta \frac{\partial e_P^2}{\partial a_{Xk}} \tag{4.28}$$

Similarly,

$$b_{Xk}(n+1) = b_{Xk}(n) - \eta \frac{\partial e_P^2}{\partial b_{Xk}} \tag{4.29}$$

Now, the chain rule is utilized to find out the partial derivative of equation (4.28) as follows:

$$\frac{\partial e_P^2}{\partial a_{X1}} = \frac{\partial e_P^2}{\partial V_{dc}} \cdot \frac{\partial P_C}{\partial i_d^*} \cdot \frac{\partial i_d^*}{\partial \bar{\xi}_1} \cdot \frac{\partial \bar{\xi}_1}{\partial \xi_1} \cdot \frac{\partial \xi_1}{\partial \xi_{X1}} \cdot \frac{\partial \xi_{X1}}{\partial a_{X1}} \tag{4.30}$$

where,

$$\frac{\partial e_P^2}{\partial V_{dc}} = -2(P_C^* - P_C) = -2e_P \tag{4.31a}$$

$$(P_C^* - P_C) = C \cdot i_d^* \Rightarrow \frac{\partial P_C}{\partial i_d^*} = -C \tag{4.31b}$$

$$i_d^* = \bar{\xi}_1 \cdot g_1^X + \bar{\xi}_2 \cdot g_2^X + \bar{\xi}_3 \cdot g_3^X \Rightarrow \frac{\partial i_d^*}{\partial \bar{\xi}_1} = g_1^X \tag{4.31c}$$

$$\bar{\xi}_1 = \frac{\xi_1}{\xi_1+\xi_2+\xi_3} \Rightarrow \frac{\partial \bar{\xi}_1}{\partial \xi_1} = \frac{(\bar{\xi}_2 + \bar{\xi}_3)}{\xi_1+\xi_2+\xi_3} \tag{4.31d}$$

$$\xi_1 = \xi_{X1} \cdot \xi_{Y1} \Rightarrow \frac{\partial \xi_1}{\partial \xi_{X1}} = \xi_{Y1} \tag{4.31e}$$

$$\xi_{X1} = \frac{\lambda_1 - a_{X1}}{b_{X1} - a_{X1}} \Rightarrow \frac{\partial \xi_{X1}}{\partial a_{X1}} = \frac{\xi_{X1} - 1}{b_{X1} - a_{X1}} \tag{4.31f}$$

After putting all the terms of equation (4.31) in (4.30), we find the updated value of a_{X1} as follows:

$$a_{X1}(n+1) = a_{X1}(n) - 2 \cdot \eta \cdot e_P(n) \cdot C \cdot g_1^X(n) \cdot \frac{\bar{\xi}_2(n) + \bar{\xi}_3(n)}{\xi_1(n) + \xi_2(n)+\xi_3(n)} \cdot \xi_{Y1} \cdot \frac{\xi_{X1}(n) - 1}{b_{X1}(n) - a_{X1}(n)} \tag{4.32}$$

Similarly,

$$b_{X1}(n+1) = b_{X1}(n) + 2 \cdot \eta \cdot e_P(n) \cdot C \cdot g_1^X(n) \cdot \frac{\bar{\xi}_2(n) + \bar{\xi}_3(n)}{\xi_1(n) + \xi_2(n)+\xi_3(n)} \cdot \xi_{Y1} \cdot \frac{\xi_{X1}(n)}{b_{X1}(n) - a_{X1}(n)} \tag{4.33}$$

Similarly, the other fuzzy membership functions are calculated as follows:

$$b_{X2}(n+1) = b_{X2}(n) - 2 \cdot \eta \cdot e_P(n) \cdot C \cdot g_2^X(n) \cdot \frac{\bar{\xi}_1(n) + \bar{\xi}_3(n)}{\xi_1(n) + \xi_2(n)+\xi_3(n)} \cdot \xi_{Y2} \cdot \frac{1 - \xi_{X2}(n)}{b_{X2}(n)} \tag{4.34}$$

$$a_{X3}(n+1) = a_{X3}(n) - 2 \cdot \eta \cdot e_P(n) \cdot C \cdot g_3^X(n) \cdot \frac{\overline{\xi_1}(n) + \overline{\xi_2}(n)}{\xi_1(n) + \xi_2(n) + \xi_3(n)} \cdot \xi_{Y3} \cdot \frac{\xi_{X3}(n) - 1}{b_{X3}(n) - a_{X3}(n)} \tag{4.35}$$

$$b_{X3}(n+1) = b_{X3}(n) + 2 \cdot \eta \cdot e_P(n) \cdot C \cdot g_3^X(n) \cdot \frac{\overline{\xi_1}(n) + \overline{\xi_2}(n)}{\xi_1(n) + \xi_2(n) + \xi_3(n)} \cdot \xi_{Y3} \cdot \frac{\xi_{X3}(n)}{b_{X3}(n) - a_{X3}(n)} \tag{4.36}$$

Consequent parameters: The following laws are utilized to update these parameters discussed in *Layer 4*.

$$a_{0_k}^{P_C}(n+1) = a_{0_k}^{P_C}(n) - \eta_c \cdot \frac{\partial e_P^2}{\partial a_{0_k}^{P_C}} \tag{4.37}$$

$$a_{1_k}^{P_C}(n+1) = a_{1_k}^{P_C}(n) - \eta_c \cdot \frac{\partial e_P^2}{\partial a_{1_k}^{P_C}} \tag{4.38}$$

Where, the learning rate of consequent parameters is η_c. The derivative of error in equation (4.37) and (4.38) is calculated by chain rule method as follows:

$$\frac{\partial e_P^2}{\partial a_{0_k}^{P_C}} = \frac{\partial e_P^2}{\partial P_C} \cdot \frac{\partial P_C}{\partial i_d^*} \cdot \frac{\partial i_d^*}{\partial g_k} \cdot \frac{\partial g_k}{\partial a_{0_k}^{P_C}} \tag{4.39}$$

$$\frac{\partial e_P^2}{\partial a_{1_k}^{P_C}} = \frac{\partial e_P^2}{\partial P_C} \cdot \frac{\partial P_C}{\partial i_d^*} \cdot \frac{\partial i_d^*}{\partial g_k} \cdot \frac{\partial g_k}{\partial a_{1_k}^{P_C}} \tag{4.40}$$

Here, the first two terms of equation (4.40) have already been obtained and remaining terms can be derived as

$$\frac{\partial i_d^*}{\partial g_k} = \frac{\xi_k}{\xi_{X_1} + \xi_{X_2} + \xi_{X_3}} \;;\; \frac{\partial g_k}{\partial a_{0_k}^{P_C}} = 1;\; \frac{\partial g_k}{\partial a_{1_k}^{P_C}} = \xi \tag{4.41}$$

On substituting derived terms in equation (4.39) and (4.40), the modified consequent parameters are as follows:

$$a_{0_k}^{P_C}(n+1) = a_{0_k}^{P_C}(n) + 2 \cdot \eta_c \cdot \xi \cdot \frac{\xi_k}{\xi_{X_1} + \xi_{X_2} + \xi_{X_3}} \tag{4.42}$$

$$a_{1_k}^{P_C}(n+1) = a_{1_k}^{P_C}(n) + 2 \cdot \eta_c \cdot \xi \cdot \frac{\xi_k}{\xi_{X_1} + \xi_{X_2} + \xi_{X_3}} \cdot \xi \tag{4.43}$$

The same approach is also applied to reactive power control loop. Thus, both the proposed ANFIS controller estimates I_d^* and I_q^* in single step without involving real system parameters.

B. Control of DC-DC converter

Table 4.2 – Controllers Gains of DC-DC Converter.

PARAMETER	SYMBOL	VALUE
Proportional constant of active power control loop	K_{p7}	12.5
Integral constant of active power control loop	K_{i7}	5.4
Proportional constant of reactive power control loop	K_{p8}	1.28
Integral constant of reactive power control loop	K_{i8}	2.47

The same controller is used in this case also as discussed in previous section and equations of second stage (DC-DC) conversion are as follows,

$$I_{bat}^* = K_{p7}(V_{DC}^* - V_{DC}) + \frac{K_{i7}}{S}(V_{DC}^* - V_{DC}) \tag{4.44}$$

$$d = K_{p8}(I_{bat}^* - I_{bat}) + \frac{K_{i8}}{S}(I_{bat}^* - I_{bat}) \tag{4.45}$$

Where, K_{p7}, K_{p7} are proportional and K_{i8}, K_{i8} are integral constant tuning values of *PI* controller for DC link voltage and battery current control loop, respectively and the values of gains are listed in Table 4.2.

4.4 Results and Discussion of *PI* Based Controller

This section presents the simulation and hardware results of *PI* based control architecture and simulation and hardware parameters are listed in Table A.1 and A.4 respectively. The MATLAB 2016a software is used to simulate the EV charger and *dSPACE-1104* for controller in real time.

4.4.1 Simulation Results

To claim the performance of controller, a simulation scenario with different *P* and *Q* commands has been developed as listed in Table A.5. In this, the initial two modes are related with charge-discharge of EV battery. In mode-1, battery is charging at the rate of 12 KW of power and discharge with same rate in mode-2. The next two modes are showing reactive power operation without charge/discharge of EV battery. In mode-3, the charger is compensating the inductive reactive power and capacitive reactive power in mode-4 without exchange of power with battery. The rest four modes are related with both active-reactive operations simultaneously. In mode-5, the charger is

charging the battery pack at the rate of 10 KW while compensating of 7.5 KVAR of inductive reactive power. Mode-6 is associated with the compensation of capacitive reactive power while charging of battery pack. In this, the charger is charging the battery at the rate of 7.5 KW while compensating capacitive reactive power of 10 KVAR. The last two modes are related with discharging operation of battery while compensating of reactive power. In mode-7, the charger is taking 5.5 KW of active power from battery while compensating 11.2 KVAR of inductive reactive power. In last mode, the charger is discharging the battery at the rate of 11.2 KW while compensating 5.5 KVAR of capacitive reactive power. In case of off-board EV charger, 600 V reference of DC-link voltage is selected and nominal voltage of EV battery pack is taken as 350 V.

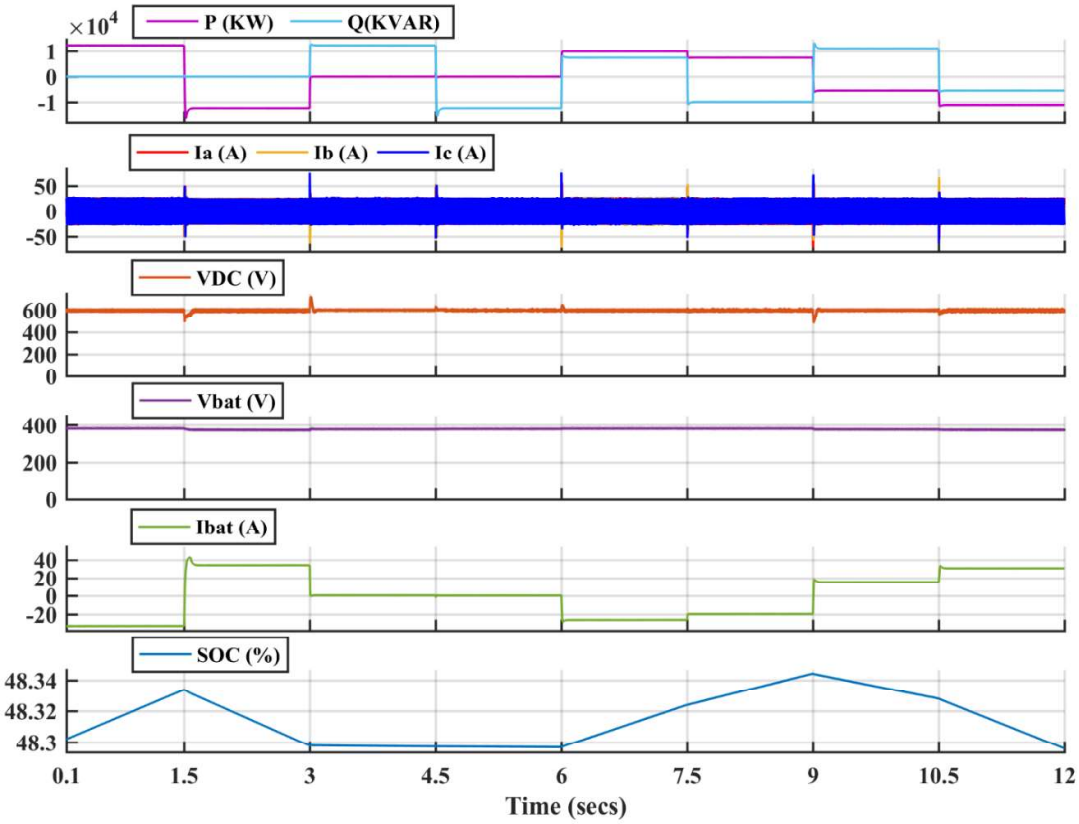

Figure 4.6: *Simulation results of P-Q, grid current (I_{abc}), DC-link voltage (V_{DC}), battery voltage (V_{bat}), battery current (I_{bat}), and SOC.*

The active (P)-reactive (Q) powers, grid side current (I_{abc}), DC-link voltage (V_{DC}), Battery voltage (V_{bat}), Battery current (I_{bat}), and SOC are shown in Fig 4.6 during all the modes. The run time of each operating mode is 1.5 seconds. The negative value of battery current shows charging and positive value shows discharging while battery voltage is positive for all cases. In can be observe that the battery current is zero in

mode-3 and 4 as there is no active power operation during these modes. For optimal utilization of EV charger, it operates at full load thereby, the grid side current is constant during all the modes i.e., 17.4 A (rms). The DC link voltage is maintained at 600 V during all working modes.

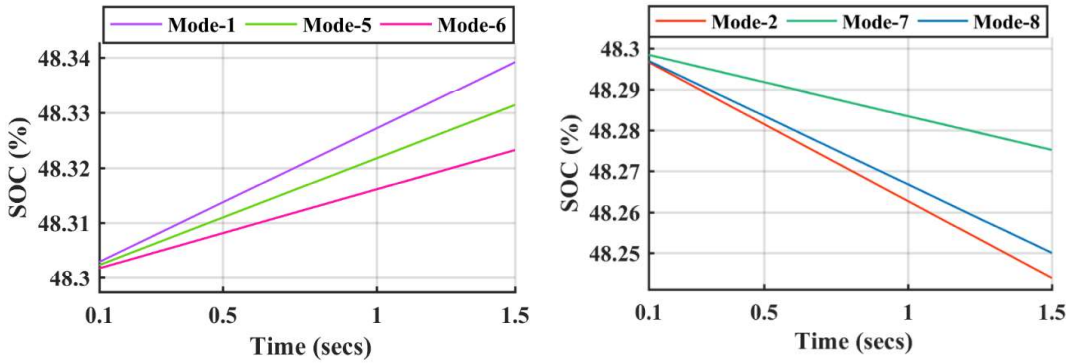

(a) (b)

Figure 4.7: *SOC (a) during charging modes and (b) during discharging modes.*

The variations of SOC with different charging/discharging rate are shown in Fig 4.7 (a) and (b) respectively. It can observe that the SOC rises faster in mode-1 and slower in mode-6 as the active power supply to EV battery pack is higher in mode-1. Similarly, SOC decreases faster in mode-2 and slower in mode-7 as amount of active power taken from the battery is higher in mode-2.

Fig. 4.8 shows the transition of active-reactive power and three-phase grid current with phase *a* voltage from one mode to another (for better clarification grid current is multiplied by factor of 5). During mode 1, current and voltage of phase *a* are in same phase. As charger shifts from mode 1 to mode 2, current I_a becomes completely out of phase with phase *a* voltage V_a as shown in Fig. 4.8 (a). As charger shifts from mode 2 to mode 3, current I_a changes from out of phase of voltage V_a to 90° lagging behind voltage as shown in Fig. 4.8 (b). In the course of changeover from mode 3 to 4, current I_a transpose from 90 degrees lagging behind voltage V_a to 90 degrees leading as shown in Fig. 4.8 (c). This indicates that charger shifts from inductive reactive to capacitive reactive operation. In mode 5, charger is in inductive charging state, and thus current I_a lags voltage V_a by 36° and the transition from mode 4 to 5 is shown in Fig. 4.8 (d). In transition from mode 5 to 6, current I_a changes from 36° lagging to 53° leading the voltage V_a. This indicates capacitive charging in mode 6 and transition from mode 5 to 6 is shown in Fig. 4.8 (e). In transition from mode 6 to 7, current I_a shifts to 243° lagging behind Voltage V_a by an angle greater than 90 degrees as shown in Fig. 4.8 (f). In

transition from mode 7 to 8, current changes to 243° lagging behind voltage to 206° leading as depicted in Fig. 4.8 (g).

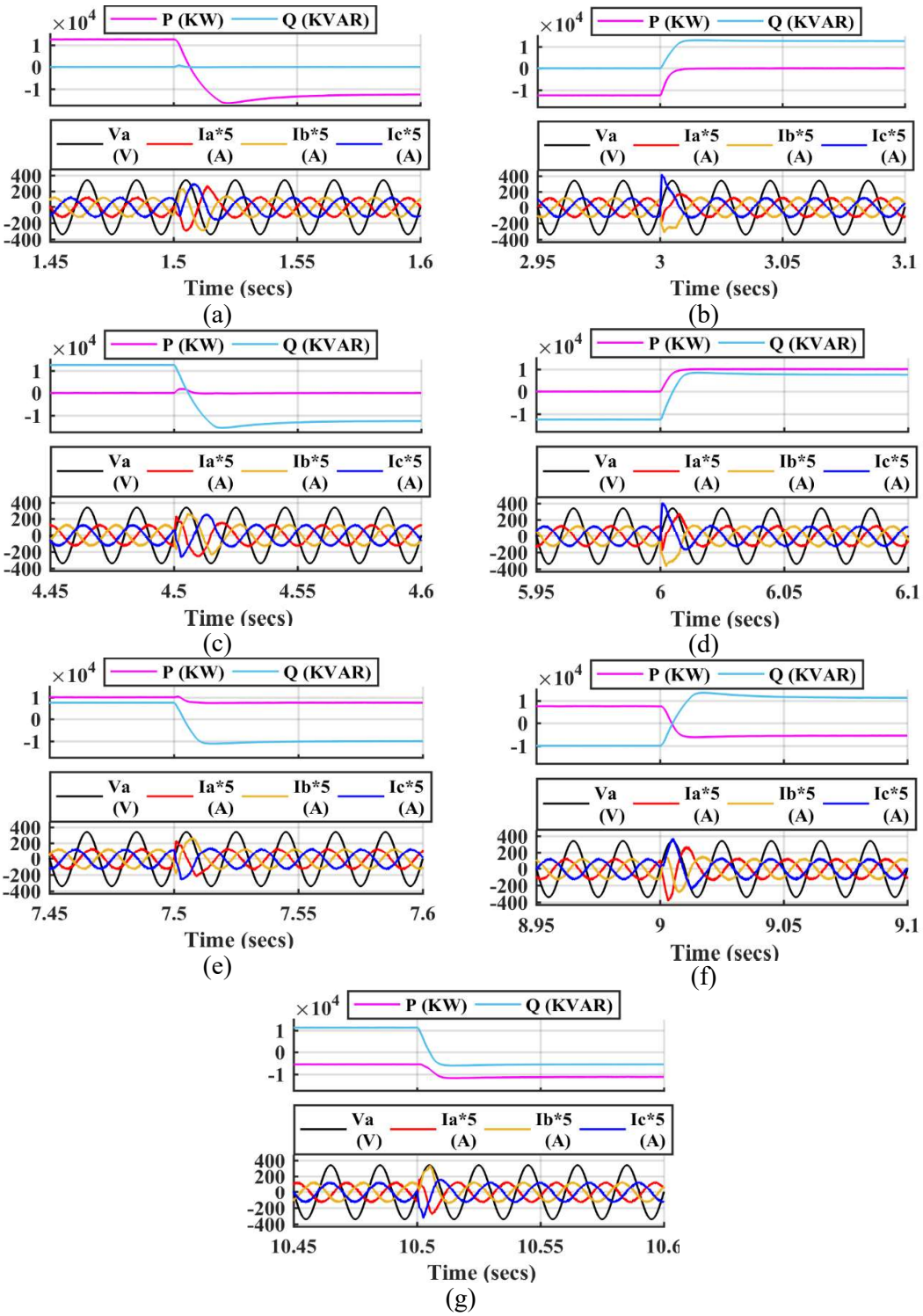

Figure 4.8: *Transition of active-reactive power and grid current from (a) Mode-1 to 2, (b) Mode-2 to 3, (c) Mode-3 to 4, (d) Mode-4 to 5, (e) Mode-5 to 6, (f) Mode-6 to 7, and (g) Mode-7 to 8.*

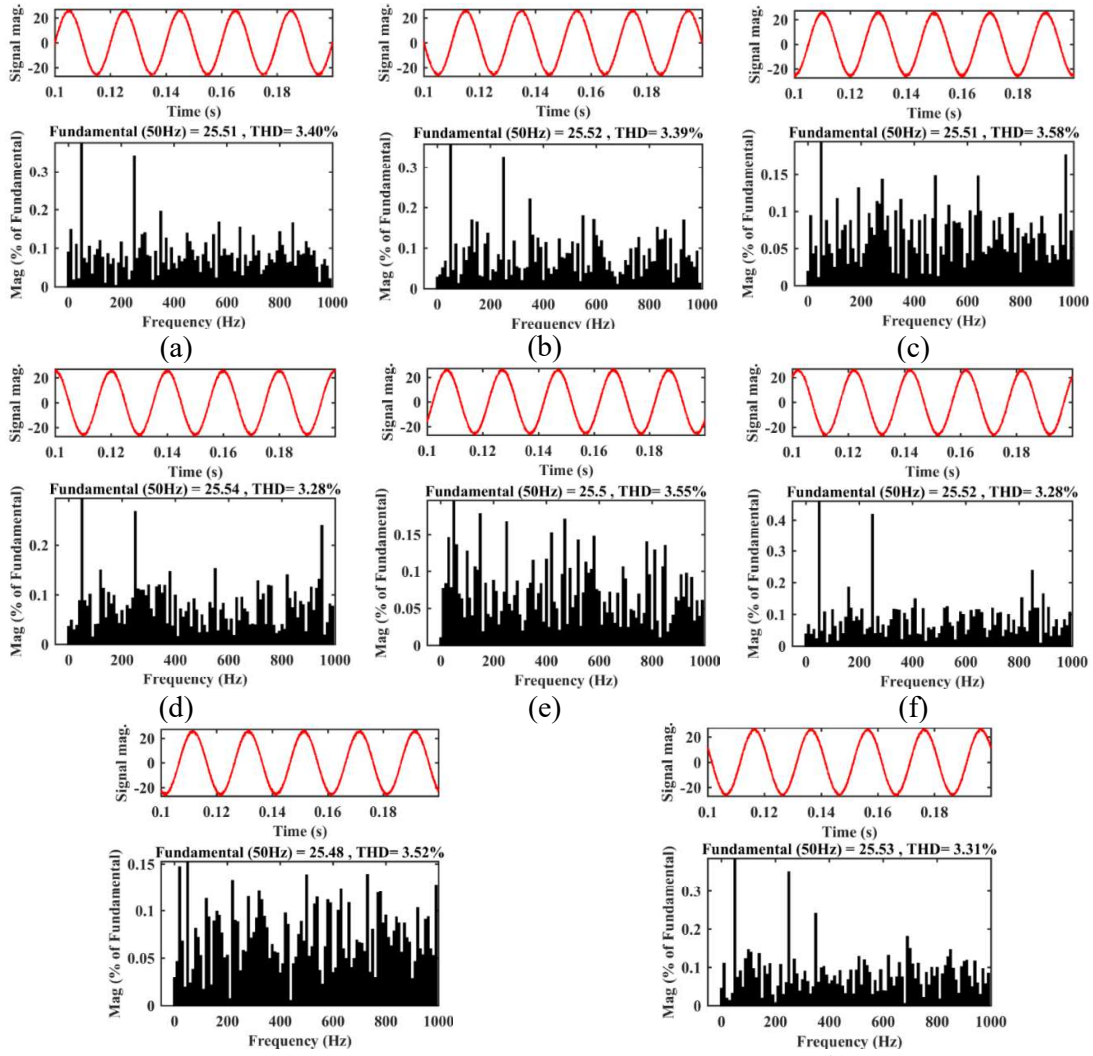

Figure 4.9: *THD in grid current (a) Mode-1, (b) Mode-2, (c) Mode-3, (d) Mode-4, (e) Mode-5, (f) Mode-6, (g) Mode-7 and (h) Mode-8.*

Fig. 4.9 shows the harmonic spectrum of phase *a* of grid current during all working modes. The results are also listed in Table 4.3 and it is found that the value of total harmonic distortion (THD) during all working modes are within the permissible limit of 5% specified by IEEE-519 standard.

Table 4.3 – THD during different working modes.

Mode	THD (%)	Mode	THD (%)
1	3.40	5	3.55
2	3.39	6	3.28
3	3.58	7	3.52
4	3.28	8	3.31

4.4.2 Experimental Results

To validate the controller performance in real time, a hardware prototype has been developed in laboratory as shown in Fig. 2.11. An eight modes hardware scenario similar as simulation has been developed as listed in Table A.7. The hardware prototype is rated as 500 VA and parameters are given in Table A.3. A 96 V battery pack is built up by connecting eight 12 V, 7 Ah batteries in series. During mode-1 and 2, charger is charger/discharge the battery pack at the rate of 500 W respectively. The next two modes i.e., 3 and 4 associated with reactive power operation and 500 VA of inductive and capacitive reactive power is compensated in mode-3 and 4 respectively. The mode-5 and 6 related to charging and reactive power compensation. In mode-5, the charger charges the battery pack at the rate of 400 W and simultaneously compensates 300 VAR of inductive reactive power. Similarly, it charges the battery pack at the rate of 300 W while compensating 400 VAR of capacitive inductive power in mode-6. The last two modes are associated with discharging operation while compensating of reactive power. In mode-7, the charger takes 200 W of power from battery while compensating of 458.3 VAR of inductive reactive power. In last mode, charger discharges the battery pack at the rate of 458.3 W while compensating of 200 VAR of capacitive reactive power.

Fig. 4.10 shows the hardware prototype results of above discussed controller with variations as listed in Table A.7. The experimental results are captured by eight channel Tektronix mixed signal oscilloscope (series 5) and total eight signals are shown in results: - three-phase voltages (V_a, V_b and V_c), three-phase current (I_a, I_b and I_c), DC-link voltage (V_{DC}) and battery current (I_{bat}). The grid line-to-line voltage is 70 V (rms) therefore, peak of grid phase voltage is around 57 V. For economical operation and optimal utilization, complete charger rating (i.e., 500 VA) is utilized during all operating modes. Therefore, the EV charger AC side current is constant i.e., 4.1 A (rms) during all operating modes. Mode-1 and 2 shows the charging-discharging operation of battery respectively at same rate i.e., ± 500 W and the changeover between mode 1 and 2 is shown in Fig. 4.10 (a). The phase angle is zero and 180° in mode-1 and 2 respectively. Since, the battery pack voltage is around 100 V, the battery charging current in mode 1 is 500/100 = 5 A and discharging current is also same in mode 2 because discharging power command is same as charging active power command. In mode 3, the charger works under inductive reactive power compensation only and the grid current changes from out of phase to 90° lagging as shown in Fig. 4.10 (b). Due to the reactive power operation, the phase angle changes from exactly 90° lagging to leading in transition of

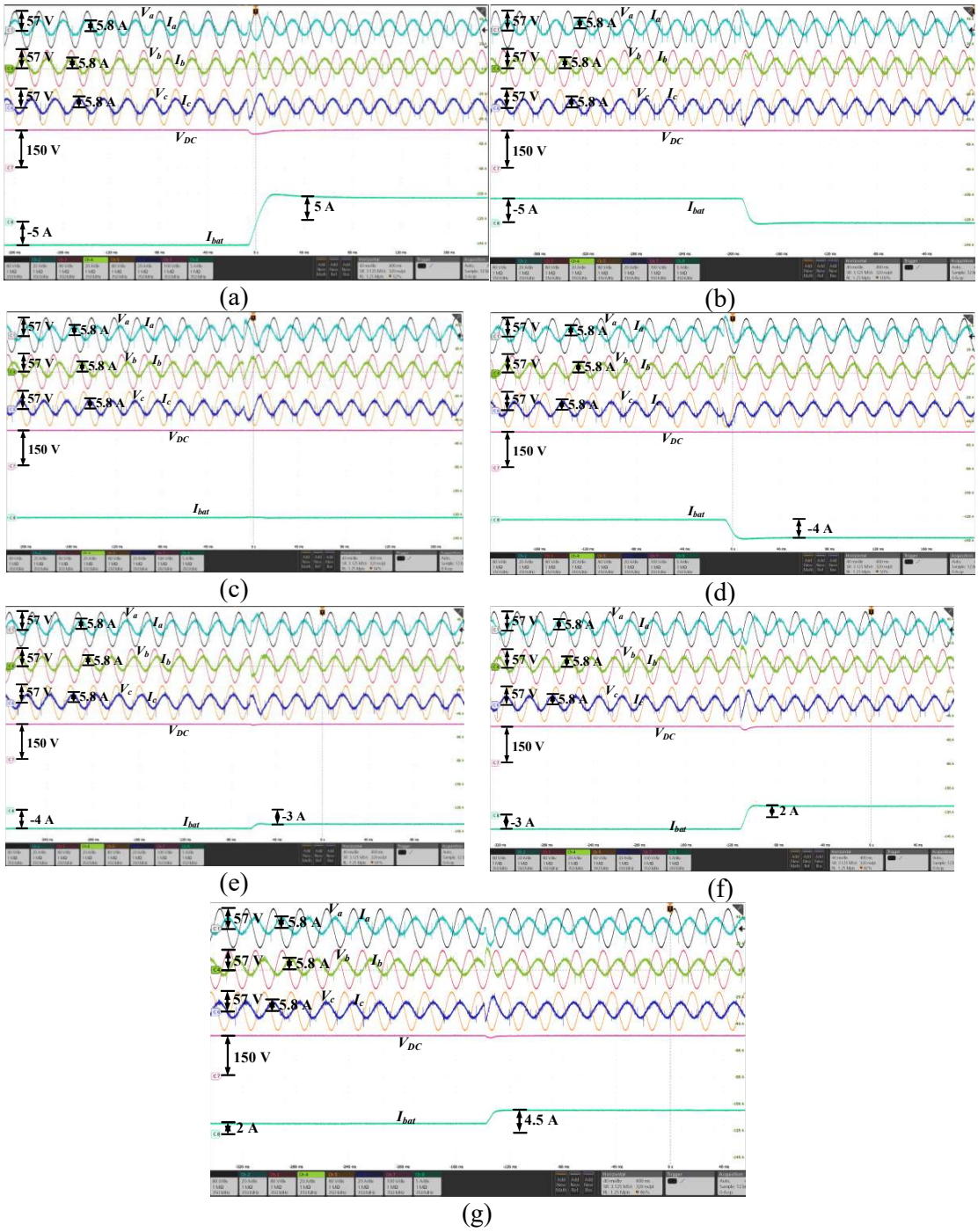

Figure 4.10: *Transition of Three-phase voltage-current, DC-link voltage and battery current from (a) Mode 1-2, (b) Mode 2-3, (c) Mode 3-4, (d) Mode 4-5, (e) Mode 5-6, (f) Mode 6-7 and (g) Mode 7-8.*

mode-3 to 4 as depicted in Fig. 4.10 (c). Therefore, the battery current is zero during this transition. The transition from mode-4 to 5 is shown in Fig. 4.10 (d). In mode 5, battery is charging at lower rate i.e., 400 W and rest of charger's rating (i.e., 300 VAR) is utilizing in compensation of inductive reactive power. Mostly, the EV charger works

under mode 5 and 6 in which charger is supply reactive power and simultaneously charge the battery pack. The power factor in these modes depends on amount of active-reactive power supplied by charger. Here, the *P* is 400 W, *Q* is 300 VAR in mode-5 and 300 W, -400 VAR in mode-6 and the changeover is shown in Fig. 4.10 (e). Therefore, the phase angle between voltage and current is 36° lagging and 53° leading in mode-5 and 6 respectively. Similarly, the transition between charging to discharging while compensating reactive power is shown in Fig. 4.10 (f). This shows the transition between mode-6 to 7 in which battery current changes from -3 A to 2 A. The battery is discharging at the rate of 200 W in mode-7 while compensating 458.3 VAR inductive reactive power this results the phase difference of 113° lagging. In mode-8, the active-reactive operation is swapped and battery is discharging at the rate of 458.3 W while compensating 200 VAR of capacitive reactive power. The changeover between the mode-7 and 8 is depicted in Fig. 4.10 (g) and phase difference is 156° leading. During all the transitions, the DC-link voltage is maintained at 150 V however, a slight variation occurs at the time of transition but it settled at 150 V quickly.

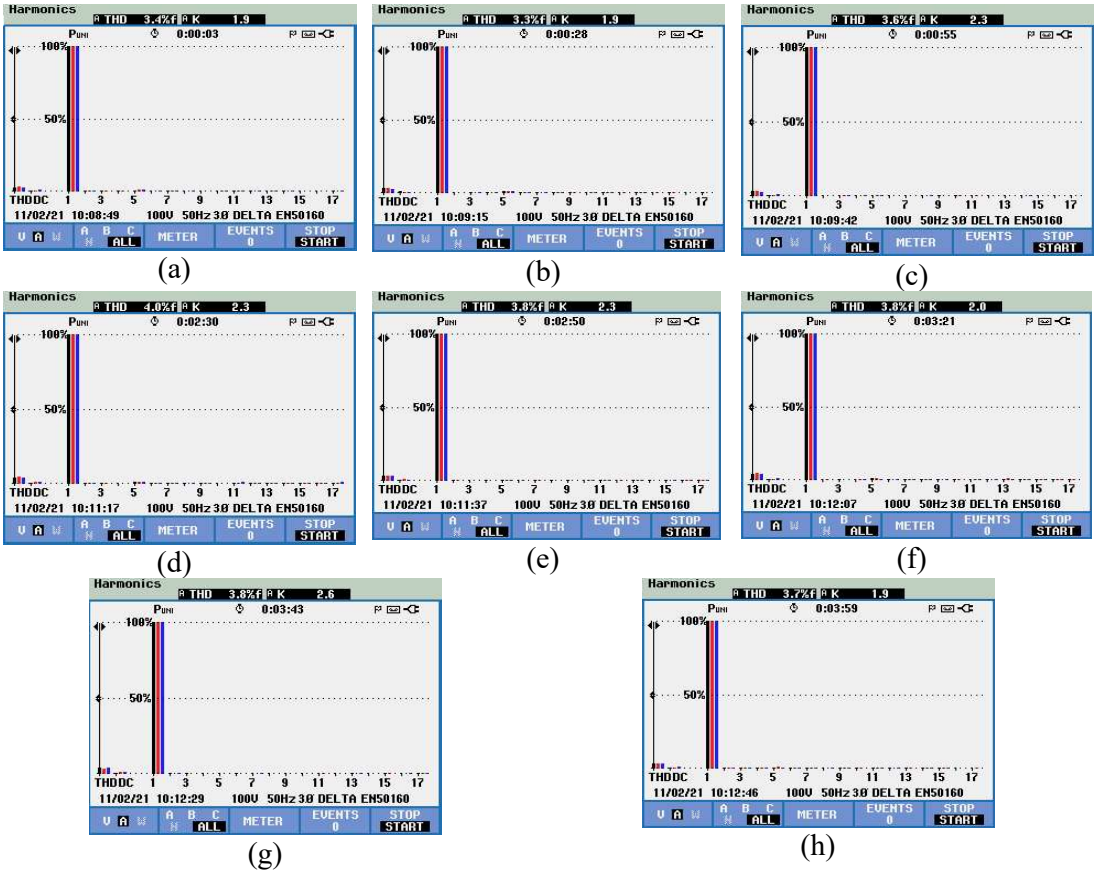

Figure 4.11: *THD in Three-phase grid current (a) Mode 1, (b) Mode 2, (c) Mode 3, (d) Mode 4, (e) Mode 5, (f) Mode 6, (g) Mode 7 and (h) Mode 8.*

Fig. 4.11 shows the harmonic spectrum of three-phase grid current during all working modes. The results are also listed in Table 4.4 and it is found that the value of THD during all working modes are within the permissible limit of 5% specified by IEEE-519 standard in real time also.

Table 4.4 – THD during different working modes.

Mode	THD (%)	Mode	THD (%)
1	3.4	5	3.8
2	3.3	6	3.8
3	3.6	7	3.8
4	4	8	3.7

4.5 Results and Discussion of ANFIS Based Controller

4.5.1 Simulation Results

A 12.5 KVA EV charger with external local load of fixed active power of 2 KW and variable reactive power is simulated in MATLAB. As battery pack voltage of EV application is usually (~ 180 – 380 V), therefore A Li-ion battery pack having nominal voltage of 350 V is utilized for proposed system. The SOC is selected as 50%, which varies with charging/discharging of battery and accordingly the battery voltage may also vary. Generally, the range of DC link voltage falls between (~ 400 – 750 V), and therefore, reference of V_{DC} is taken as 600 V.

TABLE 4.5 - Simulation Scenario of ANFIS Based Controller.

Mode	P_C (KW)	Q_C (KVAR)	S_C (KVA)	P_L (KW)	Q_L (KVAR)	S_L (KVA)	P_G (KW)	Q_G (KVAR)	S_G (KVA)	Time (sec)
1	12.5	0	12.5	2	0	2	14.5	0	14.5	0-1.5
2	-12.5	0	12.5	2	0	2	-10.5	0	10.5	1.5-3
3	0	-12.5	12.5	2	5.5	5.852	2	-7	7.28	3-4.5
4	10	-7.5	12.5	2	4	4.472	12	-3.5	12.5	4.5-6
5	-10	-7.5	12.5	2	4	4.472	-8	-3.5	8.732	6-7.5
6	10	-7.5	12.5	2	10	10.198	12	2.5	12.257	7.5-9
7	-10	-7.5	12.5	2	12	12.165	-8	4.5	9.178	9-10.5

In order to analyze the controller's performance, a simulation scenario of seven modes has been considered, where each mode is simulated for 1.5 seconds as listed in Table 4.5. The first two modes are associated with active power operation only. During mode-1, EV charger is charging the battery pack at the rate of 12.5 KW and load is also demanding active power of 2 KW, thereby total active demand of 14.5 KW is supplied by grid. In mode-2, the EV charger is taking 12.5 KW of power from the battery pack and transfer it to the AC side. During this, first it fulfils the 2 KW active demand of local load and transmit the surplus power of 10 KW back to grid. During mode-3, the EV

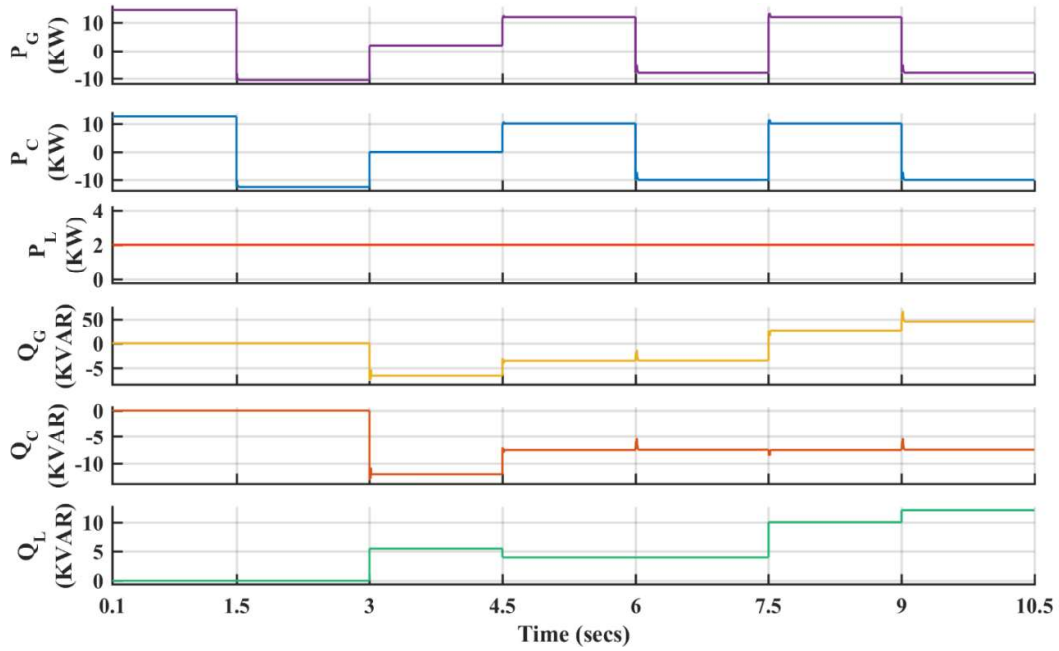

Figure 4.12: *Measured active power of grid (P_G), charger (P_C), load (P_L), reactive power of grid (Q_G), charger (Q_C) and load (Q_L).*

charger is compensating the reactive power of 12.5 KVAR without charging the battery pack. Now, load is demanding reactive power of 5.5 KVAR along with 2 KW of active power. In that case, the grid fulfils 2 KW active demand of load and charger compensates 5.5 KVAR of reactive demand. The surplus reactive power of 7 KVAR is transferred to grid. The rest four modes are associated with both active and reactive operation simultaneously by the EV charger. In mode-4, the EV charger is charging battery pack at the rate of 10 KW while compensating 7.5 KVAR of reactive power. The load is demanding 2 KW and 4 KVAR of active and reactive power respectively. Therefore, the reactive demand of load is compensated by EV charger and rest of 3.5 KVAR is transferred to grid and total active demand of 12 KW is supplied by grid. In mode-5, the load active/reactive demand is same as mode-4, however EV charger is taking 10 kW of power from battery pack in this mode. Thereby, first EV charger fulfils the 2 KW/4 KVAR active/reactive demand of external load and transferred the surplus 8 KW/3.5 KVAR of active/reactive power to grid. In mode-6, the EV charger operation is same as mode-4, however the reactive demand of external load is increase to 10 KVAR. The EV charger cannot compensate the complete reactive demand of load but it compensates 7.5 KVAR and rest 2.5 KVAR reactive demand of external load is supplied by grid. The last mode is associated with discharging of battery and EV charger operation is same as mode-5, however the reactive demand of external load is increased

to 12 KVAR. This results the increment in reactive power supply from the grid to 4.5 KVAR.

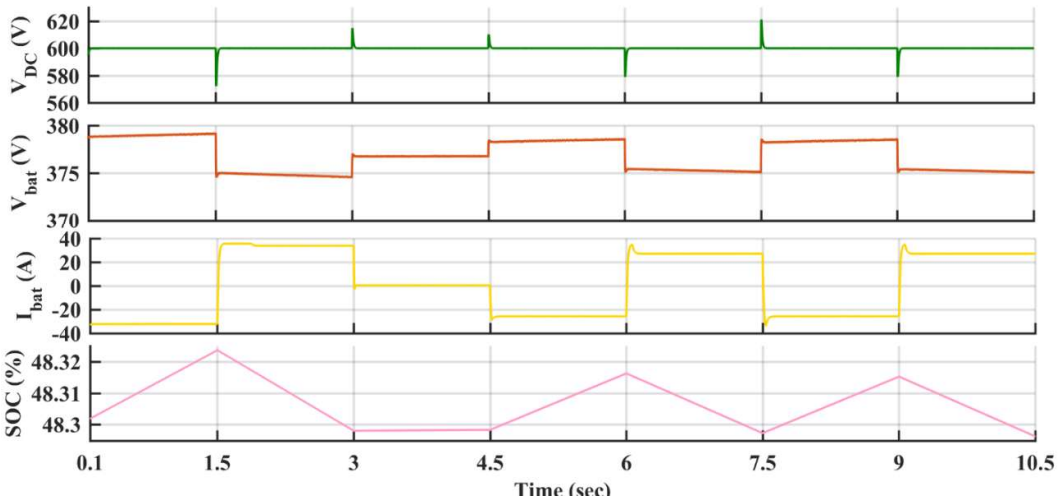

Figure 4.13: *Measured DC-link voltage (V_{DC}), battery voltage (V_{bat}), battery current (I_{bat}), and state of charge (SOC).*

Fig. 4.12 shows active-reactive power of grid, charger and load. From the active power of EV charger (P_C), it can be seen that the mode 1, 4 and 6 are associated with battery charging (G2V) and mode 2, 5 and 7 are associated with battery discharging (V2G) operation. Mode 3 is associated with reactive power compensation where the exchange of active power is limited to zero. For optimal utilization and economical operation, complete charger rating has been utilized. It is capable of transferring the surplus active as well as reactive power when demanded by grid within its capacity. The load active power demand is constant at 2 KW as shown in P_L, whereas the reactive power demand of load varies. The active and reactive power of grid side depends on EV charger operation and external load demand and it varies accordingly as shown in P_G and Q_G.

In Fig. 4.13, it can be seen that V_{DC} is maintained at 600 V during all the operating modes. The nominal variation of approximate 3 to 4 V is seen in battery voltage while changing the operating mode from charging to discharging. During mode 3, no active power is transferred as evident from zero value of the battery current and constant SOC level. Furthermore, SOC varies with respect to the charging/discharging rate (exchange of active power).

Fig. 4.14 shows the measured charger (I_{Cabc}), load (I_{Labc}) and grid (I_{Gabc}) current. The charger is operating at 12.5 KVA during all the modes. Therefore, no change in charger current is seen. The apparent power of load increases as reactive power increases

due to that load current increases. The apparent power of grid varies as both active-reactive power of grid side varies due to that grid current also varies.

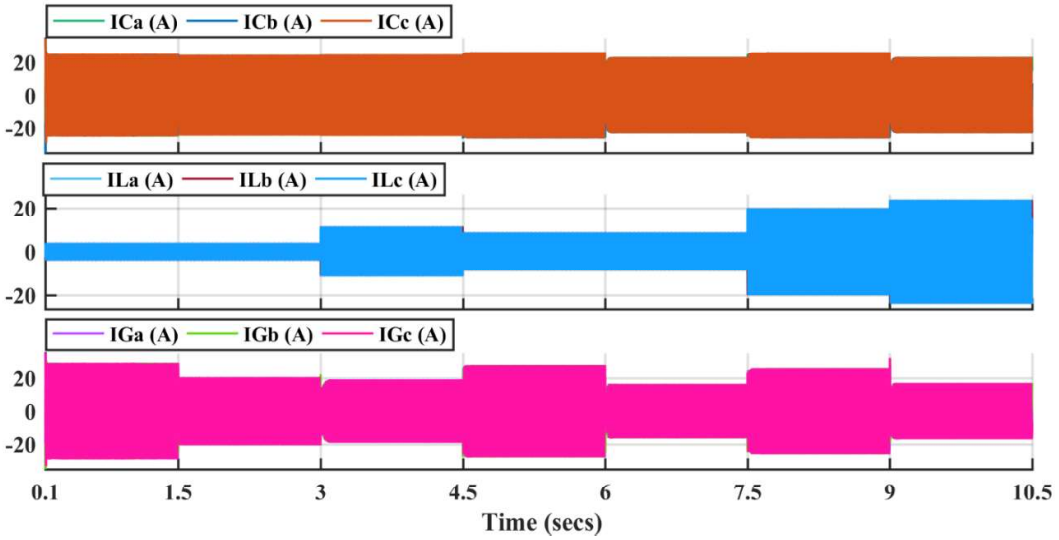

Figure 4.14: *Measured three-phase charger current (I_{Cabc}), load current (I_{Labc}), and grid current (I_{Gabc}).*

Fig. 4.15 shows the transition from one mode to another. Fig. 4.15 (a) shows the zoomed version of transition from mode-1 (charging) to 2 (discharging). It is observed that the current of phase *a* is exactly in phase with voltage of phase *a* during mode-1 and exactly out of phase in mode-2. The reactive power remains zero in mode-2 while the active power varies from +12.5 KW to -12.5 KW. In Fig. 4.15 (b), the transition from mode-2 to 3 is shown, in this the current changes from out of phase to 90° leading because charger supply reactive power without charging the battery pack. Fig. 4.15 (c) shows the transition from mode 3 to 4, the charger current starts leading behind voltage by 36° because charger is compensating reactive power while charging of battery. Similarly, the charger compensating reactive power while discharging of battery as shown in Fig. 4.15 (d). The transition from discharging to charging while supplying reactive power is shown in Fig. 4.15 (e) and phase difference is 143°. The transition from mode-6 to 7 is same as the transition from mode-4 to 5 because active/reactive power commands of EV charger are same. It is observed that during all the modes controller performs efficiently to track the reference P_C-Q_C and EV charger AC side current commands. Correspondingly, the transient and steady-state responses during all transitions are analyzed and found that it takes less than two grid cycles to track the reference active/reactive power command.

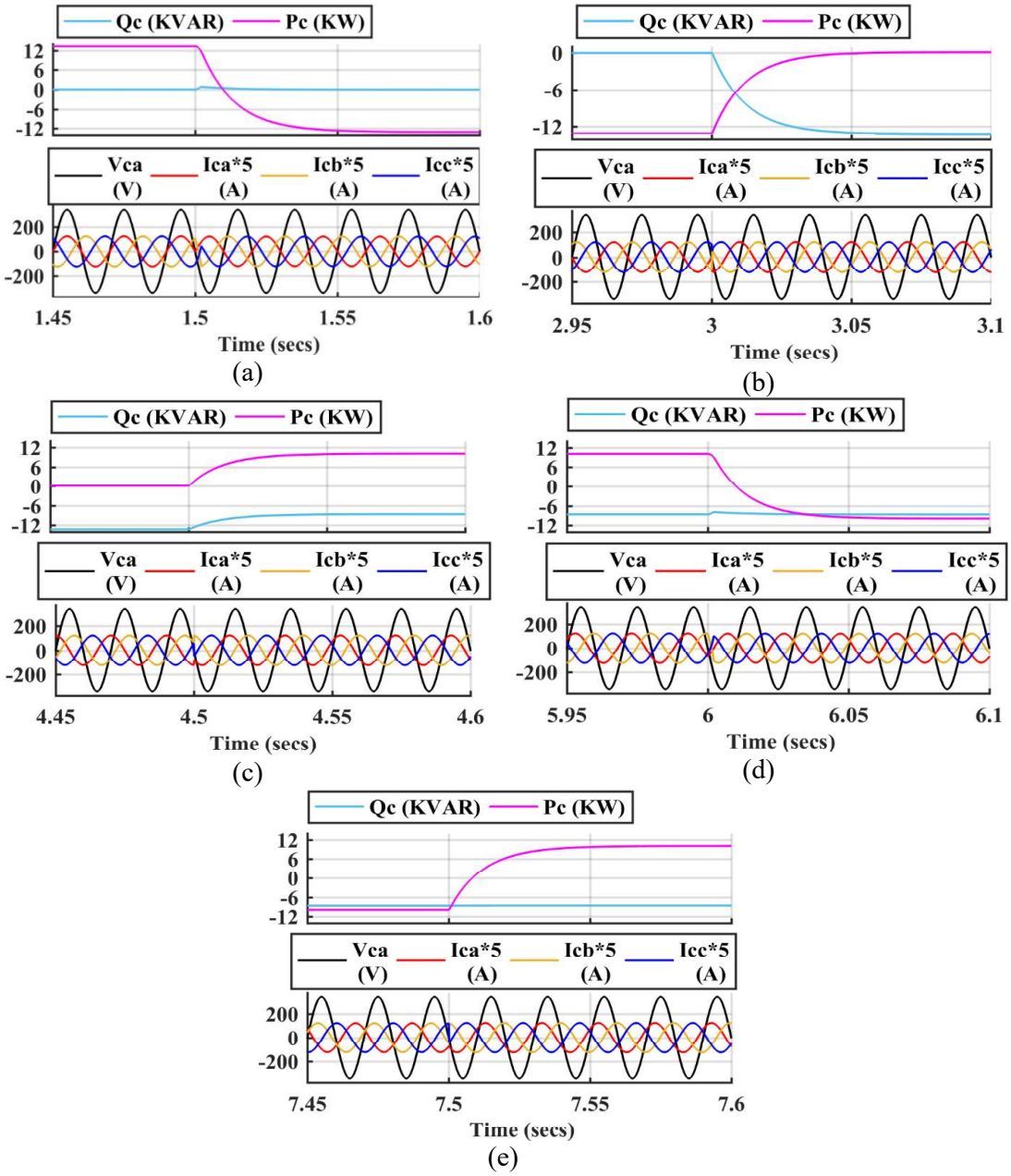

Figure 4.15: *Zoomed version transition of charger active-reactive power and charger current with phase a voltage from (a) mode 1-2, (b) mode 2-3, (c) mode 3-4, (d) mode 4-5 and (e) mode 5-6.*

Fig. 4.16 and 4.17 show the simulation results of reactive power compensation of non-linear load. During this, the EV charger turns on at 0.2 sec before that grid is acting as a source and supplying all the P_L and Q_L demand of load. At 0.2 sec, EV charger turns ON and starts compensating harmonic current demand of non-linear load without reactive power operation. At 0.5 sec, the load P_L and Q_L demand is increased to 2 KW and 1 KVAR respectively. Accordingly, the reactive power supply from EV charger is also increased and now EV charger is compensative the reactive demand of both linear

and non-linear load. In the last, at 0.8 sec the EV charger starts charging battery pack at the rate of 3 KW while compensating the total reactive demand of external linear/non-linear load. In this operation, no reactive power is taken from grid after turning ON the charger. Therefore, unity power factor operation is achieved even in the presence of non-linear load. In Fig. 4.17, it can be observed that the grid side current is always maintained sinusoidal and in phase with grid voltage despite of having highly non-linear load current at PCC.

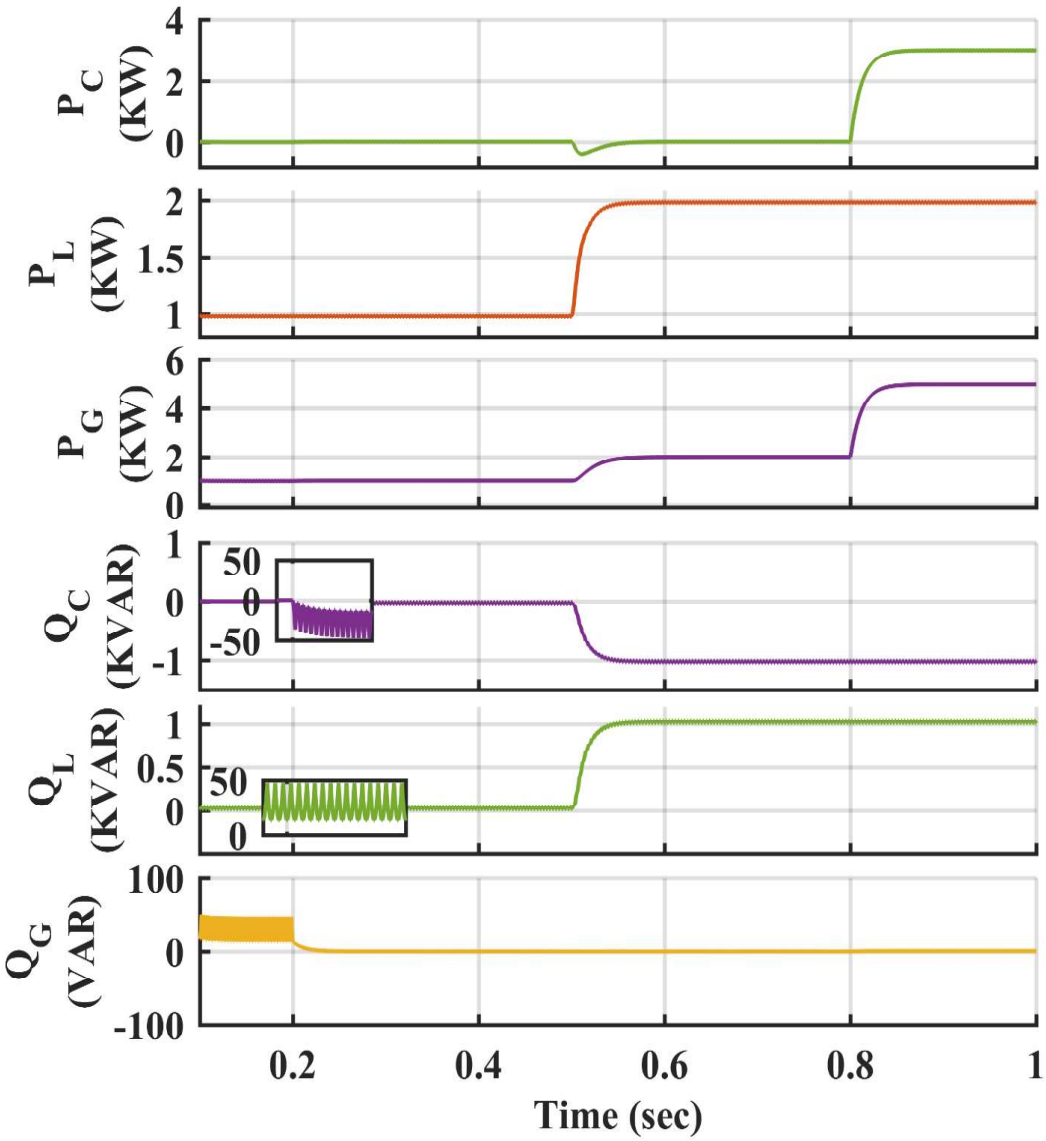

Figure 4.16: *Active-reactive power of charger, load and grid.*

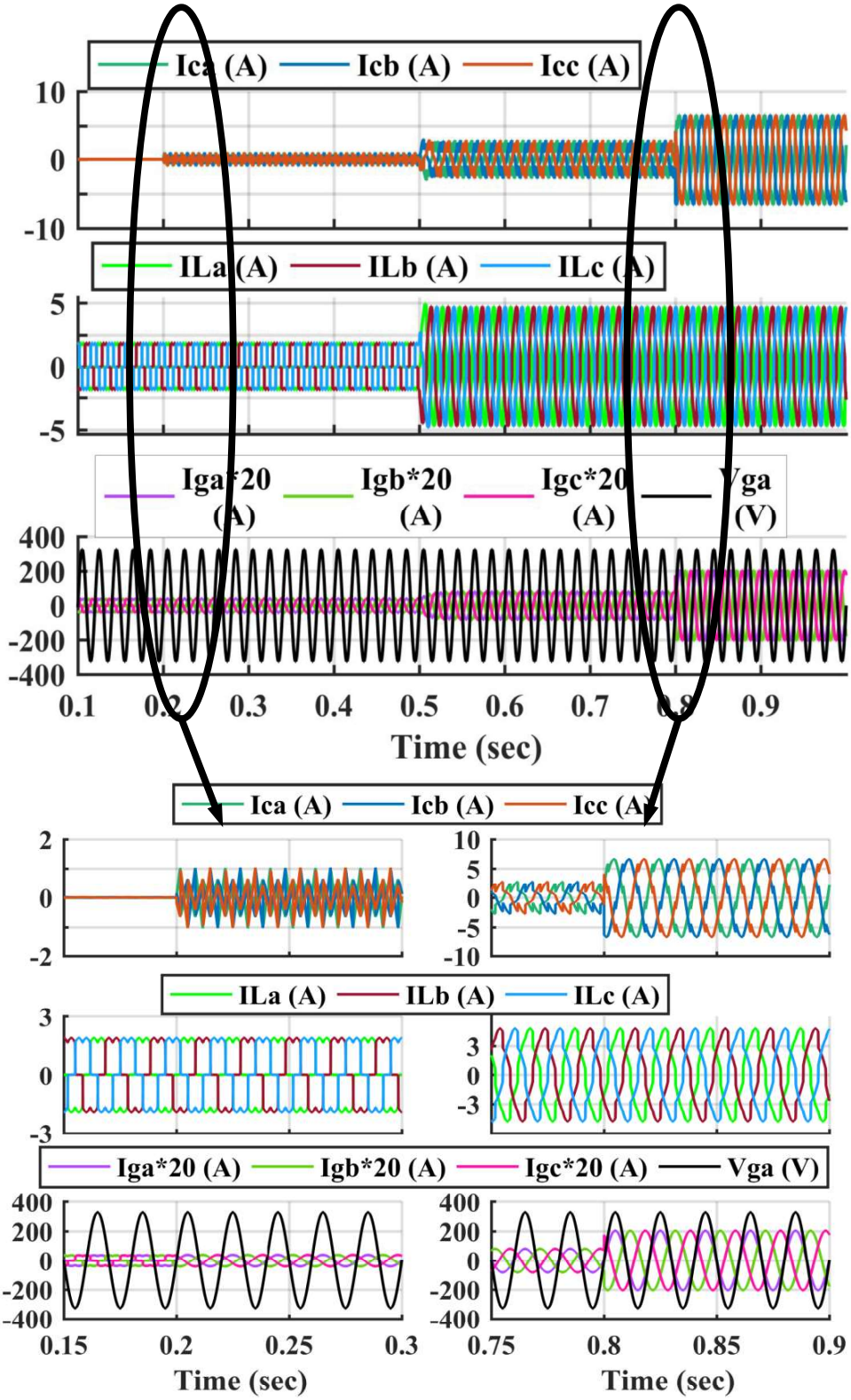

Figure 4.17: *Zoomed version of transition of charger, load and grid current.*

4.5.2 Experimental Results of ANFIS Based Controller

The experimental scenario is accounted in Table 4.6 as given below and results are shown in Fig. 4.18 & 4.19. The experimental scenario is similar as simulation with seven working modes. The EV charger is rated as 500 VA and for optimal operation it is working on 500 VA during all the modes. During first two modes, no reactive power is demanded by load and only active power exchange is done. In mode-1, EV charger is charging the battery pack at the rate of 500 W and load is also demanding 100 W of active power. In that case, the total active demand of EV charger and load i.e., 600 W is supplied by grid. During mode-2, EV charger is taking 500 W of power from battery pack. In this condition, first EV charger fulfills the 100 W active demand of external load and transfer the surplus power of 400 W to grid. The mode-3 is associated with reactive power compensation only and EV charger is compensating 500 VAR of reactive power without charging of battery pack. The load is demanding 100 W and 100 VAR of active and reactive power respectively. Thereby, first EV charger compensates the 100 VAR reactive demand of load and transfer surplus 400 VAR to grid. Now, grid is taking 400 VAR of reactive power and supplies 100 W of active power to external load. In mode-4, the EV charger is charging battery pack at the rate of 400 W and compensating 300 VAR of reactive power. The load is demanding 100 W and 150 VAR of active and reactive power respectively. In this case, EV charger compensating the 150 VAR reactive demand of external load and transfer surplus 150 VAR to grid. Whereas, grid supplies total 500 W active demand of EV charger and external load. The mode-5 related to discharging and reactive power compensation operation. During this, the EV charger is taking 400 W of power from battery pack while compensating 300 VAR of reactive power. It transfers 100 W of active power to external load and rest 300 W transferred to grid. Similarly, it compensates 150 VAR of reactive demand of external load and transfer rest 150 VAR to grid. The active/reactive operation of EV charger in mode-6 is same as mode-4 but the load reactive demand is increased to 300 VAR. Now, the EV charger can compensate 300 VAR of reactive power, therefore no exchange of reactive power is done with grid. Whereas, the grid supplies 500 W of active power to EV charger and external load. The EV charger operation in last mode is same as mode-5, however in this case the reactive demand of external load is increased to 350 VAR. whereas, the EV charger can compensate only 300 VAR, therefore during this the rest 50 VAR of reactive demand is supplied by grid. Where, the EV charger supplies 100 W to external load and rest 300 W to grid same as mode-5.

TABLE 4.6 - Experimental Scenario of ANFIS Based Controller.

Mode	P_C (W)	Q_C (VAR)	S_C (VA)	P_L (W)	Q_L (VAR)	S_L (VA)	P_G (W)	Q_G (VAR)	S_G (VA)
1	500	0	500	100	0	100	600	0	600
2	-500	0	500	100	0	100	-400	0	400
3	0	500	500	100	100	141.4	100	-400	412.3
4	400	300	500	100	150	180.3	500	-150	522
5	-400	300	500	100	150	180.3	-300	-150	335.4
6	400	300	500	100	300	316.2	500	0	500
7	-400	300	500	100	350	364	-300	50	304.1

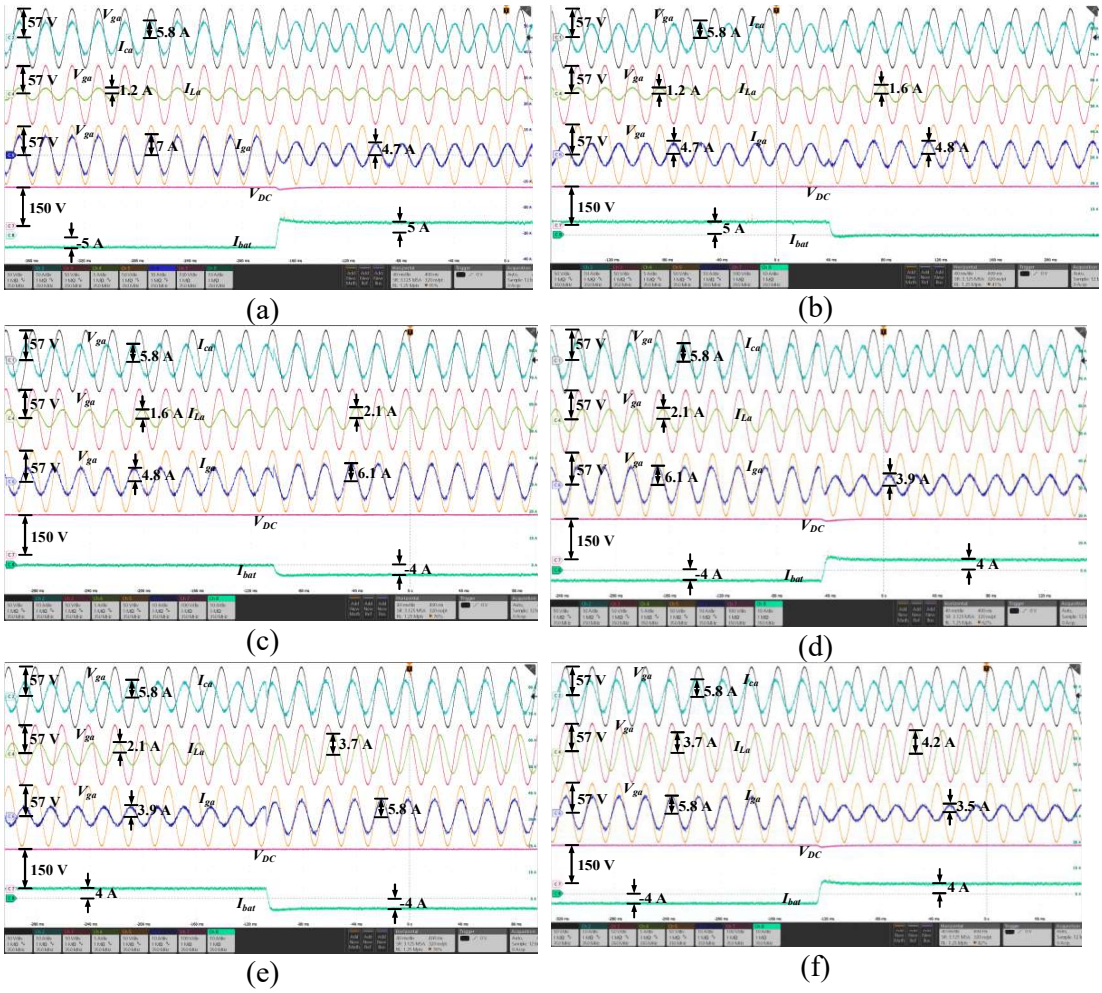

Figure 4.18: *Transition of grid phase a grid voltage (V_{ga}), phase a current of charger (I_{ca}), load (I_{La}) and grid (I_{ga}), DC-Link voltage (V_{DC}) and battery current (I_{bat}) from (a) mode 1-2, (b) mode 2-3, (c) mode 3-4, (d) mode 4-5, (e) mode 5-6 and (f) mode 6-7.*

Fig. 4.18 show the transition of phase *a* grid voltage with phase *a* current of EV charger (I_{ca}), load (I_{La}) and grid (I_{ga}), DC-link voltage (V_{DC}) and battery current (I_{bat}). Fig. 4.18 (a) show the transition from mode 1 to 2. During this, battery is charging at the rate of 500W and discharging at same rate without reactive power operation in mode 1 and 2 respectively. The active demand of load is 100 W during both working modes,

thereby the grid is supplying 600 W of active power in mode 1 and receiving 400 W in mode 2. Since, the apparent power of EV charger is same i.e., 500 VA in all working modes, the magnitude of EV charger current is 5.8 A during all modes. The apparent power of load is same in mode 1 and 2 i.e., 100 VA, therefore no change occurs in magnitude of load current and i.e., 1.2 A. However, the apparent power of grid is 600 VA and 400 VA in mode 1 and 2 respectively, therefore the magnitude of grid current is 7 A and 4.7 A in mode 1 and 2 respectively. Since, mode 1 is associated with charging of battery without reactive power operation and load is also consuming active power, the current is in phase with voltage. The mode 2 is associated with discharging operation only, therefore EV charger and grid current is exactly out of phase with voltage. The battery pack current of 100 V battery pack is -5 A and 5 A in mode 1 and 2 respectively because of 500 W charging and discharging power command.

Fig. 4.18 (b) shows the transition from mode 2 to 3. The mode 3 is associated with reactive power operation without changing of EV battery. In this, load is also consuming 100 VAR of reactive power with 100 W of active power. Therefore, total apparent power consuming by load is 141.4 VA and magnitude of load current is increased to 1.6 A from 1.2 A. Due to the reactive power demand, load current is lagging by approximately 50° by voltage. As EV charger is compensating 500 VAR of reactive demand in which 100 VAR is supplied to load and rest of reactive power is transferred to grid, therefore the EV charger current is leading exactly 90° by voltage. The grid is supplying 100 W of active power to load and receiving 400 VAR of reactive power, which results the total apparent power is 412.3 VA. Therefore, the grid current is leading 76° by voltage. Since, EV charger is not charging/discharging of battery, the battery current is zero in mode 3.

Fig. 4.18 (c) shows the transition from mode 3 to 4. The mode 4 is associated with both charging and reactive power operations. In this, EV charger is charging the battery pack at the rate of 400 W and rest of the charger's rating is utilized in compensation of 300 VAR of reactive power. The reactive demand of load is also increased in mode 4 and now total apparent power of load is 180.3 VA. Due to that, the magnitude of load current is increased to 2.1 A from 1.6 A and now the phase difference between voltage and current is 56° lagging. During this mode, the 150 VAR reactive demand of load is supplied by EV charger and rest 150 VAR is transferred to grid. The grid is supplying 500 W of active power and receiving 150 VAR of reactive power which results total apparent power is 522 VA. As a result, the magnitude of grid current

is 6.1 A and phase difference between voltage and current is 17° leading. As battery is charging at the rate of 400 W, the battery charging current is 4 A.

Fig. 4.18 (d) shows the transition from mode 4 to 5. The mode 5 is associated with both discharging and reactive power operations. In this, the EV charger is commanded to transfer the battery energy to local load and grid. The EV charger is taking 400 W of active power and rest of its rating is utilized in compensation of 300 VAR of reactive power. The apparent power of load is same as mode 3, thereby no change occurs in load current. However, the active power demand of load is fulfilled by EV charger. Since, battery is supplying 400 W of active power, in which 100 W is supplied to load and rest 300 W is transferred to grid. At the same time, EV charger is supplying 300 VAR of reactive power in which 150 VAR is consumed by load and rest 150 VAR is transferred to grid. As a result, the apparent power of grid is 335.4 VA and magnitude of grid current is 3.9 A. The phase difference between voltage and current of EV charger and grid is 143° leading and 153° leading respectively. Moreover, the battery changes from -4 A to 4 A as battery is supplying 400 W of active power to grid.

Fig. 4.18 (e) shows the transition from mode 5 to 6. The EV charger operation in mode 6 is same as mode 4, it charges the battery pack at the rate of 400 W while transferring 300 VAR of reactive power. However, in this mode the reactive demand of load is increased to 300 VAR. As a result, total apparent power of load is increased to 316.2 VA and load current is 3.7 A. In this case, the reactive demand of load is compensated by EV charger and no reactive power is exchanged with grid. However, the 400 W and 100 W of active demand of battery and load respectively is supplied by grid. As a result, total apparent power of grid is increased to 500 VA and grid current is 5.8 A. The phase difference between voltage and current of EV charger is same as mode 4 and phase difference between load voltage and current is 72° lagging. Since, there is no exchange of reactive power with grid, the grid current is in phase with voltage. Moreover, the battery current is same as mode 4 i.e., -4 A.

Fig. 4.18 (f) shows the transition from mode 6 to 7. The EV charger operation in mode 7 is same as mode 5, it discharges the battery pack at the rate of 400 W while transferring 300 VAR of reactive power. In this the reactive demand of load is increased to 350 VAR. As a result, total apparent power of load is increased to 364 VA and load current is 4.2 A. During this, EV charger is not capable to fulfill the complete reactive demand of load, therefore the rest 50 VAR of reactive power is supplied by grid. However, grid is taking 400 W of active power from battery pack which decreases the

total apparent power of grid to 304.1 VA. As a result, decrement in magnitude of grid current to 3.5 A. The phase difference between voltage and current of EV charger, load and grid is 143° leading, 74° lagging and 170° lagging respectively. Moreover, the battery current is same as mode 5 i.e., 4 A. Further, it can be seen that the DC-link voltage (V_{DC}) is maintained at 150 V during all working modes where I_{bat} changes according to the charge/discharge command.

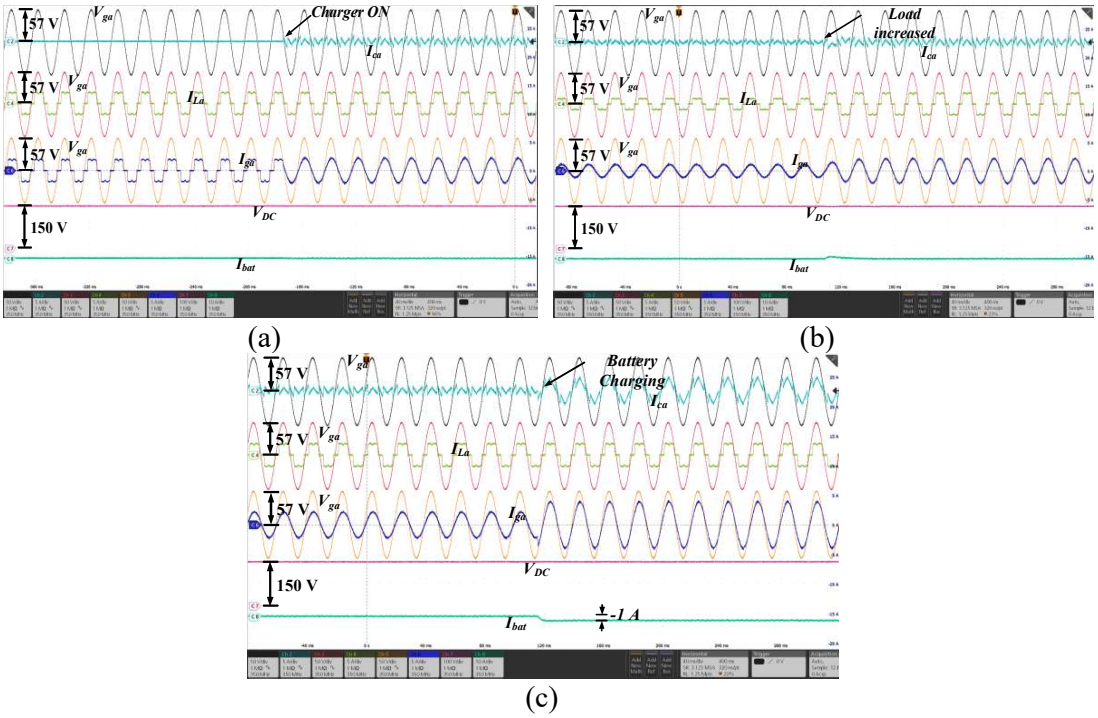

Figure 4.19: *(a) Harmonic compensation of load current, (b) harmonic and reactive power compensation and (c) harmonic and reactive power compensation while charging of battery.*

Fig. 4.19 shows the operation of EV charger as an active power filter. It is a case when charger is not charging the battery pack. It can act as an active power filter and compensate reactive demand of linear/non-liner external load. Fig. 4.19 (a) shows the compensation of reactive demand of non-linear load. In this before turning ON the charger, the grid current is same as load current. However, after turn ON the charger, it supplies the harmonic component of current and makes grid current purely sinusoidal. In Fig. 4.19 (b), the demand of load is increased. This total demand of load can be compensated by charger because it is within its compensating capacity. Therefore, complete demand of external linear/non-linear load is compensated by charger which again makes the grid current sinusoidal. In Fig. 4.19 (c), charger is charging the battery and compensating the reactive demand of external linear/non-linear load. During this,

EV charger takes active power from grid for battery charging and supplies reactive power to external load simultaneously. Due to that the charger current is distorted, but it improves the quality of grid current. The results also show the performance of controller under variable charging current rate as evident from increased grid current with increase in charger current.

Table 4.7 – THD during different working modes.

Mode	THD (%)	Mode	THD (%)
1	0.7	5	1
2	0.8	6	1.5
3	1.2	7	1.3
4	1.7	8	1.0

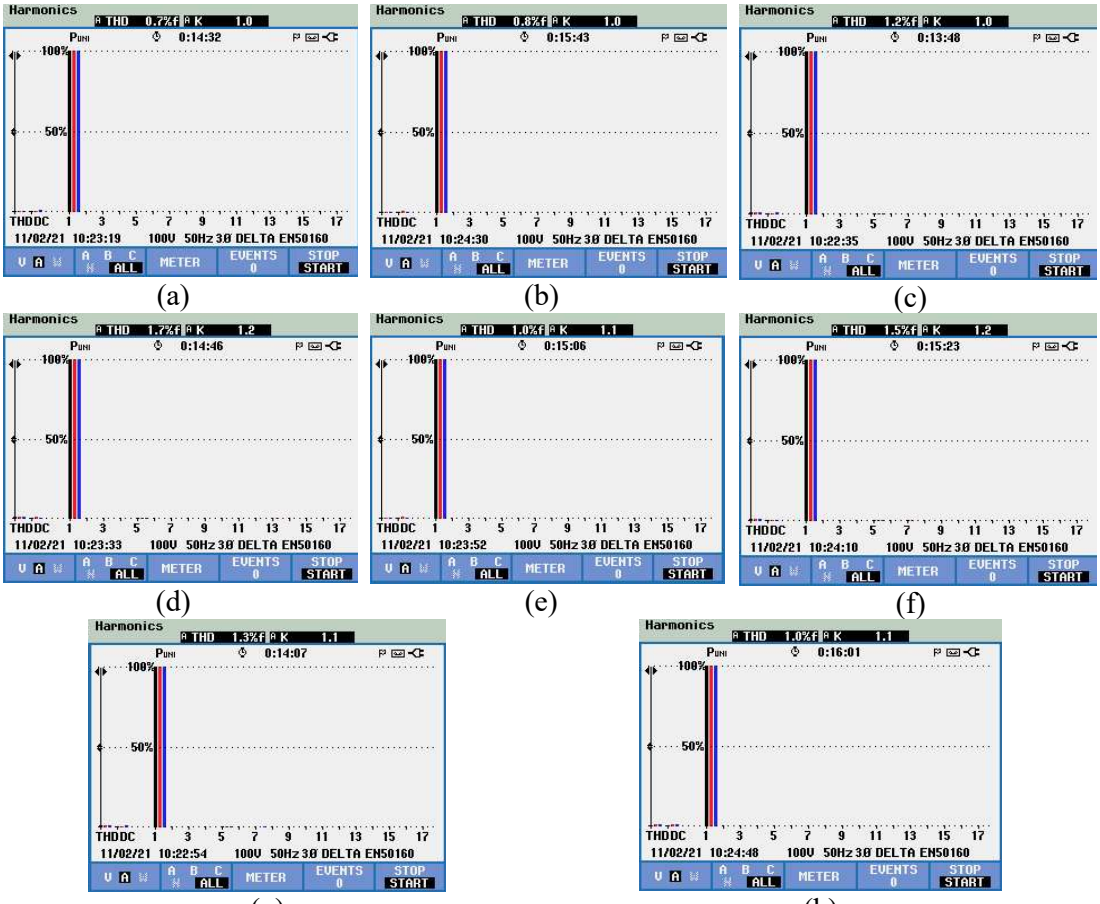

Figure 4.20: *THD in Three-phase grid current (a) Mode 1, (b) Mode 2, (c) Mode 3, (d) Mode 4, (e) Mode 5, (f) Mode 6, (g) Mode 7 and (h) Mode 8.*

Fig. 4.20 shows the harmonic spectrum of three-phase grid current during all working modes. The results are also listed in Table 4.7. and it is found that the value of

THD during all working modes are within the permissible limit of 5% specified by IEEE-519 standard in real time also.

4.6 Conclusion

This chapter has presented two control architectures for a two-stage off-board EV charger. The first controller is based on regular *PI* controller and another one is based on *ANFIS*. The overall EV charger controller consists of two different controllers each for AC-DC and DC-DC converter. The AC-DC converter control consists two control loops. The *PI* based controller having four *PI* regulators, two for outer loop and two for inner loop. Sometimes, it is very difficult to tune four *PI* regulators for a single controller specially for inner loop. The inner loop is very much fast than outer loop and difficult to tune in comparison with outer loop. The outer loop *PI* regulators are utilized to track the active/reactive power command, whereas inner ones are for tracking the grid current in *dq* frame. Further, the pulses are generated by PWM technique.

In *ANFIS* based controller, a unified *ANFIS* is utilized in outer loop for calculating the reference active and reactive current components in *dq* frame. In this control algorithm, the grid current is tracked in periodic form, therefore the calculated active and reactive *dq* current component are transformed into *abc* reference frame. Further, a hysteresis controller is used in inner loop to track the grid current and generation of pulses.

Moreover, the performance of both EV charger controller has been tested under all possible working modes of *P-Q* plane and harmonic compensation also in both simulation and real time. After implementation of both the controller, it is found that the design of *PI* controllers is very simple but they have poor performance in dynamic conditions specially for inner loop. It can be seen from the results shown in Fig. 4.8 and 4.10 that the grid current takes some time to settle down during the transition and some overshoot is also there. Therefore, it is suggested that the *PI* regulators are not suitable for tracking the grid current in inner loop. After implementing the hysteresis controller for inner current control loop, it is found that the tracking of grid current is very much better and simple in case of hysteresis controller. It can be seen that from results shown in Fig. 4.15 and 4.18 that the hysteresis controller exhibits excellent performance under both steady state and dynamic operating conditions. However, the hysteresis controller

produces variable switching frequency which may affects the converter. Moreover, it is found that the tracking of grid current is much better in periodic form rather than constant *dq* frame. Therefore, some other methods can be used for tracking the grid current in inner control loop in periodic form. On the other hand, the *ANFIS* based EV charger controller gives better performance in outer loop with less settling time and overshoot but its design is very much complex than *PI* regulator. The tracking time of active/reactive power is approximately same by both controllers i.e., around two grid cycles. Therefore, the *PI* regulators can be used in outer loop for active/reactive power tracking. For DC-DC converter control, same approach has been used for both types of controllers. The rigorous analysis of simulation results supported with experimental results is provided to validate the performance of proposed controller.

CHAPTER 5

SECOND ORDER RIPPLE MINIMIZATION IN SINGLE STAGE ON-BOARD ELECTRIC VEHICLE CHARGER

Chapter Outline

5.1 Introduction

This chapter deals with the design of single phase, single stage ON board EV charger. The single phase EV chargers have inherent problem of producing second order ripple component on DC side. This problem is further exaggerated during vehicle-to-grid (V2G) mode of operation where it may be normally controlled to supply both active as well as reactive power. During the V2G reactive power compensation, the second order harmonics ripple component at DC side will increase which further reduces the life cycle and performance of battery pack as discussed in chapter-1. Therefore, a second order ripple component compensation technique is proposed by pre-compensating the reference current itself in this proposed work. The resultant reference current is periodic in nature and accordingly, repetitive controller (*RC*) is used to track the reference current. The *RC* is well known for its capability of tracking the periodic signals. The EV

charger is controlled in both grid to vehicle (G2V) and V2G mode. Here, the performance of the controller has been tested in eight different modes on active-reactive (*P-Q*) power plane and found that ripple minimization technique successfully reduced second order ripple component on DC side. The simulation rating of on-board EV charger is 6.6 KVA. However, the hardware prototype rating of on-board EV chargers is 350 VA.

5.2 Single Stage ON board EV Charger

The single stage on-board EV charger consists of a IGBTs based single phase h-bridge AC-DC converter and can easily perform four quadrant operation due to its bidirectional capability as shown in Fig. 5.1. The EV charger is directly connected to the single-phase AC supply through interfacing inductor (L_s) to compensate harmonic of grid current and achieve sinusoidal current waveform. On the DC side EV battery pack is connected in parallel with DC link capacitor. A control switch is connected in series with battery pack to disconnect it when it has fully charged.

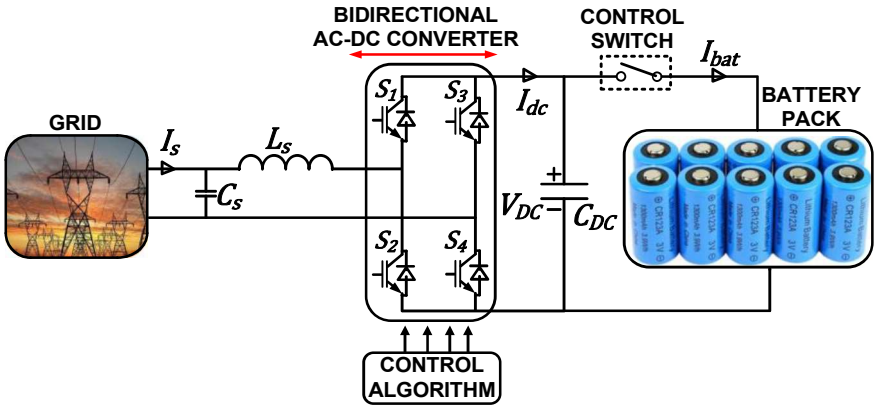

Figure 5.1: *Single Stage ON board EV charger.*

This single-phase H-bridge AC-DC converter has inherent property of producing second order ripple on DC side which is periodic in nature as shown in Fig. 5.2. Further, this problem may be exaggerated due to periodic disturbance/noise presence in input AC supply. This double frequency ripple component on DC side may increases the ripple in battery voltage and current, which affects the battery lifetime. Therefore, it is essential to minimize this double frequency ripple component on DC side voltage so that it will not affect the battery life span.

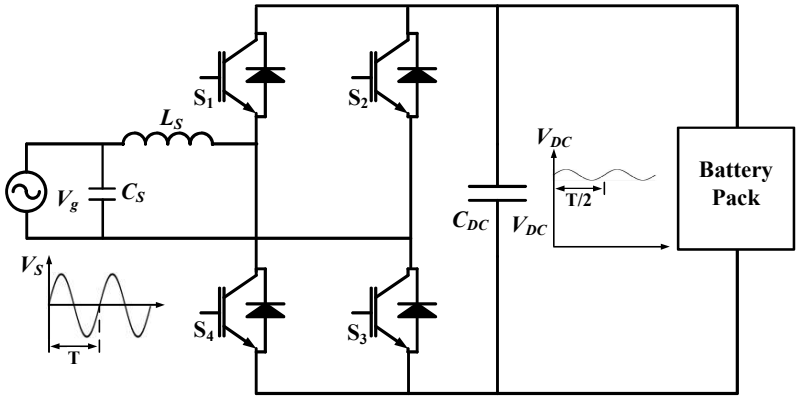

Figure 5.2: Second Order Ripple on DC Side.

5.3 Effect of Second Order ripple on Battery

The on-board charger having H-bridge AC-DC converter affects the battery life by producing two frequency ripples: one is double of grid frequency ($I_{ripple\text{-}df}$) and converter switching frequency ($I_{ripple\text{-}sw}$). To apprehend the outcome of current ripple on battery life, first it is required to know that how the extra heat is developed by ripple current. For this, consider a battery model shown in Fig. 5.3, where R_b is internal resistance of battery and V_{OC} is battery voltage. The extra heat developed by ripple current is due to battery internal resistance (R_b) and it is equal to the power loss across R_b due to ripple current [117], [118].

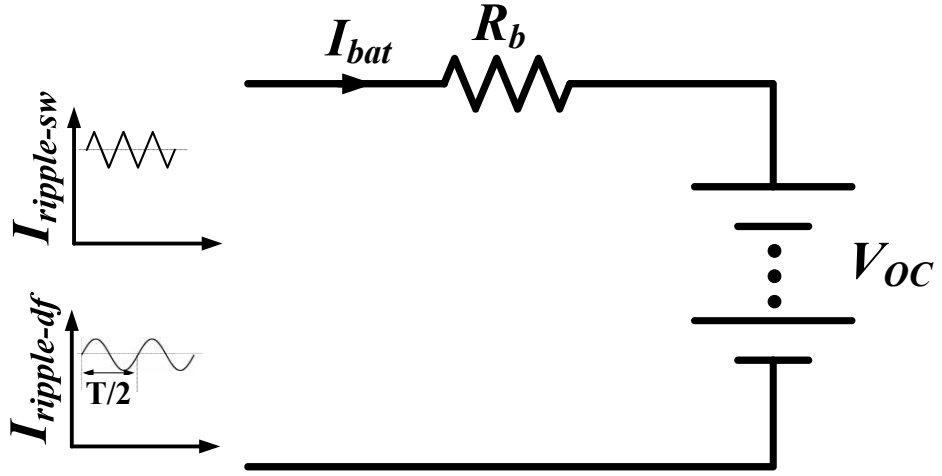

Figure 5.3: *Ripple on battery.*

$$P_{ripple} = I_{ripple}^2 \cdot R_b \tag{5.1}$$

Moreover, the battery internal resistance varies with change in frequency and it increases with decrement in frequency. Therefore, second order ripple across the battery affects more as it increases the internal resistance and P_{ripple}. However, the frequency of

switching ripple is very high and correspondingly does not produce extra heat in large amount and can be neglected.

Furthermore, the allowable amount of ripple which does not affect the life cycle of battery is given by manufacturer. It varies from *C/20* to *C/10*, where *C* is the charging current of battery as discussed in chapter-1. It means if a battery is charging at 100 A then allowable ripple in battery current is 5 A for *C/20* and 10 A for *C/10* type of battery. Therefore, from the information available about the allowable ripple in battery current, it must not be larger than C/10 [119].

There are two ways to diminish this double frequency ripple component on DC side: using large filter or by designing a control algorithm [120], [121]. The large filter may increase filter cost, overall vehicle weight and system order which increases control complexity. Therefore, it is convenient to design a controller for minimizing this ripple on DC side in case of EV charging.

5.4 Effect of Third Harmonic Injection on Ripple

In this section, the relation between third harmonic injection on ripple has been presented. For this the unity power factor is considered. The AC side voltage and current are as follows [122],

$$v = V_m \cos \omega t \tag{5.2}$$

$$i = I_m \cos \omega t \tag{5.3}$$

$$P_{ac} = v \cdot i = V_m \cos \omega t \cdot I_m \cos \omega t = \underbrace{\frac{V_m \cdot I_m}{2}}_{\approx P} + \underbrace{\frac{V_m \cdot I_m}{2} \cos 2\omega t}_{\approx Q} \tag{5.4}$$

Consider the output power equals to input power. The P is nearly equal to output constant DC power and Q is responsible for ripple DC power. Therefore, the output DC power can be expressed in terms of constant and ripple components.

$$P_{DC} = \underbrace{V_{DC\,cons} \cdot I_{DC\,cons}}_{P_{cons} \approx P} + \underbrace{V_{DC\,rip} \cdot I_{DC\,rip}}_{P_{rip} \approx Q} \tag{5.5}$$

Where, P_{cons} is output DC constant power and P_{rip} is ripple power.

$$V_{DC\,rip} \cdot I_{DC\,rip} \approx Q = \frac{V_m \cdot I_m}{2} \cos 2\omega t = V_r \cdot I_{sr} \tag{5.6}$$

From the above relation it can be inferred that the I_{DC} ripple is directly proportional to ripple in reactive component of grid current (I_{sr}). Where, V_r is rms value of grid voltage.

The harmonic current is expressed as,

$$I_n(t) = I_n \cos(n \cdot \omega t) \tag{5.7}$$

Where, n is the harmonic order and I_n is amplitude of harmonic current. The reactive power of harmonic current is,

$$Q_n = V_m \cos \omega t \cdot I_n \cos(n \cdot \omega t) - \frac{V_m \cdot I_m}{2} \tag{5.8}$$

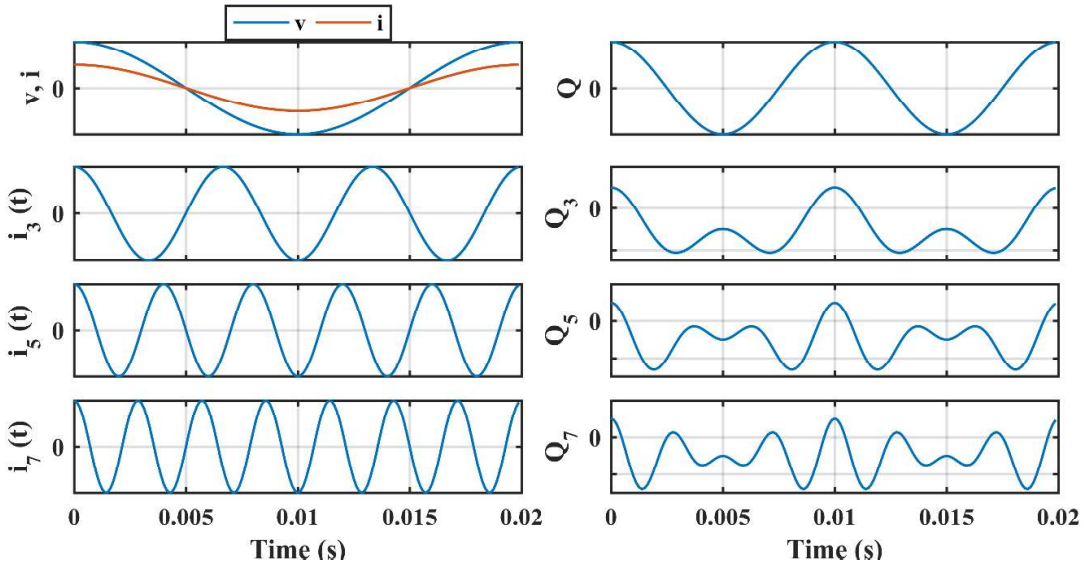

Figure 5.4: *Harmonic current and respective instantaneous Q.*

From the Fig. 5.4, it can be seen that the third harmonic is most effective in reducing the pulsation in Q.

5.5 Control Development for Second Order Ripple Minimization

This second order ripple component can be minimized by developing control architecture for AC-DC converter. The layout of proposed on-board PEV charger with its control is shown in Fig. 5.5. The controller of AC-DC converter having two loops in which inner one is for grid current control and outer one is for voltage/power control. The grid current can be controlled either in DC quantity/ dq frame as discussed in chapter-4 or AC quantity/ αβ frame. Generally, proportional integral (PI) controllers are

used to track DC quantity as they are very popular for tracking it with zero steady state error. However, they are not very much suitable for inner current loop for aforementioned application as they have limited bandwidth and it is difficult to track command under varying AC input. Moreover, while using *PI* regulators in inner loop requires αβ to *dq* transformation which is also complex in case of single-phase system. Therefore, a controller which can regulate periodic signal is required to overcome from above mentioned issues. Here, the outer control loops are used to regulate the *P* and *Q* which are inherently DC quantities and therefore, the simple *PI* regulator is used to track them. Here, the main aim is to set the reference signal for inner loop while pre-compensating the ripple terms. Therefore, it is very important to analyze the power equations on AC side which are responsible for the introduction of ripple current harmonics on the DC side. Let us assume that the AC side voltage and current are as follows [123],

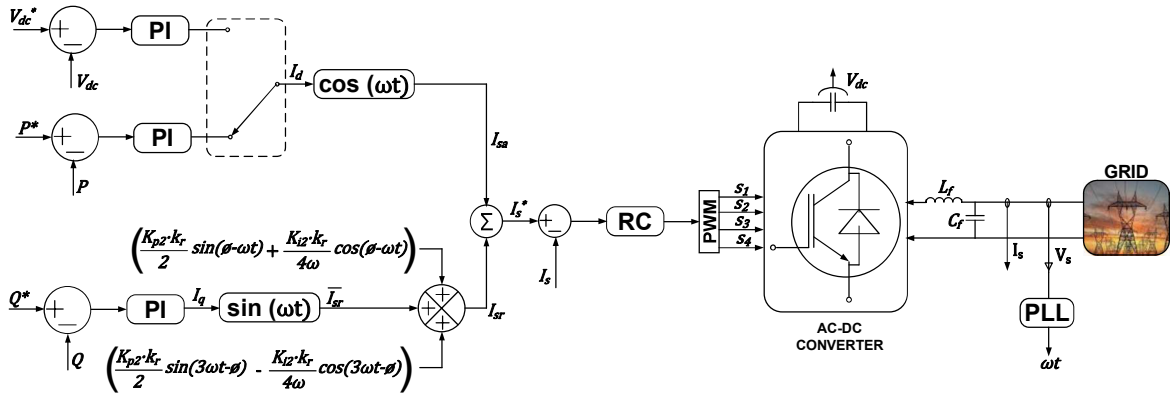

Figure 5.5: *Proposed Control System.*

$$v = v_m \cos \omega t \tag{5.9}$$

$$i = i_m \cos(\omega t - \emptyset) \tag{5.10}$$

Where, v_m and i_m are peak value of AC voltage and current respectively, and $\emptyset$ is phase angle between them.

AC power can be calculated by multiplying equations (5.9) and (5.10).

$$P_{ac} = v \cdot i = v_m \cos \omega t \cdot i_m \cos(\omega t - \emptyset)$$

$$= v_r \cdot i_r \cdot \cos \emptyset + v_r \cdot i_r \cdot \cos(2\omega t - \emptyset) \tag{5.11}$$

Here v_r and i_r are the root mean square (RMS) value of AC side voltage and current respectively.

The first term of P_{ac} represents the active power and second term represents the reactive power of the AC side.

$$P = v_r \cdot i_r \cdot \cos \emptyset = k_r \cos \emptyset \tag{5.12}$$

$$Q = v_r \cdot i_r \cdot \cos(2\omega t - \emptyset) = k_r \cos(2\omega t - \emptyset) \tag{5.13}$$

Here, $k_r = v_r \cdot i_r$

The active component of current may be determined as

$$I_d = K_{p11}(P^* - P) + K_{i11} \int (P^* - P)\, dt$$

$$= K_{p11} \cdot P^* - K_{p11} \cdot k_r \cos \emptyset + K_{i11}\, P^*\, t - K_{i11}\, k_r\, \cos \emptyset \cdot t \tag{5.14}$$

Similarly, the reactive component of current may be determined as

$$I_q = K_{p12}(Q^* - Q) + K_{i12} \int (Q^* - Q)\, dt$$

$$= K_{p12}\, Q^* - K_{p12}\, k_r\, \cos(2\omega t - \emptyset) + K_{i12}\, Q^*\, t - K_{i12}\, k_r \cdot \frac{1}{2\omega} \sin(2\omega t - \emptyset) \tag{5.15}$$

Furthermore, the instantaneous value of active current component is,

$$I_{sa} = I_d \cdot \cos \omega t$$

$$= \left(K_{p11} + K_{i11} \cdot t\right)[P^* - k_r \cdot \cos \emptyset] \cos \omega t \tag{5.16}$$

Similarly, the instantaneous value of reactive current component is,

$$\overline{I_{sa}} = I_q \cdot \sin \omega t$$

$$= Q^* \left(K_{p12} + K_{i12} \cdot t\right) \sin \omega t - \underbrace{\left[\frac{K_{p12} \cdot k_r}{2} \sin(\emptyset - \omega t) + \frac{K_{i12} \cdot k_r}{4\omega} \cos(\emptyset - \omega t)\right]}_{\text{A}}$$

$$- \underbrace{\left[\frac{K_{p12} \cdot k_r}{2} \sin(3\omega t - \emptyset) - \frac{K_{i12} \cdot k_r}{4\omega} \cos(3\omega t - \emptyset)\right]}_{\text{B}} \tag{5.17}$$

From equation (5.17), it can be seen that the reactive current component having three terms, where the first term is associated with fundamental frequency component, where the term A comprises the reactive and active lossy component and term B represents the 3rd harmonic component. Here, the term B can be easily eliminated by any

low pass filter (LPF) with appropriate cut-off frequency, but it is not advisable to eliminate the term A by LPF because it has fundamental frequency component. Therefore, in the proposed method, both the ripple component terms (i.e., term A & B) have been pre-compensated in the reactive part of reference current itself. For this, both the terms are injected in outer loop of AC-DC converter control. This second order ripple on DC side is directly depends on third harmonic component of current, therefore it can be reduced by adding this harmonic in reference current.

Since, the reference signal for inner current control loop in present case is periodic in nature, a repetitive controller (RC) which is based on internal model principle theory (IMPT) has been utilized due to its well-known capability of tracking the periodic signals [124], [125], [126], [127]. This approach of current control is found to be very helpful in seamless exchange of power in G2V and V2G mode of operation. Further, this reference control signal is modified by involving the pre-compensating terms for the reduction of DC-ripple current component. The nature of such resultant control signal is periodic in nature and very difficult to track with normal *PI* regulators.

Moreover, a very difficult task in proposed control algorithm is to tune the gains of reactive power *PI* regulator. As this regulator performs two operations i.e., tracking of reference reactive power and reduction in DC side ripple. The *PI* regulator can be work for various combination of gains. Therefore, a range of gains can be found by which both the operations can be achieved. For this, the modified reference current is the combination of active component (I_{sa}) and modified reactive component(I_{sr}).

$$I_s^* = I_{sa} + I_{sr} \tag{5.18}$$

Further as per the control logic shown in Fig. 5.5, the I_{sr} can be expressed as,

$$I_{sr} = I_q \sin \omega t + A + B \tag{5.19}$$

Where, $A = X \cdot \sin(\phi - \omega t) + Y \cdot \cos(\phi - \omega t)$ and, $B = X \cdot \sin(3\omega t - \phi) + Y \cdot \cos(3\omega t - \phi)$

Here, $X = \frac{K_{p12} \cdot K_r}{2}$ and $Y = \frac{K_{i12} \cdot K_r}{4\omega}$ and for simplicity, ϕ=0.

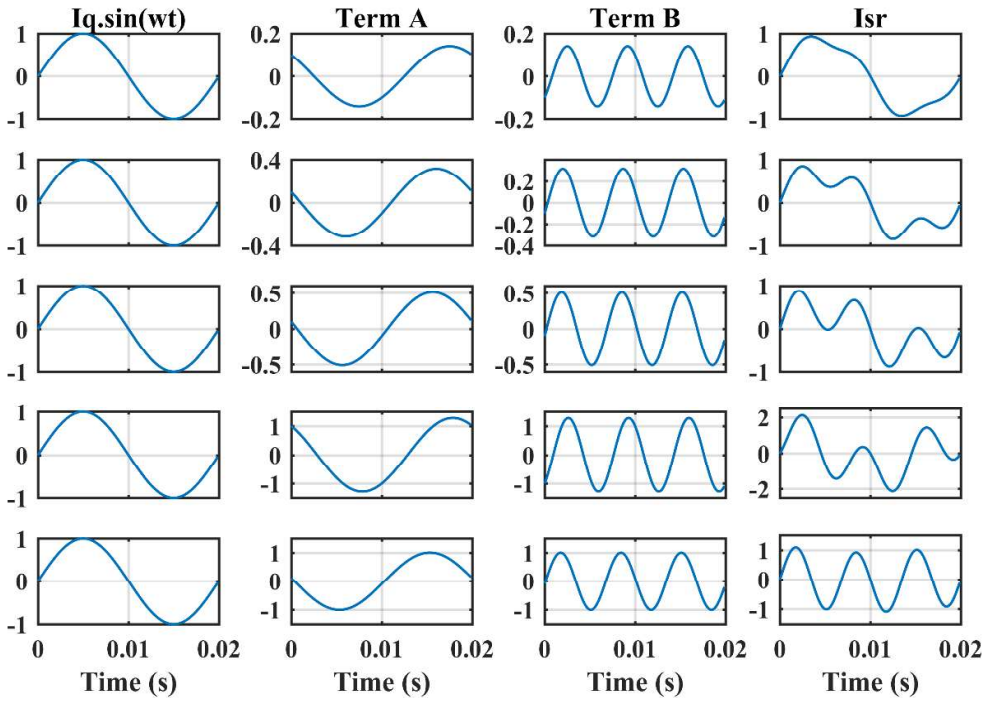

Figure 5.6: *I_{sr} with Y = 0.1 and X = 0.1, 0.3, 0.5, 0.8 and 1 respectively.*

From equation (5.6), the ripple content on battery current depends on the amount of third harmonic component on AC side, which further forms the basis of determining the optimal value of K_p and K_i. From the Fig. 5.6, it can be seen that the ripple in reactive component of AC side current is reduced for the value of X less than 0.5 and again start decreasing after 0.8, where the value of Y is taken as 0.1. By this way, various ranges can be found for the gains of *PI* regulator. This ripple component depends on both X and Y values and it can be reduced by various combination of these values within the range. Here, it is pertinent to mention that the value of K_P an K_i are chosen such that it reduces the ripple on battery side current considerably while introducing small amount of THDs on AC side current without violating the permissible limit. Further, the DC side ripple reduction will not depend on amount of third harmonics injection only. It depends on A and B term, which consist fundamental frequency term as well as controller's constants. The gains of proposed on-board EV charger controller are given in Table 5.1.

Table 5.1 – Controllers Gains of on-board EV Chargers.

PARAMETER	SYMBOL	VALUE
Proportional constant of active power control loop	K_{p11}	0.5
Integral constant of active power control loop	K_{i11}	14.9
Proportional constant of reactive power control loop	K_{p12}	1.85
Integral constant of reactive power control loop	K_{i12}	2.84

5.6 Design of Repetitive Controller Based Inner Current Loop

The main objective of proposed work is to develop a versatile control law for the proposed system. For the sake of understanding, the simplified diagram of the system is as shown in Fig. 5.7. Here, PWM driven single phase converter is connected through filtering resistance R_f, inductance L_f, and filtering capacitance C_f. The grid, which may act as both source and load depending on mode of operation (i.e., G2V, V2G) and accordingly.

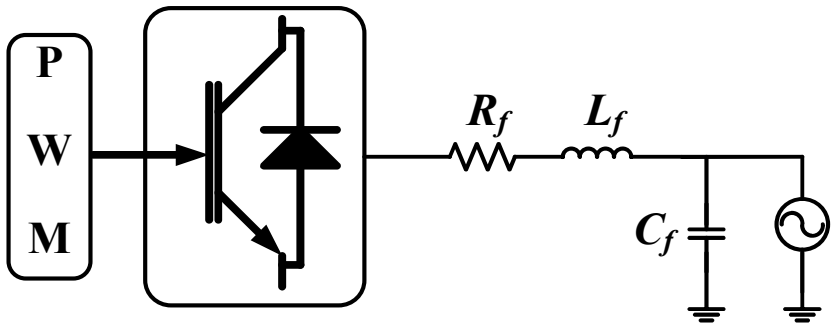

Figure 5.7: *Single line diagram of EV charger.*

The equivalent control diagram of the system as discussed above is shown in Fig. 5.8. Here, the control is performed in two stages, where the outer loop deals with *P*, *Q* regulation and being DC signals, these can be easily tracked by the *PI* regulator. Since, the inner current control loop has to deal with the periodic signal which cannot be handled by *PI* controller and accordingly a *RC* is used for inner control loop.

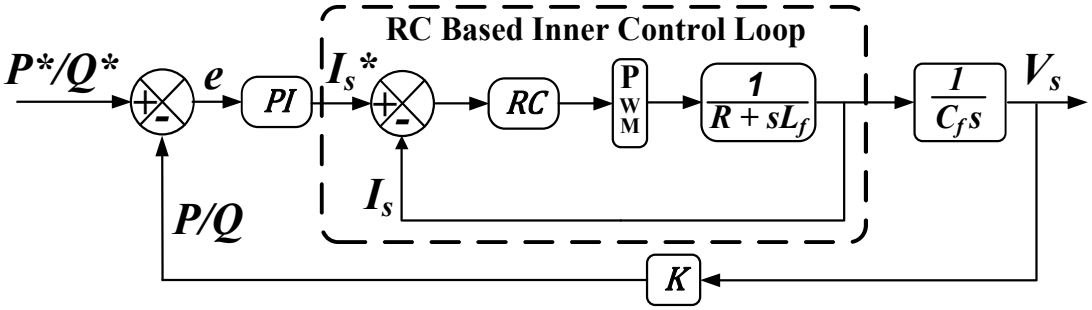

Figure 5.8: *System control.*

The RC is primarily based on internal model principle theory (IMPT) [128], [129]. According to this theory, if a fixed time delay of a given system is associated in closed loop for any periodic signal, asymptotic tracking ability with rejection of harmonic can be achieved. The general form of RC is shown in Fig. 5.9.

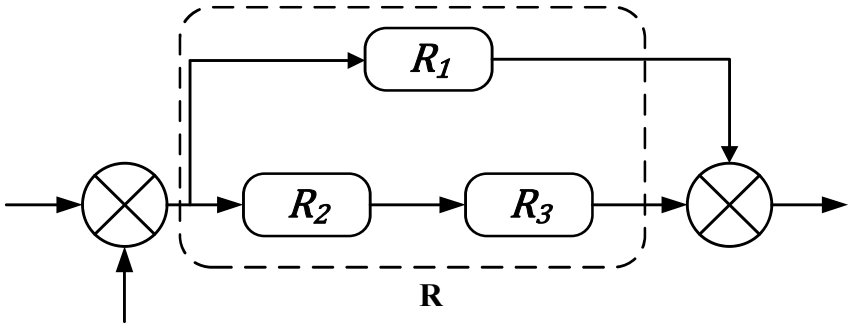

Figure 5.9: *Generalized RC.*

$$R(s) = R_1(s) + R_2(s) \cdot R_3(s) \tag{5.20}$$

Where $R_3(s)$ is internal model for periodic reference input, $R_1(s)$ and $R_2(s)$ are internally stabilizing controller (ISC) and pre-compensator, respectively. For any repetitive reference signal, internal model may be depicted by feedback time delay with LPF [130], [131].

$$R_3(s) = \frac{1}{1 + q(s)e^{-Ts}} \tag{5.21}$$

Where *T* represents the time period of fundamental signal and $q(s)$ is LPF.

According to [28], to have stabilized operation of a given plant with unity feedback, the ISC, $R_1(s)$ may be expressed as:

$$R_1(s) = \frac{X(s) + Z(s) * D_P(s)}{Y(s) - Z(s) * N_P(s)}\Big|_{Y(s)-Z(s)*N_P(s)\neq 0} \tag{5.22}$$

Where $D_P(s)$ and $N_P(s)$ are the co-prime factors of the plant $P(s)$, such that

$$P(s) = \frac{N_P(s)}{D_P(s)} \tag{5.23}$$

and $X(s)$ and $Y(s)$ are RH_∞ functions satisfying

$$X(s)\,N(s) + Y(s)\,D(s) = 1 \tag{5.24}$$

Here, the equation (5.24) is known as Bezout's identity. The term $Z(s)$ in equation (5.22) is known as rational function whose value is selected in such a way that the ISC has maximum gain at fundamental frequency. However, this kind of approach results in to increased impact of disturbance on output. Therefore, the value of $Z(s)$ must be selected in such a way that it should exhibit maximum gain of ISC while ensuring maximum attenuation to the external disturbances and that can be taken as

$$Z(s) = \frac{q(s)}{N(s)}\left(Y(s) - \frac{1}{D(s)\,W_1(s)}\right) \tag{5.25}$$

Where $W_1(s)$ is the weighing function and selected in order to shape the selectivity function $S(s)$ for a given perturbation bandwidth [25]. Here, the selectivity function is expressed as:

$$S(s) = \frac{1}{1 + P(s)R(s)} \tag{5.26}$$

Similarly, the complimentary sensitivity function T(s) which sets the upper band of R(s) is expressed as

$$T(s) = \frac{P(s)R(s)}{1 + P(s)R(s)} \tag{5.27}$$

and for the desired band width from $T(s)$, the $Z(s)$ may be expressed as

$$Z(s) < \frac{1}{N(s)}\left(Y(s) - \frac{1}{D(s)}\left(1 - \frac{1}{W_2(s)}\right)\right) \tag{5.28}$$

Here, $W_2(s)$ is the frequency dependent weighing function. For the robust performance of controller, the mixed sensitivity constraints are taken as

$$\left\|\begin{bmatrix} W_1(s)\,S(s) \\ W_2(s)\,T(s) \end{bmatrix}\right\|_\infty \leq 1 \tag{5.29}$$

Now for the present case, the plant transfer function for inner current control loop is expressed as

$$P(s) = \frac{1}{R_f + sL_f} \tag{5.30}$$

and the co-prime factors of the plant are taken as

$$N(s) = \frac{1/L_f}{(s + R_f/L_f)} \tag{5.31}$$

and $D(s) = 1$

For the simplicity of control design, the various factors have been taken as $X(s) = 0$, $Y(s) = 1$, $W_1(s) = \frac{s+\omega}{s}$, Since, the plant is strictly proper and has higher order frequency attenuation, the $W_2(s)$ is taken as unity. On using equation (5.25) the $Z(s)$ is

calculated and it is further utilized in equation (5.22) to find out the higher order ISC, $R_1(s)$. In order to reduce the order of ISC up to 2nd order, a balanced truncation method is applied by calculating the error bond of Hankel's singular value as

$$\|R_1(s) - R_1(s)\|_\infty \leq 2\sum_{k+1}^{n} \sigma_i \tag{5.32}$$

Where k is the order up to which ISC has to be reduced and σ_i is Hankel's singular values. The approximated reduced order ISC is as follows:

$$R_1(s)^{2nd} = \frac{0.995s^2 + 130.5s + 3985}{s(s + 63.25)} \tag{5.33}$$

The frequency response of the RC is shown in Fig. 5.10, where, the RC is the combination of ISC, pre-compensator and feedback delay with low pass filter. Here, the pre-compensator is taken as unity while the time delay of 20ms have been considered for LPF. From the Bode diagram of proposed system, it is evident that the controller offers sufficiently high gain at multiple fundamental frequencies in order to reject their correlated disturbances.

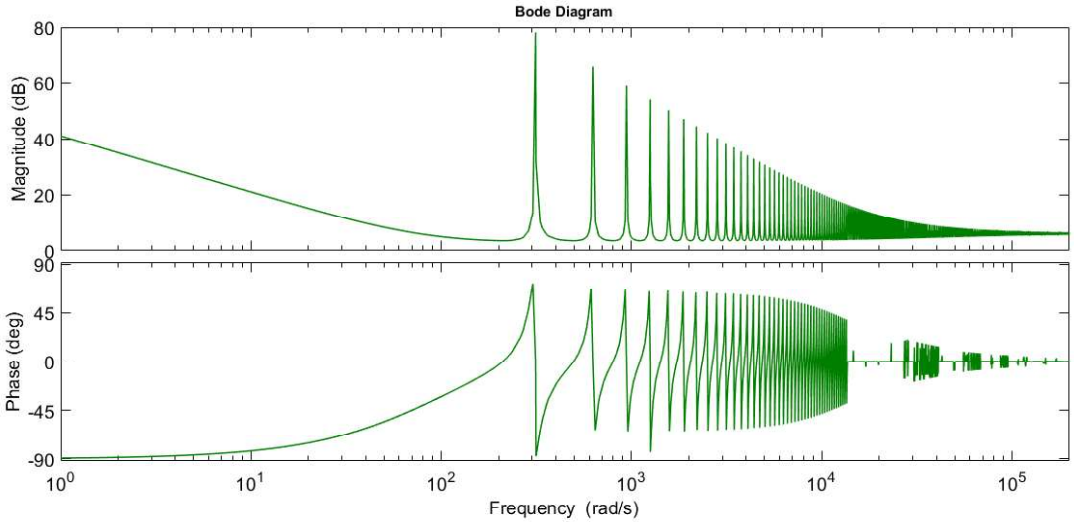

Figure 5.10: *Frequency response of inner current RC.*

5.7 Simulation Results

The proposed PEV charger with its control design is simulated in MATLAB/Simulink. The Li-ion battery and two IGBT legs-based converter is used in simulation. Initially, the battery's SOC level is taken as 50% at 350 V. The battery terminal voltage may be lower or higher than the nominal voltage depending on the SOC

level and configuration of cells. The simulations are carried out for the different operating modes of the charger as listed in Table A.6.

The main aim of this proposed work is to develop a robust control system for single phase, single stage EV charger to operate it in wide range of G2V and V2G mode of operations while minimizing the second-order ripple current component on DC side. The proposed charger may supply active power to grid if required and compensate reactive power (inductive or capacitive) if a battery charge at slower rate. In that case, the remaining rating of charger is utilized for compensating the reactive power for optimally utilization of charger's rating. Moreover, if the battery is not connected to the charger, then the proposed charger can work as an active power filter and improves the power quality. However, the reactive power compensation while charging may put lot of stress on battery and reduce its life cycle due to the presence of unwanted ripple current component in charger as explained in [25]-[26].

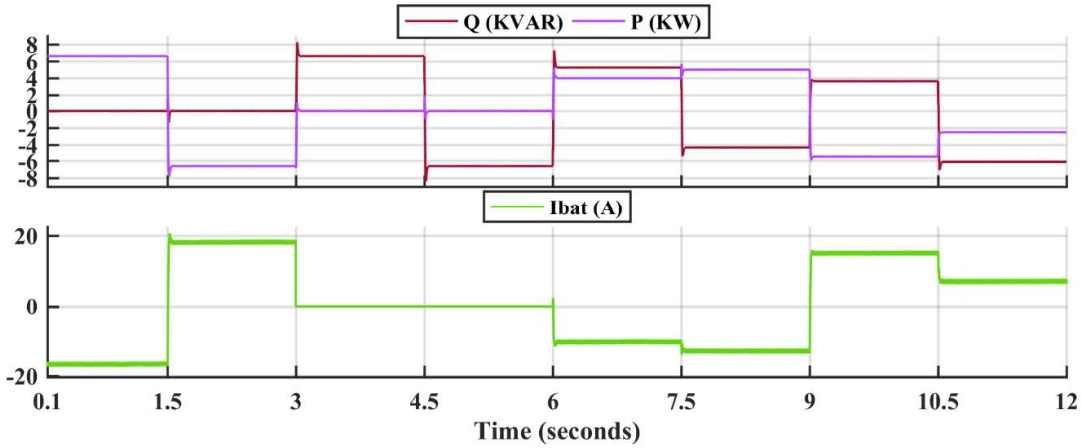

Figure 5.11: *Measured active-reactive power and battery current during all operating modes.*

The simulation results of measured active (P), reactive (Q) power and battery current (I_{bat}) during all the modes of operation are shown in Fig. 5.11. During the first four modes, only the exchange of either active or reactive power is performed. Then in next four modes, the exchange of both of the active and reactive is performed simultaneously. During mode 3 and 4, only reactive power operation is performed thereby the battery current is zero because switch connected across the battery is open and charger works as active power filter.

The controller performance is shown in expended version of simulation result as shown in Fig. 5.12. The simulation results have been presented for both steady-state as

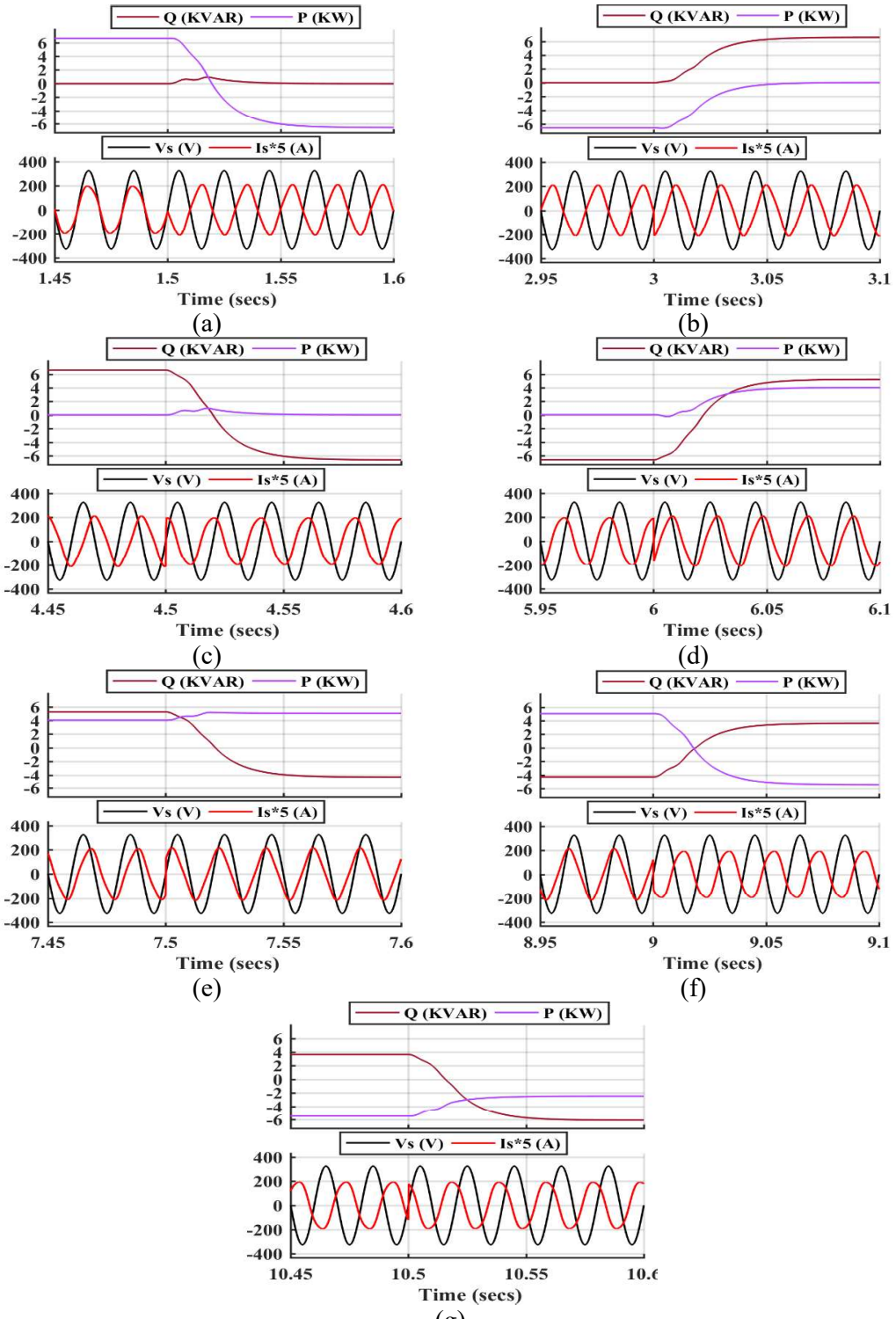

Figure 5.12: *Transition of measured grid current and voltage with active-reactive from (a) mode-1 to 2, (b) mode 2 to 3, (c) mode 3 to 4, (d) mode 4 to 5, (e) mode 5 to 6, (f) mode 6 to 7 and (g) mode 7 to 8.*

well as dynamic operating conditions. The battery pack voltage level is kept to 350 V, whereas the active and reactive power demand is varied to simulate all the eight modes

of operations. The *P* and *Q* are calculated at the AC side of the converter and fed to the controller which in turn, tracks the active and reactive power command successfully within the settling time of less than three grid cycles. Note that, the grid current remains same during all operating mode (i.e., I_g = 6600/230 = 29 A rms) since the apparent power is kept constant. Fig. 5.12 (a) shows the transition after the active power command changes from 6.6 to -6.6 KW with reactive power command is kept to 0. Here, it can be seen that the grid is in phase while charging or battery and out of phase in discharging operation. Similarly, Fig. 5.12 (c) shows the change of reactive power command from 6.6 to -6.6 KVAR while keeping the active power to 0 and now the current changes from 90° lagging to leading. Fig. 5.12 (d), (e), (f) and (g) shows the various possible cases of battery charger with non-zero active and reactive power command simultaneously.

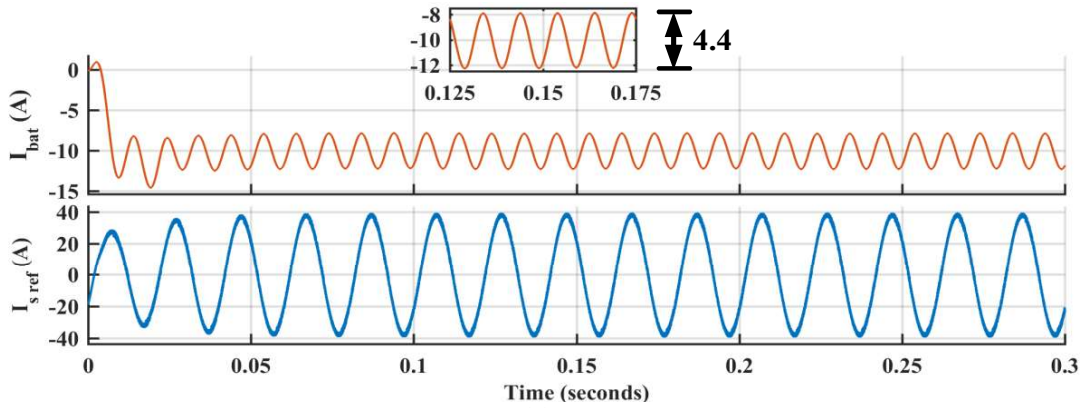

(a)

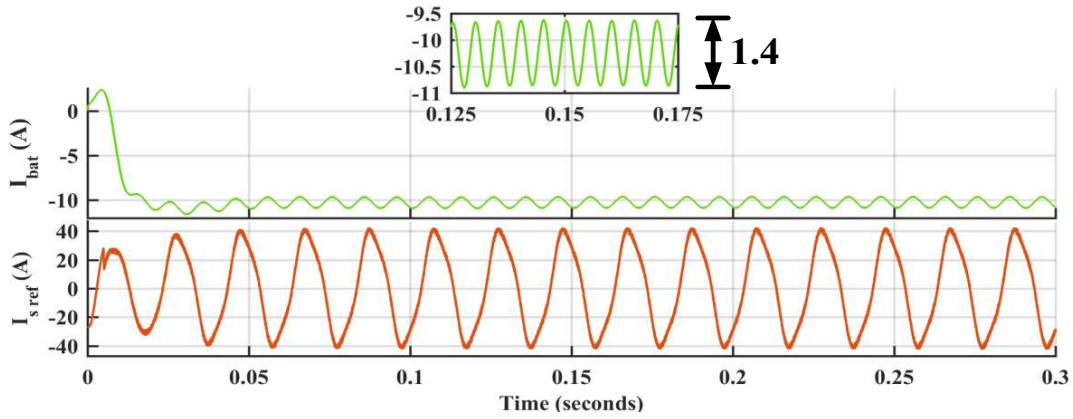

(b)

Figure 5.13: *Ripple in battery current during mode-5 (a) without ripple minimization and (b) with ripple minimization.*

Fig. 5.13 (a) and (b) represents the simulation results of DC side current and reference grid current without and with ripple minimization technique, respectively. The most challenging battery charger operation is under mode 5 (i.e., EV battery is charging

from the grid and charger is compensating reactive power) and accordingly, the results for ripple current reduction methods have been presented for this mode only. It can be clearly seen that the ripples in DC side current have been reduced to almost 11% of their original level.

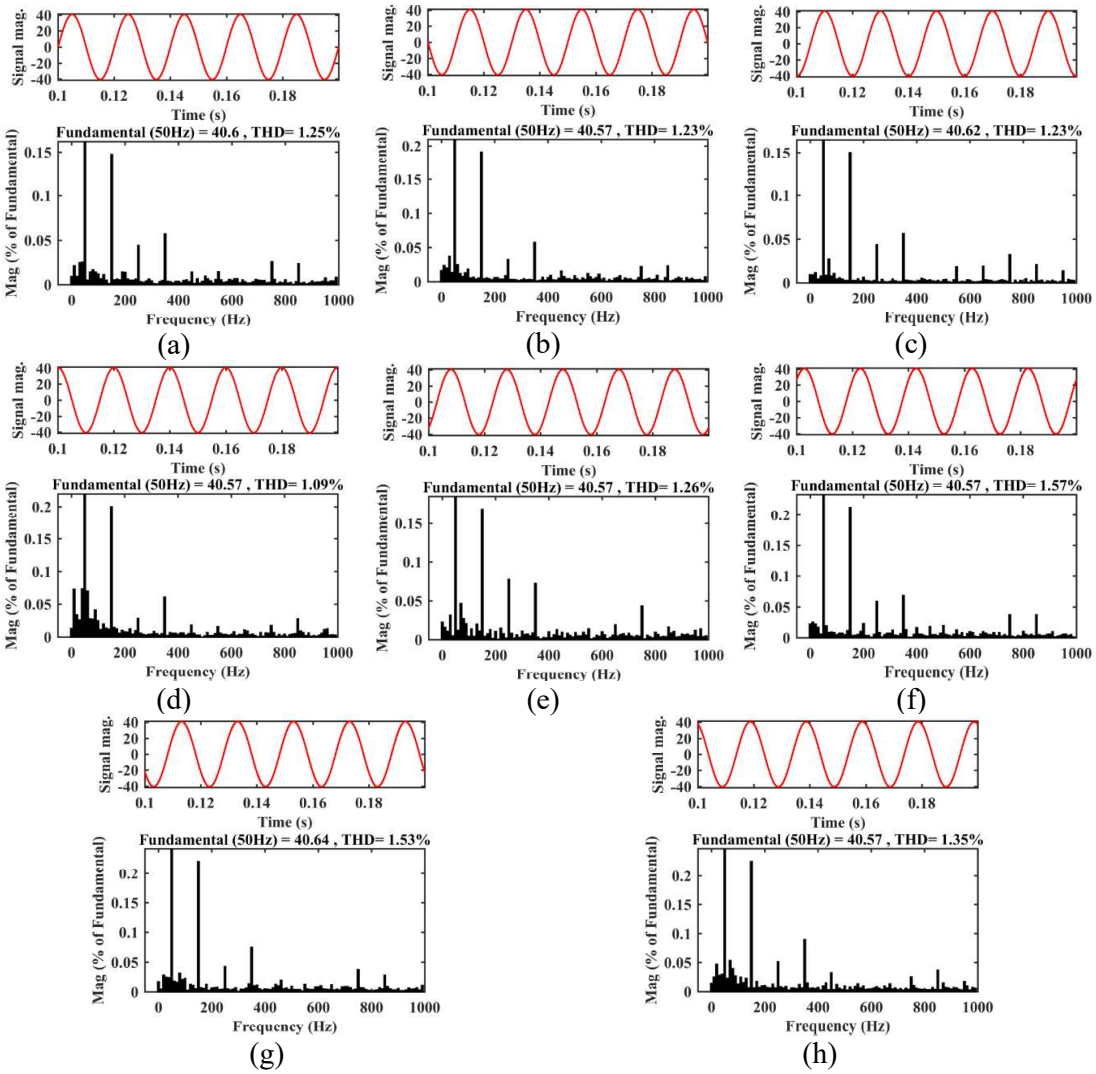

Figure 5.14: *THD in grid current without ripple minimization technique during (a) Mode-1, (b) Mode-2, (c) Mode-3, (d) Mode-4, (e) Mode-5, (f) Mode-6, (g) Mode-7 and (h) Mode-8.*

From the simulation results, it can be analyzed that controller successfully reduce the ripple in DC side current and takes less than three grid cycles to respond active and reactive power command during all the possible transition. Furthermore, the modification in reference grid current increases the THD but it is within the permissible limit of IEEE std. 519 i.e., 5%. The THD in grid current during all the modes without and with ripple minimization technique are shown in Fig. 5.14 and 5.15 respectively.

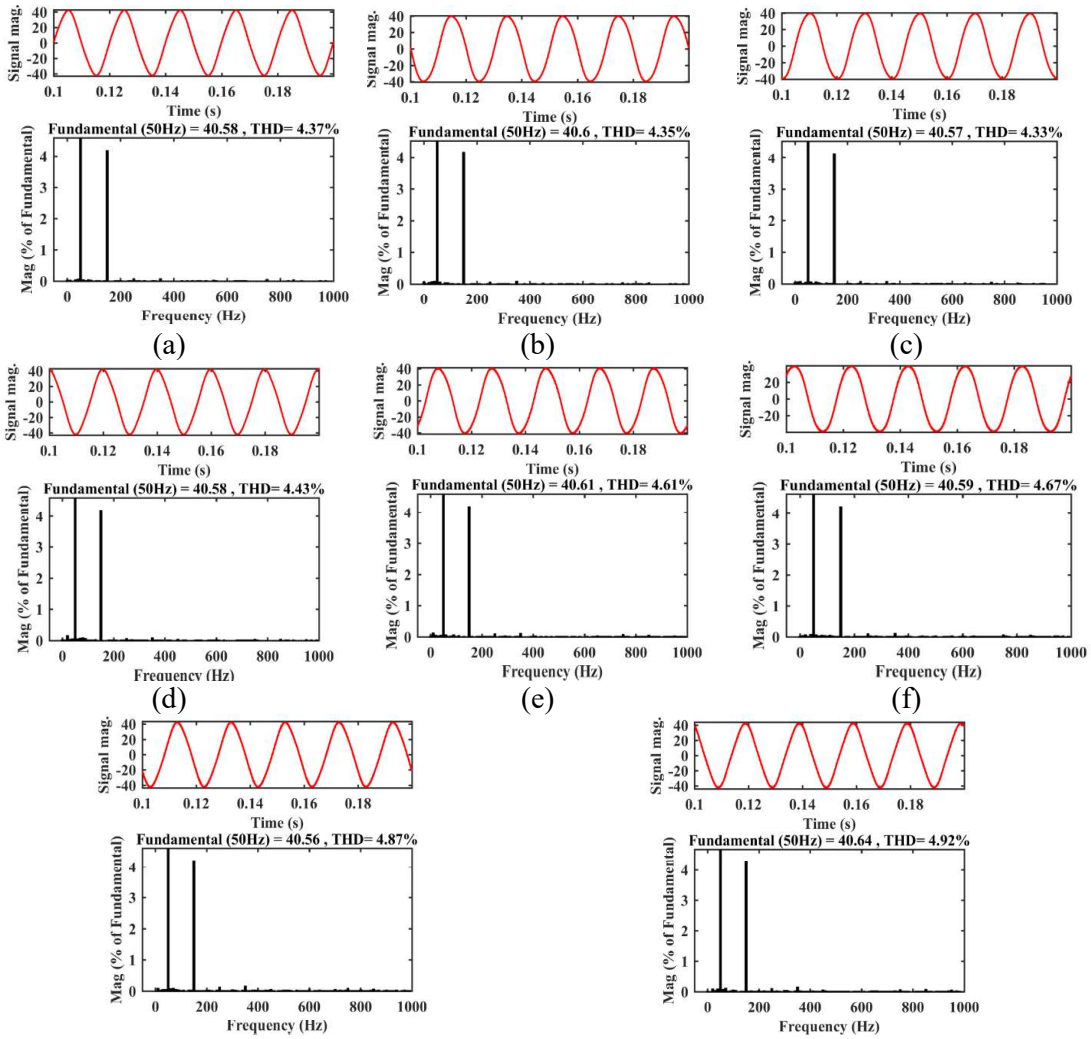

Figure 5.15: *THD in grid current with ripple minimization technique during (a) Mode-1, (b) Mode-2, (c) Mode-3, (d) Mode-4, (e) Mode-5, (f) Mode-6, (g) Mode-7 and (h) Mode-8.*

Table 5.2 – THD in grid current during all working modes with and without ripple minimization technique.

Mode	THD (%)		Mode	THD (%)	
	Without Ripple Minimization	With Ripple Minimization		Without Ripple Minimization	With Ripple Minimization
1	1.25	4.37	5	1.26	4.61
2	1.23	4.35	6	1.57	4.67
3	1.23	4.33	7	1.53	4.87
4	1.09	4.43	8	1.35	4.92

From the THD results, it can be easily seen that the THD in grid current is increased due to the presence of third harmonic component. However, the THD in grid current after adding third harmonic component is within the permissible limit of 5%.

Moreover, the THD (%) during all working modes with and without ripple minimization technique is listed in Table 5.2.

5.8 Experimental Results

A scaled hardware prototype of battery charger is also designed to validate the proposed control approach as shown in Fig. 2.11. For this purpose, two Semikron *IGBT* leg (each having two *IGBT* with antiparallel diode) converter is used and eight 12 V, 7Ahr Lead acid batteries are connected in series to make a 96 V battery pack. The experimental setup parameters are listed in Table A.4. The experimental study has been carried out in real time using *dSPACE 1104*.

The performance of the charger controller is tested as per the scenario listed in Table A.8 and the results are shown in Fig. 5.16. The experimental results have been presented in compliance of simulation results, where the maximum KVA is limited to 350. The on-board charger initially supplies the active power to battery only as shown in Fig. 5.16 (a) in mode-1 without any reactive power support and accordingly, the current is in phase with voltage. After some time, the charger is controlled to supply the battery power back to grid in mode-2 and now the current is exactly out of phase with leads the voltage as shown in Fig. 5.16 (b).

In mode-3 and 4 only the exchange of reactive power takes place without any active power support as shown in Fig. 5.16 (c) and (d). During the transition from mode-3 to 4 the current changes from 90° lagging to leading and accordingly, the battery current is almost constant zero during this transition. Later, the exchange of both active and reactive power is tested simultaneously. During mode-5, 300 W of active power is supplied from the grid side while compensating 180 VAR of inductive reactive power as shown in Fig. 5.16 (d) and (e) and during mode-6, 250 W of active power is supplied to battery pack while compensating the 245 VAR of capacitive reactive power as shown in Fig. 5.16 (e) and (f). The mode-7 and 8 are associated with discharging of battery pack while compensating of reactive power. During mode-7, 200 W of active power is taken from battery pack while compensating 287 VAR of inductive reactive power as shown in Fig. 5.16 (f) and (g). Similarly, 325 W of active power is taken from battery pack while compensating 130 VAR of capacitive reactive power during mode-8 as shown in Fig. 5.16 (g). The phase angle in last four modes are depends on amount of active reactive

power and power factor is listed in Table A.8. Further, the battery current depends on active power command, it is positive in case of discharging and negative in charging.

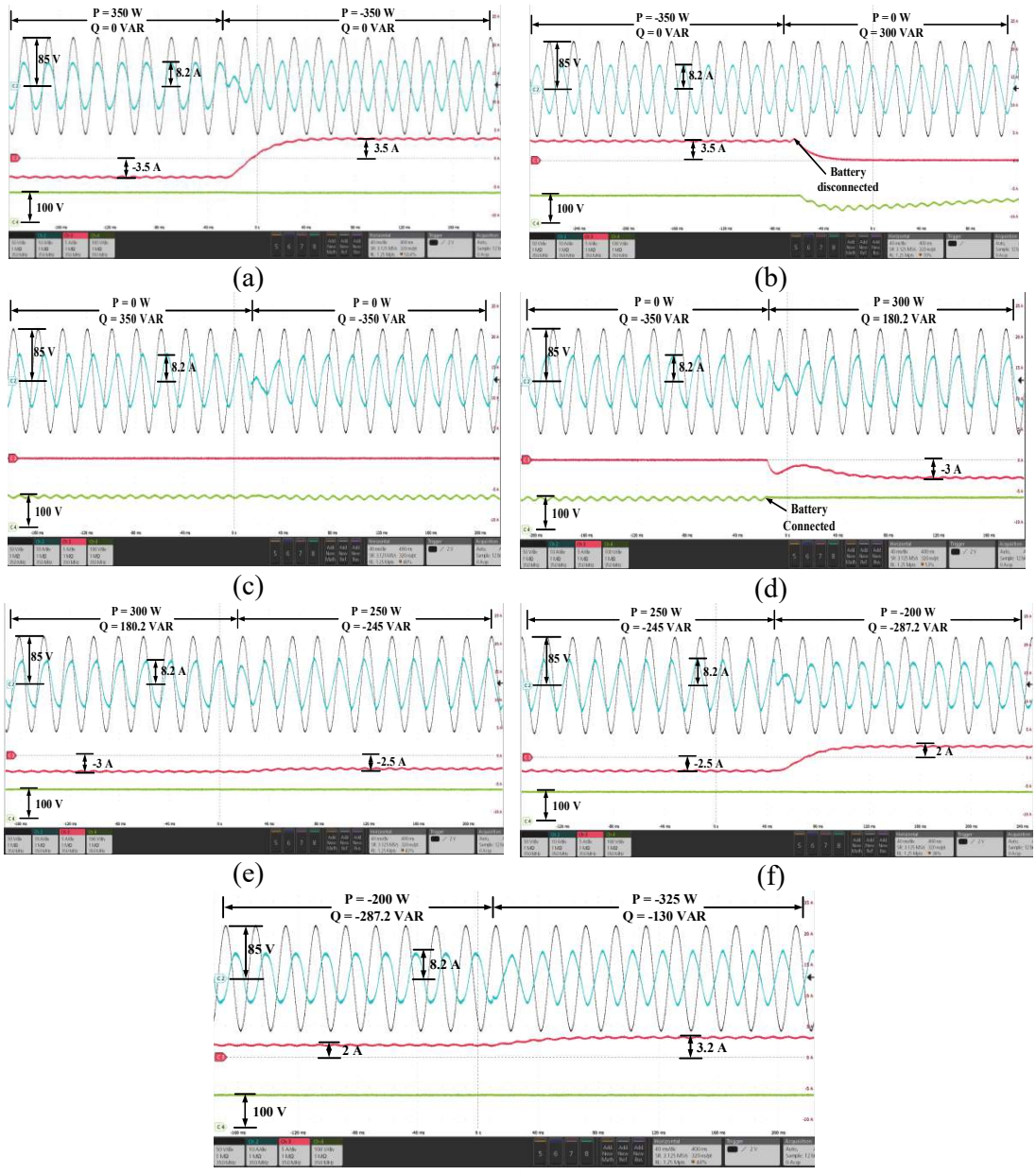

Figure 5.16: *Transition of measured grid current, voltage, battery current and voltage from (a) mode-1 to 2, (b) mode 2 to 3, (c) mode 3 to 4, (d) mode 4 to 5, (e) mode 5 to 6, (f) mode 6 to 7 and (g) mode 7 to 8.*

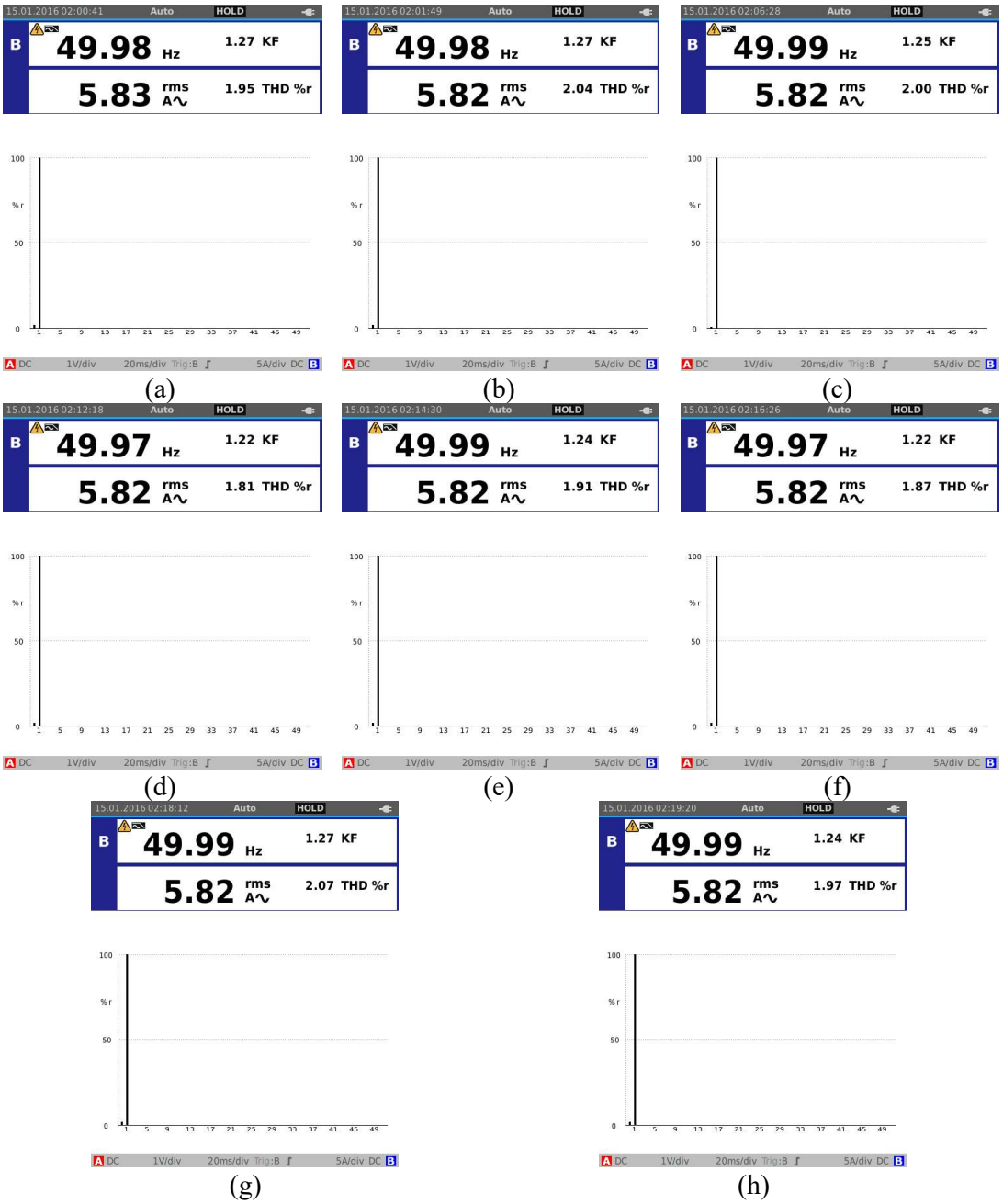

Figure 5.17: *THD in grid current without ripple minimization technique during (a) Mode-1, (b) Mode-2, (c) Mode-3, (d) Mode-4, (e) Mode-5, (f) Mode-6, (g) Mode-7 and (h) Mode-8.*

The experimental results of THD in grid current without and with ripple minimization is shown in Fig. 5.17 and 5.18 respectively. Moreover, the THD (%) during all working modes with and without ripple minimization technique is listed in Table 5.3. It is found that the THD in grid current is within the limit of 5% after using the ripple minimization technique.

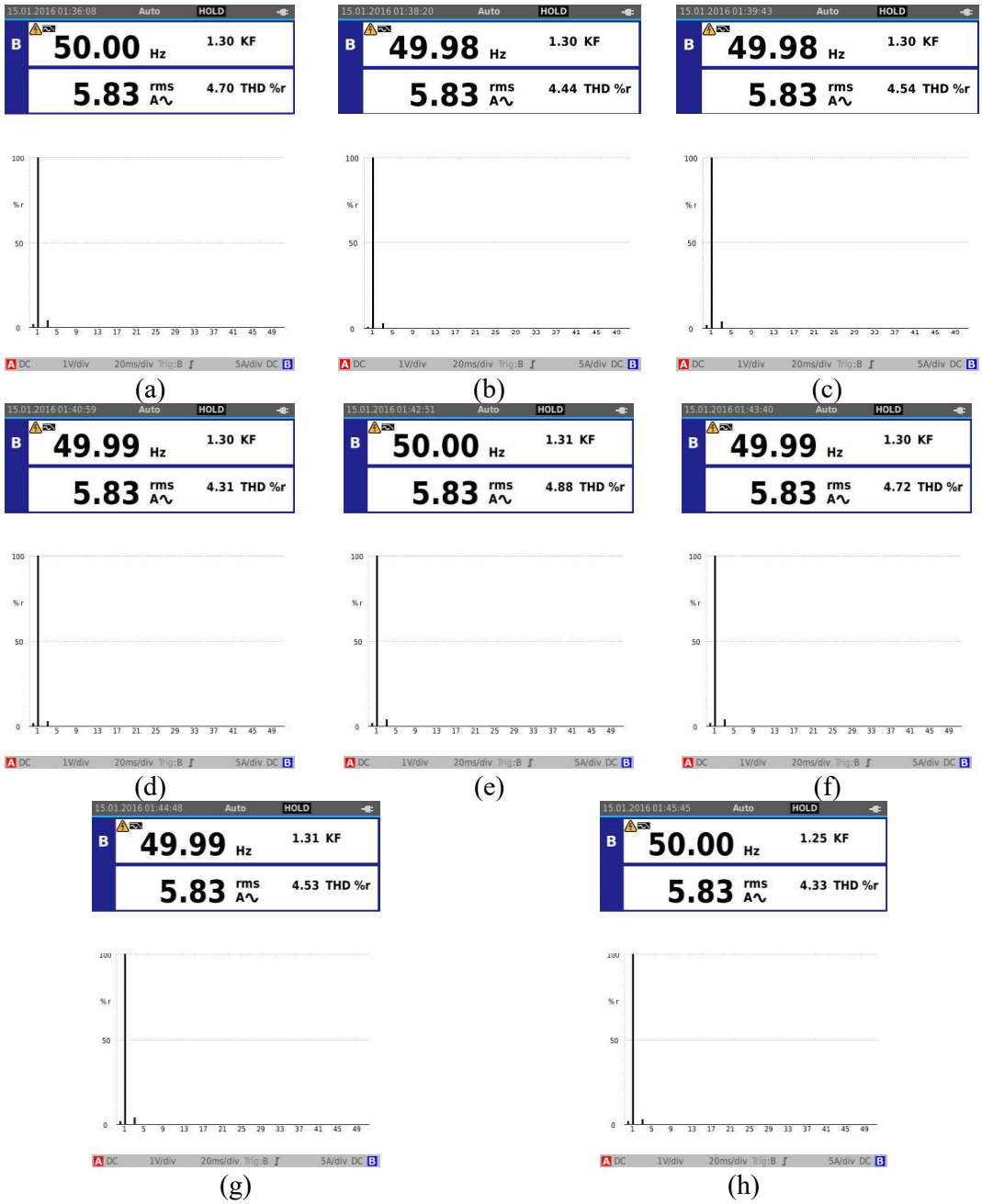

Figure 5.18: *THD in grid current with ripple minimization technique during (a) Mode-1, (b) Mode-2, (c) Mode-3, (d) Mode-4, (e) Mode-5, (f) Mode-6, (g) Mode-7 and (h) Mode-8.*

Table 5.3 – THD in grid current during all working modes with and without ripple minimization technique.

Mode	THD (%)		Mode	THD (%)	
	Without Ripple Minimization	With Ripple Minimization		Without Ripple Minimization	With Ripple Minimization
1	1.95	4.70	5	1.91	4.88
2	2.04	4.44	6	1.87	4.72
3	2.0	4.54	7	2.07	4.53
4	1.81	4.31	8	1.97	4.33

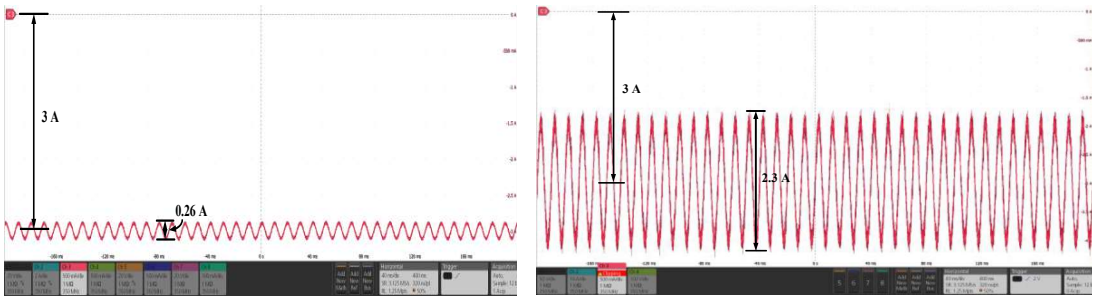

(a) (b)

Figure 5.19: *Battery Current (a) with ripple minimization technique and (b) without ripple minimization technique.*

Fig. 5.19 shows the experimental results of converter DC side current during the mode-5, where the current with ripple compensation is shown in Fig. 5.19 (a) and without compensation is shown in Fig. 5.19 (b). Here, on comparing both the results, it can be easily observed that the ripple current harmonics have been reduced to around 11%.

Moreover, the proposed control technique is compared with other ripple minimization existing techniques in Table 5.4. In proposed technique the ripple in battery current is minimized up to around 11% which is lesser than other techniques as presented in [29], [30].

TABLE 5.4- Comparison with other techniques.

#	Ref. [29]	Ref. [30]	Proposed
Ripple Reduction	12.5%	13.2%	11.6%

5.9 Conclusion

The focus of this chapter is on the controller design and implementation of single-phase single stage bidirectional on-board PEV charger. The proposed EV charger is able to operate in all four quadrants of active-reactive power plane. The proposed charger controller diminishes the second order ripple current on DC side and hence up to 11%, may be very helpful in extending the lifetime of battery which having acceptable ripple of C/10. As the tracking of grid current is difficult in *dq* frame, a RC has been designed and implemented successfully for tracking the reference current in periodic form in inner current control loop. From the control performance prospective, it has been observed that the proposed EV charger controller is fast enough in comparison to other existing controllers and takes less than three grid cycles to settle down in outer loop and less than one cycle in inner loop. Along with the fast-dynamic response it has good

steady state performance too. To confirm these facts, various cases of the step-changes in reactive power (inductive/capacitive) and active power (charging/discharging) have been presented. Furthermore, the proposed technique has drawback of increases the THD in grid current but it is within the limit of 5%. Simulation and experimental results have been presented to verify the claims. The thorough simulation study supported by experimental results has been provided to validate the claims.

CHAPTER 6

REDUCED ORDER ON-BOARD ELECTRIC VEHICLE CHARGER CONTROLLER

Chapter Outline

6.1 Introduction

This chapter deals the control design and implementation of two stage on-board EV charger. The charger is controlled to perform four quadrants operation in active-reactive (*P*-*Q*) power plane. As discussed before, the controller consists of two control loops. Therefore, in this chapter the inner control is performed in AC domain where the signals are periodic as it is difficult in *dq* frame. The proportional plus resonant (*PR*) controller is found to be very useful in tracking such type of periodic signals of fixed frequency in case of single-phase system and accordingly, it has been designed and successfully implemented for the proposed work. The *PR* is simply tuned to provide infinite gain at selected resonant frequency [132], [133]. This enables the smooth control of fast acting inner current loop with dismal steady state error. This approach also results in seamless transfer of operating modes from charging to discharging and vice-versa. Moreover, it also easily handles the dynamic rates of charging and discharging. Practically, it is impossible to implement infinite gain in hardware and the gain need to

be adjusted to certain finite value which may affect the control performance. Therefore, a modified *PR* controller is designed in which the gain is limited to some finite value.

Moreover, a reduced order plant integrated proportional integrating (*PIPI*) controller for on-board EV charger has been proposed. The proposed technique has all the functionalities of conventional *PR* controller and can track any periodic signal [134], [135]. The method is implemented in inner current control loop of first stage AC-DC converter. Since, the chapter focuses on developing a periodic reference signal tracker for first stage, therefore conventional control method based of *PI* controller is applied for second stage DC-DC converter. Furthermore, the performance of proposed EV charger controller is tested in MATLAB and validated through a 350 VA hardware prototype in eight operating modes and it is found that the proposed controller is fast and more robust than conventional *PR* control method.

Generally, the *PR* controller is utilized to track the periodic signals. They are much popular, especially in case of single-phase system and extensively available in literature [136], [137], [138]. The conventional *PR* controller may suffer from grid frequency variation, however this issue is overcome by use of quasi-*PR* (*QPR*) controller [139], [140]. In [141], a combination of notch filter and passive damping with *PR* is presented to deal with harmonics of grid voltage. In [142], multiple *PR* controllers are implemented for single phase converter control to reject the harmonics, however the use of multiple *PR* controllers makes it complex and difficult to tune. Moreover, the practical implementation of *PR* controller, especially while using fixed point arithmetic and at low frequency rate is not robust [143], [144]. A conventional *PR* compensator requires supplementary integrator to reject the DC offset. This will increase the complete controller order and makes it a third order controller because *PR* alone is a second order and integrator is first order controller [145]. Therefore, in proposed work a reduced order integrated controller-plant dynamic (ICPD) based plant integrated proportional integrating (*PIPI*) controller is designed to track the reference periodic signal for an EV charger. The *PIPI* controller has ability to accomplish all the purposes of conventional *PR* controller with reduced order. The proposed approach resolved the issues that arise during practical implementation of conventional *PR* controller and offers robust performance.

6.2 Control of Two-Stage On-Board EV Charger

The topology of on-board EV charger is shown in Fig. 2.9 and control architecture is shown in Fig. 6.1. The proposed charger controller has two control loops: outer one is for active (P)/reactive (Q) power control and inner one is for grid current control. Since, the P and Q are constant in nature, they can be regulated by PI controller. The outer loop generates reference for inner current loop and in present case it is periodic in nature. The reference current is compared with actual grid current and pulses for AC-DC converter is generated by PWM technique.

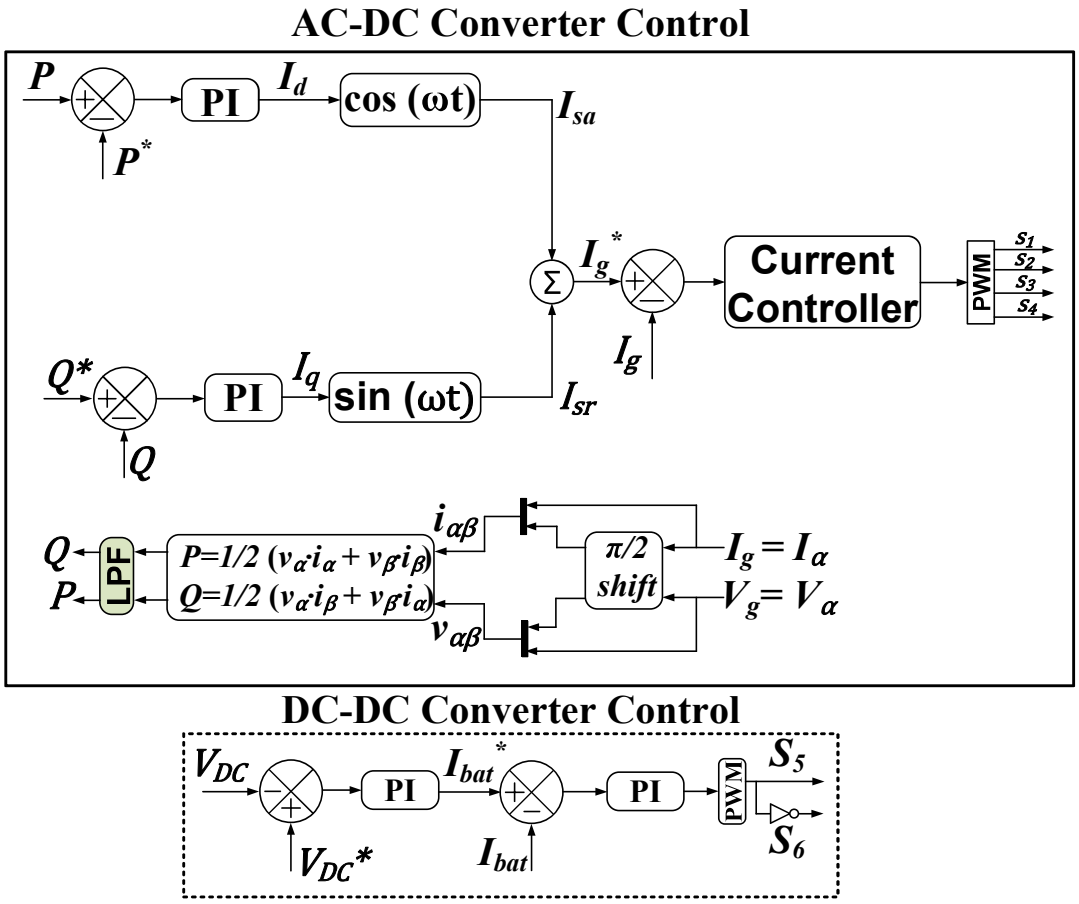

Figure 6.1: *ON board EV charger controller.*

To calculate active/reactive power, first β component is generated by applying quarter delay in actual signal. The measured active (P) and reactive (Q) power are as follows,

$$P = \frac{1}{2}\left(v_\alpha \cdot i_\alpha + v_\beta \cdot i_\beta\right) \tag{6.1}$$

$$Q = \frac{1}{2}\left(v_\alpha \cdot i_\beta + v_\beta \cdot i_\alpha\right) \tag{6.2}$$

To produce the reference grid current for inner control loop, first active and reactive component of current may be calculated as,

$$I_d = K_{p20}(P^* - P) + K_{i20}\int (P^* - P)\, dt \tag{6.3}$$

Similarly, the reactive current component may be determined as

$$I_q = K_{p21}(Q^* - Q) + K_{i21}\int (Q^* - Q)\, dt \tag{6.4}$$

Furthermore, the instantaneous value of active current component is,

$$I_{sa} = I_d \cdot \cos \omega t = \left[K_{p20}(P^* - P) + K_{i20}\int (P^* - P)\, dt\right] \cdot \cos \omega t \tag{6.5}$$

Similarly, the instantaneous value of reactive current component is,

$$I_{sr} = I_q \cdot \sin \omega t = \left[K_{p21}(Q^* - Q) + K_{i21}\int (Q^* - Q)\, dt\right] \cdot \sin \omega t \tag{6.6}$$

Further, reference current is generated by adding both active and modified reactive current component.

$$I_g^* = I_{sa} + I_{sr} \tag{6.7}$$

The values of *PI* controllers' gains are listed in Table 6.1.

Table 6.1 – Controllers Gains of AC-DC Controller.

PARAMETER	SYMBOL	VALUE
Proportional constant of active power control loop	K_{p20}	5.47
Integral constant of active power control loop	K_{i20}	2.35
Proportional constant of reactive power control loop	K_{p21}	1.84
Integral constant of reactive power control loop	K_{i21}	3.43

6.3 Design of Proportional Resonant Current Controller

The primary objective of proposed work is to evolve a versatile current control for EV charger [146]. For better understanding, the proposed system is presented in Fig. 5.7. Here, R_f, L_f and C_f are filtering resistance, inductance and capacitance, respectively. The grid may act as a source or load depending on charger operating mode (i.e., G2V or V2G).

The equivalent inner current control for proposed controller is depicted in Fig. 6.2. Since, the reference current signal is periodic in nature and accordingly a modified *PR* controller is employed to track the reference current signal.

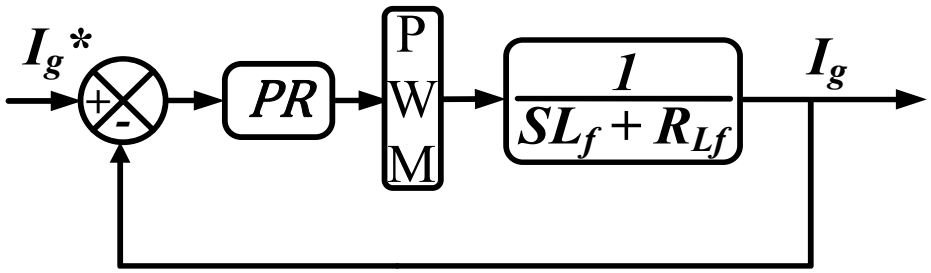

Figure 6.2: *Inner Current Control Loop.*

The transfer function of the ideal *PR* controller in continuous time domain is given in equation (6.8).

$$G_c(S) = K_p + \frac{2K_R S}{S^2 + \omega^2} \tag{6.8}$$

Where, K_p and K_R are the gains of *PR* controller with ω being the angular frequency. The transfer function of PWM in continuous time domain is given in equation (6.9).

$$G_{PWM}(S) = \frac{K_{PWM}}{1.5T_s S + 1} \tag{6.9}$$

Where, K_{PWM} is corresponding PWM gain and T_s is switching time period.

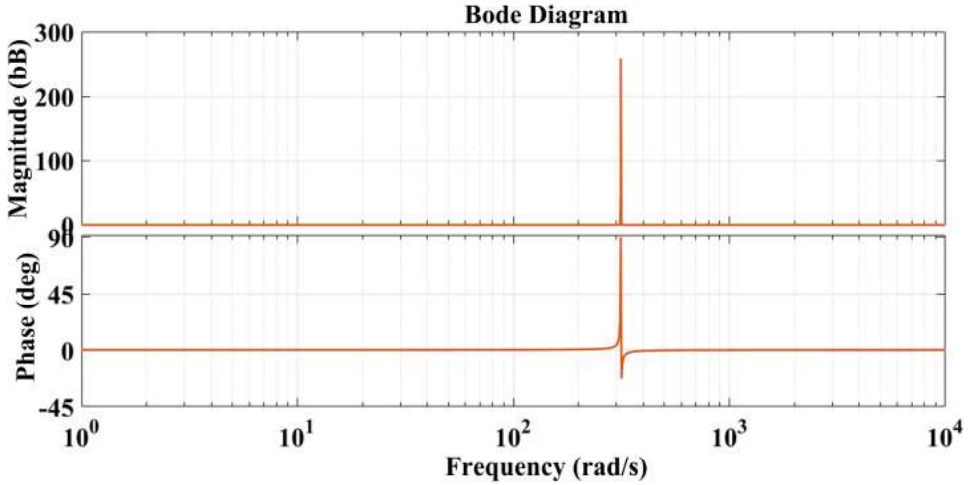

Figure 6.3: *Bode plot of ideal PR controller.*

Fig. 6.3 shows the frequency response of ideal *PR* controller $G_c(S)$ when $K_p = 1$, $K_R = 1$ and $\omega_c = 314$ rad/sec. From the Fig. 5, it can be observed that the gain value of ideal PR controller is infinite at fundamental frequency (ω).

The transfer function between error signal (E) and reference current signal (I_s^*) of inner current closed loop control system is given by,

$$\frac{E(S)}{I_s^*(S)} = \frac{1}{1 + G(S) \cdot H(S)} \tag{6.10}$$

Where, $H(S)$=1 as given closed loop system is unity feedback system and $G(S)=G_c(S) \cdot G_{PWM}(S) \cdot G_{PLANT}(S)$.

$$\frac{E(S)}{I_s^*(S)} = \frac{X(S)}{K_{PWM}\left(K_p S^2 + 2K_R S + K_p \omega^2\right) + X(S)} \tag{6.11}$$

Where, $X(S)= (S^2 + \omega^2)(1.5T_s S + 1)(L_f + R_f)$

If the reference input signal is $\frac{A\omega}{(S^2+\omega^2)}$, then the error signal is,

$$E(S = \frac{A\omega(1.5T_s S + 1)\left(L_f + R_f\right)}{K_{PWM}\left(K_p S^2 + 2K_R S + K_p \omega^2\right) + X(S)} \tag{6.12}$$

According to final value theorem, the steady state value of the error signal is,

$$\lim e(t) = \lim S \cdot E(S) = 0 \tag{6.13}$$

In ideal *PR* controller, the steady state value of error is zero but the gain at the resonance frequency is infinite. Practically, it cannot be possible to attain infinite gain at resonance frequency. Moreover, the infinite gain will fall quickly and may compromise the system stability. Due to the quick fall, it is difficult to track the fluctuations in frequency and voltage of grid [26]. Therefore, for cases modified *PR* controller would be utilized, whose transfer function in given in equation (6.15).

$$G_{mc}(S) = K_p + \frac{2K_R(\omega_c S + \omega_c^2)}{S^2 + 2\omega_c S + (\omega_c S + \omega_c^2)} \tag{6.14}$$

$$G_{mc}(S) \approx K_p + \frac{2K_R \omega_c S}{S^2 + 2\omega_c S + \omega^2} \tag{6.15}$$

The transfer function of modified *PR* controller has a frequency parameter (ω_c) in denominator, which is responsible to modify the magnitude and bandwidth at fundamental frequency. The proportional gain factor K_p is responsible for determining the value of gain margin (*GM*), phase margin (*PM*) and transient performance of the controller. Whereas, resonant gain factor K_R adjust the controller's gain at resonance frequency. The resonant bandwidth is determined by cut off frequency (ω_c). in general,

the value of ω_c is smaller i.e., between 5 to 15 rad/sec [31]. The frequency response of practical PR controller is presented in Fig. 6.4.

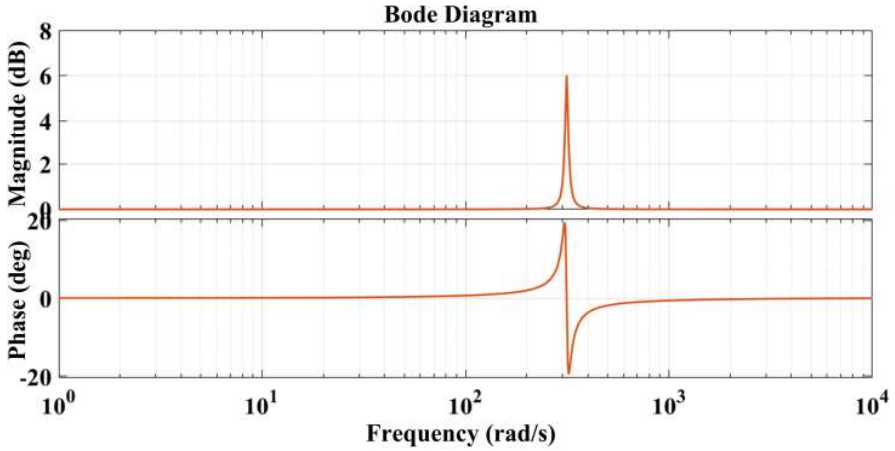

Figure 6.4: *Bode plot of modified PR controller.*

6.4 Design of *PIPI* Current Controller

In conventional inner control loop, the periodic reference current signal of AC-DC converter is tracked by *PR* controller as shown in Fig. 6.2. However, sometimes it requires additional integral controller to eliminate the DC offset as shown in Fig. 6.5. The transfer function of PR controller is $K_p + \frac{2K_r\omega_c S}{S^2+2\omega_c S+\omega^2}$, which is a second order transfer function and integrator is single order transfer function i.e., K_i/S. Where, K_p, K_r and K_i are gains of controller. Moreover, it consists of internal virtual resistance (R) or damper loop and feed-forward term V_g, which is used for soft start and initial synchronism.

The proposed *PIPI* controller is shown in Fig. 6.6. It contains a combination of proportional (P) and *PI* controller. The P controller having gain K where proportional and integral constant of *PI* controller are K_p and K_i, respectively. The open loop transfer function from E_1 to I_g is as follows,

$$\frac{I_g(S)}{E_1(S)} = K\frac{K_pS + K_i}{L_sS^2 + (K_p + R)S + K_i} \tag{6.16}$$

By choosing the K_p = -R and $K_i = L_s\omega^2$ we get,

$$\frac{I_g(S)}{E_1(S)} = \frac{K}{L_s}\frac{L\omega^2 - RS}{S^2 + \omega^2} \tag{6.17}$$

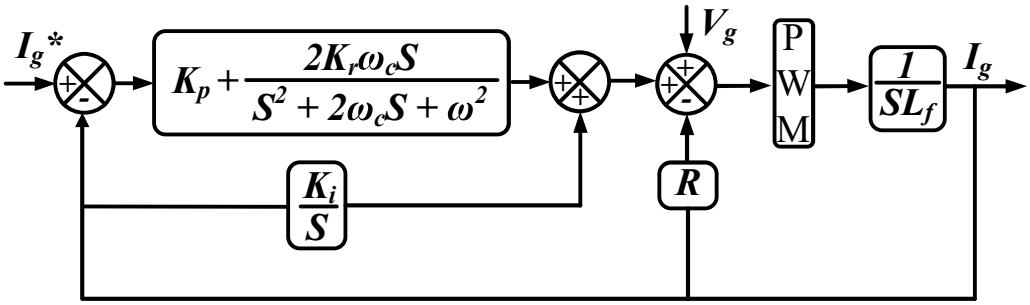

Figure 6.5: *Conventional PR controller with integrator for inner loop.*

Where, ω is grid frequency in rad/sec. The closed loop transfer function is,

$$\frac{I_g(S)}{I_g^*(S)} = \frac{K}{L_s}\frac{L_s\omega^2 - RS}{S^2 - \frac{RK}{L_s} + (1+K)\omega^2} \tag{6.18}$$

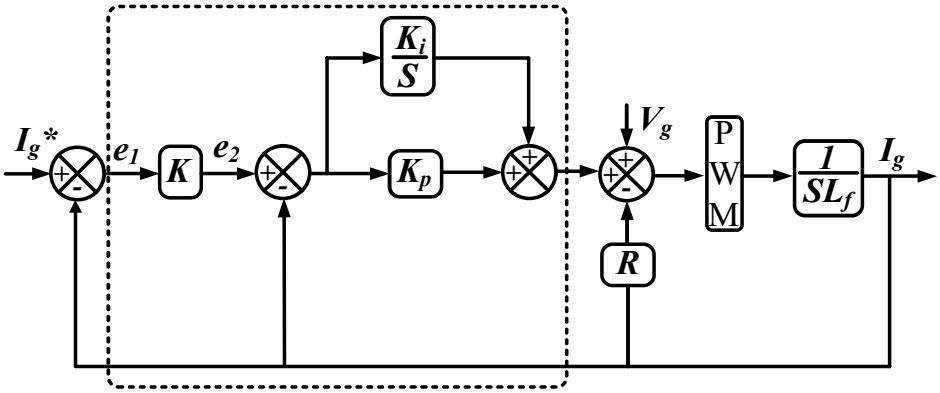

Figure 6.6: *Proposed PIPI controller.*

The stability of closed loop transfer function depends on value of *R* and *K* and their range is less and greater than zero for *R* and *K*, respectively. For this, the ω_n/ω ratio should be greater than 1, here ω_n is natural frequency. The parameters K and R are calculated by $(\omega_n/\omega)^2$*-1* and $-2\zeta L\omega_n/K$, respectively. By putting these values, the closed and open loop transfer functions are,

$$\frac{I_g(S)}{E_1(S)} = \frac{2\zeta\omega_n S + \omega_n^2 - \omega^2}{S^2 + \omega^2} \tag{6.19}$$

$$\frac{I_g(S)}{I_g^*(S)} = \frac{2\zeta\omega_n S + \omega_n^2 - \omega^2}{S^2 + 2\zeta\omega_n S + \omega_n^2} \tag{6.20}$$

In present case, $\omega_n/\omega = \sqrt{2}$ and ζ = 0.45 leads to R = -1.27$L_s\omega$ and K = 1. For 50 Hz system frequency, the locations of closed loop poles are -200 ± *j*397 and zero is -247. From the frequency response shown in Fig. 6.7, the phase margin is 131° at crossover frequency 544 rad/sec.

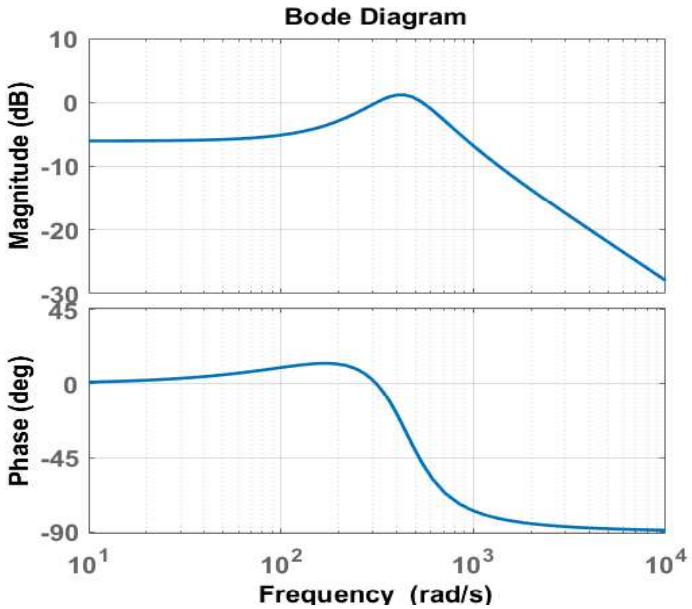

Figure 6.7: *Frequency response of closed loop transfer function.*

From the analysis, it can be seen that the proposed controller can track periodic reference signal. This is achieved due to the existence of frequency dependent $S^2 + \omega^2$ term in denominator of equation (6.18). At fundamental frequency i.e., $S = j\omega_n$, the closed loop transfer function of equation (6.20) tends to unity. This shows that the second order integrator term guarantees help to attain zero steady state error. Moreover, there is no DC offset in output current because if any DC current (i_d) flows through inductor, then the steady state error will be ($-i_d$) and $e_2 = (K + 1)\cdot(-i_d)$. This is contradictory because the input of *PI* controller cannot have a DC term. Therefore, the proposed controller can track periodic reference signal without any DC offset while having the order of first.

Control of DC-DC converter

The second stage controller is utilized to regulate active power (P) and battery current (I_{bat}). This also contains two control loops in which outer one is for active power control and inner one for battery current. Both the quantities are regulated by regular *PI* controller and pulses are generated by well-known pulse width modulation technique.

$$i_{bat}^{*} = \left(K_{p22} + \frac{K_{i22}}{s}\right)(P^{*} - P) \tag{6.21}$$

$$d = \left(K_{p23} + \frac{K_{i23}}{s}\right)(i_{bat}^{*} - i_{bat}) \tag{6.22}$$

The values of *PI* controllers gain are listed in Table 6.2.

Table 6.2 – Controllers Gains of DC-DC Controller.

PARAMETER	SYMBOL	VALUE
Proportional constant of active power control loop	K_{p22}	3.54
Integral constant of active power control loop	K_{i22}	17.64
Proportional constant of reactive power control loop	K_{p23}	25
Integral constant of reactive power control loop	K_{i23}	6.4

6.5 Simulation Results

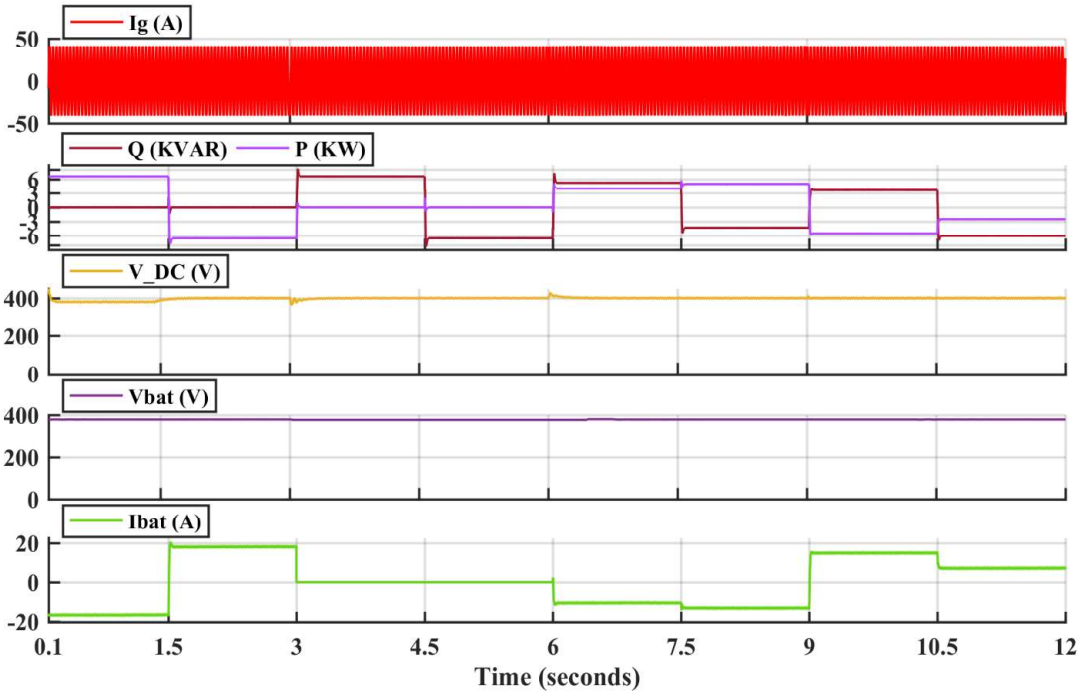

Figure 6.8: *Simulation results of grid current (I_g), active (P)-reactive (Q) power, DC link voltage (V_{DC}), battery voltage (V_{bat}) and battery current (I_{bat}) during all modes.*

A 6.6 KVA on-board EV charger as shown in Fig. 2.9 and its proposed controller has been simulated in MATLAB environment. Table A.6 listed all the simulation parameters, here input voltage of first stage AC-DC converter is 230 V and DC-link voltage is regulated at 400 V. The battery pack nominal voltage is taken as 350 V and its SOC is 50%. The battery pack voltage may be higher than nominal voltage and it is depends on SOC.

To verify the performance of proposed EV charger controller, a simulation scenario having eight operating modes has been created as listed in Table A.8. These modes are associated with active-reactive power operations, where positive active power means battery is charging from grid. Each mode is simulated for 1.5 seconds in which positive reactive power means compensation of inductive reactive power and negative

for capacitive reactive power. For optimal utilization of EV charger, it is suggested to utilize complete charger's rating. During first two modes, battery is charging without any compensation of reactive power. Similarly, charger is compensating inductive reactive

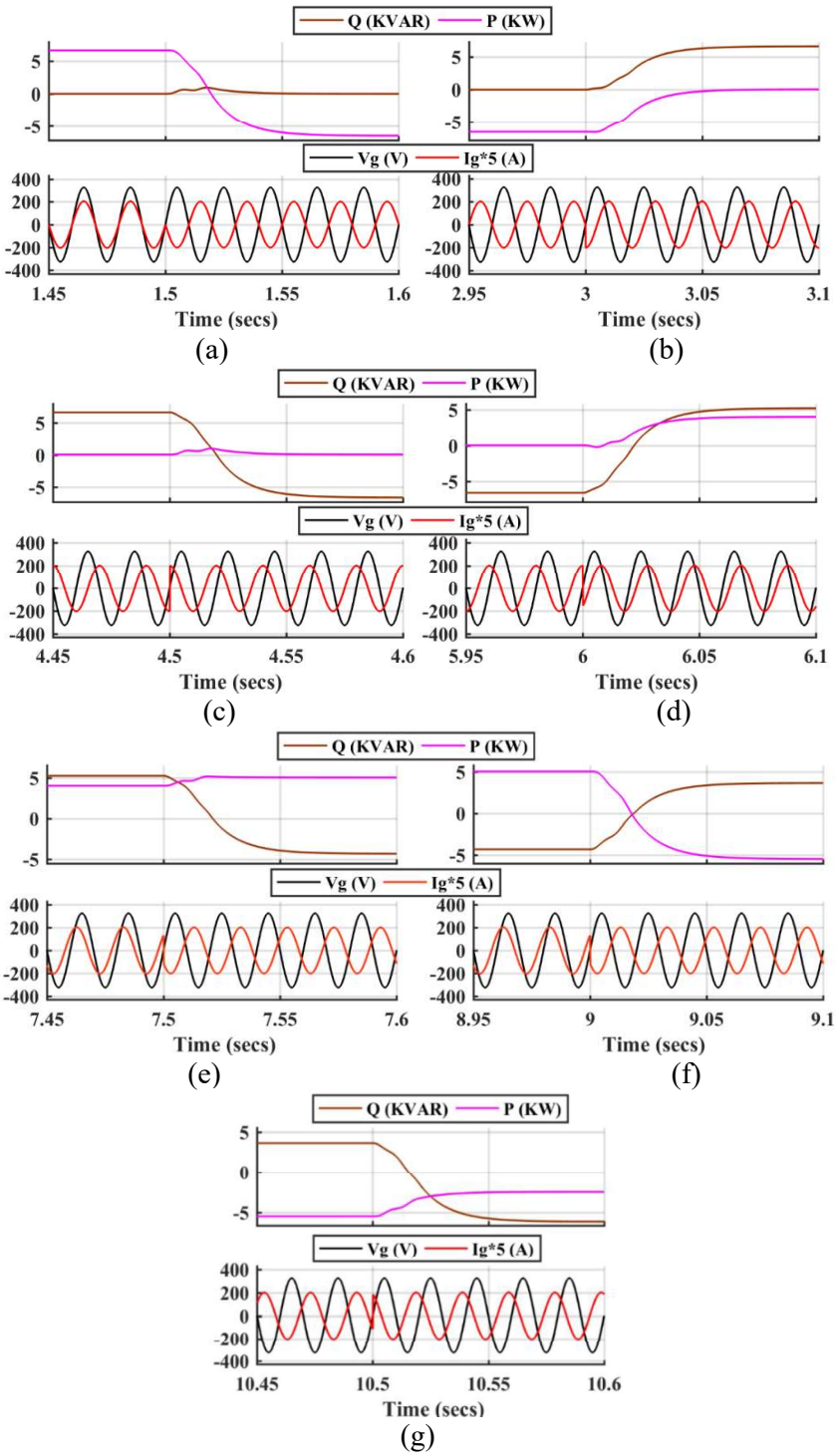

Figure 6.9: *Transition from (a) Mode 1-2, (b) Mode 2-3, (c) Mode 3-4, (d) Mode 4-5, (e) Mode 5-6, (f) Mode 6-7, (g) Mode 7-8.*

power without charging battery pack in mode-3 and 4. These are cases of fully charged battery pack and charger can compensate reactive power if requested by grid within its limit. The rest four modes are associated with both active as well as reactive power operation simultaneously. During these modes, battery is charging/discharging at slower rate and rest of charger's capacity can be used for reactive power compensation.

Fig. 6.8 Shows the Simulation results of grid current (I_g), active (P)-reactive (Q) power, DC link voltage (V_{DC}), battery voltage (V_{bat}) and battery current (I_{bat}) during all modes. Since, EV charger is operating at constant power in all modes, the grid is constant i.e., 6600/230 = 29 A (rms). The DC-link voltage is maintained at 400 V and battery voltage is around 380 V. The battery current varies according to active power command and it is negative during charging and zero in case of mode-3 and 4. Fig. 6.9 shows the transition from one mode to another. Since, only battery charging operation has been performed in mode-1, the grid current is exactly in phase with voltage. Similarly, in mode-3 and 4, grid current is lagging and leading the voltage by 90° due to inductive and capacitive reactive power operation respectively.

Fig. 6.10 shows the performance of proposed *PIPI* inner loop current controller conventional PR controller during the transition from mode 5 to 6. It is observed that the proposed controller is much faster and more robust than conventional method.

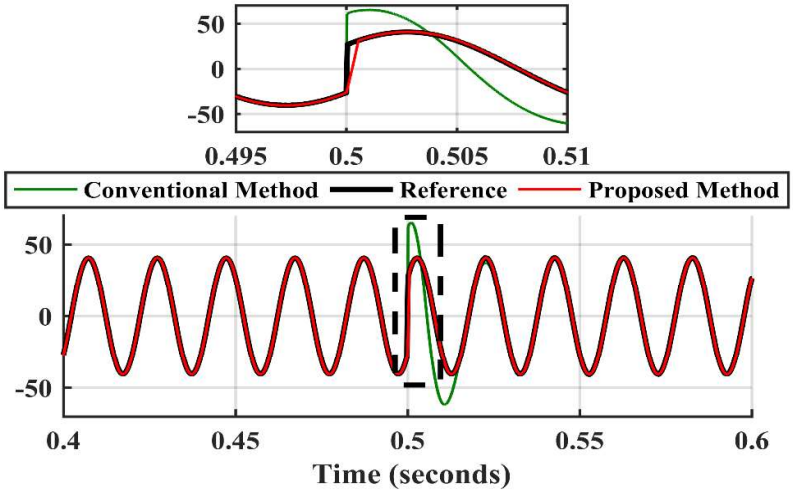

Figure 6.10: *Comparison between proposed and conventional method.*

6.6 Experimental Results

Fig. 2.11 shows the laboratory 500 VA experimental setup using dSPACE 1104 and its parameters are listed in Table A.4. Both the converters are made up from

semikron insulated gate bipolar transistor (IGBT) legs. A battery pack of 96 V is connected across the DC-DC converter. To validate the performance of proposed controller in real time, a scenario same as simulation has been developed as listed in Table A.8.

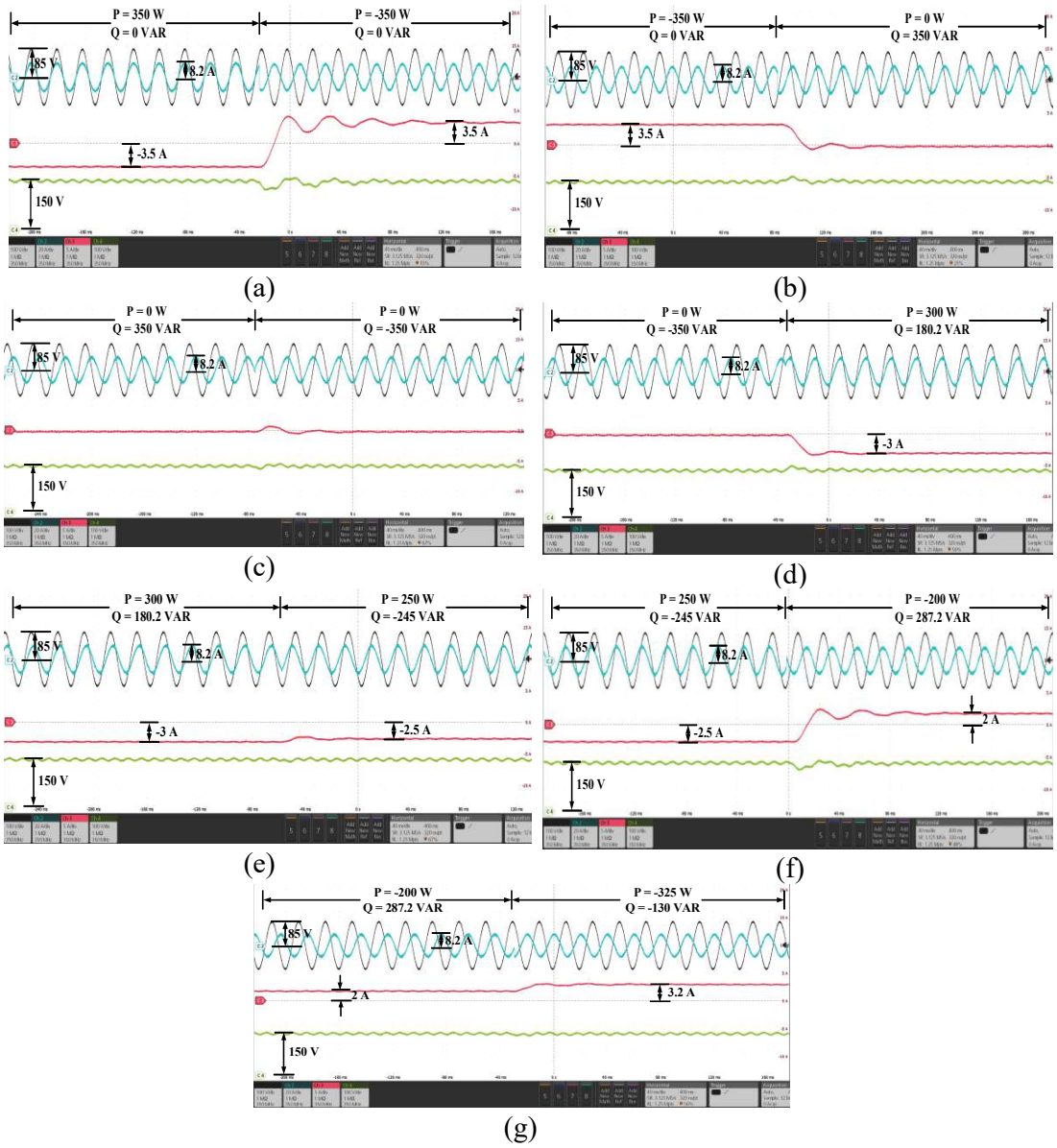

Figure 6.11: *Transition from (a) Mode 1-2, (b) Mode 2-3, (c) Mode 3-4, (d) Mode 4-5, (e) Mode 5-6, (f) Mode 6-7, (g) Mode 7-8.*

The transient and steady state performance of controller is shown in Fig. 6.11. The Fig. 6.11 (a) is associated with transition from mode 1-2. It can be seen that the voltage and current are in same phase during mode 1 and battery current is approximately -3.5 amps. In mode 2, battery is discharging with same amount of active power, thereby the battery discharging current is same as charging current of mode-1. In

Fig. 6.11 (b) transition from mode 2-3 has been shown, here both active and reactive operation is performed in mode 2 and 3 respectively. Fig. 6.11 (c) shows the transition from inductive reactive power to capacitive reactive power. During this transition, the grid current changes from lagging to leading by 90°. Since only reactive operation has been performed in mode 3 and 4, therefore battery current is zero. Fig. 6.11 (d) shows the transition from mode 4 to 5, during mode 5 the active power transferred to battery is 300 W and inductive reactive power compensation is 180.2 VA. Accordingly, the battery current is approximately 3 Amps and phase angle between voltage and current is 31° lagging. Similarly, 45° leading phase angle can be seen during mode 6 because of the compensation of capacitive reactive power as shown in Fig. 6.11 (e). The battery current is -3 Amps and -2.5 Amps during mode 5 and 6 respectively. Fig. 6.11 (f) shows the transition from charging to discharging of battery while compensation of reactive power. Accordingly, the battery current changes from -2.5 Amps to 2 Amps and phase angle changes from 45° leading to 125° lagging. In the last mode, charger supplies 325 W of battery energy to grid while compensating 130 VAR of capacitive reactive power as shown in Fig. 6.11 (g). During this the grid current is leading by 158° with grid voltage. Moreover, from the transitions it can be seen that the DC-link voltage is maintained at 150 V during all the modes and transition does not affect it too much.

Fig. 6.12 shows the performance of proposed *PIPI* inner loop current controller conventional PR controller during the transition from mode 5 to 6. It is observed that the proposed controller is much faster and more robust than conventional method in real time also.

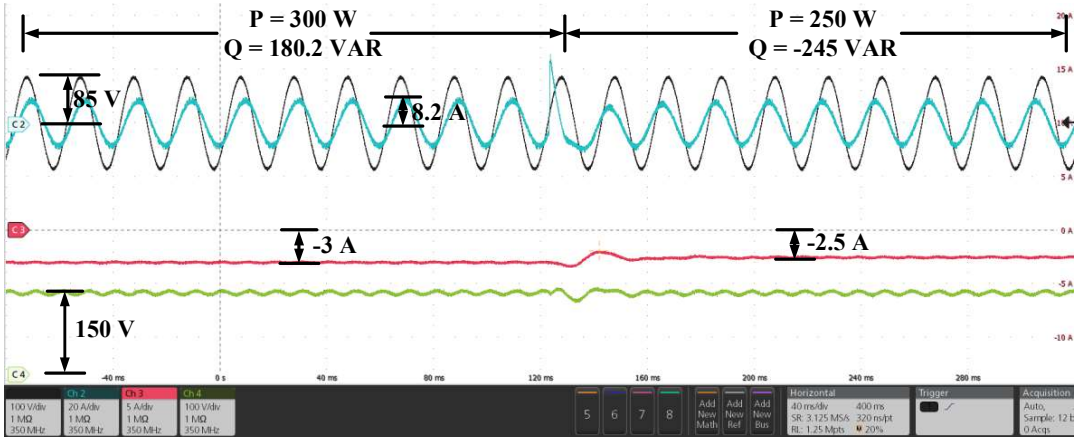

Figure 6.12: *Transition from mode 5-6 with conventional PR.*

6.7 Conclusion

This chapter presents the inner current control loop design for a two-stage single-phase on-board EV charger. The performance of the EV charger is evaluated with its ability to work under all the four quadrants of the *P–Q*-plane. In this chapter, two controllers are designed i.e., *PR* and *PIPI*. Both the controllers are able to track the periodic signal. However, the implementation of idea *PR* controller is very difficult, therefore some modification has been done to implement it in real time. Moreover, a reduced order *PIPI* controller which has the functionalities of *PR* controller is proposed for EV charging. Here, a third order conventional *PR* controller is replaced by first order *PIPI* controller. This proposed technique has been implemented for controlling the first stage of on-board EV charger in inner loop. Furthermore, the transient and steady state performance of both on-board EV charger controllers has been tested in MATLAB and claims are verified in real time using *dSPACE* 1104. For this, a scenario having eight modes has been developed for both simulation and hardware, where results show quick and smooth response by tracking the reference grid current in inner loop and active-reactive power command in outer loop less.

CHAPTER 7

CONCLUSION & FUTURE SCOPE

7.1 Conclusion

This work focuses the development of various electric vehicle (EV) charger controller. The EV charger comprises two conversion stages i.e., AC-DC (first) and DC-DC (second). These two converters are main component of an EV charger. The EV charger is designed in such a way that it charge/discharge the battery pack as well as compensates reactive power. For this, both the converters are designed with bidirectional capability. The converters are designed by IGBT switches which have a diode in anti-parallel. The EV charger can charge the battery pack as well as take the battery power and transfer it back to grid or nearby load.

In this work, both on-board and off-board EV chargers and their controllers has been developed. The two stage EV charger requires two separate controls i.e., each for AC-DC and DC-DC conversion stage. Here, two EV charger controllers have been designed for off-board EV charger and three for on-board EV charger. The main focus of this work is to develop control algorithms for first stage AC-DC converter to mitigate various problem of EV charger. However, the generalized control approach is used for second stage DC-DC converter in all the EV charger controllers. All the EV charger controllers are designed in such a way that they can follow any active/reactive power command within the rating of EV charger.

In EV charger controller, total five quantities are regulated i.e., active/reactive power, grid side current, DC link voltage and battery current. In proposed controller, three quantities are regulated by AC-DC converter control i.e., active/reactive power and grid side current. Where rest two quantities i.e., DC link voltage and battery current are regulated by DC-DC converter control. In present case, total three references are given and rest two are generated by them. The control of AC-DC converter consists of two

loops i.e., outer and inner. The outer loop generates reference for inner control loop. In outer loop, the active/reactive power is tracked and it generates the reference of grid current for inner current control loop. Therefore, two separate regulators are required each for inner and outer control loop. Similarly, two control loop architecture is used for DC-DC converter control. Here, the DC link voltage is tracked in outer loop and it generates the reference of battery current which further tracked in inner current control loop.

The thesis comprises of total six chapters in which first chapter described the basic introduction, types and standards of EV charger. The second chapter presented working modes and experimental setup development of EV charger. For this, *dSPACE 1104* controller is used to validate the performance of EV charger controller in real time. The third chapter presented mathematical modeling of a bidirectional EV charger. In fourth chapter, two EV charger control strategies have been developed for an off-board EV charger. In first control strategy, four proportional integral (*PI*) regulators are utilized for controlling of first stage AC-DC converter and two for second stage DC-DC converter. For AC-DC converter control, two *PI* regulators are required to track active/reactive power in outer loop and two for grid current control in inner loop in *dq* frame. It is found that sometimes it is very difficult to tune four *PI* regulators simultaneously for a single controller especially for inner loop. Moreover, this type of EV charger controller requires multiple frame transformations. In second control strategy, a unified adaptive neuro-fuzzy inference system (*ANFIS*) control is used in outer loop for tracking active/reactive power and generation of reference grid current. In inner loop, a hysteresis control is utilized for tracking the grid current in periodic form. It is found that the hysteresis control gives better performance than *PI* regulator in inner loop. The implementation of hysteresis control is simple but it produces variable switching frequency. Moreover, the *ANFIS* control gives better dynamic performance than *PI* regulator in tracking of active/reactive power in outer loop. However, the *ANFIS* is very much complex in design in respect of *PI* regulator and its settling time is nearly equals to *PI* regulator in case of tracking active/reactive power in outer loop. Therefore, the *PI* regulators can be used in tracking of active/reactive power in outer loop for simplicity of control design but it is not suitable for inner current control loop.

In fifth chapter, a control strategy has been developed for a single stage on-board EV charger. This EV charger has an inherent problem of producing second order ripple

on DC side, thereby it is not preferable for battery charging purpose. To minimize this second order ripple on DC side, a control strategy has been proposed in which the reference grid current is modified by adding third harmonic component. In this, two *PI* regulators are used in outer loop for tracking active/reactive power and a simple repetitive control (*RC*) for grid current control in inner loop. It can be seen that the RC has better transient and steady state performance and it has better control in harmonic rejection. Further, the proposed control technique has been implemented in real time also and it is suitable for charging the battery which has allowable ripple limit of less than 10%. However, the proposed control technique increases THD in grid current but it is less than the allowable IEEE limit of 5%.

In sixth chapter, two control strategies have been developed for a two stage ON board EV charger. Here, proportional resonant (*PR*) and plant integrated proportional integrating (*PIPI*) regulators are used in inner loop for grid current control. Generally, a *PR* controller has an integrator in parallel to remove DC offset which makes total control a third order system. In replacement of this, a first order *PIPI* regulator has been designed which has all the functionalities of a conventional third order *PR* regulator. The proposed PIPI regulator has very fast dynamic response than conventional PR controller and simple in design for tracking periodic grid current reference in inner loop.

Table 7.1: Comparison between outer loop controllers.

Controller	Performance	Design	Remark
PI	Slow dynamic response	Simple	Can be used in outer loop as very simple in design.
ANFIS	Faster dynamic response than *PI*	Very complex	Dynamic performance is fast but approximately equals to *PI* regulator, due to the limitation of hardware *PI* can be adopted in outer loop and give similar performance.

Total five controllers have been developed for EV charging application. The *ANFIS* and *PI* controller are used for tracking active/reactive power command in outer loop. It is found that the ANFIS has better performance than PI but it is complex in design. On the other hand, five different controllers are used in inner current control loop. It is found that the tracking of grid current is simpler in periodic form. Moreover, *PIPI* regulator is found very much suitable for inner current control loop as it has faster

dynamic response and simple in design. The comparison of all controller has been listed in Table 7.1 and 7.2.

Table 7.2: Comparison between inner loop controllers.

Controller	Performance	Design	Remark
PI	Slow dynamic response	simple	Difficult to tune as inner loop is very fast, required two frame transformations.
Hysteresis	Faster dynamic response	Very Simple	Very fast dynamic response but generates variable switching frequency.
RC	Good	Complex	Better transient and steady state performance and better control in multiple harmonic rejection.
PR	Moderate	Moderate	Conventional third order PR controller has slow dynamic performance.
PIPI	Good	Simple	Fast dynamic response, simplest way to track a periodic reference signal.

7.2 Future Scope

There are four future studies that can be further investigated:

- In case of hysteresis control, some methods can be implemented which can convert the variable switching frequency into fixed switching frequency.
- In case of single stage single phase on-board EV charger, some control techniques may be implemented which reduces the THD and ripple as well, therefore it may be used for 5% allowable ripple battery pack also.
- In case of periodic reference controller, disturbance can be taken into account. As large amount of EVs is connected to grid which may create disturbance in grid parameters.
- Since, periodic controllers are sensitive to frequency variation, therefore frequency adaption technique can be included in inner current control loop.

APPENDIX

SYSTEM PARAMETERS AND OPERATING MODES

Table A.1: Simulation Parameters of OFF Board EV Charger.

PARAMETER	SYMBOL	VALUE
kVA rating of charger	S	12.5 kVA
Grid voltage (line-to-line)	V_g	415 V
Supply frequency	f	50 Hz
Line inductors	L_s	2 mH
DC link capacitor	C_{DC}	1200 μF
DC link voltage	V_{DC}	600 V
DC-DC converter inductor	L_f	2.5 mH
DC-DC converter capacitor	C_f	10 μF
Battery voltage	V_{bat}	350V

Table A.2: Simulation Parameters of ON Board EV Charger.

PARAMETER	SYMBOL	VALUE
kVA rating of charger	S	6.6 kVA
Grid voltage	V_g	230 V
Supply frequency	f	50 Hz
Line inductors	L_s	1 mH
DC link capacitor	C_{DC}	500 μF
DC link voltage	V_{DC}	400 V
DC-DC converter inductor	L_f	1.5 mH
DC-DC converter capacitor	C_f	5 μF
Battery voltage	V_{bat}	350V

Table A.3: Experimental Parameters of OFF Board EV Charger.

PARAMETER	SYMBOL	VALUE
kVA rating of charger	S	500 VA
Grid voltage (line-to-line)	V_g	70 V
Supply frequency	f	50 Hz
Line inductors	L_s	4 mH
DC link capacitor	C_{DC}	1650 μF
DC link voltage	V_{DC}	150 V
DC-DC converter inductor	L_f	6 mH
DC-DC converter capacitor	C_f	47 μF
Battery voltage	V_{bat}	100V

Table A.4: Experimental Parameters of ON Board EV Charger.

PARAMETER	SYMBOL	VALUE
kVA rating of charger	S	350 VA
Grid voltage	V_g	60 V
Supply frequency	f	50 Hz
Line inductors	L_s	2 mH
DC link capacitor	C_{DC}	1650 μF
DC link voltage	V_{DC}	150 V
DC-DC converter inductor	L_f	6 mH
DC-DC converter capacitor	C_f	47 μF
Battery voltage	V_{bat}	100V

Table A.5: Simulation Scenario of OFF Board EV Charger.

Mode	Real Power (KW)	Reactive Power (KVAR)	Apparent Power (KVA)	Power Factor	Time (sec)
1	12.5	0	12.5	Unity	0-1.5
2	-12.5	0	12.5	-1	1.5-3
3	0	12.5	12.5	0	3-4.5
4	0	-12.5	12.5	0	4.5-6
5	10	7.5	12.5	0.8 (lag)	6-7.5
6	7.5	-10	12.5	0.6 (lead)	7.5-9
7	-5.5	11.2	12.5	0.44 (lag)	9-10.5
8	-11.2	-5.5	12.5	0.89 (lead)	10.5-12

Table A.6: Simulation Scenario of ON Board EV Charger.

Mode	Real Power (KW)	Reactive Power (KVAR)	Apparent Power (KVA)	Power Factor	Time (sec)
1	6.6	0	6.6	Unity	0-1.5
2	-6.6	0	6.6	-1	1.5-3
3	0	6.6	6.6	0	3-4.5
4	0	-6.6	6.6	0	4.5-6
5	4	5.25	6.6	0.6 (lag)	6-7.5
6	5	-4.31	6.6	0.75 (lead)	7.5-9
7	-5.5	3.65	6.6	0.83 (lag)	9-10.5
8	-2.5	-6.11	6.6	0.38 (lead)	10.5-12

Table A.7: Hardware Scenario of OFF Board EV Charger.

Mode	Real Power (W)	Reactive Power (VAR)	Apparent Power (VA)	Power Factor
1	500	0	500	Unity
2	-500	0	500	-1
3	0	500	500	0
4	0	-500	500	0
5	400	300	500	0.8 (lag)
6	300	-400	500	0.6 (lead)
7	-200	458.3	500	0.44 (lag)
8	-458.3	-200	500	0.9 (lead)

Table A.8: Hardware Scenario of ON Board EV Charger.

Mode	Real Power (W)	Reactive Power (VAR)	Apparent Power (VA)	Power Factor
1	350	0	350	Unity
2	-350	0	350	-1
3	0	350	350	0
4	0	-350	350	0
5	300	180.2	350	0.85 (lag)
6	250	-245	350	0.71 (lead)
7	-200	287.2	350	0.57 (lag)
8	-325	-130	350	0.92 (lead)

LIST OF PUBLICATIONS

Journal Publications

1. **A. K. Seth** and M. Singh, “Modified Repetitive control Design for Two Stage OFF Board Electric Vehicle Charger”, in *ISA Transactions (Elsevier),* https://doi.org/10.1016/j.isatra.2021.09.015, 2021, Impact Factor 5.486.
2. **A. K. Seth** and M. Singh, “Unified adaptive neuro-fuzzy inference system control for OFF board electric vehicle charger”, in *International Journal of Electrical Power & Energy Systems (Elsevier),* vol. 130, 2021, Impact Factor 4.63.
3. **A. K. Seth** and M. Singh, "Second Order Ripple Minimization in Single Phase Single Stage On-Board PEV Charger," in *IEEE Transactions on Transportation Electrification*, vol. 7, no. 3, pp. 1186-1195, Sept. 2021, Impact Factor 5.444.
4. **A. K. Seth** and M. Singh, "Resonant controller of single-stage off-board EV charger in G2V and V2G modes," in *IET Power Electronics*, vol. 13, no. 5, pp. 1086-1092, 2020, Impact Factor 2.672.

Conference Publications

1. Sakshi Chalia, **A. K. Seth** and M. Singh, "Electric Vehicle Charging Standards in India and Safety Consideration," *8th IEEE Uttar Pradesh Section International Conference on Electrical, Electronics and Computer Engineering (UPCON 2021)*, Dehradun, India, 2021.
2. **A. K. Seth** and M. Singh, "Control of Two-Stage OFF-Board Electric Vehicle Charger," *2021 1st IEEE International Conference on Power Electronics and Energy (ICPEE)*, Bhubaneswar, India, 2021, pp. 1-6, doi: 10.1109/ICPEE50452.2021.9358732.

Book Chapter

1. **Seth A.K.**, Singh M. (2022), ”Control of On-Board Electric Vehicle Charger”. In: Dubey H.M., Pandit M., Srivastava L., Panigrahi B.K. (eds) *Artificial Intelligence and Sustainable Computing. Algorithms for Intelligent Systems*. Springer, Singapore. https://doi.org/10.1007/978-981-16-1220-6_1.

REFERENCE

[1] G. Pistoia, Electric and hybrid vehicles, Italy: Elsevier, 2010.

[2] Willamson, S.S., Rathore, A.K., Musavi, F., "Industrial electronics for electric transportation: current state-of-the-art and future challenges," *IEEE Trans. Ind. Electron,* vol. 62, no. 5, pp. 3021-3032, 2015.

[3] Chan, C.C., Bouscayrol, A, Chen, K., "Electric, hybrid, and fuel-cell vehicles: architecture and modeling," *IEEE Trans. Veh. Technol.,* vol. 59, no. 52, pp. 589-598, 2010.

[4] I. Husain, Electric and Hybrid Vehicles: Design Fundamentals, CRC Press, 2010.

[5] Un-Noor, F., Sanjeev Kumar P., Mihet-popa, L., Mollah, M.N., Hossain, E, "A comprehensive study of key electric vehicle (EV) components, technologies, challenges, impacts, and fiture direction of development," *Energies,* vol. 10, p. 1217, 2017.

[6] M. Y. Metwly, M. S. Abdel-Majeed, A. S. Abdel-Khalik, R. A. Hamdy, M. S. Hamad and S. Ahmed, "A Review of Integrated On-Board EV Battery Chargers: Advanced Topologies, Recent Developments and Optimal Selection of FSCW Slot/Pole Combination," *IEEE Access,* vol. 8, pp. 85216-85242, 2020.

[7] G. Soares dos Santos, F. José Grandinetti, R. Augusto Rocha Alves and W. de Queiróz Lamas, "Design and Simulation of an Energy Storage System with Batteries Lead Acid and Lithium-Ion for an Electric Vehicle: Battery vs. Conduction Cycle Efficiency Analysis," *IEEE Latin America Transactions,* vol. 18, no. 8, pp. 1345-1352, 2020.

[8] A. Emadi, Y. J. Lee and K. Rajashekara, "Power Electronics and Motor Drives in Electric, Hybrid Electric, and Plug-In Hybrid Electric Vehicles," *IEEE Transactions on Industrial Electronics,* vol. 55, no. 6, pp. 2237-2245, 2008.

[9] F. U. Syed, M. L. Kuang and H. Ying, "Active Damping Wheel-Torque Control System to Reduce Driveline Oscillations in a Power-Split Hybrid Electric Vehicle," *IEEE Transactions on Vehicular Technology,* vol. 58, no. 9, pp. 4769-4785, 2009.

[10] S. Shafiee, M. Fotuhi-Firuzabad and M. Rastegar, "Impacts of controlled and uncontrolled PHEV charging on distribution systems," in *9th IET International Conference on Advances in Power System Control, Operation and Management (APSCOM 2012)*, 2012.

[11] R. Jurgen, "Fuel-Cell hybrid EVs," *Electric and hybrid electric vehicles,* p. 9, 2011.

[12] S. Habib, M. M. Khan, F. Abbas, L. Sang, M. U. Shahid and H. Tang, "A Comprehensive Study of Implemented International Standards, Technical Challenges, Impacts and Prospects for Electric Vehicles," *IEEE Access,* vol. 6, pp. 13866-13890, 2018.

[13] A. Emadi, Y. J. Lee and K. Rajashekara, "Power Electronics and Motor Drives in Electric, Hybrid Electric, and Plug-In Hybrid Electric Vehicles," *IEEE Transactions on Industrial Electronics,* vol. 55, no. 6, pp. 2237-2245, 2008.

[14] F. Zhang, X. Zhang, M. Zhang and A. S. E. Edmonds, "Literature review of electric vehicle technology and its applications," in *2016 5th International Conference on Computer Science and Network Technology*, Changchun, 2016.

[15] Krein, M. Yilmaz and P. T., "Review of Battery Charger Topologies, Charging Power Levels, and Infrastructure for Plug-In Electric and Hybrid Vehicles," *IEEE Transactions on Power Electronics,* vol. 28, no. 5, pp. 2151-2169, 2013.

[16] J. G. Pinto, V. Monteiro, H. Gonçalves and J. L. Afonso, "Onboard Reconfigurable Battery Charger for Electric Vehicles With Traction-to-Auxiliary Mode," *IEEE Transactions on Vehicular Technology,* vol. 63, no. 3, pp. 1104-1116, 2014.

[17] F. K. a. S. Hattori, "Single stage AD-DC full-bridge converter for battery charger," in *IEEE International Telecommunications Energy Conference (INTELEC)*, Osaka, 2015.

[18] M. Kesler, M. C. Kisacikoglu and L. M. Tolbert, "Vehicle-to-Grid Reactive Power Operation Using Plug-In Electric Vehicle Bidirectional Offboard Charger," *IEEE Transactions on Industrial Electronics,* vol. 61, no. 12, pp. 6778-6784, 2014.

[19] C. Shi and A. Khaligh, "A Two-Stage Three-Phase Integrated Charger for Electric Vehicles With Dual Cascaded Control Strategy," *IEEE Journal of Emerging and Selected Topics in Power Electronics,* vol. 6, no. 2, pp. 898-909, 2018.

[20] V. Monteiro, J. C. Ferreira, A. A. Nogueiras Meléndez, C. Couto and J. L. Afonso, "Experimental Validation of a Novel Architecture Based on a Dual-Stage Converter for Off-Board Fast Battery Chargers of Electric Vehicles," *IEEE Transactions on Vehicular Technology,* vol. 67, no. 2, pp. 1000-1011, 2018.

[21] B. T. Vankayalapati, R. Singh and V. K. Bussa, "Two stage integrated on-board charger for EVs," in *IEEE International Conference on Industrial Technology (ICIT)*, Lyon, 2018.

[22] Z. Huang, S. Wong and C. K. Tse, "An Inductive-Power-Transfer Converter With High Efficiency Throughout Battery-Charging Process," *IEEE Transactions on Power Electronics,* vol. 34, no. 10, pp. 10245-10255, 2019.

[23] S.S. Williamson and B. Peschiera , "Review and comparison of inductive charging power electronic converter topologies for electric and plug-in hybrid electric vehicles," in *IEEE Transportation Electrification Conference and Expo (ITEC)*, Detroit, MI, 2013.

[24] M. Forouzesh, Y. P. Siwakoti, S. A. Gorji, F. Blaabjerg and B. Lehman, "Step-Up DC–DC Converters: A Comprehensive Review of Voltage-Boosting Techniques, Topologies, and Applications," *IEEE Transactions on Power Electronics,* vol. 32, no. 12, pp. 9143-9178, 2017.

[25] (Sep, 2021) BMW i3 Specifications, "[online]. Available: https://www.press.bmwgroup.com/global/article/%20attachment/T0284828EN/415571".

[26] (Sep, 2021) Jaguar I-Pace Specifications, "[online]. Available: https://www.jaguar.co.uk/Images/Jaguar-I-PACE-Specification-And-Price-Guide-1X5901910000SGBEN01P_tcm634-609065.pdf".

[27] (Sep, 2021) Nissan Leaf Specifications, "online Available: https://www.nissan.co.uk/vehicles/new-vehicles/leaf/prices-specifications.html".

[28] (Sep, 2021) Polestar 2 Specifications, " online Available: https://ev-database.org/car/1170/Polestar-2.".

[29] (Sep, 2021) MG ZS Specifications, " online Available: https://ev-database.org/car/1201/MG-ZS-EV.".

[30] (Sep, 2021) Tata Nexon Specifications, "[online]. Available: https://cars.tatamotors.com/images/nexon/brochures%20/NEXON-MCE-REVISEDBROCHURE_A4_WEB%20.pdf".

[31] (Sep, 2021) Hyundai Kona Specifications, " online Available: https://www.evspecifications.com/en/model/2dee6c".

[32] (Sep, 2021) Toyota Prius Specifications, " online Available: https://www.toyota.com/prius/".

[33] (Sep, 2021) Honda e Specifications. , " online Available: https://electrek.co/2019/06/13/honda-e-battery-platform/.".

[34] (Sep, 2021) Audi eTron Specifications, " online Available: https://www.audi-mediacenter.com/en/audi-e-tron-75".

[35] (Sep, 2021) Mercedes-Benz B-Class Specifications, "[online]. Available: http://www.roperld.com/Science/%20MercedesBClassED.htm".

[36] (Sep, 2021) Ford Focus-Electric Specifications, " [online]. Available: https://ev-database.org/car/1010/Ford-Focus-Electric".

[37] (Sep, 2021) Kia Niro Specifications, "online Available: https://www.kia.com/us/en/niro-ev.".

[38] (Sep, 2021) Renault Zoe Specifications, "online Available: https://www.renault.co.uk/electric-vehicles/zoe.html.".

[39] (Sep, 2021) Peugeot 2008 Specifications, "online Available: https://www.peugeot.co.uk/showroom/new-2008-SUV/".

[40] (Sep, 2021) Tesla Model 3 Specifications, " online Available: https://www.tesla.com/model3.".

[41] (Sep, 2021) Chevrolet volt Specifications, "online Available: https://media.chevrolet.com/content/media/us/en%20/chevrolet/vehicles/bolt-ev/2018/_jcr_content/iconrow/textfile/file.res/2018-Chevrolet-Bolt-EV-Product%20-Guide.pdf".

[42] (Sep, 2021) Porsche Taycan Specifications., "Available Online: https://www.porsche.com/international/models%20/taycan/taycan-models/taycan-turbo/".

[43] (Sep, 2021) Volkswagen e-Golf Specifications, " online Available: https://www.volkswagen.co.uk/new/e-golf.".

[44] (Sep, 2021) Mitsubishi i-Mi Specifications, " online Available: https://en.wikipedia.org/wiki/Mitsubishi_i-MiEV".

[45] Szczepanek, C. Botsford and A., "Fast charging vs. slow charging: Pros and cons for the new age of electric vehicles," in *24th Electric Vehicle Symposium*, Stavanger, Norway, 2009.

[46] T. Anegawa, "Development of quick charging system for electric vehicle," in *Proc. World Energy Congress*, 2010.

[47] D. Aggeler, F. Canales, H. Zelaya - De La Parra, A. Coccia, N. Butcher, and O. Apeldoorn, "Ultra-fast dc-charge infrastructures for EV-mobility and future smart

grids," in *Proc. IEEE Power Energy Soc. Innovative Smart Grid Technol. Conf.*, Europe, 2010.

[48] F. Xia, H. Chen, L. Chen and X. Qin, "A Hierarchical Navigation Strategy of EV Fast Charging Based on Dynamic Scene," *IEEE Access,* vol. 7, pp. 29173-29184, 2019.

[49] Jingshan Li; Shiyu Zhou; Yehui Han, "A BAYESIAN APPROACH TO BATTERY PROGNOSTICS AND HEALTH MANAGEMENT," in *Advances in Battery Manufacturing, Service, and Management Systems*, IEEE, 2017, pp. 151-174.

[50] M. T. Lawder et al., "Battery Energy Storage System (BESS) and Battery Management System (BMS) for Grid-Scale Applications," in *Proceedings of the IEEE*, 2014.

[51] Ronald Jurgen, EV Batteries," in Electric and Hybrid-Electric Vehicles: Batteries, SAE, 2011.

[52] Gregory Plett, Battery Management Systems, Volume I: Battery Modeling, Artech, 2015.

[53] (Sep, 2021) Online available: , https://storage.googleapis.com/geotab-sandbox/ev-battery-degradation/index.html.

[54] Jingshan Li; Shiyu Zhou; Yehui Han, "IMPROVING BATTERY MANUFACTURING THROUGH QUALITY AND PRODUCTIVITY BOTTLENECK INDICATORS," in *Advances in Battery Manufacturing, Service, and Management Systems*, IEEE, 2017, pp. 29-56.

[55] M. A. Hannan, M. M. Hoque, S. E. Peng and M. N. Uddin, "Lithium-Ion Battery Charge Equalization Algorithm for Electric Vehicle Applications," *IEEE Transactions on Industry Applications,* vol. 53, no. 3, pp. 2541-2549, 2017.

[56] S. R. Ovshinsky et al., "Advanced materials for next generation NiMH portable, HEV and EV batteries," *IEEE Aerospace and Electronic Systems Magazine,* vol. 14, no. 5, pp. 17-23, 1999.

[57] X. Wei, X. Zhao and Y. Yuan, "Study of Equivalent Circuit Model for Lead-Acid Batteries in Electric Vehicle," in *International Conference on Measuring Technology and Mechatronics Automation*, Zhangjiajie, Hunan, 2009.

[58] (Sep, 2021) online available:, "https://batteryuniversity.com".

[59] Kisacikoglu, Mithat Can, Vehicle-to-grid (V2G) Reactive Power Operation Analysis of the EV/PHEV Bidirectional Battery Charger, PhD diss., University of Tennessee, 2013.

[60] J. Saikrishna Goud, Kalpana R., Kiran R., Bhim Singh, "Low Frequency Ripple Charging of LiIon Battery using Bidirectional Zeta DC-DC Converter to Improve Charge Transfer Efficiency," in *IEEE 7th International Conference on Power and Energy (PECon)*, 2018.

[61] (Sep, 2021) Online availabl):, "https://www.iec.ch/homepage.".

[62] (Sep, 2021) Online available:, " https://webstore.iec.ch/preview/info_iec62196-1%7Bed3.0%7Db.pd".

[63] M. C. Falvo, D. Sbordone, I. S. Bayram and M. Devetsikiotis, ""EV charging stations and modes: International standards," in *International Symposium on Power Electronics, Electrical Drives Automation and Motion*, Ischia, 2014.

[64] (Sep, 2021) Online available: , "https://webstore.iec.ch/preview/info_iec61980-1%7Bed1.0%7Den.pdf".

[65] (Sep, 2021) Online available :, " https://webstore.iec.ch/publication/6582".

[66] T.S. Ustun, C.R. Ozansoy, A. Zayegh, "Implementing Vehicleto-Grid (V2G) Technology with IEC 61850-7-420," *IEEE Transactions on Smart Grid,* vol. 4, no. 2, pp. 1180-1187, 2013.

[67] (Sep, 2021) Online available :, " https://www.sae.org".

[68] T. Bohn and H. Chaudhry, ""Overview of SAE standards for plug-in electric vehicle," in *IEEE PES Innovative Smart Grid Technologies (ISGT),*, Washington, DC, 2012.

[69] A. Zahedmanesh, D. Sutanto and K. M. Muttaqi, "Analyzing the impacts of charging plug-in electric vehicles in low voltage distribution networks: A case study of utilization of droop charging control system based on the SAE J1772 Standard," in *Australasian Universities Power Engineering Conference (AUPEC)*, Melbourne, 2017.

[70] S. Habib, M. M. Khan, F. Abbas, L. Sang, M. U. Shahid and H. Tang, "A Comprehensive Study of Implemented International Standards, Technical Challenges, Impacts and Prospects for Electric Vehicles," *IEEE Access,* vol. 6, pp. 13866-13890, 2018.

[71] SAE Electric Vehicle and Plug-in Hybrid Electric Vehicle Conductive Charge Coupler, " SAE Standard J1772," Jan, 2010.

[72] (Sep, 2021) Online available :, "https://www.sae.org/servlets/pressRoom?OBJECT_TYPE=PressReleases&PAGE=showRelease&RELEASE_ID=1587".

[73] "IEEE Draft Standard Technical Specifications of a DC Quick Charger for Use with Electric Vehicles," IEEE P2030.1.1/D2.0, 2015.

[74] (Sep, 2021) Online available :, "https://www.chademo.com/chademo-to-jointly-develop-next-gen-ultra-fast-charging-standard-with-china/".

[75] (Sep, 2021) Online available :, "https://www.services.bis.gov.in:8071/php/BIS/bisconnect/pow/is_details?IDS=MjMzMzI%3D".

[76] (Sep, 2021) Online available :, "https://emobility.araiindia.com/wp-content/uploads/2018/06/AIS_138_Part_2.pdf".

[77] (Sep, 2021) Online available :, "https://indiasmartgrid.org/site/admin/upload/201809Thu225447.pdf".

[78] (Sep, 2021) Online available :, " https://evreporter.com/guide-to-ev-charging-and-standards-in-india".

[79] S. Nair, N. Rao, S. Mishra and A. Patil, "India's charging infrastructure — biggest single point impediment in EV adaptation in India," in *IEEE Transportation Electrification Conference (ITEC-India)*, Pune, 2017.

[80] O. C. Onar, J. Kobayashi and A. Khaligh, "A Fully Directional Universal Power Electronic Interface for EV, HEV, and PHEV Applications," *IEEE Transactions on Power Electronics,* vol. 28, no. 12, pp. 5489-5498, 2013.

[81] G. Buja, M. Bertoluzzo and C. Fontana, "Reactive Power Compensation Capabilities of V2G-Enabled Electric Vehicles," *IEEE Transactions on Power Electronics,* vol. 32, no. 12, pp. 9447-9459, 2017.

[82] M. Y. Metwly, M. S. Abdel-Majeed, A. S. Abdel-Khalik, R. A. Hamdy, M. S. Hamad and S. Ahmed, "A Review of Integrated On-Board EV Battery Chargers: Advanced Topologies, Recent Developments and Optimal Selection of FSCW Slot/Pole Combination," *IEEE Access,* vol. 8, pp. 85216-85242, 2020.

[83] A. Narula and V. Verma, "Bi – directional trans – Z source boost converter for G2V/V2G applications," in *IEEE Transportation Electrification Conference (ITEC-India)*, Pune, 2017.

[84] M. Singh, V. Khadkikar, A. Chandra and R. K. Varma, "Grid Interconnection of Renewable Energy Sources at the Distribution Level With Power-Quality

Improvement Features," *IEEE Transactions on Power Delivery,* vol. 26, no. 1, pp. 307-315, 2011.

[85] S. Kulkarni, A. R. Thorat and I. Korachagaon, "Bidirectional converter for vehicle to grid (V2G) reactive power operation," in *International Conference on Circuit ,Power and Computing Technologies (ICCPCT)*, 2017.

[86] K. Sinjari and J. Mitra, "Electric Vehicle Charging with Reactive Power Compensation to Distribution Systems," in *IEEE Industry Applications Society Annual Meeting*, 2020.

[87] W. Choi, W. Lee and B. Sarlioglu, "Reactive power compensation of grid-connected inverter in vehicle-to-grid application to mitigate balanced grid voltage sag," in *IEEE Power and Energy Society General Meeting (PESGM)*, 2016.

[88] D. B. W. Abeywardana, P. Acuna, B. Hredzak, R. P. Aguilera,, "Single-phase boost inverter-based electric vehicle charger with integrated vehicle to grid reactive power compensation," *IEEE Trans. Power Electron.,* vol. 33, no. 4, pp. 3462-3471, 2018.

[89] B. Singh, A. Chandra, K. Al-haddad, Power Quality: Problem and Mitigation Techniques, UK: John Wiley and Sons, 2015.

[90] F. Chishti, S. Murshid and B. Singh, "Development of Wind and Solar Based AC Microgrid With Power Quality Improvement for Local Nonlinear Load Using MLMS," *IEEE Transactions on Industry Applications,* vol. 55, no. 6, pp. 7134-7145, 2019.

[91] D. W. Hart, Power Electronics, Mc Graw Hill, 2010.

[92] (Datasheet), "online available: https://www.lem.com/sites/default/files/products_datasheets/la_55-p_e.pdf".

[93] (LEM 25P Datasheet), "online available: https://www.lem.com/sites/default/files/products_datasheets/lv_25-p.pdf".

[94] (SKYPER 32 Datasheet), "Online available: https://www.semikron.com/dl/service-support/downloads/download/semikron-datasheet-skyper-32-r-l6100102/".

[95] (TLP 350 Datasheet), "Online available: https://www.glynshop.com/erp/owweb/Daten/Datenblaetter/Toshiba/TLP350_datasheet_en_20140922.pdf".

[96] Sylvain LECHAT SANJUAN, Voltage Oriented Control of Three-Phase Boost PWM Converters, CHALMERS UNIVERSITY OF TECHNOLOGY, 2010.

[97] M. Narimani and G. Moschopoulos, "Modeling and control of a single-stage three-level power factor correction AC-DC converter," in *24th Canadian Conference on Electrical and Computer Engineering(CCECE)*, 2011.

[98] Tasi-Fu Wu and Yu-Kai Chen, "Modeling PWM DC/DC converters out of basic converter units," *IEEE Transactions on Power Electronics,* vol. 13, no. 5, pp. 870-881, 1998.

[99] M. Kesler, M. C. Kisacikoglu and L. M. Tolbert, "Vehicle-to-Grid Reactive Power Operation Using Plug-In Electric Vehicle Bidirectional Offboard Charger," *IEEE Transactions on Industrial Electronics,* vol. 61, no. 12, pp. 6778-6784, 2014.

[100] A. K. Seth and M. Singh, "Control of Two-Stage OFF-Board Electric Vehicle Charger," in *1st International Conference on Power Electronics and Energy (ICPEE)*, India, 2021.

[101] Amirnaser Yazdani and Reza Iravani, Voltage-Sourced Converters in Power Systems: Modeling Control and Applications, Wiley-IEEE Press, 2010.

[102] H. Akagi, E. H. Watanabe and M. Aredes, Instantaneous Power Therory and Applications to Power Conditioning, USA: John Wiley and Sons, 2007.

[103] M. Singh, "Adaptive Network-Based Fuzzy Inference System for Sensorless Control of PMSG Based Wind Turbine with Power Quality Improvement Features," Ecole De Technologie Superieure, Montreal, 2010.

[104] A.H.R. Rosa, L.M.F. Morais, G.O. Fortes, S.I. Seleme Júnior. , "Practical considerations of nonlinear control techniques applied to static power converters: A survey and comparative study," *International Journal of Electrical Power & Energy Systems,* vol. 127, 2021.

[105] J.-S. R. Jang. , "ANFIS: Adaptive-network-based fuzzy inference system," *IEEE Trans. Syst. Man, Cybern.,* vol. 23, no. 3, pp. 665-685, 1993.

[106] M. Singh and A. Chandra. , "Application of Adaptive Network-Based Fuzzy Inference System for Sensorless Control of PMSG-Based Wind Turbine With Nonlinear-Load-Compensation Capabilities," *IEEE Transactions on Power Electronics,* vol. 26, no. 1, pp. 165-175, 2011.

[107] Nitin Kumar Saxena, Ashwani Kumar. , "Reactive power control in decentralized hybrid power system with STATCOM using GA, ANN and ANFIS methods," *International Journal of Electrical Power & Energy Systems,* vol. 83, pp. 175-187, 2016.

[108] P.K. Gayen, A. Jana. , "An ANFIS based improved control action for single phase utility or micro-grid connected battery energy storage system," *Journal of Cleaner Production,* vol. 164, pp. 1034-1049, 2017.

[109] Mossad Mohamed I, Salem Fawzan. , "LFC based adaptive PID controller using ANN and ANFIS techniques," *J Electr Syst Inform Technol,* vol. 1, 2014.

[110] J. Saroha, M. Singh and D. K. Jain. , "ANFIS-Based Add-On Controller for Unbalance Voltage Compensation in a Low-Voltage Microgrid," *IEEE Transactions on Industrial Informatics,* vol. 14, no. 12, pp. 5338-5345, 2018.

[111] N. Mohan, T.M. Undeland and W.P. Robbins, Power Electronics Converters, Applications and Design, John Wiley & Sons, 2003.

[112] A.K. Seth and M. Singh, "Unified adaptive neuro-fuzzy inference system control for OFF board electric vehicle chargerr," *International Journal of Electrical Power and Energy Systems ,* vol. 130, 2021.

[113] H. Saxena, A. Singh and J. N. Rai, "Application of Time Delay Recurrent Neural Network for Shunt Active Power Filter in 3-Phase Grid-tied PV System," in *National Power Electronics Conference (NPEC)*, Tiruchirappalli, 2019.

[114] K. P. Chou, M. Prasad, Y. Y. Lin, S. Joshi, C. T. Lin and J. Y. Chang. ,, "Takagi-Sugeno-Kang type collaborative fuzzy rule based system," in *IEEE Symposium on Computational Intelligence and Data Mining (CIDM)*, Orlando, FL, 2014.

[115] Shun-ichi Amari. , "Backpropagation and stochastic gradient descent method," *Neurocomputing,* vol. 5, no. 4-5, pp. 185-196, 1993.

[116] Rumelhart, David E. et al., "Learning internal representations by error propagation," *Computer Science, Mathematics,* 1986.

[117] A. D. Kupchinov, N. N. Smotrov and Y. P. Gusev, "The compatibility verification of batteries and battery chargers to ripples in battery float charge mode," in *IEEE Conference of Russian Young Researchers in Electrical and Electronic Engineering (EIConRus)*, 2018.

[118] A. D. Kupchinov, Y. P. Gusev and Y. V. Monakov, "Batteries current ripples in float charge mode," in *IEEE Conference of Russian Young Researchers in Electrical and Electronic Engineering (EIConRus)*, 2017.

[119] Kisacikoglu, Mithat Can, "Vehicle-to-grid (V2G) Reactive Power Operation Analysis of the EV/PHEV Bidirectional Battery Charger," PhD diss., University of Tennessee, 2013.

[120] D. B. Wickramasinghe Abeywardana, P. Acuna, B. Hredzak, R. P. Aguilera and V. G. Agelidis, "Single-Phase Boost Inverter-Based Electric Vehicle Charger With Integrated Vehicle to Grid Reactive Power Compensation," *IEEE Transactions on Power Electronics,* vol. 33, no. 4, pp. 3462-3471, 2018.

[121] Linlin Gu; Xinbo Ruan; Ming Xu; Kai Yao, "Means of Eliminating Electrolytic Capacitor in AC/DC Power Supplies for LED Lightings," *IEEE Transactions on Power Electronics,* vol. 24, no. 5, pp. 1399-1408, 2009.

[122] G. Pandove, A. Trivedi, and M. Singh, "Repetitive control-based single-phase bidirectional rectifier with enhanced performance," *IET Trans. Power Electronics,* vol. 9, no. 5, pp. 1029-1036, 2016.

[123] A. K. Seth and M. Singh, "Second-Order Ripple Minimization in Single-Phase Single-Stage Onboard PEV Charger," *IEEE Transactions on Transportation Electrification,* vol. 7, no. 3, pp. 1186-1195, 2021.

[124] A. Trivedi, and M. Singh, “, "Repetitive Controller for VSIs in Droop Based AC-Microgrid," *IEEE Trans. Power Electronics,* vol. 32, no. 8, pp. 6595-6604, 2017.

[125] Qingzeng Yan, Xiaojie Wu, X. Yuan, and Y. Geng, "An Improved Grid-Voltage Feedforward Strategy for High-Power Three-Phase Grid-Connected Inverters Based on the Simplified Repetitive Predictor," *IEEE Trans. Power Electronics,* vol. 31, no. 5, pp. 3880-3897, 2016.

[126] B. G. Sun, Y. X. Xie, H. Ma and L. Cheng, "Analysis and application of repetitive control scheme for three-phase active power filter with frequency adaptive capability," *Journal of Electrical Engineering and Technology,* vol. 11, no. 3, pp. 618-628, 2016.

[127] B. A. Francis and W. M. Wonham, "The internal model principle for linear multivariable regulators," *J. Appl. Math. Optim.,* vol. 2, pp. 170-194, 1975.

[128] R. Costa-Castello, J. Nebot and R. Grino, "Demonstration of the internal model principle by digital repetitive control of an educational laboratory plant," *IEEE Transactions on Education,* vol. 48, no. 1, pp. 73-80, 2005.

[129] S. Galeani, L. Menini and A. Potini, "Robust Trajectory Tracking for a Class of Hybrid Systems: An Internal Model Principle Approach," *EEE Transactions on Automatic Control,* vol. 57, no. 2, pp. 344-359, 2012.

[130] L. Zheng, F. Jiang, J. Song, Y. Gao and M. Tian, "A Discrete-Time Repetitive Sliding Mode Control for Voltage Source Inverters," *IEEE Journal of Emerging and Selected Topics in Power Electronics,* vol. 6, no. 3, pp. 1553-1566, 2018.

[131] G. A. Ramos, R. I. Ruget and R. Costa-Castelló, "Robust Repetitive Control of Power Inverters for Standalone Operation in DG Systems," *IEEE Transactions on Energy Conversion,* vol. 35, no. 1, pp. 237-247, 2020.

[132] R. Teodorescu, F. Blaabjerg, M. Liserre, and P. Loh, "Proportional-resonant controllers and filters for grid-connected voltage-source converters," *IEE Proc. Elect. Power Appl.,* vol. 153, no. 5, pp. 750-762, 2006.

[133] Ran Jiao, Jie Zhu, Longfei Ma, Yutong Zhao and Shuo Yang, "Dead-beat instantaneous power control for off-board charger of electric vehicle for V2G application," *International Journal of Hydrogen Energy,* vol. 42, no. 29, pp. 18174-1818, 2017.

[134] H. Gholizade-Narm, S. A. Khajehoddin and M. Karimi-Ghartemani, "Reduced-Order Controllers Using Integrated Controller-Plant Dynamics Approach for Grid-Connected Inverters," *IEEE Transactions on Industrial Electronics,* vol. 68, no. 8, pp. 7444-7453, 2021.

[135] B. Li, W. Yao, L. Hang and L. Tolbert, "Robust proportional resonant regulator for grid-connected voltage source inverter (vsi) using direct pole placement design method," *IET Power Electron.,* vol. 5, no. 8, pp. 1367-1373, 2012.

[136] W. Chen and J. Lin, "One-Dimensional Optimization for Proportional–Resonant Controller Design Against the Change in Source Impedance and Solar Irradiation in PV Systems," *IEEE Transactions on Industrial Electronics,* vol. 61, no. 4, pp. 1845-1854, 2014.

[137] L. Herman, I. Papic and B. Blazic, ", "A Proportional-Resonant Current Controller for Selective Harmonic Compensation in a Hybrid Active Power Filter," *IEEE Transactions on Power Delivery,* vol. 29, no. 5, pp. 2055-2065, 2014.

[138] L. F. A. Pereira and A. S. Bazanella, "Tuning Rules for Proportional Resonant Controllers," *IEEE Transactions on Control Systems Technology,* vol. 23, no. 5, pp. 2010-2017, 2015.

[139] Q. An, J. Zhang, Q. An, and A. Shamekov, "Quasi-proportional-resonant controller based adaptive position observer for sensorless control of pmsm drives under low carrier ratio," *IEEE Transactions on Industrial Electronics,* vol. 67, no. 4, pp. 2564-2573, 2019.

[140] Q. An, J. Zhang, Q. An and A. Shamekov, "Quasi-Proportional-Resonant Controller Based Adaptive Position Observer for Sensorless Control of PMSM

Drives Under Low Carrier Ratio," *IEEE Transactions on Industrial Electronics,* vol. 67, no. 4, pp. 2564-2573, 2020.

[141] Y. Liu, W. Wu, Y. He, Z. Lin, F. Blaabjerg, and H. S. Chung, "An efficient and robust hybrid damper for LCL- or LLCL-based grid-tied inverter with strong grid-side harmonic voltage effect rejection," *IEEE Transactions on Industrial Electronics,* vol. 63, no. 2, pp. 926-936, 2016.

[142] S. A. Khajehoddin, M. Karimi-Ghartemani, and M. Ebrahimi, "Optimal and systematic design of current controller for grid-connected inverters," *IEEE Journal of Emerging and Selected Topics in Power Electronics,* vol. 6, no. 2, pp. 812-824, 2017.

[143] A. G. Yepes, F. D. Freijedo, J. Doval-Gandoy, O. L ´ opez, J. Malvar, ´ and P. Fernandez-Comesana, "Effects of discretization methods on the performance of resonant controllers," *IEEE Transactions on Power Electronics,* vol. 25, no. 7, pp. 1692-1712, 2010.

[144] A. G. Yepes, F. D. Freijedo, O. Lopez, and J. Doval-Gandoy, "High- ´ performance digital resonant controllers implemented with two integrators," *IEEE Transaction on Power Electronics,* vol. 26, no. 2, pp. 563-576, 2011.

[145] M. Karimi-Ghartemani, S. A. Khajehoddin, M. Mojiri, P. Jain, and A. Bakhshai, "A resonant controller with robust features for digital implementations at low sampling frequency," in *IECON 38th Annual Conf. on Industrial Elec. Society*, 2012.

[146] A. K. Seth and M. Singh, "Resonant controller of single-stage off-board EV charger in G2V and V2G modes," *IET Power Electronics,* vol. 13, no. 5, pp. 1086-1092, 2020.